Membrane Flutter in Inviscid Flow

by

Christiana Mavroyiakoumou

A dissertation submitted in partial fulfillment
of the requirements for the degree of
Doctor of Philosophy
(Applied and Interdisciplinary Mathematics and Scientific Computing)
in The University of Michigan
2022

Doctoral Committee:

Professor Silas Alben, Chair
Professor Karthik Duraisamy
Professor Robert Krasny
Professor Shravan Veerapaneni

Christiana Mavroyiakoumou

chrismav@umich.edu

ORCID iD: 0000-0001-5828-6855

Dedicated to my family

ACKNOWLEDGEMENTS

I would like to express my gratitude to my advisor, Professor Silas Alben, for his constant support and guidance at every stage of my Ph.D. at the University of Michigan. He has always been very generous with his time and I am grateful for his dedication, advice, patience, and encouragement to solve interesting, challenging problems. I have benefited immensely from our discussions, from his incredible mathematical and physical insight, and feedback throughout my thesis research. Working with such an outstanding mathematician has been a privilege and I could not have wished for a better advisor. The lessons that I have learned from him helped me grow as a mathematician and will be with me for the rest of my career. Thank you for everything!

I would also like to thank my committee members. Professor Karthik Duraisamy for welcoming me in his wonderful group at the Department of Aerospace Engineering and for teaching me about unsteady aero-acoustics and data-driven modeling techniques. I have been extremely lucky to be his student. I am also grateful to Professor Robert Krasny for his invaluable feedback, for comments and discussions on my work, and for his support, and to Professor Shravan Veerapaneni for his helpful feedback and for teaching me about fast algorithms. I have learned so much from all of you and I admire you all.

The Department of Mathematics at the University of Michigan has been a stimulating environment to learn mathematics and do research, with fantastic teachers,

great seminars, and a collaborative atmosphere among the graduate students. I am also thankful to the administrative staff at the Department of Mathematics and the support staff at the university's Advanced Research and Computing Technology Services (ARC-TS) who always provided me with timely assistance.

I am also indebted to my friends and close ones who made my graduate studies really enjoyable and with whom I shared many beautiful moments that I will always cherish. You made Ann Arbor feel like home. Finally, I am forever grateful to my parents and brother, for always being there for me and supporting me in every way possible. Thank you so much for all you have given me!

This work was generously supported by the NSF Mathematical Biology program under award number DMS-1811889, the Michigan Institute for Computational Discovery and Engineering (MICDE) Fellowship, the Rackham International Student Fellowship, and the Rackham Predoctoral Fellowship Award at the University of Michigan.

TABLE OF CONTENTS

LIST OF FIGURES

Figure

LIST OF TABLES

Table

LIST OF APPENDICES

Appendix

ABSTRACT

Despite the advantages associated with extensible membranes in biological and engineering applications, the majority of previous studies have focused on the motion of bending-dominated flexible bodies through a fluid flow. In this thesis, we develop a variety of mathematical models and numerical methods to analyze the small- and large-amplitude dynamics of thin membranes (of zero bending rigidity) with vortex-sheet wakes in two- and three-dimensional inviscid flows.

In chapter II, we study the dynamics of membranes initially aligned with a uniform background flow. This is a benchmark fluid-structure interaction that has previously been studied mainly in the small-deflection limit, where the flat state may be unstable. Here we study the initial instability and large-amplitude dynamics with respect to three parameters: membrane mass density, stretching rigidity, and pretension. With both membrane ends fixed, we find that all membranes become unstable by divergence below a critical pretension close to the value identified in previous studies, and converge to steady deflected shapes. With the leading edge fixed and trailing edge free, divergence and/or flutter occurs, and a variety of periodic and aperiodic oscillations are found. With both edges free, the membrane may also translate transverse to the flow, with steady, periodic, or aperiodic trajectories.

In chapter III, we investigate the instability of membranes in terms of growth rates, angular frequencies, and eigenmode shapes, by solving a nonlinear eigenvalue problem iteratively. When both membrane ends are fixed, the stability boundary is

fairly simple: light membranes become unstable by divergence and heavy membranes lose stability by flutter and divergence, which occurs for a pretension value that increases with the mass. With the leading edge fixed and trailing edge free, or both edges free, the membrane eigenmode shapes become more complicated and eigenmodes transition in shape across the stability boundary. We also compare our results against the simulations of the corresponding initial value problem in the growth regime and find excellent agreement.

In chapter IV, we consider membranes that are held by freely-rotating tethers and find that the tethered boundary condition allows a variety of unsteady large-amplitude motions—both periodic and chaotic. We characterize the oscillations over ranges of: membrane mass density, stretching stiffness, pretension, and tether length and determine the region of instability and small-amplitude behavior by solving a nonlinear eigenvalue problem. We additionally consider a simplified model: an infinite periodic membrane, which yields a regular eigenvalue problem, analytical results, and asymptotic scaling laws. We find qualitative similarities among all three models in terms of the oscillation frequencies and membrane shapes at small and large values of membrane mass, pretension, and tether length/stiffness.

In chapter V, we develop a model and numerical method to study the large-amplitude flutter of rectangular membranes that shed a trailing vortex-sheet wake in a 3D inviscid fluid flow. For all 12 combinations of boundary conditions at the membrane edges we compute the stability thresholds and the subsequent large-amplitude dynamics across the same three-parameter space as before. We find that 3D dynamics in the 12 cases naturally form four groups based on the conditions at the leading and trailing edges. The conditions at the side edges, though generally less important, may have qualitative effects on the membrane dynamics—e.g. steady versus

unsteady, periodic versus chaotic, or the variety of spanwise curvature distributions—depending on the group and the physical parameter values.

CHAPTER I

Introduction

1.1 Motivation

Interactions between flexible structures and high-Reynolds-number flows are ubiquitous in nature and engineering applications. The physical mechanisms that govern these fluid-structure interactions provide us with important insights into the fluid dynamics of biolocomotion. For example, fish can exploit energy from surrounding vortices and move efficiently by undulating their bodies [49, 189], or synchronize their motions with the oncoming vortices [104]. These observations have inspired engineers to design and manufacture continuously deformable robots that exhibit these behaviors [98, 101, 148]. Birds and other flying animals also take advantage of such mechanisms to achieve efficient locomotion. In particular, bats—one of nature's most agile fliers [27, 157, 158, 164, 165]—can adapt to the surrounding flow conditions by deforming their thin, compliant membrane wings.

An extensible membrane is a soft material that undergoes significant stretching in a fluid flow and has negligible bending modulus. When it is aligned with a fluid flow, the surrounding fluid forces can cause it to flutter and become unstable. Being able to predict the onset of membrane instability across parameter space, either by flutter, divergence, or a combination of the two, is fundamental to a wide range

of applications. Stable membranes can be used in a variety of configurations in pneumatic membrane structures such as roofs in civil engineering [64, 92, 166–168], supersonic aircraft and rockets [15, 118, 192], ballutes for space exploration [142, 152], parachutes [135, 161], and bio-inspired propulsion: aircraft and shape-morphing airfoils [74, 79, 102, 137, 151, 191], micro-air vehicles [1, 11, 103, 157, 160], and sails [30, 91, 126, 127, 130].

When a rigid wing moves through a flow its upper surface may experience flow separation and significant reductions in aerodynamic efficiency in both steady and unsteady flows, thus limiting the aircraft's maneuverability and performance. However, a flexible membrane is able to adapt quickly to unsteady airflow conditions by assuming a deformed shape that can inhibit flow separation and enhance aircraft maneuverability. [137] studied how a membrane wing adjusts its shape to fluid pressure loading at various angles of attack. [191] coupled thin airfoil theory with a membrane equation to study the effects of wing compliance, inertia, and flapping kinematics on aerodynamic performance. The passive adaptivity of a membrane wing has the potential to increase lift forces and delay the occurrence of stall to higher angles of attack for micro-air vehicles (MAVs) [74, 102, 160]. [151] used electrostatic forces to control a membrane shape and delay the transition from a laminar boundary layer, reducing viscous drag. Recent developments in membrane aerodynamics are reviewed in [103, 185].

There is a wealth of literature describing the fluid dynamics induced by the motion of a flexible body through a fluid flow. In most studies the body motion is bending-dominated, with a moderate bending modulus, but essentially inextensible [3, 10, 14, 42, 43, 93, 117, 153, 154, 173, 178, 179, 196, 207, 208, 210]. The important case of extensible *membranes* of zero bending modulus has received somewhat less attention. In this

thesis we develop models and numerical methods for extensible membranes with a vortex-sheet wake. This extends the work on inextensible bending bodies [2, 4].

1.2 Literature Review

1.2.1 Range of Parameters

The initial, small-amplitude stage of the flutter instability has been the focus of several experimental, theoretical, and numerical studies. We classify these works and the results within this thesis in terms of three dimensionless parameters: membrane mass density (R_1), stretching modulus (R_3), and pretension (T_0), with typical ranges shown in table 1.1. The methods developed in this thesis allow us to consider wider ranges of the parameters than those of the previous studies.

Table 1.1: Typical values of parameter ranges relevant to our current work as used in previous membrane studies. Computational (^{c}), experimental (^{e}), or theoretical (^{t}) ranges of the dimensionless body mass density R_1, stretching modulus R_3, and pretension T_0.

Reference	Material	$R_1 = \dfrac{\rho_s h}{\rho_f L}$	$R_3 = \dfrac{Eh}{\rho_f U^2 L}$	$T_0 = \dfrac{\overline{T}}{\rho_f U^2 LW}$
[128]^t	sail	0–6	—	0–2
[99]^e	sail	0–0.8	$10^1, 50,\ 10^2, 500, 10^3$	—
[168]$^{e\,\&\,t}$	latex rubber	$0.1, 1$	—	$130.6, 217$
[79]$^{c\,\&\,e}$	latex rubber	2.4	$100, 200, 400, 614$	$4, 10, 20, 30.7$
[184]^c	—	0–80	—	0–6
[124]^c	—	0–60	—	0–3
[32]^e	silicone rubber	2.5–31.25	3.75×10^{-5}–0.04	1–4
[33]^e	silicone rubber	2.5–31.25	3.75×10^{-5}–0.04	1–4
Chapter II$^{c\,\&\,t}$	—	10^{-3}–10^2	10^0–10^4	10^{-3}–10^3
Chapter III$^{c\,\&\,t}$	—	10^{-3}–10^3	—	$10^{-1.5}$–10^2
Chapter IV$^{c\,\&\,t}$	—	10^{-4}–10^4	$10^{0.5}$–10^4	10^{-3}–10^2
Chapter V$^{c\,\&\,t}$	—	10^{-3}–10^2	10^0–10^4	$10^{-1.5}$–10^2

Next, we give a brief summary of the contents of each work mentioned in table 1.1. [128] used an infinite periodic membrane model with a low-mode approximation and found that stability is lost through divergence. [99] used a vortex sheet model to study a more complex situation—the motions of a sail membrane under harmonic

perturbations of the trailing edge and with randomly perturbed inflow velocities. [168] studied the membrane flutter threshold and divergence modes theoretically, with some experimental validation. Although most works omit specific values of the thickness ratio h/L and the bending modulus $R_2 = Eh^3/(12\rho_f U^2 L^3) = R_3(h/L)^2/12$, an example is given in [79] for a latex rubber, where the thickness ratio is $h/L = 1/750$ and the bending modulus is therefore about a factor of 10^{-7} smaller than R_3. There they studied a heaving and pitching membrane airfoil in a fluid stream numerically at Reynolds number 2500, and found elastic modulus and prestress parameters that led to enhanced thrust and propulsive efficiency. [184] presented a more detailed flutter threshold calculation using an inviscid, small amplitude vortex sheet model. [124] compared a reduced-order model with direct numerical simulations to study the effect of Reynolds number on the flutter stability threshold and small-amplitude membrane deflection modes.

[32] modeled the material properties of ultrasoft dielectric elastomers over a range of elastic properties, prestretch, and thicknesses. They measured the mechanical response of the silicone membranes and found that stiffer membranes harden at lower stretch ratios due to the increased fraction of polymer chains in them. [33] studied the deformations, forces, and flow fields associated with a highly compliant membrane disk placed head-on in a uniform flow field. With increasing flow velocity, the membrane deforms hyper-elastically into parachute-like shapes. A resulting drag increase correlates with the unsteady fluid-structure interactions between the membrane and the flow.

So far there has been relatively little work on the large-amplitude dynamics following the initial flutter instability, and this is the focus of chapters II and V. Throughout this thesis, we set the bending modulus R_2 to zero and study the dynamics of mem-

branes over wide ranges of the remaining parameters—R_1, R_3, and T_0—as well as the tether length or stiffness (in chapter IV). There unsteady dynamics are possible because, unlike in previous studies, the membrane is attached to inextensible rod tethers whose lengths set the transition between steady and unsteady motions.

1.2.2 Boundary Conditions

In an early work, Nielsen [130] studied a membrane with both edges fixed in a two-dimensional flow, and determined the critical value of the pretension parameter that gives rise to a fully convex membrane shape. An overview of early models based on potential-flow aerodynamics can be found in [126]. Previous works have studied the difference between the flutter of membranes with zero bending rigidity and plates in the limit of zero bending rigidity. Because the bending rigidity term has the highest (fourth-order) spatial derivative, it is a singular limit, and thus the two problems can have significant differences. In the case of panels in supersonic flows, the membrane is stable whereas the plate can be unstable to flutter in the limit [39, 82, 159]; see also [38, pp. 25–26]. This so-called "membrane paradox" also arises in solar sails [53], and a related boundary-layer phenomenon occurs for heaving plates, hanging under gravity [110]. Over the past few decades, theoretical [128, 168], computational [79, 113, 124, 184], and experimental [99] studies of membrane stability have revealed a wide range of membrane stability behavior and dynamics with various boundary conditions.

In chapters II and III we investigate how the membrane dynamics change when using different boundary conditions at the two ends of the membrane. In the first case, fixed–fixed, the membrane ends were held fixed, as in most previous studies of membrane flutter [99, 124, 168, 184]. In the second case, fixed–free, we allowed the trailing edge of the membrane to move, but only in the direction perpendicular to the

oncoming flow. This gives the free-end boundary condition for a string or membrane in classical mechanics [45, 59], where the membrane end has horizontal slope. The physical meaning of the boundary condition is that the end slides without friction perpendicularly to the membrane's flat equilibrium state (for example, in [45] the end is attached to a frictionless, massless ring). The third case, free–free, corresponds to a membrane whose leading and trailing edges are both free to move in the vertical direction.

Although well known in classical mechanics, free-end boundary conditions have not been studied much in membrane (as opposed to beam/plate) flutter problems. In [74], the authors study membrane wings with partially free trailing edges and find that trailing edge fluttering may occur at relatively low angles of attack. Another recent experimental study found that membrane wing flutter can be enhanced by the vibrations of flexible leading and trailing edge supports [13]. Partially free edges occur also in sails: the shape of a sail membrane can be controlled by altering the tension in cables running along its free edges [91]. Flutter can occur when the tension in these edges is sufficiently low [30]. A related application is to energy harvesting by membranes mounted on tensegrity structures (networks of rigid rods and elastic fibers) and placed in fluid flows [163, 204]. In such cases the membrane ends have some degrees of freedom akin to the free-end boundary conditions defined above.

1.2.3 Three-dimensional Flows

The regions in parameter space where membrane flutter occurs have been predicted by linear models that mostly assume an infinite membrane span and two-dimensional (2D) flow. In chapter V of this thesis we use a three-dimensional (3D) inviscid flow model based on the vortex lattice method to study membrane stability in the linear regime of small deflections as well as large-amplitude nonlinear mem-

brane dynamics. We find qualitative changes in flutter behavior in some cases due to three-dimensionality.

Only a small number of studies have considered fully-coupled interactions of flexible bodies and 3D inviscid flows. The formulation of the mechanical force balance laws and the numerical methods are more complicated in 3D than in 2D and the computational expense is much higher. Inviscid flow models such as the vortex lattice method are widely used to model viscous high-Reynolds-number flows for aquatic and aerodynamic propulsion [17, 86, 88, 116, 156, 202] because the computational cost is generally much lower than for direct solvers (e.g., in the case of complex and deforming body geometries, immersed-boundary, lattice-Boltzmann, and deforming-mesh methods [72, 90, 199, 209]). In the inviscid models computational elements are distributed along surfaces rather than throughout the flow volume. However, traditional inviscid approximations of flow separation work well only in certain cases such as low-angle-of-attack airfoils where trailing edge separation is dominant. Recently leading-edge separation has been included in such models [100, 134, 141].

Several recent works have studied the effect of various dimensionless control parameters such as Reynolds number, density ratio, shear modulus, and aspect ratio on the flutter of one or more thin plates or flags with bending rigidity in three-dimensional viscous, high-Reynolds-number flows [18, 26, 37, 76, 180, 206]. Immersed boundary methods were used by [76, 180], while [206] used a fictitious domain method and [18] used a coordinate transformation method.

Immersed boundary methods have also been used to study a number of 3D swimming problems, such as the self-propulsion of flapping flexible plates [112, 174], the role of active muscle contraction, passive body elasticity and fluid forces in forward swimming [20, 34, 70, 72, 119], and the propulsive forces acting on flexible fish bod-

ies [71].

Boundary element methods have helped identify the effects of body kinematics on thrust production and efficiency of 3D swimmers with non-deforming [106, 107] and deforming wakes [211]. [120] used a boundary element method to examine the self-propelled swimming of undulatory fins and manta rays [48], and to derive three-dimensional heaving and pitching scaling laws [16, 17].

There are relatively few studies of 3D coupled interactions of inviscid flows and flexible bodies. Recently, [66, 68] used nonlinear beam theory and the vortex-lattice method to analyze the limit cycle oscillations of a rectangular plate and plate vibration under harmonic forced excitation [67]. Previously [52, 54] studied the 3D linear stability problem for a flexible plate in an inviscid flow with various boundary conditions. [175,176] used the method to study the stability of delta wings and rectangular plates, and [122] reviewed the vortex lattice method in similar applications.

1.3 Thesis Overview

We now provide an overview of this thesis and emphasize the aims and main contributions of each chapter. Any appendices appear after the main body of all the chapters and all references may be found at the end of the thesis. Broadly speaking, chapters II–IV address membrane-fluid interactions in *two-dimensional* inviscid flow and chapter V considers small- and large-amplitude dynamics of membranes in *three-dimensional* inviscid flow.

1.3.1 Chapter II: Large-amplitude Membrane Flutter in Inviscid Flow

We begin by focusing on extensible membrane flutter: *how a membrane, initially aligned with a fluid flow, becomes unstable to transverse deflections and eventually reaches steady-state large-amplitude dynamics.* We classify the membrane dynamics

in terms of three dimensionless parameters:

- membrane mass density (R_1),
- stretching modulus (R_3),
- pretension (T_0)—the tension in the membrane in its flat, undeflected state.

The governing equations are the extensible membrane equation:

$$\overbrace{R_1 \partial_{tt}\zeta}^{\text{mass}\times\text{acceleration}} - \overbrace{\underbrace{\partial_\alpha((T_0 + R_3(\partial_\alpha s - 1))\hat{\mathbf{s}})}_{\text{stretching resistance}} = \underbrace{-[p]^+_- \partial_\alpha s\, \hat{\mathbf{n}}}_{\text{pressure jump}}}^{\text{forces}},$$

the unsteady Bernoulli equation (which couples the membrane to the fluid), and the Birkhoff-Rott equation (to evolve the vortex sheet).

Aim 1: to determine the typical large-amplitude steady-state dynamics that occur when the flat state is unstable, for a wide range of parameters and for three canonical boundary conditions—both ends fixed, one end fixed and one free, and both free.

Aim 2: to approximate the large-amplitude behaviors using asymptotic scaling laws. For example, we find that the time-averaged deflection scales as $R_3^{-1/2}$ and that the temporal frequency scales as $R_1^{-1/2}$.

We approximate the thin viscous boundary layers along the body with vortex sheets, which are advected from the membrane's trailing edge into the flow downstream. Such flows are challenging to simulate directly due to the need to resolve sharp layers of vorticity in the vicinity of an unsteady, deforming solid boundary. In this approximation we only compute flow quantities on one-dimensional contours (the body and the vortex sheet wake), which is orders of magnitude less expensive to compute than fully-resolved viscous simulations. We use an explicit two-step Adams-Bashforth scheme for the free vortex sheet evolution. For the membrane and bound

vortex sheet equations we implement a nonlinear quasi-Newton solver (Broyden's method).

This work is the first time a large-amplitude model has been developed to study the dynamics of membranes following the initial flutter instability for a wide range of parameter values. We believe that our study enhances our understanding of stability, leading to an improved understanding of micro-air and underwater vehicles with membrane propulsors having a wide range of physical properties.

This chapter is published in the *Journal of Fluid Mechanics* [113].

1.3.2 Chapter III: Eigenmode Analysis of Membrane Stability in Inviscid Flow

In this chapter, we investigate in more detail the small-amplitude fluid flow solutions by focusing on the linearized version of the membrane-vortex-sheet model. By assuming a certain form for the solutions we convert the problem to a quadratic eigenvalue problem:

$$[\sigma^2 A_2 + \sigma A_1 + A_0(\sigma_0)]w = 0,$$

where the matrices A_2, A_1, A_0 are known from the governing equations. Since a generic perturbation is a superposition of all the eigenmodes multiplied by the corresponding $e^{i\sigma t} = e^{i\sigma_{\mathrm{R}} t} e^{-\sigma_{\mathrm{I}} t}$, we classify the instability of generic perturbations in the (R_1, T_0) parameter space based on the eigenmode shape and the value of σ_{R} for the most unstable mode (with the most negative σ_{I}) at a given (R_1, T_0).

Aim 1: to predict the onset of membrane instability across parameter space, either by flutter, divergence, or a combination of the two, for three boundary conditions—both ends fixed, one end fixed and one free, and both free.

Aim 2: to show quantitative agreement with unsteady time-stepping simulations (chapter II) for small amplitude motions.

We solve the nonlinear eigenvalue problem iteratively with large ensembles of initial guesses, for the three boundary conditions. Due to the vortex wake, simple exact eigenmode solutions are difficult to obtain, but in this work we present a comprehensive characterization of the modes and growth rates in the vicinity of the stability boundary.

A version of this method was previously used to study the flutter instability of bending beams in inviscid flows [3]. There, solutions were obtained by continuation, starting from the known oscillation modes of a beam in a vacuum. Here we study membranes and find that the continuation approach is more susceptible to jumping between different eigenmode branches as we vary parameters. Therefore, we solve the nonlinear eigenvalue problem using dense meshes of initial eigenvalue guesses that cover the range of lower-mode states. As a result, we obtain a larger ensemble of eigenmodes at each parameter value set. We obtain good agreement with the stability results in chapter II, but are able to extend the results to much larger and smaller values of the membrane-to-fluid density ratio, and resolve shapes with finer structures.

Previous work by other groups was limited to the fixed–fixed case and a smaller range of membrane mass densities (R_1). The time-stepping simulations in chapter II are difficult to resolve for small-amplitude motions at small R_1 due to limited spatial resolution, and at large R_1 due to the very slow growth of instabilities. In this chapter, our nonlinear eigenmode solver is a less expensive alternative to study the stability problem.

This chapter is published in *Physical Review Fluids* [115].

1.3.3 Chapter IV: Dynamics of Tethered Membranes in Inviscid Flow

Our work in chapter II has shown that membranes with fixed ends—the focus of most membrane studies—converge to a fixed steady deflected shape when they become unstable. With one or both ends free, unsteady motions are possible, but such boundary conditions have not been realized experimentally. In this chapter, we consider a simple physical setup that can be carried out in an experiment—a membrane held by tethers with hinged ends. In particular, we attach the membrane's leading and trailing edges to two inextensible rods of equal length R. We show that a variety of unsteady, periodic, and chaotic oscillations can occur. The dynamics obtained from these tethered membranes could be useful in the design of systems for energy harvesting from flows.

Aim 1: to analyze how large-amplitude dynamics depend on four key parameters: membrane mass density, stretching stiffness, pretension, and tether length.

Aim 2: to investigate via a nonlinear eigenvalue problem how the stability properties of tethered membranes change.

Aim 3: to study a more analytically tractable model than the nonlinear eigenvalue problem and compute asymptotic scaling laws for the frequencies, growth rates, and eigenmodes' dependences on membrane pretension and mass density.

To achieve Aim 3 we propose an infinite membrane model mounted on a periodic array of Hookean springs with spring stiffness k_s (localized spring forces at $x = 0, \pm 1, \pm 2, ...$). To solve this problem we use approximate delta functions for the spring forces and solve for the spatial Fourier modes of $y(x,t)$. This model corresponds to a standard eigenvalue problem, and is much faster to compute than the nonlinear eigenvalue problem of the membrane-vortex-wake model. We can thus extend our

study to a much wider range of the physical parameters R_1, T_0, and k_s.

This chapter is published in *Journal of Fluids and Structures* [114].

1.3.4 Chapter V: Membrane Flutter in Three-dimensional Inviscid Flow

In chapters II–IV we studied membrane dynamics in a 2D flow, where the membrane is a 1D curvilinear segment that undergoes small and large deflections. In this chapter, we consider a 2D membrane in a 3D flow.

We develop a model and numerical method to investigate the large-amplitude flutter of thin membranes, with zero bending rigidity, that shed a flat trailing vortex-sheet wake in a 3D inviscid fluid flow. The computational method involves a 3D nonlinear, unsteady vortex-lattice method [88] and Broyden's method [140] to solve for the coupled system of equations for the membrane position, vortex sheet strength, and pressure jump, using suitable initial and boundary conditions.

Aim 1: to determine the stability boundary location in mass-pretension parameter space, for a total of 12 distinct boundary conditions.

Aim 2: to compute scaling laws for the deflection magnitudes and oscillation frequencies.

Aim 3: to classify the large-amplitude dynamics for all 12 boundary conditions based on the membrane mass density ratio, pretension, and stretching modulus and draw meaningful conclusions about the effect of three-dimensionality on their behavior.

To our knowledge this work is the first 3D study of large-amplitude dynamics of membranes (of zero bending rigidity) in inviscid flows.

This chapter is currently under review.

CHAPTER II

Large-amplitude Membrane Flutter in Inviscid Flow

2.1 Introduction

In this chapter, we study the large-amplitude flutter of membranes (of zero bending rigidity) with vortex-sheet wakes in 2D inviscid fluid flows. We apply small initial deflections and track their exponential decay or growth and subsequent large-amplitude dynamics in the space of three dimensionless parameters: membrane pretension, mass density, and stretching modulus.

Previous work investigated the nonlinear dynamics of a periodically pitching flexible body in a fluid stream [4] and the flapping-flag instability [10], among many other studies of this problem [7, 25, 43, 76, 117, 153, 177]. As bending rigidity is decreased below the flutter threshold, the flag transitions from periodic to chaotic dynamics. Our model, presented in this chapter, includes the separation of vortex sheets at sharp edges [83, 84, 96, 131], and regularizes free vortex sheets to avoid singularities [5, 21, 28, 94, 132].

In this model, vortex sheets approximate the thin viscous boundary layers along the body, which are advected from its trailing edge into the flow downstream. This can be regarded as the inviscid limit of the viscous flow, and gives a good representation of the large-scale features of the flow and the vortex wake dynamics

at Reynolds numbers of $\mathcal{O}(10^2$–$10^5)$ [131, 155, 156, 203]. These flows are challenging to simulate directly due to the need to resolve sharp layers of vorticity in the vicinity of an unsteady, possibly deforming solid boundary. The immersed boundary method [50, 61, 63, 136, 171, 181, 190, 210] can successfully simulate this class of problems. Very fine grids are needed to resolve the vorticity, and these are refined adaptively for efficiency [60, 147]. However, by only computing flow quantities on one-dimensional contours (the body and the vortex sheet wake), the vortex sheet model is typically much less expensive to compute when the far-field wake is approximated, as described at the end of this thesis, in appendix B.

With both ends fixed, all the membranes converge to steady deflected shapes with single humps that are nearly fore-aft symmetric, except when the deformations are unrealistically large. With leading edges fixed and trailing edges free to move in the transverse direction, the membranes flutter periodically at intermediate values of mass density. As mass density increases, the motions are increasingly aperiodic, and the amplitudes increase and spatial and temporal frequencies decrease. As mass density decreases from the periodic regime, the amplitudes decrease and spatial and temporal frequencies increase until the motions become difficult to resolve numerically. With both edges free to move in the transverse direction, the membranes flutter similarly to the fixed–free case but also translate vertically with steady, periodic, or aperiodic trajectories, and with nonzero slopes that lead to small angles of attack with respect to the oncoming flow.

The rest of the chapter is as follows: §2.2 presents the membrane and vortex sheet model, §2.3 presents the membrane dynamics for each of the three sets of boundary conditions: fixed–fixed, fixed–free, and free–free. We characterize the dynamics in terms of the time-averaged deflection of the membrane, the mean frequency, and

the number of zero crossings which is associated with the waviness of the membrane profile. §2.4 summarizes our findings.

2.2 Membrane-vortex-sheet Model

We first consider the motion of an extensible membrane that is fixed at two endpoints and held in a two-dimensional fluid flow, like much of the previous work. A uniform background flow is prescribed with velocity U, directed parallel to the chord connecting the endpoints (see figure 2.1). The instantaneous position of the membrane is given by $\mathbf{X}(\alpha, t) = (x(\alpha, t), y(\alpha, t))$, parameterized by the material coordinate $\alpha, -L \leq \alpha \leq L$ (L is half the chord length), and time t. It is convenient to also describe the membrane position in complex notation, $\zeta(\alpha, t) = x(\alpha, t) + iy(\alpha, t)$. The inviscid flow can be represented by a vortex sheet—a curve across which the tangential velocity component is discontinuous [149]—and whose position and strength evolve in time. The vortex sheet consists of two parts. One is "bound" (it coincides with the membrane, for $-L \leq \alpha \leq L$), and the other is "free," emanating from the trailing edge of the membrane at $\alpha = L$. The bound and free vortex sheets have strength densities denoted by γ and positions denoted by ζ.

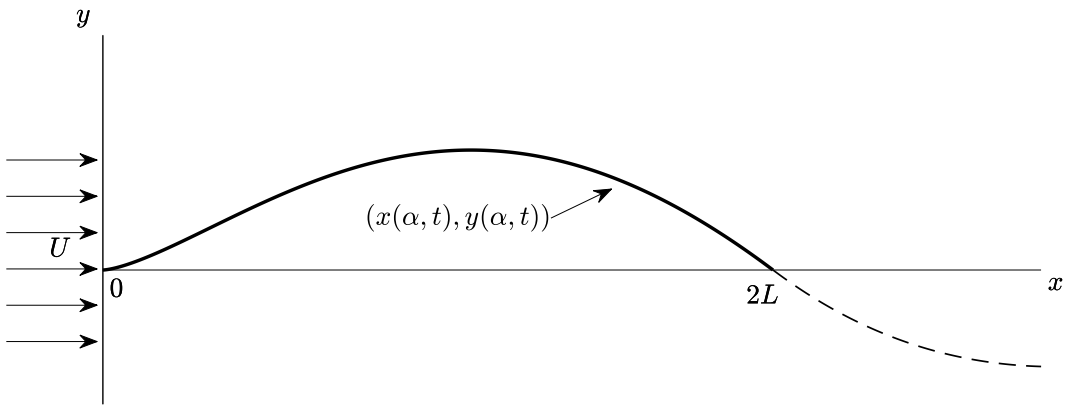

Figure 2.1: Schematic diagram of a flexible membrane (solid curved line) at an instant in time. Here $2L$ is the chord length (the distance between the endpoints), U is the oncoming flow velocity, $(x(\alpha, t), y(\alpha, t))$ is the membrane position, and the dashed line is the free vortex sheet wake.

The membrane dynamics are described by the unsteady extensible elastica equation with body inertia, stretching resistance, and fluid pressure loading [169], obtained by writing a force balance equation for a small section of membrane lying between α and $\alpha + \Delta\alpha$:

(2.1)

$$\rho_s h W \partial_{tt}\zeta(\alpha,t)\Delta\alpha = T(\alpha+\Delta\alpha,t)\hat{\mathbf{s}} - T(\alpha,t)\hat{\mathbf{s}} - [p](\alpha,t)\hat{\mathbf{n}}W\left(s(\alpha+\Delta\alpha,t) - s(\alpha,t)\right).$$

Dividing by $\Delta\alpha$ and taking the limit $\Delta\alpha \to 0$, we obtain:

$$\rho_s h W \partial_{tt}\zeta(\alpha,t) = \partial_\alpha(T(\alpha,t)\hat{\mathbf{s}}) - [p](\alpha,t)W\partial_\alpha s\hat{\mathbf{n}}, \tag{2.2}$$

where ρ_s is the mass per unit volume of the undeflected membrane, h is its thickness, and W is its out-of-plane width, all uniform along the length. The material coordinate $\alpha \in [-L, L]$ is the x-coordinate of the membrane in the initial flat, uniformly prestretched state. Other quantities that appear in (2.2) are $\hat{\mathbf{s}}, \hat{\mathbf{n}} \in \mathbb{C}$, which represent the unit vectors tangent and normal to the membrane, respectively,

$$\hat{\mathbf{s}} = \partial_\alpha\zeta(\alpha,t)/\partial_\alpha s(\alpha,t) = e^{i\theta(\alpha,t)} \quad \text{and} \quad \hat{\mathbf{n}} = i\hat{\mathbf{s}} = ie^{i\theta(\alpha,t)}, \tag{2.3}$$

with $\theta(\alpha,t)$ the local tangent angle, $s(\alpha,t)$ the local arc length coordinate, and $\kappa(\alpha,t) = \partial_\alpha\theta/\partial_\alpha s$ the membrane's curvature. $[p](\alpha,t)$ is the local pressure difference across the membrane, from the side toward which $\hat{\mathbf{n}}$ points to the other side.

The membrane tension $T(\alpha,t)$ is given by linear elasticity [22, 23, 123, 125]:

$$T(\alpha,t) = \overline{T} + EhW(\partial_\alpha s(\alpha,t) - 1), \tag{2.4}$$

where E is the Young's modulus. Thus the tension is a constant $\overline{T}$, the "pretension," in the (initial) undeflected equilibrium state $\zeta(\alpha,0) = \alpha$.

2.2.1 Nondimensionalization

We nondimensionalize the governing equations by the density of the fluid ρ_f, the half-chord L, and the imposed fluid flow velocity U. In particular, we use

$$\tilde{t} = \frac{t}{L/U}, \quad (\tilde{\zeta}, \tilde{\alpha}, \tilde{s}) = \frac{(\zeta, \alpha, s)}{L}, \quad \widetilde{[p]} = \frac{[p]}{\rho_f U^2}. \tag{2.5}$$

The membrane equation (2.2) becomes

$$\frac{\rho_s h U^2 W}{L} \widetilde{\partial_{tt}\zeta} = \frac{1}{L} \widetilde{\partial_\alpha}[(\overline{T} + EhW(\widetilde{\partial_\alpha s} - 1))\hat{\mathbf{s}}] - \rho_f U^2 W \widetilde{[p]} \widetilde{\partial_\alpha s} \hat{\mathbf{n}}, \tag{2.6}$$

with dimensionless quantities (and their dimensionless derivatives) denoted by tildes. Dividing (2.6) by $\rho_f U^2 W$ throughout yields

$$\frac{\rho_s h}{\rho_f L} \widetilde{\partial_{tt}\zeta} = \frac{1}{\rho_f U^2 L W} \widetilde{\partial_\alpha}[(\overline{T} + EhW(\widetilde{\partial_\alpha s} - 1))\hat{\mathbf{s}}] - \widetilde{[p]} \widetilde{\partial_\alpha s} \hat{\mathbf{n}}. \tag{2.7}$$

Thus the dimensionless membrane equation (dropping tildes) is

$$R_1 \partial_{tt}\zeta - \partial_\alpha \left((T_0 + R_3(\partial_\alpha s - 1))\hat{\mathbf{s}}\right) = -[p]\partial_\alpha s \hat{\mathbf{n}}. \tag{2.8}$$

The dimensionless parameters of the membrane are

$$R_1 = \frac{\rho_s h}{\rho_f L}, \quad T_0 = \frac{\overline{T}}{\rho_f U^2 L W}, \quad \text{and} \quad R_3 = \frac{Eh}{\rho_f U^2 L}, \tag{2.9}$$

where R_1, T_0, and R_3 are the dimensionless membrane mass density, pretension, and stretching modulus, respectively. We assume that the thickness ratio h/L is small, but ρ_s/ρ_f may be large, so R_1 may assume any non-negative value. We have neglected bending rigidity, denoted R_2 in [10]. In the extensible membrane regime studied here, R_3 is finite, so $R_2 = R_3 h^2/12L^2 \to 0$ in the limit $h/L \to 0$. By contrast, the inextensible beam or plate regime studied previously [7,25,43,76,117,153,177] has R_2 finite and $R_3 \to +\infty$ as $(h/L)^{-2}$ in the limit $h/L \to 0$, resulting in inextensibility. We have also neglected the effects of rotary inertia and the Poisson ratio (the transverse

contraction due to axial stretching), which have usually been neglected at leading order in nonlinear membrane models [125] and the aforementioned membrane studies. The rotary inertia and bending rigidity terms are given in [169], and those involving Poisson ratio are given in [125].

For large-Reynolds-number flows, there are thin viscous boundary layers along the sides of the membrane. Across these boundary layers, the component of fluid velocity that is tangent to the membrane is brought to zero on the membrane [19]. When the fluid in the boundary layer is advected off of the membrane's trailing edge, a free shear layer forms [5, 149]. In the limit of large Reynolds number, the two boundary layers tend to vortex sheets which coincide as a single bound vortex sheet (approximating the body thickness as zero for the fluid computation). The free shear layer tends to a free vortex sheet [149]. The free sheet circulation is defined as an integral of the vortex sheet strength γ (the jump in the tangential component of the fluid velocity) over the free vortex sheet

$$\Gamma(s,t) = -\int_s^{s_{\max}} \gamma(s',t)\,\mathrm{d}s', \quad 0 < s < s_{\max}, \tag{2.10}$$

where s is arc length along the free sheet, starting from 0 where the free sheet meets the membrane's trailing edge and ending at $s_{\max}$ at the free sheet's far end. Following [83] and [4] we define the (negative of the) total circulation in the free sheet:

$$\Gamma_+(t) = \Gamma(0,t) = -\int_0^{s_{\max}} \gamma(s,t)\,\mathrm{d}s. \tag{2.11}$$

The complex conjugate of the flow velocity $\mathbf{u} = (u_x, u_y)$ at any point z in the flow (not on the vortex sheets) can be calculated in terms of γ by integrating the vorticity

in the bound and free vortex sheets against the Biot-Savart kernel [149]:

(2.12)
$$u_x(z) - iu_y(z) = 1 + \frac{1}{2\pi i}\int_{-1}^{1} \frac{\gamma(\alpha,t)}{z-\zeta(\alpha,t)}\partial_\alpha s(\alpha,t)\,\mathrm{d}\alpha + \frac{1}{2\pi i}\int_{0}^{s_{\max}} \frac{\gamma(s,t)}{z-\zeta(s,t)}\,\mathrm{d}s,$$

with unity on the right hand side representing the imposed background flow and the dimensionless material coordinate α ranging from -1 to 1 on the membrane. By Kelvin's circulation theorem, Γ is conserved at fixed material elements of the free vortex sheet. Thus we reparameterize the free sheet position as $\zeta(\Gamma,t)$ and evolve the position at a fixed Γ simply by following the local fluid velocity. This is done by taking the average of the limits of (2.12) as z approaches $\zeta(\Gamma,t)$ from both sides [149]:

(2.13)
$$\frac{\partial\overline{\zeta}}{\partial t}(\Gamma,t) = 1 + \frac{1}{2\pi i}\int_{-1}^{1} \frac{\gamma(\alpha,t)}{\zeta(\Gamma,t)-\zeta(\alpha,t)}\partial_\alpha s(\alpha,t)\,\mathrm{d}\alpha - \frac{1}{2\pi i}\fint_{0}^{\Gamma_+(t)} \frac{\mathrm{d}\Gamma'}{\zeta(\Gamma,t)-\zeta(\Gamma',t)}.$$

In (2.13), $\partial\overline{\zeta}/\partial t$ is the complex conjugate velocity at $\zeta(\Gamma,t)$, and the second integral is a Cauchy-principal-value integral. We have reparameterized the free sheet integral using $\gamma\,\mathrm{d}s = -\mathrm{d}\Gamma$. This form of the integral appears in the Birkhoff-Rott equation for the evolution of a free vortex sheet [83, 84, 139, 149]. In this form $\mathrm{d}\Gamma$ may have either sign.

We may solve for the bound vortex sheet strength $\gamma(\alpha,t)$ in terms of the membrane velocity by equating the components of the fluid and membrane velocities normal to the membrane ("the kinematic condition"), which are found by taking the average of the limits of (2.13) as z approaches the *membrane* from both sides:

(2.14)
$$\mathrm{Re}(\hat{\mathbf{n}}\,\partial_t\overline{\zeta}(\alpha,t)) = \mathrm{Re}\left(\hat{\mathbf{n}}\left(1 + \frac{1}{2\pi i}\fint_{-1}^{1} \frac{\gamma(\alpha',t)\partial_\alpha s(\alpha',t)}{\zeta(\alpha,t)-\zeta(\alpha',t)}\,\mathrm{d}\alpha' - \frac{1}{2\pi i}\int_{0}^{\Gamma_+(t)} \frac{\mathrm{d}\Gamma'}{\zeta(\alpha,t)-\zeta(\Gamma',t)}\right)\right).$$

When the left hand side and the second integral on the right hand side of (2.14) are known, the general solution $\gamma(\alpha,t)$ has inverse-square-root singularities at $\alpha = \pm 1$.

Therefore we define $v(\alpha,t)$, the bounded part of $\gamma(\alpha,t)$, by

$$\gamma(\alpha,t) = \frac{v(\alpha,t)}{\sqrt{1-\alpha^2}}. \tag{2.15}$$

An additional scalar constraint is required to uniquely specify the solution γ (or v) to (2.14). It is the conservation of total circulation (Kelvin's circulation theorem):

$$\int_{-1}^{1} \gamma \partial_\alpha s \, \mathrm{d}\alpha = \int_{-1}^{1} \frac{v(\alpha,t)}{\sqrt{1-\alpha^2}} \partial_\alpha s \, \mathrm{d}\alpha = \Gamma_+(t). \tag{2.16}$$

In (2.13) and (2.14) it is helpful to replace the free-sheet integral with a regularized version to avoid singularities in the sheet curvature [94]. The second integral in (2.13) becomes

$$-\frac{1}{2\pi i} \int_0^{\Gamma_+(t)} \frac{\overline{\zeta(\Gamma,t) - \zeta(\Gamma',t)}}{|\zeta(\Gamma,t) - \zeta(\Gamma',t)|^2 + \delta(\Gamma',t)^2} \, \mathrm{d}\Gamma', \tag{2.17}$$

with a regularization parameter

$$\delta(\Gamma,t) = \delta_0 \left(1 - e^{-s(\Gamma,t)^2/\varepsilon^2}\right). \tag{2.18}$$

The effect of δ is to inhibit the growth of free sheet structures (e.g., inner turns of spirals) on scales smaller than δ while maintaining the shape and motion of the sheet on larger scales. Our choice of δ tends to 0 quadratically over a scale given by ε as the membrane trailing edge is approached, to decrease the effect of regularization on the flow near the trailing edge and the production of circulation [4, 5]. Here we set ε to 0.4 and δ_0 to 0.2, choices that make the effect of regularization on circulation production small without a significant increase in the total number of points needed to resolve the free sheet [5]. The Kutta condition determines the rate of circulation production $\mathrm{d}\Gamma_+(t)/\mathrm{d}t$ by making the fluid velocity at the trailing edge finite. This means $\gamma(1,t)$ must be finite, and thus $v(1,t) = 0$ by (2.15).

The vortex sheet strength $\gamma(\alpha,t)$ is coupled to the pressure jump $[p](\alpha,t)$ across the membrane using a version of the unsteady Bernoulli equation written at a fixed material point on the membrane:

$$\partial_\alpha s \partial_t \gamma + (\mu - \tau)\partial_\alpha \gamma + \gamma(\partial_\alpha \mu - \partial_\alpha s \nu \kappa) = \partial_\alpha [p]. \tag{2.19}$$

This equation is derived in appendix A, and generalizes the derivation in [6, appendix A] to the case of an extensible body.

In (2.19), μ is the tangential component of the average flow velocity at the membrane,

$$\mu(\alpha,t) = \mathrm{Re}\left(\hat{\mathbf{s}}\left(1 + \frac{1}{2\pi i}\int_{-1}^{1} \frac{\gamma(\alpha',t)\partial_\alpha s(\alpha',t)}{\zeta(\alpha,t) - \zeta(\alpha',t)}\,\mathrm{d}\alpha' - \frac{1}{2\pi i}\int_0^{\Gamma_+(t)} \frac{\mathrm{d}\Gamma'}{\zeta(\alpha,t) - \zeta(\Gamma',t)}\right)\right), \tag{2.20}$$

and τ and ν are the components of the membrane's velocity tangent and normal to itself, respectively:

$$\tau(\alpha,t) = \mathrm{Re}\left(\partial_t \overline{\zeta}(\alpha,t)\hat{\mathbf{s}}\right) \quad ; \quad \nu(\alpha,t) = \mathrm{Re}\left(\partial_t \overline{\zeta}(\alpha,t)\hat{\mathbf{n}}\right). \tag{2.21}$$

The pressure jump across the free sheet is zero, which yields

$$[p]|_{\alpha=1} = 0, \tag{2.22}$$

the boundary condition we use to integrate (2.19) and obtain $[p](\alpha,t)$ on the membrane.

2.2.2 Boundary and Initial Conditions

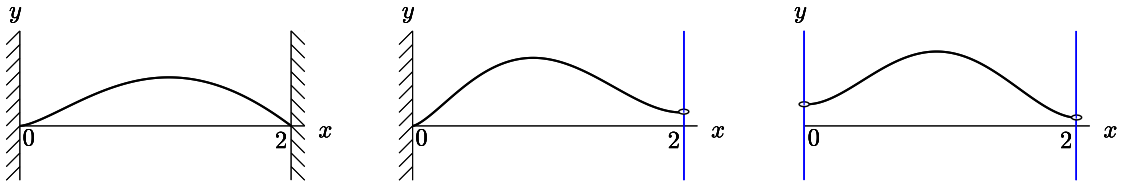

Figure 2.2: Schematic diagrams of the three sets of boundary conditions considered: fixed–fixed (left), fixed–free (center), and free–free (right).

We investigate three cases of boundary conditions at the two ends of the membrane, shown schematically in figure 2.2. In all three cases, the x-coordinates of the ends are constant: $x(-1,t) = 0$ and $x(1,t) = 2$. In the first case, "fixed–fixed," the membrane is flat at $t = 0$, and we set the deflection to zero at both ends of the membrane after a small initial perturbation. More precisely, we smoothly perturb y at the leading edge slightly away from zero and relax it to zero exponentially in time:

$$y(-1,t) = \sigma \left(\frac{t}{\eta}\right)^3 e^{-(t/\eta)^3}, \tag{2.23}$$

where σ is a constant chosen in the range 10^{-6}–10^{-3} (depending on whether small or large amplitude dynamics are studied) and $\eta = 0.2$. We set the trailing edge deflection $y(1,t)$ to zero for all t. This is essentially the case considered by most previous studies of membrane flutter [99,124,168,184], and here we find, surprisingly, that all physically-reasonable deflected membrane states are steady (i.e., without oscillations). In the second case, "fixed–free," we again make the membrane flat initially and then set the leading edge position according to (2.23), but allow the trailing edge to deflect freely in the vertical direction. This is the classical free-end boundary condition for a membrane [45, 59] and corresponds to the membrane end fixed to a massless ring that slides without friction along a vertical pole (see figure 2.2, center). Without friction, the force from the pole on the ring at the membrane end is horizontal. The tension force from the membrane on the ring must also be horizontal, or else the ring would have an infinite vertical acceleration. Therefore, $\hat{\mathbf{s}} = \hat{\mathbf{e}}_x$ at the trailing edge, or equivalently, $\partial_\alpha y(1,t) = 0$.

Although well-known in classical mechanics, free-end boundary conditions have not been studied much in membrane (as opposed to beam/plate) flutter problems. [172] studied membrane wings with partially free trailing edges and found that trail-

ing edge fluttering may occur at relatively low angles of attack. Another recent experimental study found that membrane wing flutter can be enhanced by the vibrations of flexible leading and trailing edge supports [13]. Partially free edges occur also in sails: the shape of a sail membrane can be controlled by altering the tension in cables running along its free edges (the "leech" and "foot") [91]. Flutter can occur when the tension in these edges is sufficiently low [30]. A related application is to energy harvesting by membranes mounted on tensegrity structures (networks of rigid rods and elastic fibers) and placed in fluid flows [163, 204]. In such cases the membrane ends have some degrees of freedom akin to the free-end boundary conditions we have defined.

We will show that free ends allow for a wide range of unsteady membrane dynamics, unlike in the fixed–fixed case. Related work has studied the dynamics and flutter of membranes and cables under gravity with free ends [110, 188]. Here we neglect gravity to focus specifically on the basic flutter problem [154]. Without gravity, some restriction on the motion of the free membrane ends is needed to avoid ill-posedness due to membrane compression [188]. This is provided by the vertical poles in figure 2.2. Although this type of free-end boundary condition has mainly been studied theoretically, it has been realized experimentally by [87], with the membrane represented by an extensional spring that is tethered by steel wires to vertical supports.

In the third case, "free–free," both ends are free: $\partial_\alpha y(-1,t) = \partial_\alpha y(1,t) = 0$. Here the membrane is perturbed differently: it is initially set with a small nonzero slope,

$$\zeta(\alpha,0) = (\alpha+1)(1+i\sigma) \tag{2.24}$$

for $\sigma = 10^{-3}$.

2.3 Numerical Results and Discussion

We now describe the range of dynamics of the extensible membrane with the three sets of boundary conditions. In each case, we first present the flutter stability region for the flat membrane in the R_1-T_0 plane (it is independent of R_3 because it depends only on the small-deflection behavior). We then consider the large-amplitude dynamics using three main quantities to characterize them. One is the time-averaged deflection of the membrane,

$$\langle y_{\mathrm{defl}} \rangle \equiv \frac{1}{t_2} \int_{t_1}^{t_1+t_2} \left(\max_{-1 \le \alpha \le 1} y(\alpha, t) - \min_{-1 \le \alpha \le 1} y(\alpha, t) \right) \mathrm{d}t, \tag{2.25}$$

where t_1 and t_2 are sufficiently large (typically 50–100) that $\langle y_{\mathrm{defl}} \rangle$ changes by less than 1% with further increases in these values. $\langle y_{\mathrm{defl}} \rangle$ is the maximum membrane deflection minus the minimum deflection, averaged over time.

The second quantity is the frequency, defined as the mean frequency in the power spectrum computed using Welch's method [197]. The power spectrum is obtained from a time series of the free sheet circulation when the membrane has reached steady-state large-amplitude dynamics. The third quantity is the time-averaged number of zero crossings along the membrane, computed with the same temporal data as the power spectrum. The number of zero crossings is a measure of the "waviness" of the membrane shape.

2.3.1 Fixed–fixed Membranes

We begin by presenting the dynamics of membranes with both ends fixed, the case considered by previous studies on membrane flutter. The most detailed linear stability analysis of the problem is by [184]. Their model is essentially a linearized version of ours, and includes a flat vortex wake extending to infinity downstream. They find that all membranes become unstable when the pretension T_0 drops below

a critical value ≈ 1.73, independent of R_1. A qualitatively similar result was found by [128] for an infinite periodic membrane with no free vortex wake. Below the critical pretension, the membranes in [184] lose stability by divergence (exponential growth of deflection) at small R_1 or by divergence with flutter (exponential growth with a complex growth rate—i.e., growth with oscillation) at large R_1.

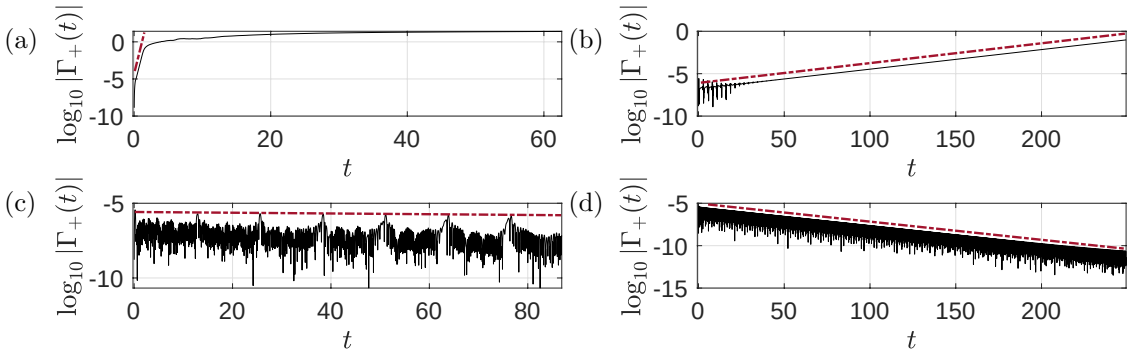

Figure 2.3: (Fixed–fixed.) Examples of the $\log_{10}$ of the total wake circulation versus time with (a) $(R_1, T_0) = (10^{-1.8}, 10^{-1.2})$, (b) $(R_1, T_0) = (10^{-0.2}, 10^{0.2})$, (c) $(R_1, T_0) = (10^{2}, 10^{1})$, and (d) $(R_1, T_0) = (10^{1}, 10^{3})$. The growth/decay rates are given by the slopes of the dot-dashed red lines. In all cases we set $R_3 = 1$, but the linear growth rates are independent of R_3 (we show the R_3 term to be cubic in deflection in equation (2.26), and therefore negligible in the linear growth regime).

We use our nonlinear simulation to compute the stability threshold for membranes by applying the small transient perturbation (2.23) at the leading edge and observing exponential growth (followed by large-amplitude, nonlinear dynamics) or exponential decay, in membrane deflection and wake circulation $\Gamma_+(t)$. Examples are shown in figure 2.3. For the stability results presented in figures 2.3 and 2.4 we use (2.23) with $\sigma = 10^{-6}$.

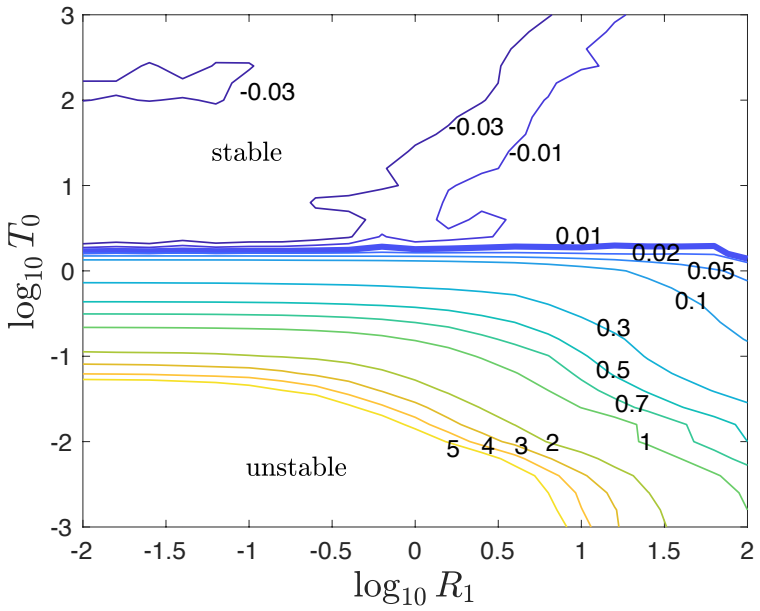

Figure 2.4: A contour plot of the exponential (base 10) growth and decay rates of wake circulation after a small transient perturbation, in the fixed–fixed case. The thicker line separates the stable and unstable cases.

We compute the growth and decay rates of the initial perturbation from data analogous to those in figure 2.3, on a fine grid of values in the R_1-T_0 space spanning several orders of magnitude in each parameter. Figure 2.4 is a contour plot of the growth/decay rates, i.e., β in the early-time interval where $\Gamma_+(t) \approx K\, 10^{\beta t}$ for some constant K. Values (well) above 5 occur in the lower left corner but are omitted for visual clarity. Above a critical pretension $T_0 \approx 1.78$ the membranes are stable, with small transient deflections decaying to the flat state. Below the critical pretension we have a divergence instability: small transient deflections grow exponentially at a rate that is purely real. [184] found a critical pretension of 1.73 in a slightly different model; unlike that study, we do not find evidence of neutral flutter or divergence with flutter in the fixed–fixed case at any R_1. The main differences are that our wake length grows from zero while that in [184] is infinite, and our model is a nonlinear, unsteady version of that in [184].

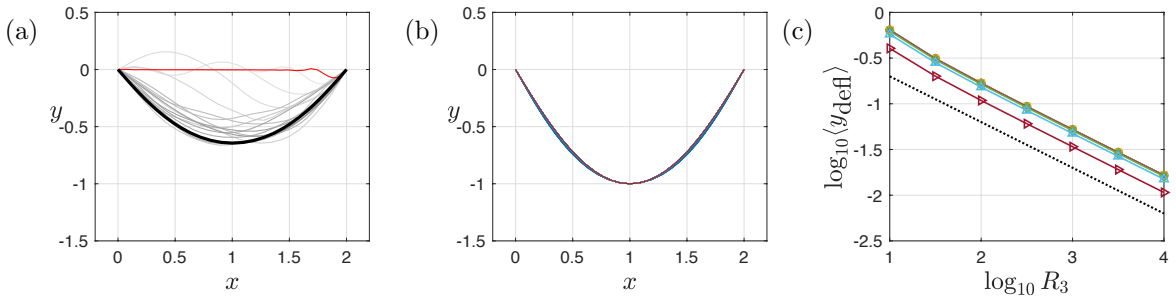

Figure 2.5: Fixed–fixed membrane shapes. (a) For $R_1 = 10^{-0.5}$, $R_3 = 10^1$, and $T_0 = 10^{-3}$ the membrane shapes at $t = 1$ (red), 1.5, 2.5, 3.5, 4.5, ..., 16.5 (light gray to black), (b) steady membrane shapes at late times, with y coordinates scaled by maximum deflection, for R_3 ranging from 10^1 to 10^4 and T_0 ranging from 10^{-3} to 1. (c) The maximum membrane deflection at steady state versus the stretching modulus R_3.

During the initial stages of the divergence instability, the membrane deflection grows from small amplitude without change of shape. Nonlinearities become important when the amplitude reaches order one, and the membrane shape evolves to its eventual steady state. For the large-amplitude analysis of fixed–fixed membranes that follows, the small transient perturbation (2.23) applied at the leading edge is used with $\sigma = 10^{-4}$. Figure 2.5(a) shows a sequence of membrane snapshots during the nonlinear dynamics. The earliest shape (red) is similar to those during the linear instability, with largest deflection near the trailing edge. Subsequent shapes (ranging from light to dark gray and black) show the evolution to the eventual steady-state. The final membrane shape is nearly fore-aft symmetrical, similar to those in [124, 127, 144, 191, 193, 194]. These works also discuss membrane dynamics at nonzero angle of attack with applications to lift and thrust generation by membrane airfoils (possibly heaving and/or pitching [79]). Then vortices shed from the membrane's leading edge provide an unsteady forcing, causing membrane oscillations even in the fixed–fixed case. However, the present work is focused on the problem of membrane flutter at zero angle of attack, for which leading edge vortex shedding should be less significant. As for most vortex panel methods [88], leading

edge separation is difficult to represent in our model, so we focus on situations where trailing-edge vortex shedding is expected to be dominant, i.e., membranes at zero angle of attack with small-to-moderate deflections.

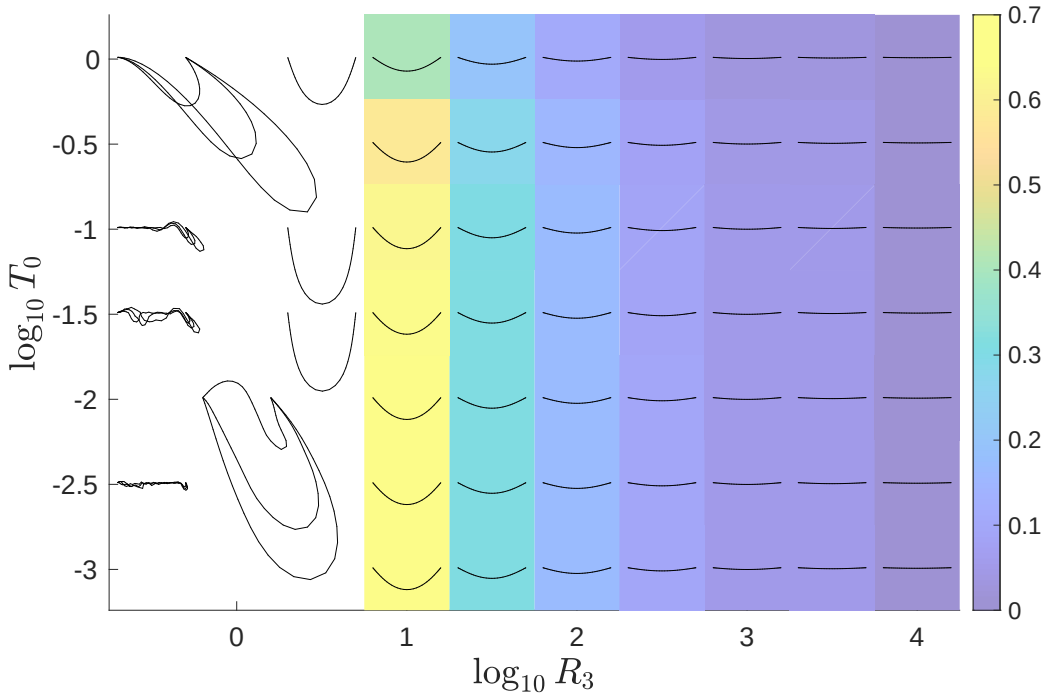

Figure 2.6: Membrane profiles in the fixed–fixed case, at steady state with moderate deflections (colored background), or unphysically large or unsteady deflections (white background). In the unsteady cases a few snapshots at large times are shown. The colors show the deflection of the membrane (equation (2.25)). Here, $R_1 = 10^{-0.5}$ but the steady shapes are independent of R_1, the dimensionless mass.

Figure 2.6 shows the late-time membrane shapes across several decades of R_3 and T_0. The shapes are all steady for $R_3 > 10^{0.5}$ (and thus independent of R_1 here, as the acceleration term in (2.8) is zero), but may oscillate chaotically for $R_3 \leq 10^{0.5}$, in which case a few snapshots are shown at late times. In these cases, the deflections are so large as to violate the assumption that vortex shedding is confined to the trailing edge, so we do not consider them further. For $R_3 > 10^{0.5}$, the colors show the maximum membrane deflection. At a given R_3, the deflection increases slightly as T_0

decreases from the stability threshold to ≈ 0.1, then converges as T_0 decreases further, the T_0 term becoming insignificant in the membrane equation (2.8). At a given T_0, the deflection decreases with increasing R_3 as a power law. Figure 2.5(b) shows that the shapes are almost identical, however, when the amplitudes are normalized. Figure 2.5(c) shows that the deflection $\langle y_{\text{defl}} \rangle \sim 1/\sqrt{R_3}$ (for $R_1 = 10^{-0.5}$ here, but these values are independent of R_1).

We explain how the scaling $\langle y_{\text{defl}} \rangle \sim 1/\sqrt{R_3}$ arises from the y-component of the membrane equation (2.8) with small deflections. For this we assume $\partial_\alpha y \ll 1$ and $\partial_\alpha x \approx 1$. Then $\partial_\alpha s - 1 = \sqrt{(\partial_\alpha x)^2 + (\partial_\alpha y)^2} - 1 \approx \partial_\alpha y^2/2$ and $\hat{s}_y \approx \partial_\alpha y$. With these approximations, the y-components of the T_0 and R_3 terms in (2.8) are linear and cubic in deflection, respectively:

$$\partial_\alpha \left(T_0 \hat{s}_y\right) \approx T_0 \partial_{\alpha\alpha} y \quad ; \quad \partial_\alpha \left(R_3 (\partial_\alpha s - 1)\hat{s}_y\right) \approx R_3 \partial_\alpha \left(\left(\partial_\alpha y\right)^3 /2 \right). \tag{2.26}$$

The R_1 term (multiplying $\partial_{tt} y$) is also linear in deflection (and zero here at steady state, but not for the oscillating membranes considered later). The pressure jump is linear in the bound vortex sheet strength because the left side of (2.19) $\approx \partial_t \gamma + \partial_\alpha \gamma$ with small deflections. The bound vortex sheet strength is linear in the deflection by the linearized version of (2.14),

$$\partial_t y(\alpha, t) \approx \frac{1}{2\pi} \fint_{-1}^{1} \frac{\gamma(\alpha', t)}{x(\alpha, t) - x(\alpha', t)} \, \mathrm{d}\alpha' - \frac{1}{2\pi} \int_0^{\Gamma_+(t)} \frac{x(\alpha, t) - x(\Gamma', t)}{(x(\alpha, t) - x(\Gamma', t))^2 + \delta(\Gamma', t)^2} \, \mathrm{d}\Gamma', \tag{2.27}$$

in which the second integral consists of bound vorticity advected from the trailing edge, so it has the same dependence on deflection as the bound vorticity. Here, with small deflections, we have assumed $\partial_\alpha x \approx 1$, and then the linearization is the same as in [10]. Without viscous stresses, horizontal membrane deformations arise only through nonlinear terms in the elastic and pressure forces associated with

large deflections, so it is reasonable to neglect them, and this is consistent with the simulation results. Balancing the terms that are linear in deflection with the product of R_3 and a term that scales with deflection cubed gives $\langle y_{\text{defl}} \rangle \sim 1/\sqrt{R_3}$.

2.3.2 Fixed–free Membranes

We now investigate membranes with the leading edge fixed and the trailing edge free to move vertically (with $\partial_\alpha y = 0$ there—an extra equation that determines $y(1,t)$, now an extra unknown). With the free end, the membrane has a wide range of unsteady dynamics with small and moderate amplitude, unlike in the fixed–fixed case, and similar in some respects to the fixed–free flag with bending rigidity [10].

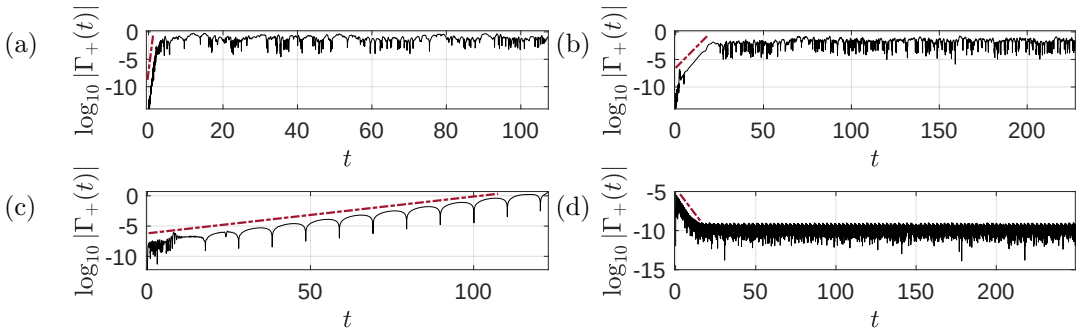

Figure 2.7: (Fixed–free.) Examples of the total wake circulation versus time for $R_3 = 1$ on a log scale, with (a) $(R_1, T_0) = (10^{-3}, 10^{-2.8})$, (b) $(R_1, T_0) = (10^{-1.4}, 10^{-1.4})$, (c) $(R_1, T_0) = (10^{1}, 10^{-0.2})$, and (d) $(R_1, T_0) = (10^{-0.8}, 10^{2.2})$. The slopes of the dot-dashed red lines give the growth/decay rates. Recall that R_1 is the dimensionless membrane mass, T_0 is the dimensionless pretension, and R_3 is the dimensionless stretching modulus.

Figure 2.7 shows examples of the growth of wake circulation in time after small transient perturbations, analogous to figure 2.3. As before, for the analysis of the small-amplitude dynamics we use (2.23) with $\sigma = 10^{-6}$. The main novelty is panel (c), an example of divergence with flutter—shown by the regularly-spaced vertical asymptotes in the logarithm of wake circulation, corresponding to an oscillatory component—exponential growth with a complex growth rate.

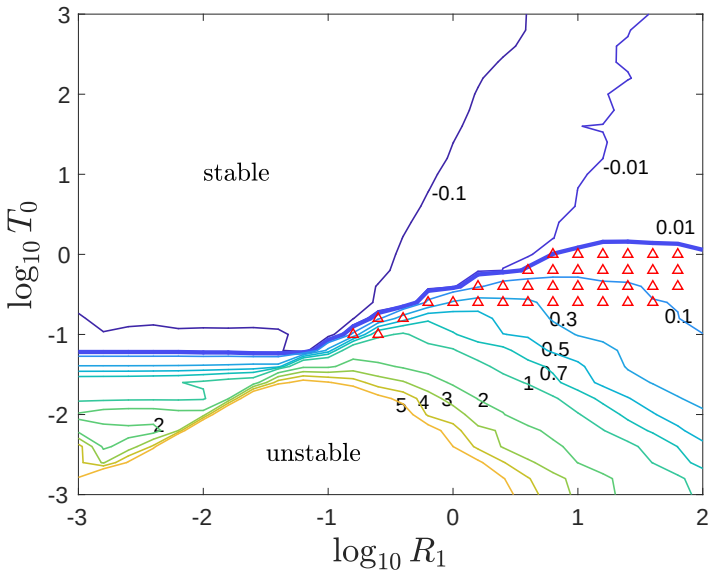

Figure 2.8: A contour plot of the exponential (base 10) growth and decay rates of wake circulation after a small transient perturbation, in the fixed–free case. The thicker line separates the regions where the membranes are stable and unstable. Growth rates (well) above 5 occur at the lower left but are omitted for visual clarity.

Figure 2.8 is a contour plot of the growth/decay rates and stability boundary in R_1-T_0 space, analogous to figure 2.4. Notable differences are that the stability boundary now varies with R_1. The critical pretension is close to that in figure 2.4 at the largest R_1, but decreases as R_1 decreases, and eventually reaches a lower plateau at $R_1 \ll 1$. The red triangles in figure 2.8 show cases like figure 2.7(c), membranes that become unstable through flutter and divergence.

The membranes in the unstable region of figure 2.8 eventually reach large amplitudes, where nonlinearities (e.g. the R_3 term) determine the eventual steady-state motion. With fixed–free boundary conditions, oscillatory motions are typical, unlike for the fixed–fixed case. As for the fixed–fixed case, unrealistically large deflections occur for $R_3 \leq 1$, so we focus on $R_3 \gtrsim 1$.

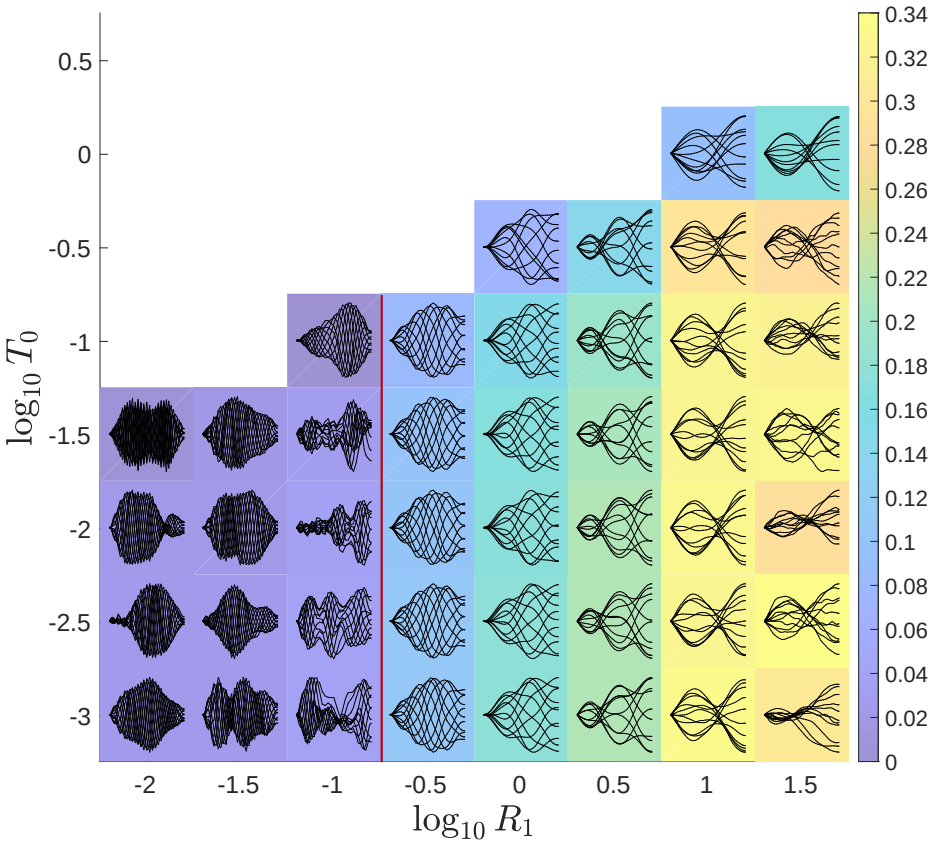

Figure 2.9: (Fixed–free.) Snapshots of large-amplitude membrane motions in the unstable region of R_1-T_0 space, for fixed $R_3 = 10^{1.5}$. Colors denote $\log_{10}$ of the average deflection defined by equation (2.25). At each (R_1, T_0) value, the set of snapshots is normalized by the maximum deflection of the snapshots to show the deformation modes more clearly and scaled to fit within a colored rectangle at the (R_1, T_0) value.

Now we study the large-amplitude dynamics and we use $\sigma = 10^{-4}$ in (2.23). Figure 2.9 shows typical membrane snapshots in the unstable region of R_1-T_0 space from figure 2.8. At each (R_1, T_0) value, the set of snapshots is normalized by the maximum deflection of the snapshots to show the motions more clearly and scaled to fit within a colored rectangle at the (R_1, T_0) value. Each snapshot has the corresponding R_1 value at its horizontal midpoint, and the T_0 value at its leading edge. Here R_3 is fixed at $10^{1.5}$, a value giving moderately large deflections for the steady-state motion.

The colors denote the average deflection of the membrane (equation (2.25)).

The motions in figure 2.9 have largest deflection amplitudes and smallest spatial frequency components at the largest R_1 ($10^{1.5}$). Intuitively speaking, large R_1 (membrane inertia) allows the membrane to maintain its momentum for longer times against restoring fluid forces, and obtain larger deflections before reversing direction. The same has been observed for flutter with bending rigidity [10,31]. As R_1 decreases, the membrane deflection amplitudes progressively decrease and spatial frequencies increase until the motions become difficult to resolve numerically (to the left of the red vertical line). In this region, we find chaotic membrane oscillations with very small amplitudes and high spatial frequencies that become independent of R_1. When the number of points on the membrane is increased from 40 (here) to 80, 160, and 200, the membranes with $R_1 \leq 10^{-1}$ still oscillate chaotically but with even higher spatial frequency components, while those with $R_1 \geq 10^{-0.5}$ do not change significantly. Although the motions to the left of the red line are not converged with respect to the spatial grid, we retain their snapshots in figure 2.9 to indicate the behavior of the simulations. We find quasi-periodic motions in a finite band of R_1 values between $10^{-0.5}$ and $10^{0.5}$. Above and below this range, the motions become more irregular and chaotic, and more up-down asymmetrical at large R_1. The membrane motion depends weakly on T_0 except near the stability boundary (at the largest T_0 shown). At smaller T_0, the pretension does not affect the dynamics because it is negligible compared to the R_3 (stretching) term.

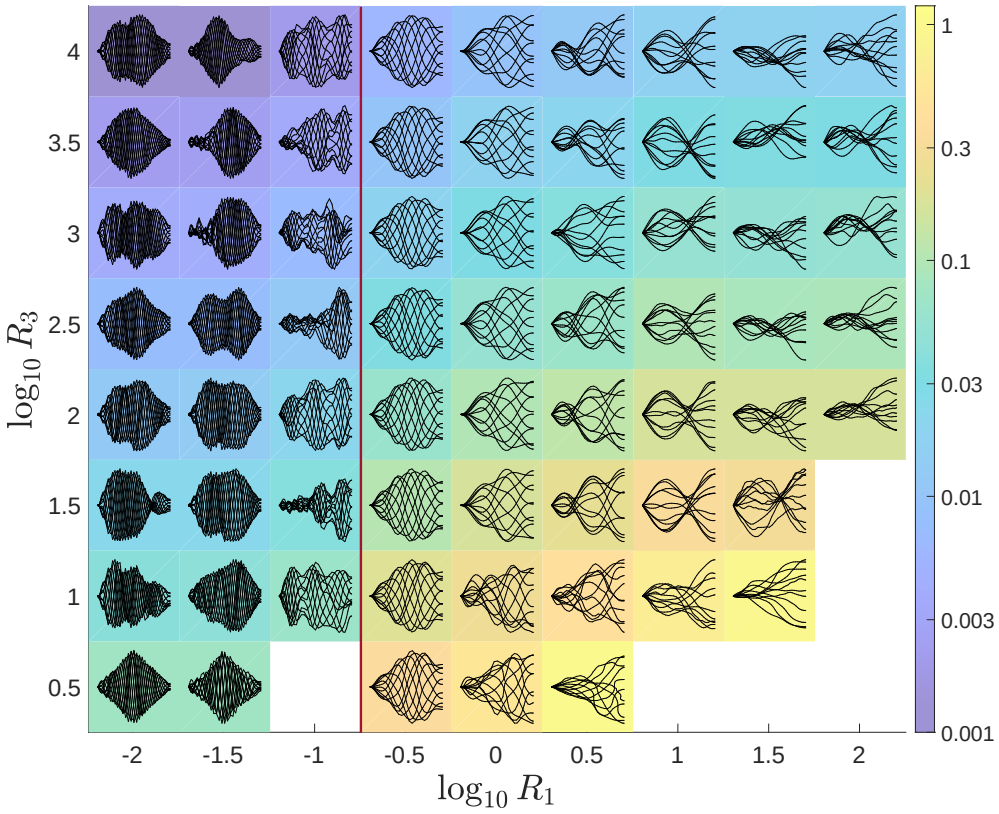

Figure 2.10: (Fixed–free.) Snapshots of large-amplitude membrane motions in R_1-R_3 space, for fixed $T_0 = 10^{-2}$. Colors denote $\log_{10}$ of the average deflection defined by equation (2.25). To the right of the vertical red dividing line the membrane motions are nearly periodic but to the left of the red line, the membrane oscillations are chaotic. At each (R_1, R_3) value, the set of snapshots is scaled to fit within a colored rectangle at the (R_1, R_3) value and normalized by the maximum deflection of the snapshots to show the motions more clearly.

Next we look at the same quantities in a different two-dimensional slice through R_1-T_0-R_3 space. We fix $T_0 = 10^{-2}$ and in figure 2.10 show the membrane motions across R_1 and R_3. In the lower right corner and at $(R_1, R_3) = (10^{-1}, 10^{0.5})$, snapshots are omitted because steady-state membrane motions were not obtained. We find that R_3 mainly affects the amplitudes of the snapshots, but not their shapes, particularly for the periodic motions with $R_1 = 10^{-0.5}$. The shapes do change noticeably for the more irregular and chaotic motions, which are sensitive to small changes in parameters, and near the smallest stretching modulus where steady-state motions

occur, $R_3 \approx 10^{0.5}$.

We find that membranes with $R_1 = 10^{-0.5}$–$10^{0.5}$ move almost like traveling waves: their peaks and troughs translate downstream in forward time. Some of those with larger R_1 (10^1 and $10^{1.5}$) move approximately like standing waves, with a node and an antinode at certain locations. Similar dynamics have been found for fixed–fixed membranes perturbed by vortices shed from the leading edge [56, 158, 182].

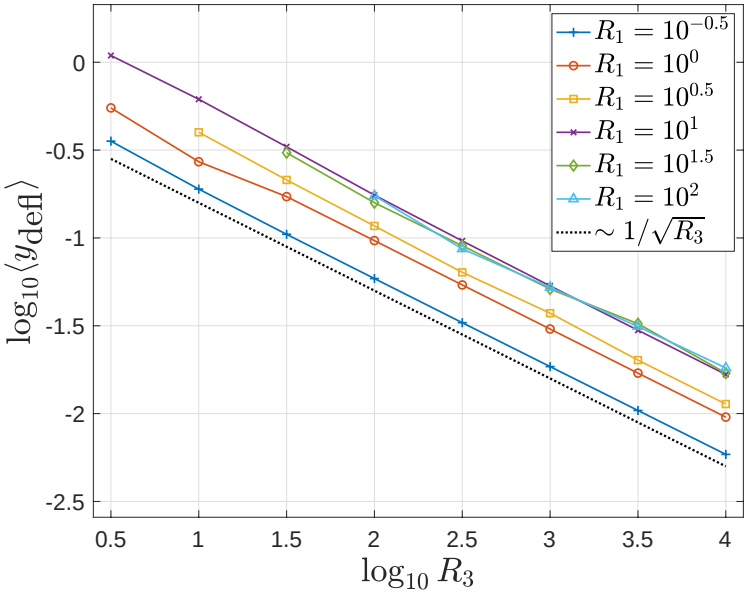

Figure 2.11: (Fixed–free.) Time-averaged deflections of the membranes (defined by equation (2.25)) versus R_3, for various R_1 and fixed $T_0 = 10^{-2}$. The black dashed line indicates the scaling $1/\sqrt{R_3}$.

We show how the time-averaged deflection depends on R_3 at several fixed values of R_1 in figure 2.11. The plots follow the same $1/\sqrt{R_3}$ dependence at large R_3 as in the fixed–fixed case and for the same reason (explained in section 2.3.1).

Figure 2.10 has shown the typical membrane motions at various R_1 and R_3 at fixed T_0 (and the phenomena are similar at other T_0 that yield flutter). We now quantify the membrane shapes in terms of the time-averaged number of "zero crossings"—the number of times the membrane crosses $y = 0$. This is one way to measure the "waviness" of a shape which is not sinusoidal (so the wavelength is not

well defined) [7, 10]. Figure 2.12 shows examples of shapes with zero, one, and two zero-crossings, respectively.

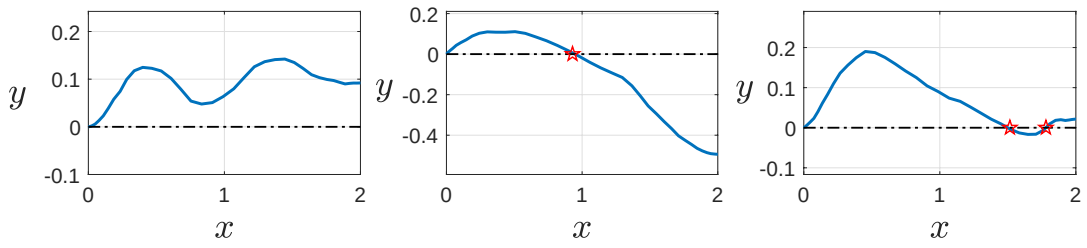

Figure 2.12: Examples of where zero crossings (red stars) are counted for model membranes (blue solid lines). Note that the leading edge of the membrane is not included as a zero crossing.

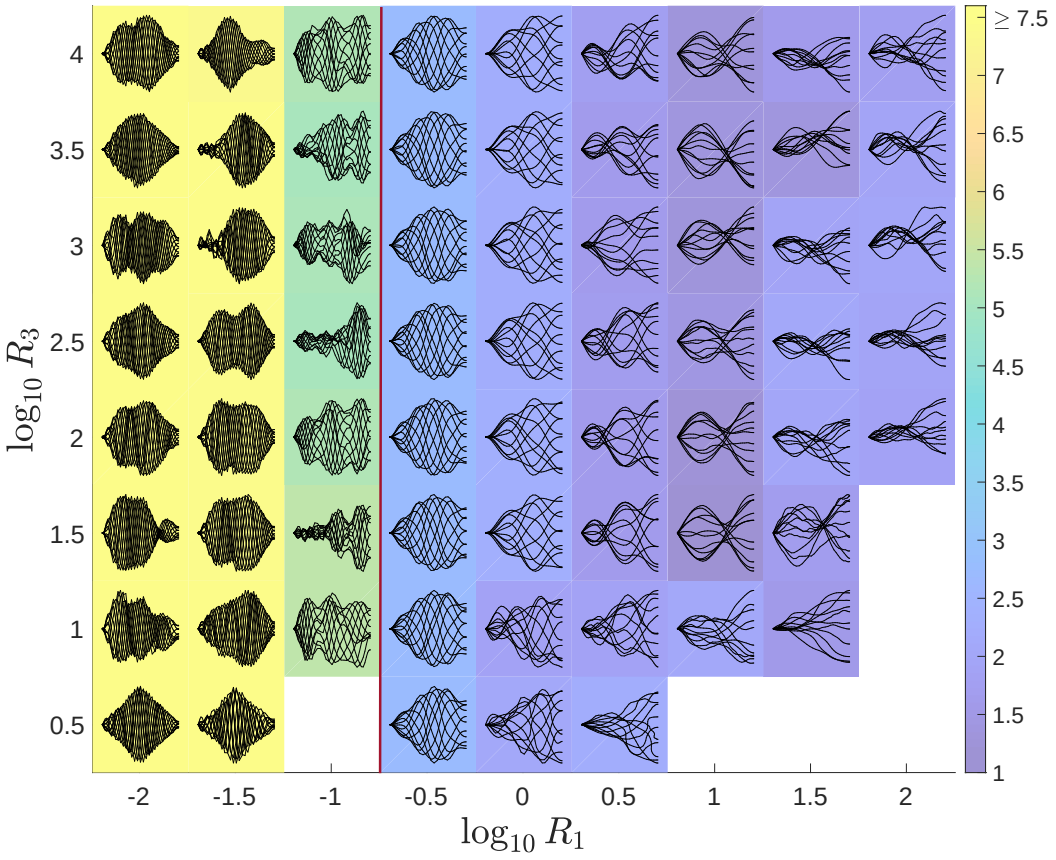

Figure 2.13: (Fixed–free.) Colors denote the time-averaged number of zero-crossings for membrane flutter in the R_1-R_3 parameter space, for fixed $T_0 = 10^{-2}$. In the lower right corner and at $(R_1, R_3) = (10^{-1}, 10^{0.5})$, snapshots are omitted because steady-state membrane motions were not obtained. Note that R_1 is the dimensionless membrane mass, T_0 is the dimensionless pretension, and R_3 is the dimensionless stretching modulus. At each (R_1, R_3) value the set of snapshots is normalized by the maximum deflection of the snapshots to show the motions more clearly.

We have already mentioned the trend to higher spatial frequency components with decreasing R_1. Figure 2.13 quantifies this relationship by showing the average number of zero crossings for the same snapshots in figure 2.10 (where the deflection amplitude was plotted). Decreasing R_1 from the largest value (10^2), the average number of zero crossings actually decreases slightly to about 1 near 10^1 and then increases with further decreases in R_1 as the motions become more periodic and then more irregular at yet smaller R_1 where the motions are not fully resolved spatially.

The temporal dynamics corresponding to these motions are quantified by computing the power spectra of time series of the total wake circulation, $\Gamma_+(t)$. Figure 2.14 shows examples of the time series of $\Gamma_+(t)$ that correspond to the different types of power spectra. Panel (a) shows an example with a periodic motion at $R_1 = 10^{-0.5}$. The corresponding $\Gamma_+(t)$ is periodic though not sinusoidal, resulting in a sequence of sharp peaks in the power spectrum. Panel (b) shows a less periodic response at larger R_1, still dominated by a single frequency but with clear variations from one cycle to the next. In panel (c) at still larger R_1, the trend toward aperiodicity continues. Nonetheless, the time series (left) shows peaks with a somewhat regular spacing. The corresponding power series (right) has a single peak close to zero frequency and a gradual decay in the power spectrum at higher frequencies, typical of chaotic dynamics.

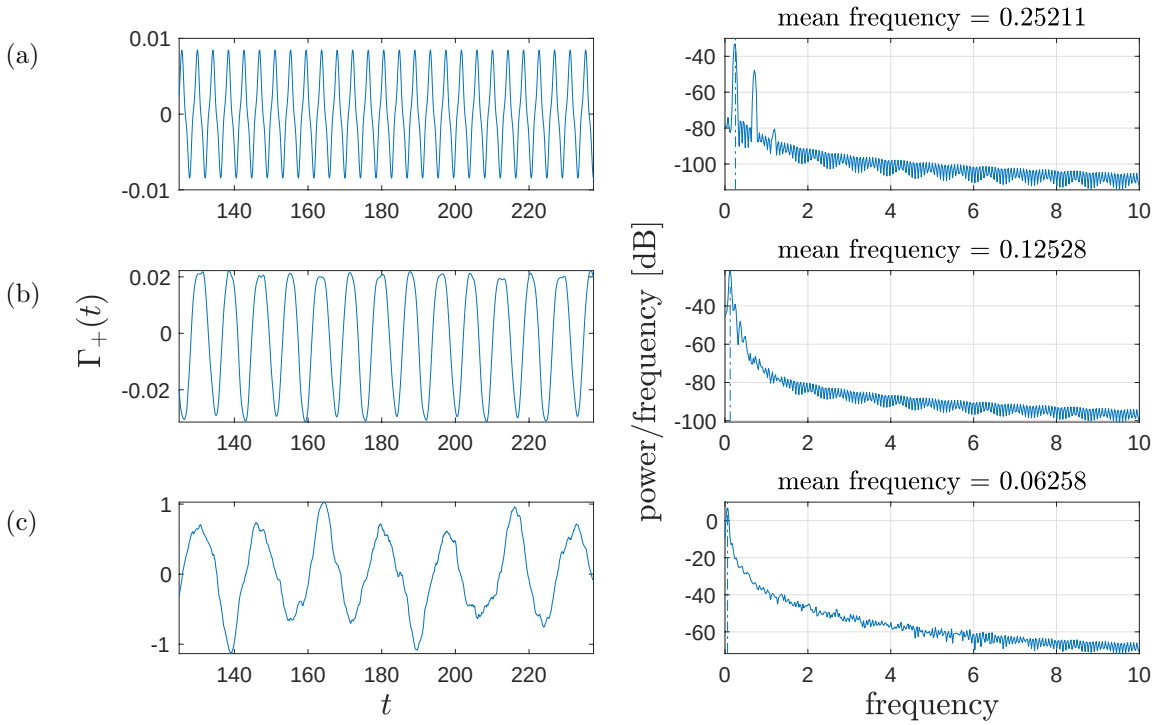

Figure 2.14: (Fixed–free.) Portion of time series of total wake circulation $\Gamma_+(t)$ (left) and corresponding power spectra (right) for membranes with increasing mass density R_1 from top to bottom: (a) $(R_1, R_3) = (10^{-0.5}, 10^2)$, (b) $(R_1, R_3) = (10^{0.5}, 10^{3.5})$, and (c) $(R_1, R_3) = (10^{1.5}, 10^{1.5})$. In all cases $T_0 = 10^{-2}$.

Figure 2.15 shows these spectra, computed using Welch's method [197], across R_1-R_3 space, with $T_0 = 10^{-2}$. The colors denote the mean frequencies—i.e., the first moments of the power spectra, normalized by total power. As R_1 increases from $10^{-0.5}$ to 10^2 and the dynamics change from periodic to chaotic, the power spectra change as described in the previous figure, with little dependence on R_3 except at the lowest values. The mean frequencies decrease by about a factor of five. Thus there is a strong correlation between number of zero-crossings (or flutter mode) and oscillation frequency, as has been seen previously in flag flutter problems [7,10,43,153]. The two are in linear proportion for the modes of the linear wave equation for a membrane in a vacuum [45,59]. The power spectra to the left of the red line (for motions which are not converged with respect to grid spacing) show higher frequencies and a broadband

response, reflecting chaotic dynamics.

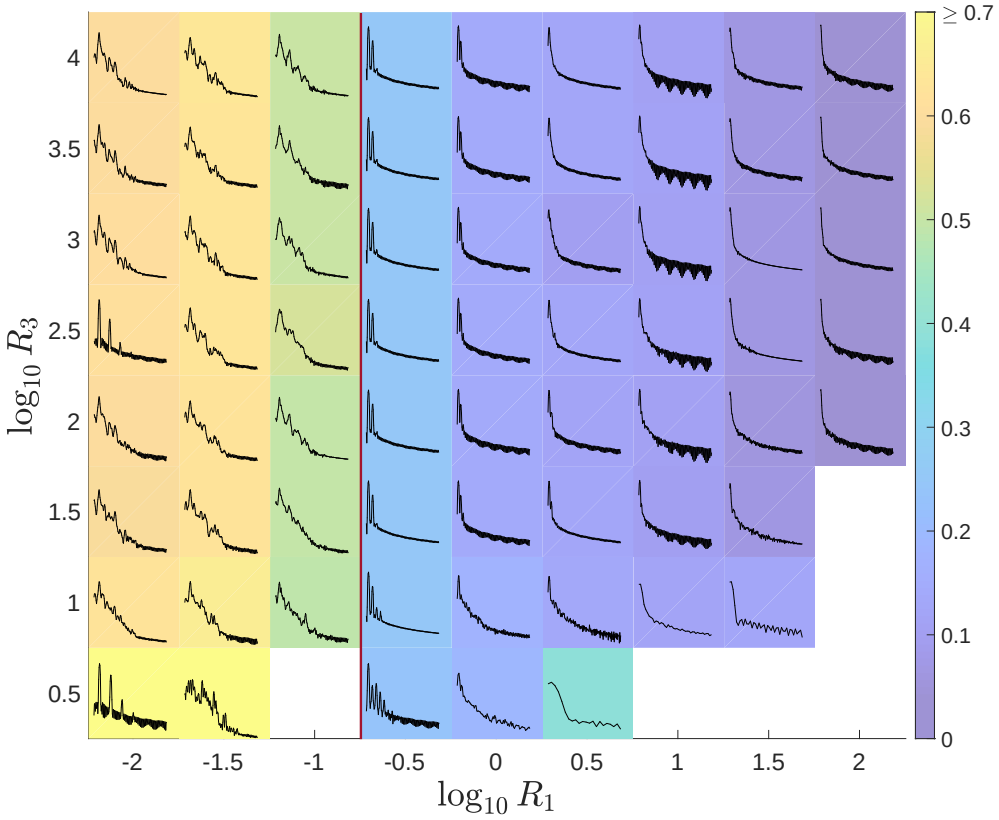

Figure 2.15: Colors denote the mean frequencies of large-amplitude motions in the fixed–free case for various R_1 and R_3, all with $T_0 = 10^{-2}$. The corresponding power spectra for each membrane are plotted in black. In the lower right corner and at $(R_1, R_3) = (10^{-1}, 10^{0.5})$, power spectra are omitted because steady-state membrane motions were not obtained. Each power spectrum is a plot of power density (per unit frequency) versus frequency as in the panels of figure 2.14, right side. The axis scales are omitted due to space constraints but our focus here is on the qualitative features only.

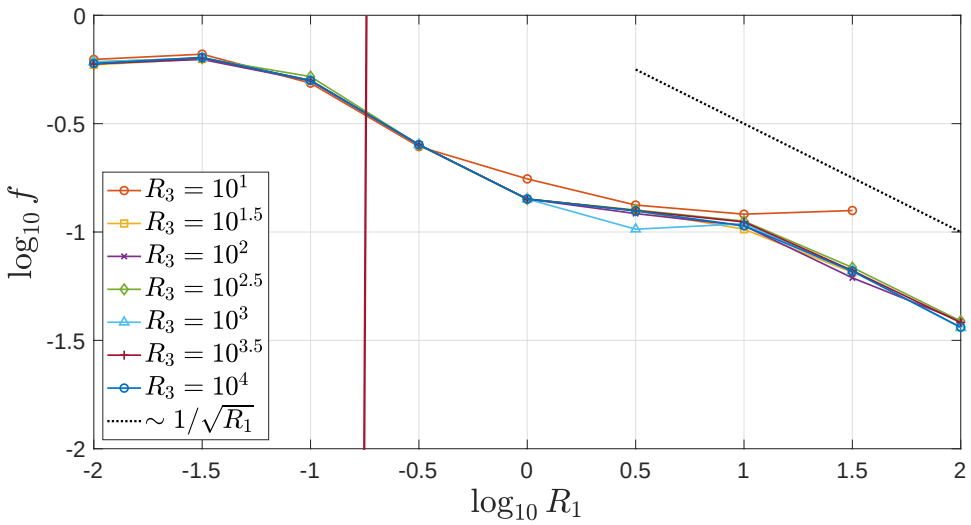

Figure 2.16: (Fixed–free.) Plots of the mean frequency $\log_{10} f$ versus mass density $\log_{10} R_1$ with various R_3 and fixed $T_0 = 10^{-2}$. The black dashed line shows $f = 1/\sqrt{R_1}$.

Figure 2.16 shows more quantitatively how the mean frequency varies with parameters. There is very little dependence on R_3 except near the smallest R_3 where stable motions can be computed, $\approx 10^1$. There is a steady decrease from $R_1 = 10^{-1}$ to 10^0 followed by a small plateau for $10^0 \le R_1 \le 10^1$, and another decrease within $10^1 \le R_1 \le 10^2$. The trend at the largest R_1 is well approximated by $f \sim 1/\sqrt{R_1}$ (admittedly over a short range of R_1), except at the two smallest R_3 values. This scaling arises when one approximates the normal component of the membrane equation (2.8) by its y component, and chooses a characteristic time scale t_0 so that $R_1 \partial_{tt} y$ balances other terms that depend on y but not its time-derivatives (i.e., the R_3 and T_0 terms and some of the fluid pressure terms). At large R_1, $R_1 \partial_{tt} y$ is comparable to the other terms when $R_1/t_0^2 \sim 1$ or $t_0 \sim \sqrt{R_1}$, giving a typical frequency $f_0 \sim 1/\sqrt{R_1}$.

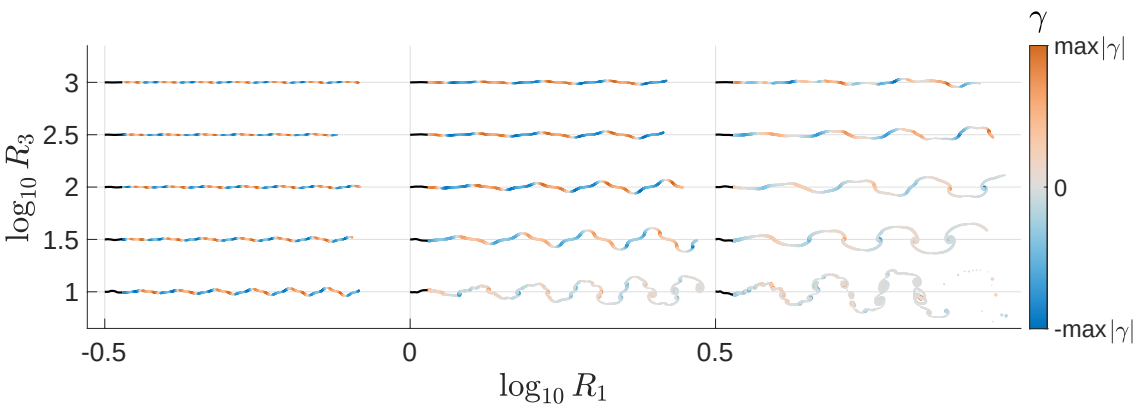

Figure 2.17: (Fixed–free.) Snapshots of the membrane motion (in black) and the vortex wake in a portion of the R_1-R_3 parameter space for fixed $T_0 = 10^{-2}$. In each case the (R_1, R_3) values are marked at the left endpoint of the membrane. The wake is color-coded according to the vortex sheet strength at the last time step. It is also thickness-coded according to $15|\gamma|^{1/3}$. Counterclockwise rotating vortices are shown in orange and clockwise rotating vortices in blue. For example, for $(R_1, R_3) = (10^{-0.5}, 10^3)$ we have $\max|\gamma| = 0.0041$ and for $(R_1, R_3) = (10^{0.5}, 10^1)$ we have $\max|\gamma| = 1.9$.

We have mainly focused on the membrane dynamics, but we conclude this section by briefly considering the vortex sheet wake dynamics. Figure 2.17 shows snapshots of vortex wakes in a small portion of R_1-R_3 space where the membranes' motions transition from small to large amplitudes. At smaller amplitudes (top and left), the wakes are mostly flat (despite the complexity of the corresponding membrane snapshots, shown in figure 2.10), and have periodic undulations, as the membrane motions are approximately periodic at these parameters. Here the vorticity is weak, so there is little vortex wake roll-up before the wake is advected many body lengths downstream by the background flow. With smaller membrane deflections, we observe two pairs of oppositely signed vortices per flapping period ($R_1 = 10^{-0.5}$ with $R_3 = 10^1$–10^3, and $R_1 = 10^0$ with $R_3 = 10^{1.5}$–10^3), akin to a 2P wake [198]. At larger deflections, there is more roll-up and the wake resembles a von Kármán vortex street in some cases ($R_1 = 10^{0.5}$ with $R_3 = 10^{1.5}$–$10^{2.5}$), or a less regular wake with many spirals per flapping period (bottom right, $R_1 = 10^0$–$10^{0.5}$ with $R_3 = 10^1$). In general, the wake is spatially periodic to the extent that the membrane motion is temporally

periodic. The more irregular wakes reflect the greater aperiodicity of the membrane motion at large amplitudes.

2.3.3 Free–free Membranes

We have seen that changing the trailing edge boundary condition from fixed to free dramatically changes the membrane dynamics, from static deflections with a single maximum to a wide range of oscillatory modes that have some commonalities with flapping plates and flags [154]. Therefore it is natural to consider the effect of making both ends free, and determine if the membrane dynamics undergo further dramatic changes. Computationally, the method is the same as before, but the system of unknowns now includes the values of y at both endpoints, corresponding to the two equations $\partial_\alpha y(-1,t) = \partial_\alpha y(1,t) = 0$.

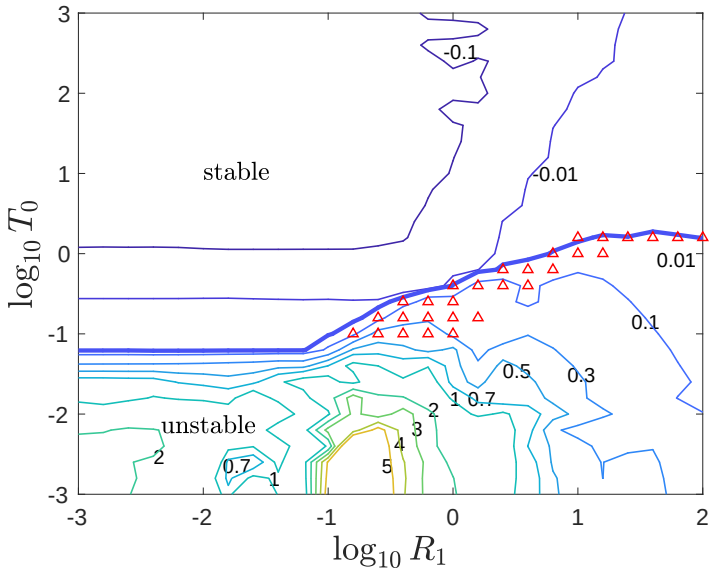

Figure 2.18: A contour plot of the exponential (base 10) growth and decay rates of wake circulation after a small transient perturbation, in the free–free case. The thicker line separates the stable membranes from the unstable ones.

The contour plot of growth/decay rates of the initial perturbation (equation (2.24)

with $\sigma = 10^{-3}$) is shown in figure 2.18. It is similar to that in the fixed–free case (figure 2.8), particularly in the location of the stability boundary and the contours in the stable region. In the unstable region, the growth rates are significantly smaller and there are slight differences in where divergence with flutter occurs (red triangles).

We now consider the large-amplitude membrane motions in R_1-R_3 space with T_0 fixed at 10^{-2}, the free–free analog of figure 2.10. Figure 2.19 shows the motions superposed on a color field that labels the time-averaged membrane deflections (2.25). The membrane is now free to translate in the y-direction, which leads to additional complexities in the motions. Like in the fixed–free case (figure 2.10), increasing R_3 decreases the deflections of the snapshots without significantly changing the qualitative features of their shapes. Decreasing R_1 generally decreases the deflections also, except near the largest R_1. The membranes mostly oscillate within a fixed vertical region, except at $R_1 = 10^{0.5}$, where the membranes mostly translate steadily in y, and with a steady shape. The membranes are somewhat straighter than in the fixed–free case, possibly because their translational freedom allows them to align more closely with the oncoming flow. As R_1 decreases below $10^{0.5}$, the membranes develop sharper curvatures until they again become difficult to resolve numerically at and below 10^{-1}. To the left of the red dividing line, increasing the number of points on the membrane leads to similarly complex oscillatory motions with somewhat sharper curvatures in most cases.

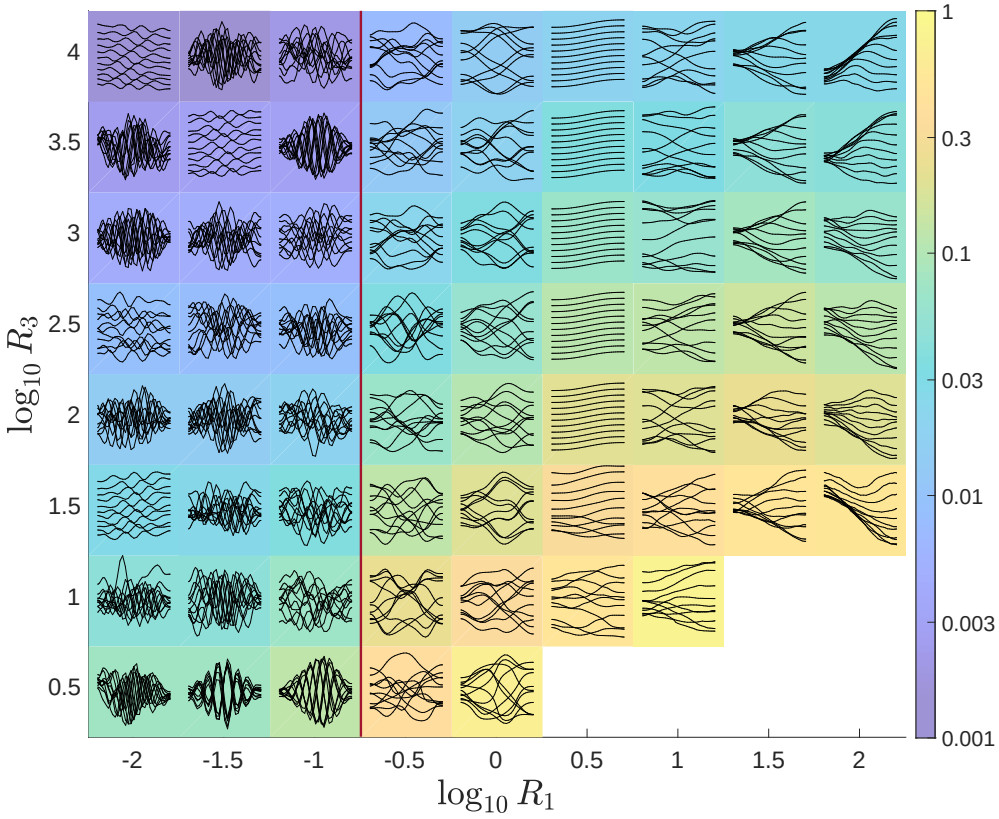

Figure 2.19: Membrane snapshots in the free–free case superposed on colors labeling the time-averaged deflection for each (R_1, R_3) pair with $T_0 = 10^{-2}$ defined by equation (2.25). Recall that R_1 is the dimensionless membrane mass, T_0 is the dimensionless pretension, and R_3 is the dimensionless stretching modulus. At each $(R_1,\ R_3)$ value, the set of snapshots is scaled to fit within a colored rectangle at the $(R_1,\ R_3)$ value and normalized by the maximum deflection of the snapshots to show the motions more clearly.

To show the net translational motions of the membranes, we plot in figure 2.20 the y coordinates of the membranes' midpoints over time. The color denotes the net y displacement up to $t = 250$. At $R_1 = 10^2$, the membranes' translational motions are generally oscillatory with long time intervals between changes in vertical direction. Decreasing R_1 generally decreases the lengths of these intervals, corresponding to higher frequency translational motions. At $R_1 = 10^{0.5}$, the membranes translate steadily (with occasional changes in direction, at $R_3 = 10^1$ and $10^{1.5}$). We find that steady (or nearly steady) translational motions actually occur at various R_1 in the

range $(10^{0.4}, 10^{1})$. At $R_1 = 10^{0}$, essentially periodic trajectories occur (at this R_1, periodic motions were also seen in the fixed–free case, figure 2.10). Decreasing R_1 to $10^{-0.5}$, we have many cases of oscillation superposed on a steady (or somewhat meandering) translation. This trend continues to the left of the red line, where the solutions become difficult to resolve numerically. The net membrane translations generally decrease with increases in R_3, presumably because the membranes are flatter, so they have a more tangential motion with respect to the oncoming flow if their vertical translations are smaller, and tangential motions are not resisted in this inviscid model.

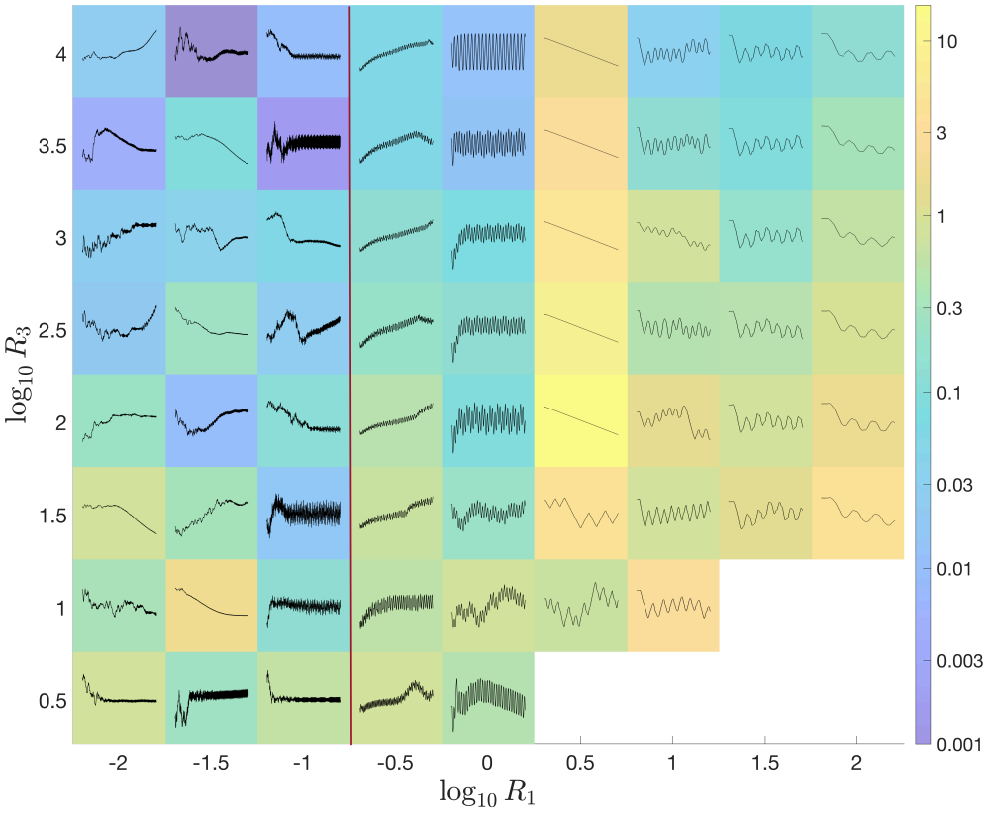

Figure 2.20: Time series of the y coordinates of the free–free membranes' midpoints, superposed on colors giving the maximum values of the time series for each (R_1, R_3) pair with $T_0 = 10^{-2}$. In the lower right corner, data are omitted because long-time trajectories were not obtained. For each membrane's midpoint y-coordinate time series, the axis scales are omitted due to space constraints but our focus here is on the qualitative features only.

We can use the power spectra of the total wake circulation to again characterize the membranes' temporal dynamics in the same R_1-R_3 parameter space. We find properties that are similar to the fixed–free case: low-frequency, somewhat aperiodic motions at the largest R_1, and a steady transition to higher-frequency motions with decreasing R_1 until, near $R_1 = 10^{0.5}$, the steady motions appear which have only a zero-frequency component in the wake circulation (the total wake circulation decays to zero in these cases). At $R_1 = 10^0$, periodic motions appear, and then become increasingly aperiodic with further decreases in R_1. The diverse types of translational motions do not lead to large qualitative changes in the power spectra, except for the steadily translating motions. We present power spectrum data for the free–free case in appendix C.

When both membrane ends are free, the "waviness" of the membrane is more difficult to define. Our definition is the number of crossings that a membrane makes with the line connecting its two endpoints, averaged over time. A definition based on crossings of a horizontal line would ignore the fact that many of the free–free membranes have small undulations about a line with nonzero net slope. The combination of a steady background flow with a nearly steady vertical translation makes a line with nonzero slope the state of pure tangential motion relative to the fluid, and thus the basic state of minimal resistance to the fluid. Figure 2.21 illustrates the zero crossings using this definition for several membrane examples. We omit the two endpoints from the set of zero crossings.

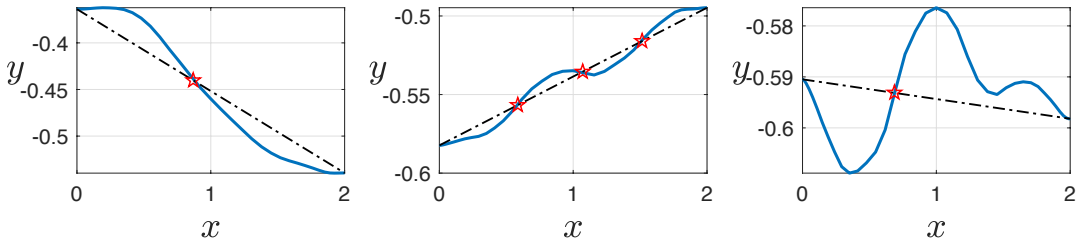

Figure 2.21: Schematic diagram that explains the term *zero-crossings* for a membrane with both endpoints free. The dot-dashed black line is the linear line that connects the two endpoints of the membrane at each time step, the blue solid line resembles the membrane at an instant of time, and the red star denotes the zero-crossing, which is the intersection point between the linear line and the membrane profile.

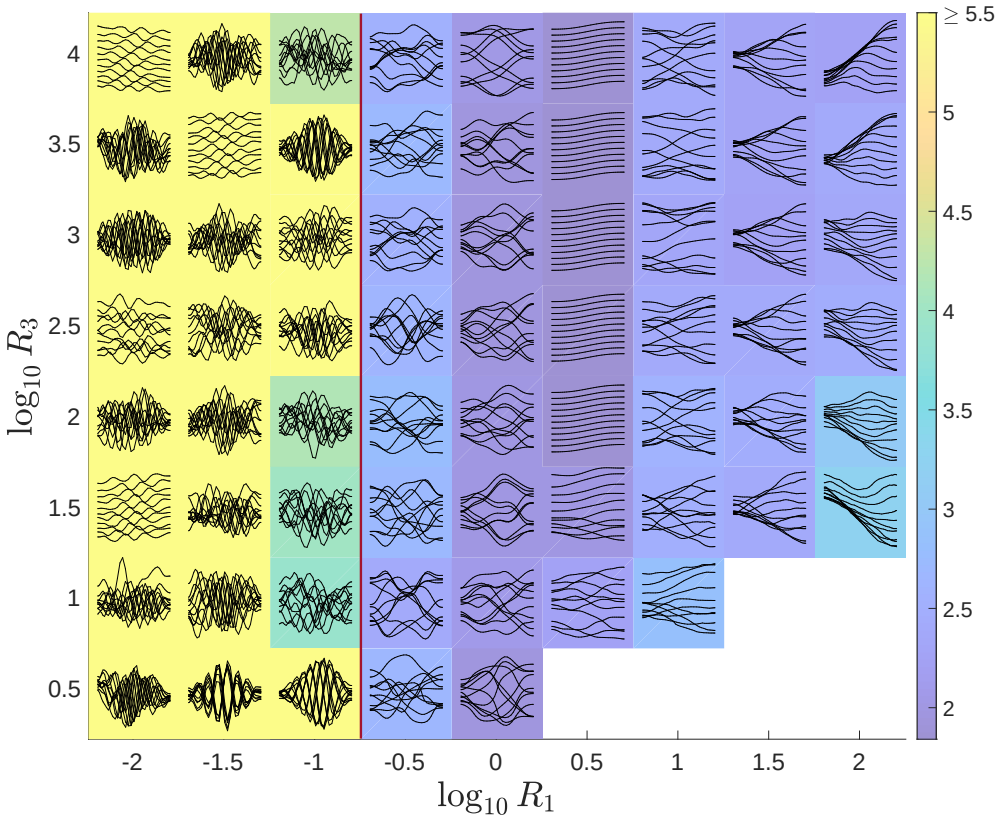

Figure 2.22: (Free–free.) Snapshots of the membrane motion at the large-amplitude regime, plotted on top of colors that correspond to the number of zero-crossings in the R_1-R_3 parameter space for fixed $T_0 = 10^{-2}$. The data in the right bottom corner are obtained for a shorter time and so, we neglect the computational results for those values of R_1 and R_3. At each (R_1, R_3) value, the set of snapshots is scaled to fit within a colored rectangle at the (R_1, R_3) value and normalized by the maximum deflection of the snapshots to show the motions more clearly.

Figure 2.22 shows the average number of zero crossings in the R_1-R_3 space already

discussed. Like the power spectra, this measure of membrane motion filters out some of the differences in translational motion. Starting at $R_1 = 10^2$, the number of zero crossings decreases to about 2 for the steady translating motions near $R_1 = 10^{0.5}$, and then increases with further decreases in R_1 as the motions become more periodic and then more irregular at yet smaller R_1 where the motions are not fully resolved spatially. The trend is generally the same as in the fixed–free case.

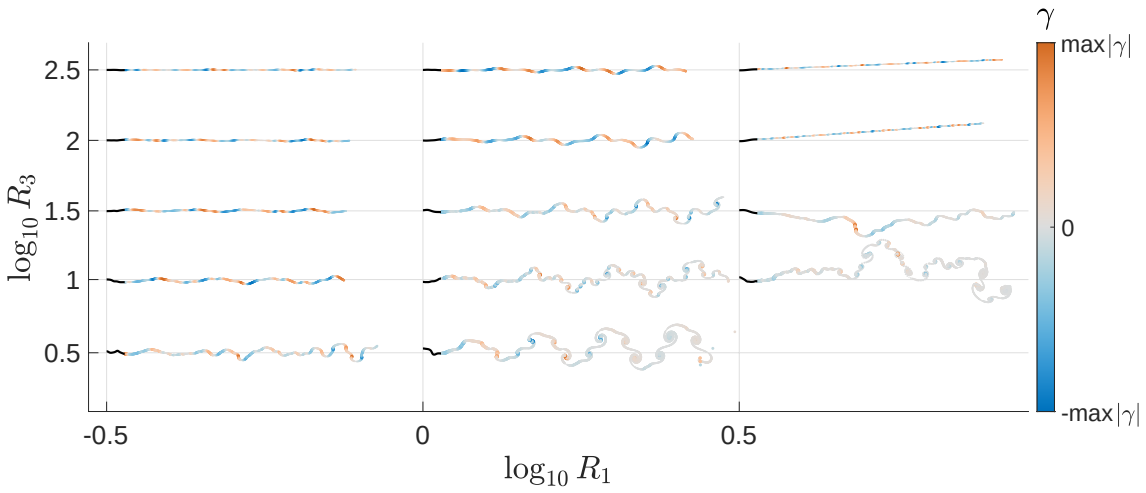

Figure 2.23: (Free–free.) Snapshots of the membrane motion (in black) and the vortex wake in a portion of the R_1-R_3 parameter space for fixed $T_0 = 10^{-2}$. In each case the (R_1, R_3) values are marked at the left endpoint of the membrane. The wake is color-coded according to the vortex sheet strength at the last time step. It is also thickness-coded according to $15|\gamma|^{1/3}$. Counterclockwise rotating vortices are shown in orange and clockwise rotating vortices in blue. For example, for $(R_1, R_3) = (10^{-0.5}, 10^{2.5})$ we have $\max|\gamma| = 0.0076$ and for $(R_1, R_3) = (10^{0.5}, 10^{1})$ we have $\max|\gamma| = 2.3$.

Examples of vortex wakes in the free–free case are shown in figure 2.23. The wakes have oscillatory patterns like those in the fixed–free case (figure 2.17). Here, however, the membranes' translational motion leads to more complexity in the wakes' spatial configurations. Fewer of these cases resemble a von Kármán vortex street than those in the fixed–free case. For example, the membrane with $R_1 = 10^0$ and $R_3 = 10^{0.5}$ in figure 2.22 oscillates almost periodically in the y direction. The motion is shown enlarged in figure 2.24(a). The corresponding vortex wake, shown in figure 2.23

Table 2.1: Comparison of frequencies in the small-amplitude and large-amplitude regimes with $R_3 = 10^{1.5}$ for three pairs of (R_1, T_0) at the flutter and divergence region for fixed–free and free–free membranes.

	(R_1, T_0)	Small-amplitude frequency	Large-amplitude frequency
Fixed–free	$(10^0, 10^{-0.5})$	0.1717	0.1313
	$(10^{0.5}, 10^{-0.5})$	0.0970	0.1240
	$(10^{1.5}, 10^0)$	0.0362	0.0543
Free–free	$(10^0, 10^{-0.5})$	0.1607	0.1303
	$(10^1, 10^0)$	0.0241	0.0542

(middle column, bottom row) is more complex than a von Kármán vortex street. At the upper right of figure 2.23 are approximately straight-line wakes, corresponding to membranes that translate steadily with a constant shape, e.g., the enlarged example in figure 2.24(b). Here the vortex wakes have zero strength density in the large-time limit, and so they translate steadily downstream without any self-induced undulatory motion or roll-up.

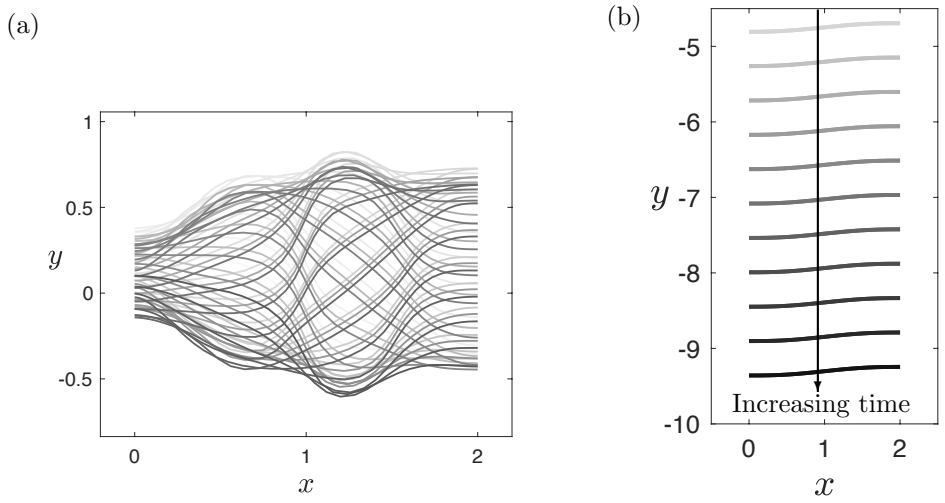

Figure 2.24: (Free–free.) Membrane snapshots at the large-amplitude regime, for (a) $R_1 = 10^0$ and $R_3 = 10^{0.5}$ and (b) $R_1 = 10^{0.5}$ and $R_3 = 10^{2.5}$. The shading of the membrane indicates the different phases in the motion, varying from gray at earlier times to black at current times.

Our final results are a brief comparison of membrane frequencies in the small-amplitude exponential growth regime, the focus of previous membrane flutter studies, and the large-amplitude steady-state regime. The top three rows of table 2.1 compare

the small- and large-amplitude frequencies of three fixed–free membranes, shown in figure 2.9 (at $R_3 = 10^{1.5}$), that become unstable through flutter and divergence and oscillate with a single dominant frequency. The bottom two rows compare the frequencies for two free–free membranes that also oscillate with single dominant frequencies. We note that the frequency may become significantly lower or higher as the membranes transition from small to large amplitude. It is unclear in general if aspects of the large amplitude motion can be inferred from the shapes and frequencies of the unstable modes in the linearized, small-amplitude regime.

2.4 Conclusions

In this chapter we have studied the flutter instability and large amplitude dynamics of thin membranes. These are made of elastic materials—e.g., rubber, textile fabric, or the skin of swimming or flying animals—with Young's moduli sufficiently small that stretching provides the primary resistance to fluid forces and bending resistance is negligible. Previous studies have considered the flutter instability of membranes with fixed ends. We find that all such membranes become unstable by divergence below a critical pretension T_0 close to the value identified in previous studies. Surprisingly, we find that all cases that exhibit large (but physically reasonable) deflections converge to states of steady deflection with single humps that are almost fore-aft symmetric, and the deflections scale as $1/\sqrt{R_3}$, where R_3 is the stretching modulus. These deformations are similar to those found with linearized models that assumed steady deflection at a fixed angle of attack [191, 194].

We then considered membranes with the leading edge fixed and the trailing edge free, and found a wide range of unsteady dynamics, somewhat similar to those seen in studies of flapping plates or flags. The critical pretension T_0 now depends on the

membrane mass density R_1. Membranes become unstable with divergence or with a combination of flutter and divergence in some cases near the stability boundary. The large-amplitude dynamics are independent of the pretension except close to the stability boundary, where the dynamics are in some cases more periodic and have smaller amplitudes. The dynamics depend most strongly on the membrane mass density R_1. At the largest R_1 studied we find the smallest oscillation frequencies and largest membrane deflections corresponding to somewhat chaotic and asymmetrical membrane motions. Here the mean temporal frequency scales as $1/\sqrt{R_1}$. As R_1 decreases, the membrane motions become more periodic and symmetrical, and with larger spatial frequency components (sharper curvatures and more zero-crossings). At $R_1 \leq 0.1$, the motions become more chaotic again, with much finer spatial features that are difficult to resolve numerically.

With both edges free, the membrane motions show two new features—a vertical translational component that may be nearly steady or oscillatory, and a nonzero slope. The combination of the two yields a small angle of attack with respect to the oncoming flow. The translational motion may be steady, periodic, or chaotic, and switch among these states with small changes of parameters. Superposed on the translational motions with nonzero slope are modes with oscillatory spatial and temporal features, similar to those in the fixed–free case in how they vary with T_0, R_1, and R_3.

Membrane (as opposed to beam/plate) flutter with free ends has barely been explored. However, our study shows that these boundary conditions allow for a much wider range of membrane dynamics with potential future applications in enhancing the performance of membrane wings [13,172], sails [30,91], and energy harvesting by membranes mounted on tensegrity structures [163, 204]. Extensional deformations

may be used in conjunction with [24, 40] or as an alternative to bending-dominated deformations for energy harvesting, e.g., the flutter of piezoelectric beams and bilayers [36, 44, 51, 89, 133, 138, 195].

CHAPTER III

Eigenmode Analysis of Membrane Stability in Inviscid Flow

3.1 Introduction

In chapter II we used a non-linear time-stepping algorithm to compute the stability thresholds for membranes with three sets of boundary conditions: fixed–fixed, fixed–free, and free–free leading and trailing edges. Membrane tension has a stabilizing effect in all cases. The ratio of membrane-to-fluid inertia has a less obvious effect—heavier membranes may be unstable when a lighter membrane was not, but the instability grows more slowly as membrane mass increases, to the point where it is difficult to determine whether the membrane is stable or not. Nonlinear time-stepping simulations with evolving vortex sheet wakes are expensive when large simulation times are required (i.e., to assess the stability of heavy membranes), and when the membrane develops fine deformations (as occurs for lighter membranes and smaller pretension values). In the latter case a fine grid on the membrane is required, increasing the size of the coupled system of equations that is solved implicitly, and making it more ill-conditioned, slowing convergence at each time step.

Therefore, in this chapter, we develop a less expensive alternative to study the stability problem—a nonlinear eigenmode solver. We solve for an ensemble of eigenmodes and corresponding eigenvalues (growth rates and frequencies) corresponding

to small-amplitude deformations. By comparing with unsteady simulations, we find that the modes accurately capture the early stages of the unsteady motion starting from the undeflected state. By comparing at later times, we find that the mode shapes qualitatively resemble those of the steady-state large amplitude motions to varying degrees.

Due to the vortex wake, it is difficult to obtain simple exact eigenmode solutions, and the physical mechanisms that underlie the membrane instability are somewhat elusive, but in this chapter we are able to present a comprehensive characterization of the modes and growth rates in the vicinity of the stability boundary. The eigenmode approach has been used previously to study membrane stability with fixed–fixed [124, 130, 168, 184] and periodic [128] boundary conditions. We use our method on the fixed–fixed case, as well as the fixed–free and free–free cases introduced in chapter II, where a wider range of dynamics can occur. In each case, we study a much wider range of membrane mass density and pretension values than previous studies.

Over several orders of magnitude of membrane mass density, we find instability by divergence or flutter (particularly at large mass density, or with one or both ends free). The most unstable eigenmodes generally become "wavier" at smaller mass density and smaller tension, but with regions of nonmonotonic behavior. We find good quantitative agreement with unsteady time-stepping simulations at small amplitude, but only qualitative similarities with the eventual steady-state large-amplitude motions.

The structure of this chapter is as follows. In §3.2 we present the membrane and vortex sheet model and in §3.3 its linearized, small-amplitude version, along with a summary of the numerical method for determining the eigenvalues and eigenmodes (§3.3.1). In §§3.4–3.6 we present our results for an extensive range of parameters for

each of the three boundary conditions. We then turn to simulations of the initial value problem and examine how the unsteady motions compare to the eigenmode shapes from the linearized model (§3.7). §3.8 presents conclusions.

3.2 Membrane-vortex-sheet Model

We model the dynamics of an extensible membrane that is nearly aligned with a two-dimensional background fluid flow with speed U in the far field (see figure 3.1).

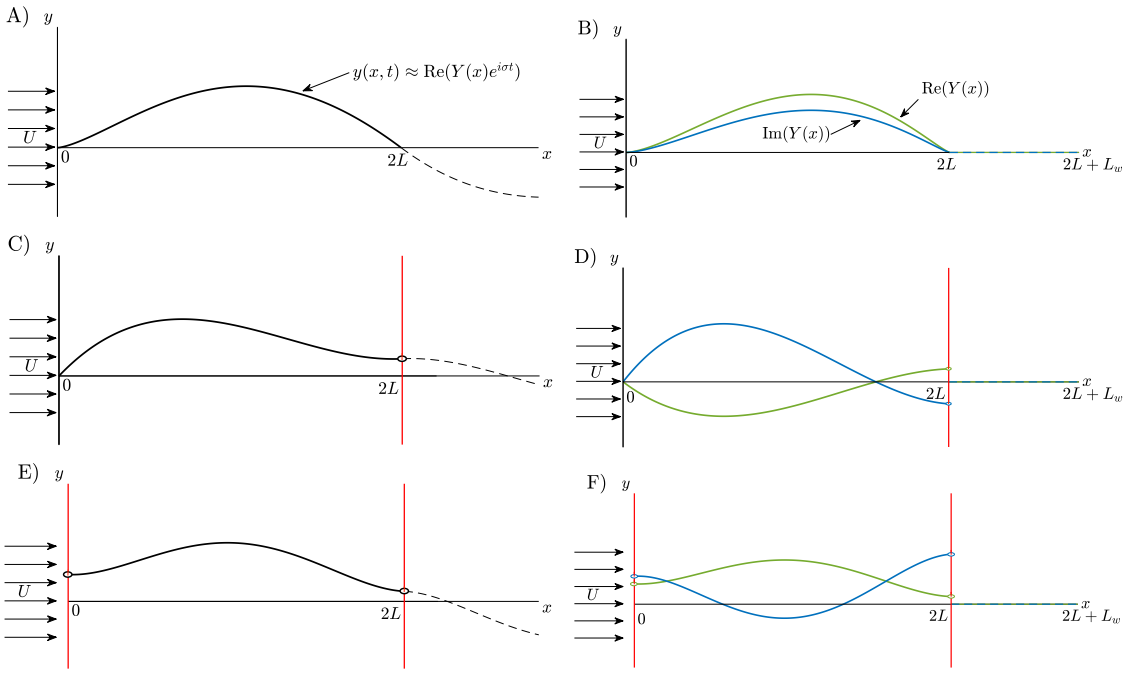

Figure 3.1: Schematic diagram of flexible membranes (solid curved black lines) at an instant in time. Here $2L$ is the chord length (the distance between the endpoints) and U is the oncoming flow velocity. For the nonlinear, large-amplitude model (panels A, C, and E), $y(x,t)$ is the membrane deflection and the dashed line is the free vortex wake. The right columns show the corresponding linearized, small-amplitude eigenvalue problems, where the motions are represented by the real and imaginary parts of the eigenmodes $Y(x)$, shown as green and blue lines, respectively, and flat vortex wakes of fixed length L_w shown as dashed lines at $y = 0$ (panels B, D, and F). The boundary conditions shown are: fixed–fixed membranes (panels A and B), fixed–free membranes (panels C and D), and free–free membranes (panels E and F).

In figure 3.1, we illustrate schematically the three cases of boundary conditions at the two ends of the membrane that we investigated in chapter II: fixed–fixed (panels A and B), fixed–free (panels C and D), and free–free (panels E and F). In all three cases,

the x-coordinates of the ends are fixed at 0 and $2L$. In the "fixed–fixed" case, we set the deflection to zero at both ends of the membrane; most previous studies of membrane flutter considered this boundary condition [99, 124, 146, 168, 184]. In the "fixed–free" case, the leading edge deflection is again set to zero but the trailing edge is allowed to deflect freely in the vertical direction. This is the classical free-end boundary condition for a membrane [45, 59]. The membrane end is fixed to a massless ring that slides along a vertical frictionless pole (represented by the red lines in figure 3.1). Since the pole is frictionless and the ring is massless, the membrane can exert no vertical force on the free end by tension, and hence the membrane slope must be zero.

Free-end boundary conditions have been implemented in various problems in classical mechanics such as beam flutter [10, 12, 14, 31, 35, 42, 58, 75, 80, 81, 89, 93, 109, 117, 121, 133, 153, 177, 186, 210], but they have not been used to a great extent in membrane flutter problems. Recently, an experimental study determined that membrane wing flutter can be enhanced by the vibrations of flexible leading and trailing edge supports [13]. For membrane wings with partially free trailing edges, trailing edge fluttering may occur at relatively low angles of attack [74]. Partially free edges occur also in sails. In [91], it is shown that by altering the tension in cables running along its free edges one can control the shape of a sail membrane and when the tension in these edges is sufficiently low, flutter can occur [30]. A related application is to energy harvesting by membranes mounted on tensegrity structures and placed in fluid flows [163, 204].

The authors in [110, 188] consider the dynamics and flutter of membranes and cables under gravity with free ends. In chapter II and in the current work, to focus on the basic flutter problem [154], we do not include gravity in the model. However, we

still need to ensure that the problem remains well-posed by requiring some restriction on the motion of the free membrane ends to eliminate the possibility of membrane compression [188]. This restriction is provided by the vertical frictionless poles. This has been carried out experimentally by representing a membrane as an extensional spring tethered by steel wires to vertical supports [87], for example.

The model here is the same as in chapter II but we repeat the main points for completeness. The membrane dynamics are described by the unsteady extensible elastica equation with body inertia, stretching resistance, and fluid pressure loading, obtained by writing a force balance equation for a small section of membrane lying between α and $\alpha + \Delta\alpha$:

(3.1)

$$\rho_s h W \partial_{tt}\zeta(\alpha,t)\Delta\alpha = T(\alpha+\Delta\alpha,t)\hat{\mathbf{s}} - T(\alpha,t)\hat{\mathbf{s}} - [p]^+_-(\alpha,t)\hat{\mathbf{n}} W \left(s(\alpha+\Delta\alpha,t) - s(\alpha,t)\right).$$

Here ρ_s is the mass per unit volume of the undeflected membrane, h is its thickness, and W is its out-of-plane width, all uniform along the length. In (3.1), $\zeta(\alpha,t) = x(\alpha,t) + iy(\alpha,t)$ is the membrane position in the complex plane, parameterized by the material coordinate α, $-L \le \alpha \le L$ (L is half the chord length) and time t. The pressure jump across the membrane is $[p]^+_-$, the local arc length coordinate is $s(\alpha,t)$, the local stretching factor is $\partial_\alpha s$, and the unit vectors tangent and normal to the membrane are $\hat{\mathbf{s}}$ and $\hat{\mathbf{n}}$, respectively. These are given by

$$\hat{\mathbf{s}} = \partial_\alpha\zeta(\alpha,t)/\partial_\alpha s(\alpha,t) = e^{i\theta(\alpha,t)} \quad \text{and} \quad \hat{\mathbf{n}} = i\hat{\mathbf{s}} = ie^{i\theta(\alpha,t)}, \tag{3.2}$$

with $\theta(\alpha,t)$ the local tangent angle. For the pressure jump term we use $+$ to denote the side towards which the membrane normal $\hat{\mathbf{n}}$ is directed, and $-$ for the other side. However, for the remainder of this chapter, we drop the $+$ and $-$ for ease of notation.

Dividing (3.1) by $\Delta\alpha$ and taking the limit $\Delta\alpha \to 0$, we obtain:

$$\rho_s h W \partial_{tt}\zeta(\alpha,t) = \partial_\alpha(T(\alpha,t)\hat{\mathbf{s}}) - [p](\alpha,t) W \partial_\alpha s \hat{\mathbf{n}}. \tag{3.3}$$

The membrane tension $T(\alpha,t)$ is given by linear elasticity [22, 123, 125] as

$$T(\alpha,t) = \overline{T} + EhW(\partial_\alpha s(\alpha,t) - 1), \tag{3.4}$$

where E is the Young's modulus and $\overline{T}$ is the tension in the (initial) undeflected equilibrium state. Equation (3.3) is made dimensionless by nondimensionalizing length by the membrane's half-chord L, time by L/U, and pressure by $\rho_f U^2$, where ρ_f is the density of the fluid and U is the oncoming flow velocity. The nonlinear, extensible membrane equation becomes

$$R_1 \partial_{tt}\zeta - \partial_\alpha((T_0 + R_3(\partial_\alpha s - 1))\hat{\mathbf{s}}) = -[p]\partial_\alpha s \hat{\mathbf{n}}. \tag{3.5}$$

The dimensionless membrane mass is $R_1 = \rho_s h/(\rho_f L)$, the dimensionless stretching rigidity is $R_3 = Eh/(\rho_f U^2 L)$, and finally, $T_0 = \overline{T}/(\rho_f U^2 LW)$ is the dimensionless pretension. The model is linearized for small-amplitude membrane deflections in §3.3 (shown schematically in figure 3.1, right column).

We let $z = x + iy$ to use the complex representation of the xy flow plane. The complex conjugate of the fluid velocity at any point z not on the vortex sheets is a sum of the horizontal background flow with dimensionless speed unity and the flow induced by the bound and free vortex wakes:

$$u_x(z) - iu_y(z) = 1 + \frac{1}{2\pi i}\int_{-1}^{1} \frac{\gamma(\alpha,t)}{z - \zeta(\alpha,t)} \partial_\alpha s \mathrm{d}\alpha + \frac{1}{2\pi i}\int_0^{s_{\max}} \frac{\gamma(s,t)}{z - \zeta(s,t)} \mathrm{d}s, \tag{3.6}$$

where s is the arc length along the free sheet starting at 0 at the membrane's trailing edge and extending to $s_{\max}$ at the free sheet's far end. To determine the bound vortex sheet strength γ we require that the fluid does not penetrate the membrane,

i.e., the kinematic boundary condition. Here γ also represents the jump in the component of the flow velocity tangent to the membrane from the $-$ to the $+$ side, i.e., $\gamma = -[(u_x, u_y) \cdot \hat{\mathbf{s}}]$. The normal components of the fluid and membrane velocities are equal:

(3.7)
$$\mathrm{Re}(\hat{\mathbf{n}}\partial_t\overline{\zeta}(\alpha,t)) = \mathrm{Re}\left(\hat{\mathbf{n}}\left(1 + \frac{1}{2\pi i}\int_{-1}^{1}\frac{\gamma(\alpha,t)}{z-\zeta(\alpha,t)}\partial_\alpha s \mathrm{d}\alpha + \frac{1}{2\pi i}\int_0^{s_{\max}}\frac{\gamma(s,t)}{z-\zeta(s,t)}\mathrm{d}s\right)\right),$$

where $\hat{\mathbf{n}}$ is written as a complex scalar. Solving (3.7) for γ on the body requires an additional constraint that the total circulation is zero for a flow started from rest. At each instant the part of the circulation in the free sheet, or alternatively, the strength of γ where the free sheet meets the trailing edge of the membrane, is set by the Kutta condition which makes the flow velocity finite at the trailing edge. At every other point of the free sheet, γ is set by the criterion that circulation (the integral of γ) is conserved at material points of the free sheet. The vortex sheet strength $\gamma(\alpha,t)$ is coupled to the pressure jump $[p](\alpha,t)$ across the membrane using a version of the unsteady Bernoulli equation written at a fixed material point on the membrane:

$$\partial_\alpha s \partial_t \gamma + \partial_\alpha\left(\gamma(\mu-\tau)\right) + \gamma(\partial_\alpha\tau - \nu\kappa\partial_\alpha s) = \partial_\alpha[p], \tag{3.8}$$

where μ is the average flow velocity tangent to the membrane, τ and ν are the tangential and normal components of the membrane velocity, respectively, and $\kappa(\alpha,t) = \partial_\alpha\theta/\partial_\alpha s$ is the membrane's curvature. At the trailing edge, $[p]|_{\alpha=1} = 0$. The derivation of (3.8) is included in appendix A.

3.3 Small-amplitude Linearization

The large-amplitude, nonlinear system described in §3.2 becomes more amenable to analysis in the small-amplitude regime. Here we focus on the computation of

eigenmodes and eigenvalues for the three boundary conditions studied in chapter II: "fixed–fixed," "fixed–free," and "free–free" membranes. We are thereby able to present the small-amplitude motions of the membranes at larger and smaller membrane densities than in the previous work, and in much greater detail. A similar linearized model was derived in [3] for the dynamics of a flapping flag. We consider small deflections $y(x,t)$ from the straight configuration, aligned with the flow. Since the membrane stretching factor is $\partial_\alpha s \approx 1 + \partial_x y^2/2$, to linear order $\alpha \approx s \approx x$, all α-derivatives in (3.5) are x-derivatives, and $\zeta(\alpha,t) \approx \zeta(x,t) = x + iy(x,t)$. At linear order, the tangent and normal vectors are:

$$\hat{\mathbf{s}} \approx (1, \partial_x y)^\top, \quad \hat{\mathbf{n}} \approx (-\partial_x y, 1)^\top. \tag{3.9}$$

The linearized version of the membrane equation is

$$R_1 \partial_{tt} y - T_0 \partial_{xx} y = -[p]. \tag{3.10}$$

The term in the tension force $T(\alpha,t) = T_0 + R_3(\partial_\alpha s - 1)$ involving R_3 (dimensionless stretching rigidity) is of quadratic order, so the linear dynamics are governed by the dimensionless membrane mass R_1 and the dimensionless pretension T_0. The boundary conditions are:

$$\text{fixed–fixed:} \quad y(\pm 1, t) = 0, \tag{3.11}$$

$$\text{fixed–free:} \quad y(-1,t) = 0,\ \partial_x y(1,t) = 0, \tag{3.12}$$

$$\text{free–free:} \quad \partial_x y(\pm 1, t) = 0. \tag{3.13}$$

The dynamics of the membrane are coupled to the fluid flow through the pressure jump term $[p](x,t)$. The linearized version of the pressure jump equation is

$$\partial_t \gamma + \partial_x \gamma = \partial_x [p]. \tag{3.14}$$

The set of equations is closed by relating the vortex sheet strength $\gamma(x,t)$ back to the membrane position $y(x,t)$, through the kinematic condition, in linearized form:

$$\partial_t y(x,t) = -\partial_x y(x,t) + \frac{1}{2\pi}\fint_{-1}^{1} \frac{v(x',t)}{\sqrt{1-x'^2}(x-x')}\,\mathrm{d}x' + \frac{1}{2\pi}\int_{1}^{\ell_w+1} \frac{\gamma(x',t)}{x-x'}\,\mathrm{d}x', \tag{3.15}$$

with $-1 < x < 1$. Here, we use that $\partial_t\overline{\zeta}(x,t) \approx -i\partial_t y$ and from (3.9), the normal velocity component $\mathrm{Re}(\hat{\mathbf{n}}\partial_t\overline{\zeta}) \approx \partial_t y$. The general solution $\gamma(x,t)$ has inverse square-root singularities at $x = \pm 1$ and so we define $v(x,t)$, the bounded part of $\gamma(x,t)$ by $\gamma = v/\sqrt{1-x^2}$. The second integral in (3.15) represents the velocity induced by the vortex sheet wake, which extends downstream from the membrane on the interval $1 < x < \ell_w + 1$, $y = 0$. Therefore, the eigenvalue problem assumes a free vortex wake of a given fixed length ℓ_w, which we take to be large (i.e., we assume we start with a deflection that is sufficiently small that we remain in the small-amplitude regime for a long time).

The circulation in the wake,

$$\Gamma(x,t) = -\int_{x}^{\ell_w+1} \gamma(x',t)\,\mathrm{d}x', \tag{3.16}$$

is conserved along material points of the wake by Kelvin's circulation theorem. At linear order, the wake moves at the constant speed (unity) of the free stream; self-interaction is negligible.

At each time t, the total circulation in the wake, $\Gamma(1,t)$, is set by the Kutta condition, which in linearized form is unchanged, i.e.,

$$v(1,t) = 0. \tag{3.17}$$

Using the system of equations (3.10), (3.14), (3.15), and (3.17) we solve for the following unknowns: the motion of the membrane and the strengths of the vortex sheets along the membrane and in the wake.

For the linearized system, we may write solutions in the following form:

$$y(x,t) = Y(x)e^{i\sigma t}, \tag{3.18}$$

$$\gamma(x,t) = g(x)e^{i\sigma t}, \tag{3.19}$$

$$v(x,t) = V(x)e^{i\sigma t}, \tag{3.20}$$

$$\Gamma(1,t) = \Gamma_0 e^{i\sigma t}, \tag{3.21}$$

where Y, g, V, and Γ_0 are components of eigenmodes with complex eigenvalues $\sigma = \sigma_{\mathrm{R}} + i\sigma_{\mathrm{I}} \in \mathbb{C}$. The real parts of the eigenvalues are the angular frequencies and the imaginary parts are the temporal growth rates. If $\sigma_{\mathrm{I}} > 0$, small perturbations decay exponentially and the mode is stable, while if $\sigma_{\mathrm{I}} < 0$, small perturbations grow exponentially and the mode is unstable. If $\sigma_{\mathrm{I}} = 0$ the mode is neutrally stable.

We wish to identify the region of R_1-T_0 space in which unstable eigenmodes exist, and when there are multiple unstable modes, identify the fastest growing mode.

Since Γ is conserved at material points of the free vortex sheet as they move downstream (at speed 1), and the material point at location $x \geq 1$ at time t was at location $x = 1$ at time $t - (x-1)$, we can write

$$\Gamma(x,t) = \Gamma_0 e^{i\sigma(t-(x-1))} = \Gamma_0 e^{-i\sigma(x-1)} e^{i\sigma t}, \quad 1 < x < \ell_w + 1, \tag{3.22}$$

$$\gamma(x,t) = \partial_x \Gamma(x,t) = -i\sigma\Gamma_0 e^{-i\sigma(x-1)} e^{i\sigma t}, \quad 1 < x < \ell_w + 1, \tag{3.23}$$

using (3.21). Inserting the eigenmodes (3.18)–(3.21) into the governing equations, (3.10) and (3.15), yields

$$-\sigma^2 R_1 Y = T_0 \partial_{xx} Y - i\sigma \int_{-1}^{1} g \,\mathrm{d}x - g, \tag{3.24}$$

and

$$i\sigma Y = -\partial_x Y + \frac{1}{2\pi} \fint_{-1}^{1} \frac{V(x')}{\sqrt{1-x'^2}(x-x')} \,\mathrm{d}x' - \frac{1}{2\pi} i\sigma\Gamma_0 \int_{1}^{\ell_w+1} \frac{e^{-i\sigma(x'-1)}}{x-x'} \,\mathrm{d}x', \ -1 < x < 1, \tag{3.25}$$

respectively. Because σ appears in the exponential in the second integral in (3.25), this is a nonlinear eigenvalue problem.

3.3.1 Numerical Method for Finding the Eigenvalues and Eigenmodes

We solve the nonlinear eigenvalue problem iteratively. At each iteration, we have an approximation σ_0 to a given eigenvalue σ. We approximate the equations as a quadratic eigenvalue problem:

$$[\sigma^2 A_2 + \sigma A_1 + A_0(\sigma_0)]w = 0, \tag{3.26}$$

where the matrices A_2, A_1, A_0 are known from equations (3.24), (3.25), and $g(x) = V(x)/\sqrt{1-x^2}$. The eigenvector w consists of: (a) values of the eigenmodes, defined as $Y(x)$ on the Chebyshev grid $\{x_j = \cos\theta_j,\, \theta_j = (j-1)\pi/m,\, j = 1, \ldots, m+1\}$ and (b) the scalar Γ_0. The term $A_0(\sigma)w$ includes the exponential integral involving σ in (3.25) as well as terms that are constant in σ. In the exponential integral, σ is fixed at σ_0, the value of σ from the previous iteration, resulting in the quadratic eigenvalue problem (3.26), which is solved using `polyeig` in MATLAB. Equation (3.26) has $2m+4$ eigenvalue solutions. As in [3], we define an error function as the difference between σ_0 and the eigenvalue (out of the $2m+4$ possibilities) closest to it. We also compute the derivatives of the error function (i.e., the Jacobian matrix) with respect to σ_{R} and σ_{I} using finite differences at the initial iterate, and update it at subsequent iterates using Broyden's approximate formula [140]. The error function and Jacobian define the search direction (via Newton's formula) for the next iterate. With this approach we obtain superlinear convergence to a given eigenvalue. By using a wide range of initial guesses, we obtain convergence to various eigenvalues and corresponding eigenmodes.

The numerical solution procedure followed in the current work differs from [3].

There we used a continuation method, which for the current problem would start from the analytical solution for each eigenvalue in the limit $R_1, T_0 \gg 1$, and use the solution at a given (R_1, T_0) as an initial guess for slightly smaller (R_1, T_0) (continuing to smaller and smaller (R_1, T_0)). We find that this method fails to find solutions at certain (R_1, T_0) and therefore at smaller values also, so we use a more robust approach here. We compute a large set of eigenvalues at each (R_1, T_0) using a large grid of initial eigenvalue guesses in the complex plane covering in most cases $\sigma_{\rm R} \in [-8, 8]$ and $\sigma_{\rm I} \in [-3, -0.5]$. For each initial guess we perform the eigenvalue iteration described above until it converges. This reveals the basins of attraction of the eigenvalues under Broyden's iteration, which shows that the imaginary part is not as important as the real part of the eigenvalue guess (especially for large R_1 values). We note that in the system of equations (3.24)–(3.25) the eigenvalue σ appears in powers of $i\sigma$. For each solution $\{i\sigma, w\}$, the complex conjugate $\{-i\bar{\sigma}, \bar{w}\}$ is also a solution, so we need only compute one member of the pair, and obtain the other by conjugation. For the eigenvalue $i\sigma = i\sigma_{\rm R} - \sigma_{\rm I}$, the conjugate is $-i\bar{\sigma} = -i\sigma_{\rm R} - \sigma_{\rm I}$; i.e., the sign of $\sigma_{\rm R}$ is reversed. Thus we can restrict to $\sigma_{\rm R} \geq 0$.

We now present typical examples of our eigenmode computations. Throughout the present chapter we use $m = 120$ for the Chebyshev grid, unless noted otherwise. Comparisons between $m = 80$ and 120 (as well as 240) are presented in appendix D. Figure 3.2 shows results for $(R_1, T_0) = (10^{-1}, 10^{-0.27})$ with both membrane edges fixed. The coloring in panels A and B indicates the converged values of $\sigma_{\rm R}$ (panel A) and $\sigma_{\rm I}$ (panel B) over a grid of initial eigenvalue guesses in the complex plane spanning 320 values in the real direction and 4 values in the imaginary direction. In panel C we plot the 25 distinct eigenvalues found with this set of initial guesses and in D, the corresponding eigenmodes from the most unstable (smallest—or most

negative—σ_{I}) on the left to the most stable (largest σ_{I}) on the right. The vertical black line in D separates the (only) unstable mode (on its left) from the stable modes (on its right). The unstable mode loses stability through divergence as is evident from panel C, where the associated eigenvalue has $\sigma_{\mathrm{R}} \approx 10^{-9}$ and $\sigma_{\mathrm{I}} < 0$. We also illustrate with a red circle in panels A and B an instance of an initial guess that gives rise to this mode. The converged σ values are more sensitive to the real than to the imaginary part of the initial guess, which motivates the wider range of σ_{R} used here and subsequently.

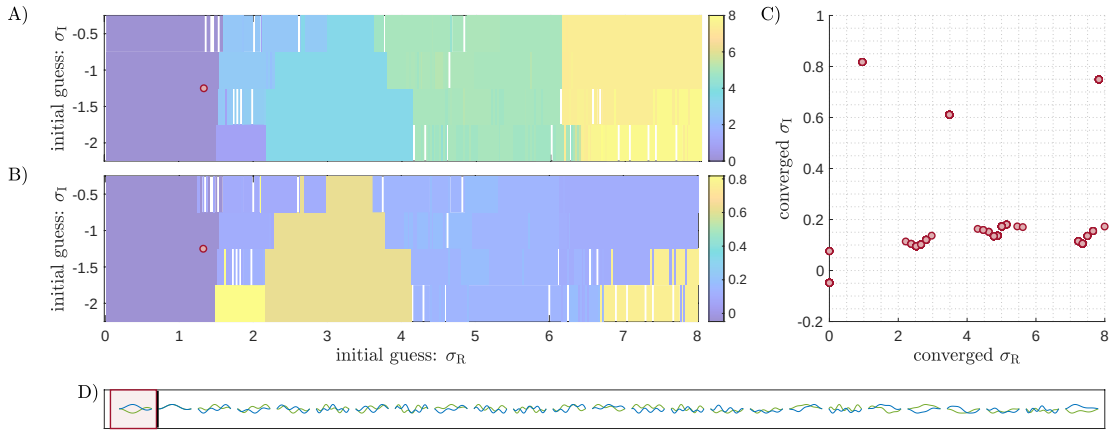

Figure 3.2: Fixed–fixed eigenvalues and eigenmodes with $R_1 = 10^{-1}$ and $T_0 = 10^{-0.27}$. Computed σ_{R} (panel A, values in colorbars at right) and computed σ_{I} (panel B, values in colorbars at right), both plotted over the initial guess complex plane. C) The distinct eigenvalues generated by the numerical method replotted as red dots in the $(\sigma_{\mathrm{R}}, \sigma_{\mathrm{I}})$ plane. D) The corresponding eigenmodes ($\mathrm{Re}(Y(x))$ in green, $\mathrm{Im}(Y(x))$ in blue) from the only unstable one (with negative σ_{I}) on the left to the most stable one (largest σ_{I}) on the right. The vertical black line separates the unstable mode (on its left) and stable modes (on its right).

In figure 3.3 we show another example of the eigenvalue computation for fixed–fixed membranes, with larger membrane mass and pretension: $(R_1, T_0) = (10^3, 10^{1.5})$. In panels A and B we use a grid of initial eigenvalue guesses spanning 640 values in the real direction and 6 values in the imaginary direction. For smaller R_1 (as in figure 3.2) the converged σ vary more with the initial choice of σ_{I} compared to the larger R_1 here, where the converged eigenvalues are independent of the initial σ_{I}, and

depend only on the initial σ_{R}.

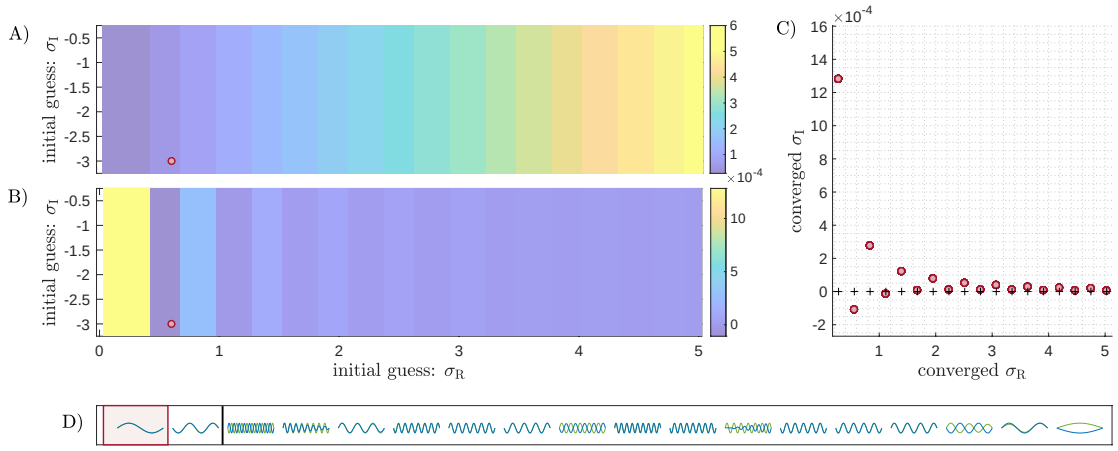

Figure 3.3: Fixed–fixed eigenvalues and eigenmodes with $R_1 = 10^3$ and $T_0 = 10^{1.5}$ and other quantities as described in figure 3.2.

Since a generic perturbation is a superposition of all the eigenmodes multiplied by $e^{i\sigma t} = e^{i\sigma_{\mathrm{R}} t} e^{-\sigma_{\mathrm{I}} t}$, we classify the stability of generic perturbations in the (R_1, T_0) parameter space based on the value of $\sigma_{\mathrm{R}} + i\sigma_{\mathrm{I}}$ for the smallest σ_{I} at a given (R_1, T_0):

1. $\sigma_{\mathrm{I}} > 0$: stable,
2. $\sigma_{\mathrm{I}} = 0$: stability boundary location,
3. $\sigma_{\mathrm{I}} < 0$ and $\sigma_{\mathrm{R}} = 0$: divergence ("static" instability),
4. $\sigma_{\mathrm{I}} < 0$ and $\sigma_{\mathrm{R}} \neq 0$: flutter and divergence.

3.4 Fixed–fixed Membranes

We start with membranes that have both edges fixed at zero deflection (satisfying (3.11)). We plot the stability boundary as the red dots connected by red lines in figure 3.4A and B. Below and to the right is the unstable region. The red dots are computed by linear interpolation of σ_{I} between neighboring T_0 values (shown by the horizontal black bars) that bracket the boundary: all σ_{I} are positive at the larger of the T_0 values and above, but one σ_{I} is negative at the smaller of the T_0 values.

The stability boundary (red line) agrees well with that of our nonlinear time-stepping simulations (orange line, from chapter II) and with the results of [184]. For each R_1, an eigenmode first becomes unstable when the pretension T_0 drops below a critical value $T_{0C}(R_1)$. For $R_1 < 10^2$, $T_{0C}(R_1) \in [1.7, 2]$, almost independent of R_1. In our nonlinear, unsteady simulations (chapter II), we found a similar range of $T_{0C}(R_1)$, $[1.7, 1.92]$, for $R_1 < 10^{1.5}$. The small discrepancy could arise from the δ-smoothing on the free vortex sheet (that is not used in the eigenvalue solution but is used in the time-stepping simulation). Another possible explanation (as stated in [3]) is that in the time-stepping simulation in chapter II the wake grows from zero length but in the current eigenvalue problem the wake has fixed length ℓ_w. In our simulations we use $\ell_w = 39$, and the modes are essentially unchanged at larger ℓ_w. In chapter II we were not able to compute the upward sloping portion of the stability boundary for $R_1 > 10^{1.5}$ using the unsteady simulations, due to the slow growth/decay of small perturbations with large R_1.

In figure 3.4 the colored dots give the imaginary (panel A) and real parts (panel B) of the most unstable eigenvalues (with corresponding eigenmodes shown later, in figure 3.5). The gray dots in panel B indicate negative σ_{I} and nearly zero σ_{R} ($\sigma_{\mathrm{R}} \leq 10^{-9}$) for the most unstable eigenmode, which corresponds to divergence. The colored dots in panel B indicate a nonzero real part (value in colorbar at right) for the most unstable eigenmode, corresponding to flutter and divergence. Within the instability region (region below the red line) we find that for a fixed T_0, the fastest growing mode has a growth rate (σ_{I}) that generally decreases in magnitude as R_1 increases. We also find that membranes with $R_1 \lesssim 10^{1.5}$, in general, lose stability by divergence for $T_0 \in (10^{-0.5}, T_{0C}(R_1)]$ but then for a smaller T_0 ($\lesssim 10^{-0.5}$), by flutter and divergence. Heavier membranes generally lose stability by flutter and divergence for

$T_0 \in (10^{0.25}, T_{0C}(R_1)]$.

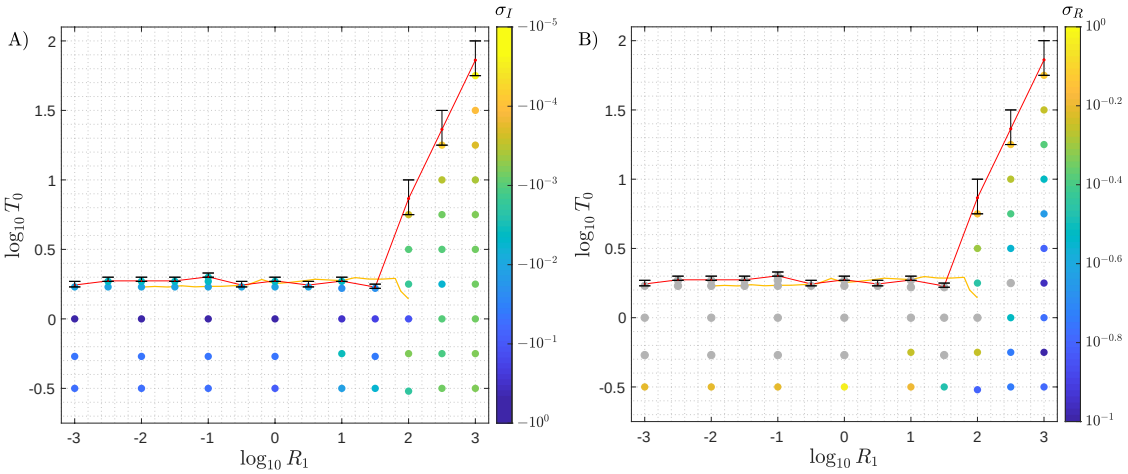

Figure 3.4: The region in R_1-T_0 space in which the fixed–fixed membrane is unstable. The red line and red dots indicate the position of the stability boundary computed by linear interpolation between σ_I of the smallest T_0 that gives a stable membrane and the σ_I of the largest T_0 that gives an unstable membrane (shown in the error bars). The colors of the dots below the stability boundary label: A) The imaginary parts of the eigenvalues (σ_I) corresponding to the most unstable modes. They represent the temporal growth rate. B) The real parts of the eigenvalues (σ_R) for the most unstable modes, representing the angular frequencies. The gray dots correspond to modes that lose stability by divergence and have $\sigma_\mathrm{R} \leq 10^{-9}$. The orange line that spans $\log_{10} R_1 \in [-2, 2]$ represents the stability boundary computed numerically in chapter II.

In the limit $R_1, T_0 \gg 1$, the fluid pressure is negligible and the linearized membrane equation (3.10) reduces to the homogeneous wave equation

$$R_1 \partial_{tt} y - T_0 \partial_{xx} y = 0, \tag{3.27}$$

which after substituting (3.18) becomes

$$-\sigma^2 R_1 Y - T_0 \partial_{xx} Y = 0. \tag{3.28}$$

The eigenmodes are linear combinations of $\cos(kx)$ and $\sin(kx)$, with $k = \pm\sigma\sqrt{R_1/T_0}$, satisfying the boundary conditions (3.11). Nontrivial linear combinations exist for k values for which the determinant of the matrix

$$\begin{pmatrix} \sin(-k) & \cos(-k) \\ \sin(k) & \cos(k) \end{pmatrix} \tag{3.29}$$

vanishes, which occurs at $k = n\pi/2$ for $n \in \mathbb{Z}_{>0}$. Each k gives a pair of eigenvalues:

$$\sigma = \pm k\sqrt{\frac{T_0}{R_1}}, \tag{3.30}$$

and eigenmodes of the form

$$Y(x) = \sin\left(\frac{n\pi}{2}(x+1)\right), \tag{3.31}$$

for $n \in \mathbb{Z}_{>0}$ and $-1 \leq x \leq 1$, where the amplitude is arbitrary.

Similar to [3], in the limit of $R_1, T_0 \gg 1$ equation (3.30) shows that the frequency scales as $\sqrt{T_0/R_1}$. We have observed this in our simulations: σ_{R} is approximately constant along lines of constant T_0/R_1 in the upper right portion of figure 3.4B (toward the vacuum limit). At smaller R_1, the angular frequency is less sensitive to the membrane pretension.

The numerical results for the eigenvalues (red dots) shown in figure 3.3C show excellent agreement with the analytical form (3.30) of σ (black plusses), with very small imaginary parts (vertical axis). In panel D there are two unstable modes ($n = 2$ and 4 in equation (3.31)), which are also the unstable modes that were found in [184] for large values of R_1 and T_0.

In figure 3.5 we plot again the instability region in the R_1-T_0 parameter space for fixed–fixed membranes, but with the eigenmode shapes corresponding to the most unstable eigenvalues in figure 3.4. The real and imaginary parts of the eigenmode $Y(x)$ are shown in green and blue, respectively. We place gray rectangles around the modes that lose stability by divergence. For $R_1 < 10^2$ and T_0 just below T_{0C}, the unstable eigenmode is a single-hump shape that is nearly fore-aft symmetric. As the pretension is decreased further below T_{0C} the divergent eigenmode becomes asymmetric, its maximum deflection point shifting towards the trailing edge. This agrees with [184, Fig. 10]. In the divergence region of figure 3.5 when $T_0 = 10^0$ and

R_1 decreases from 10^2 to 10^{-1}, the maximum deflection point also shifts from the midchord towards the trailing edge, in agreement with [184, figure 5]. For heavier membranes ($R_1 \geq 10^2$), the membrane loses stability with an even-numbered mode shape through flutter and divergence. In particular the second mode ($n = 2$) is the most unstable mode for $R_1 \geq 10^2$ and $T_0 \in [10^{0.5}, T_{0C}(R_1)]$, as well as $(R_1, T_0) = (10^2, 10^{0.25})$ and $(10^3, 10^{0.25})$. Decreasing the pretension value below $10^{0.25}$, the fourth mode ($n = 4$) becomes the most unstable for $R_1 > 10^2$, followed by the sixth mode at $(R_1, T_0) = (10^2, 10^{-0.25})$, $(10^{2.5}, 10^{-0.5})$. For heavy membranes with decreasing T_0, the most unstable mode apparently moves to progressively higher even-numbered modes.

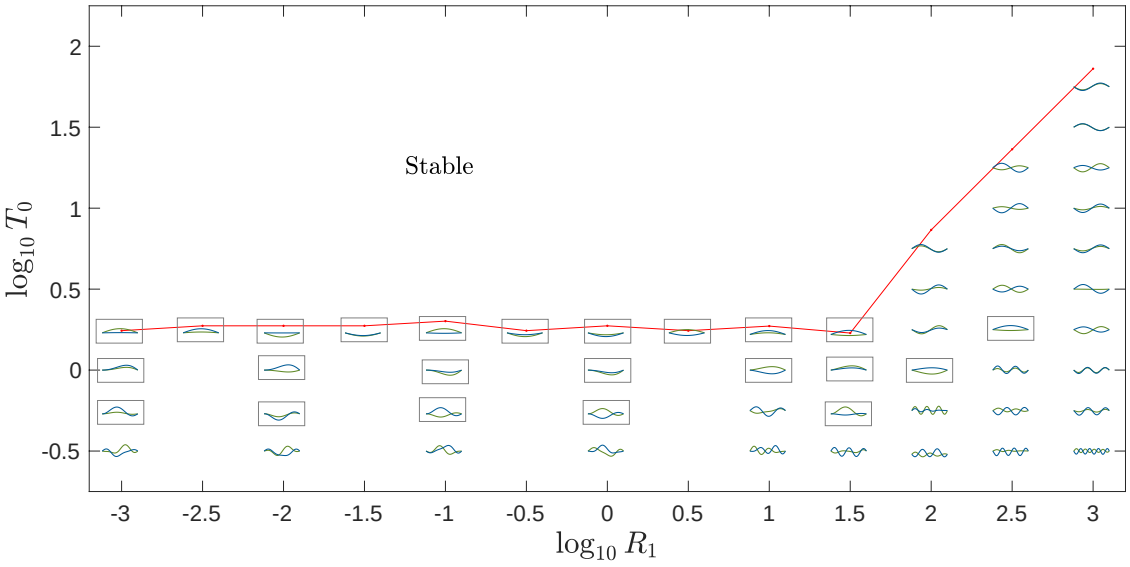

Figure 3.5: The shapes $Y(x)$ of the most unstable eigenmodes as a function of R_1 and T_0 in the fixed–fixed case. The real and imaginary parts of $Y(x)$ are shown in green and blue, respectively. Each shape is scaled both vertically and horizontally to fit within the plot. The shapes are superposed on the same stability boundary (red line) as in figure 3.4. Modes exhibiting a divergence instability have a gray rectangle outline.

We now study in more detail how the eigenvalues change in R_1-T_0 space by examining what happens when T_0 passes through the stability boundary. We track the stable and unstable modes using a grid of initial eigenvalue guesses in the complex

plane covering $\sigma_{\mathrm{R}} \in (0, 8]$ and $\sigma_{\mathrm{I}} \in [-3, 3]$, with 160 values in the real direction and 13 values in the imaginary direction. As can be observed in figure 3.5, in general, as we move to smaller T_0 values higher wavenumber modes become the most unstable ones. We now consider the instability of higher wavenumber modes as we cross the stability boundary, by fixing two values of R_1 and decreasing T_0, while tracking the real and imaginary parts of the computed eigenvalues.

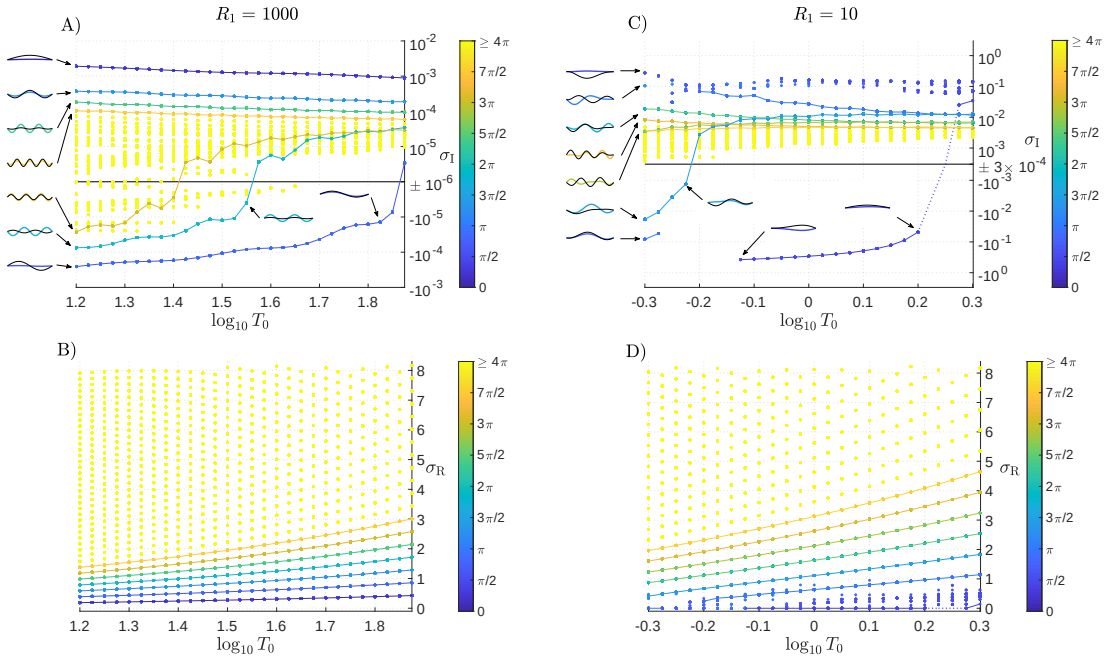

Figure 3.6: For two values of membrane mass (R_1), 10^3 (left column) and 10^1 (right column), the imaginary (A, C) and real parts (B, D) of the eigenvalues versus pretension (T_0) for fixed–fixed membranes. The coloring represents the RMS of the membrane's slope, Y'_{RMS} (3.32) for each (R_1, T_0) pair. The horizontal black lines in the top panels located at A) $\sigma_{\mathrm{I}} = \pm 10^{-6}$ and C) $\sigma_{\mathrm{I}} = \pm 3 \times 10^{-4}$ distinguish stable modes (above) and unstable modes (below). To the left of and within panels A and C, we show typical modes for branches with $Y'_{\mathrm{RMS}} < 4\pi$.

In figure 3.6 we show the real (bottom row) and imaginary parts (top row) of the eigenvalues for $R_1 = 10^3$ (left column) and 10^1 (right column), while decreasing T_0. The colors show the normalized root mean square (RMS) slope of each membrane

eigenmode on the Chebyshev mesh, defined by

$$Y'_{\mathrm{RMS}} := \sqrt{\int_{-1}^{1} \left|\frac{\mathrm{d}Y}{\mathrm{d}x}\right|^2 \,\mathrm{d}x \;\Big/\; \int_{-1}^{1} |Y|^2 \,\mathrm{d}x}, \tag{3.32}$$

which is a measure of the "waviness" of each mode. Each branch that possesses approximately the same color (lying in a particular, small range of Y'_{RMS}) indicates a distinct mode. At the highest mass ($R_1 = 1000$), panels A and B, we connect the eigenvalues by polygonal lines for the modes that are sufficiently distinct from the others—the seven lowest wavenumber modes. The branches in panel A are somewhat jagged when $|\sigma_{\mathrm{I}}|$ drops below 10^{-5}. The corresponding σ_{R} (panel B) vary much more smoothly, probably because their magnitudes are larger relative to numerical errors. The blue branch with the most negative σ_{I} values first becomes unstable (σ_{I} changes from positive to negative) at $T_0 \approx 10^{1.87}$, which coincides with the loss of stability in figure 3.5. The mode associated with this blue branch is the second mode ($n = 2$ in equation (3.31)). The next branch to become unstable corresponds to the fourth mode ($n = 4$) at $T_0 \approx 10^{1.56}$ and then the sixth mode ($n = 6$) at $T_0 \approx 10^{1.41}$. Representative mode shapes at the smallest $T_0 = 10^{1.2}$ are shown to the left of panel A, for the three unstable branches ($n = 2$, 4, and 6) and four stable branches ($n = 1$, 3, 5, and 7). The Y'_{RMS} values that correspond to these seven lowest wavenumber modes are approximately those of the analytical eigenmodes in (3.31), $n\pi/2$ for $n = 1, 2, \ldots, 7$. We also illustrate examples at larger T_0 values for the $n = 2$ and 4 branches, and find that the mode shapes are almost unchanged. In particular, we note that the seven modes shown to the left of $T_0 = 10^{1.2}$ all remain approximately the same across the corresponding colored branch for $T_0 \in [10^{1.2}, 10^{1.875}]$. In figure 3.6 we focus on the lowest wavenumber shapes, as the higher wavenumber shapes (yellow dots) are not numerically resolved. The odd-numbered modes remain stable for all values of T_0 shown. As we decrease the pretension T_0 the number of distinct

modes found—with the range of initial guesses that we are using—increases. This is indicated by the higher density of dots at smaller T_0 in figure 3.6B. Panels C and D show the corresponding data for a smaller membrane mass, $R_1 = 10$. The modes deviate more from the analytical expression of equation (3.31), and change more significantly across T_0, compared to panel A. Representative modes at the smallest $T_0 = 10^{-0.3}$ are shown at the left side of panel C. The shape of the curves that connect the real part of the eigenvalues associated with a particular mode shape (lower panels) seems to be similar for the two mass densities. However for the smaller mass ($R_1 = 10$) there is a "disordered" band of dark blue dots (with $Y'_{\mathrm{RMS}} < \pi/4$) that are stable ($\sigma_{\mathrm{I}} \approx 10^{-1}$ is panel C) and have low frequency ($\sigma_{\mathrm{R}} \lesssim 1$ in panel D).

To summarize, in agreement with [184], we have found that the stability boundary has an upward slope for $R_1 \geq 10^2$, whereas for $R_1 < 10^2$ the critical T_0 for instability lies in $[1.7, 2]$, almost independent of R_1. When R_1 and T_0 are dominant over fluid pressure forces, the membrane eigenmodes tend to neutrally-stable sinusoidal functions. When the fluid forces are small but nonnegligible the mode shapes are similar, with the even-numbered modes becoming unstable with very small growth rates, starting with the second modes. We find roughly two regions: (a) at small R_1 divergence occurs with the most unstable mode becoming more fore-aft asymmetric as we decrease T_0; and (b) at large R_1 flutter and divergence occur with approximately sinusoidal eigenmodes. In both of these regions, the most unstable modes become more wavy at smaller T_0. We have extended previous studies of the fixed–fixed membrane to a wider range of R_1-T_0 space. Next, we study cases in which the membrane ends can move freely, which are less well-known.

3.5 Fixed–free Membranes

We now investigate the stability of membranes with the leading edge fixed and the trailing edge free to move vertically, i.e., satisfying the boundary conditions (3.12). In chapter II we found that with one end free, the membrane has a wider range of unsteady dynamics. In particular, in the steady-state large-amplitude regime we showed in chapter II that this set of boundary conditions has a mixture of periodic and chaotic dynamics as opposed to the steady single-hump solutions observed in fixed–fixed membranes. In the small-amplitude (growth) regime we will now show that the eigenmodes can also be somewhat more complicated.

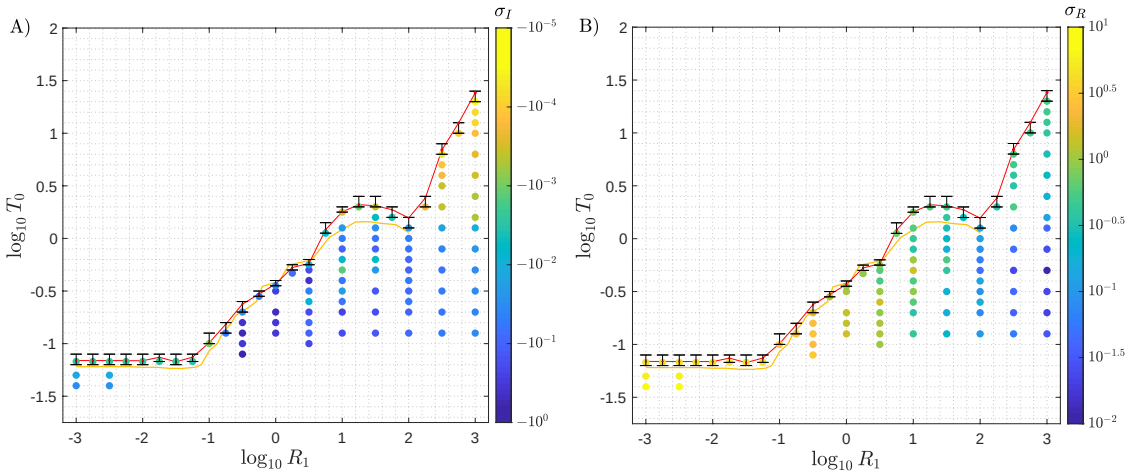

Figure 3.7: The region in R_1-T_0 space in which the fixed–free membrane is unstable. The red line and red dots indicate the position of the stability boundary computed using linear interpolation between σ_{I} of the smallest T_0 that gives only stable eigenmodes and the σ_{I} of the largest T_0 that gives an unstable eigenmode (shown in the error bars). The color of the dots below the stability boundary labels: A) The imaginary part of the eigenvalue (σ_{I}) corresponding to the most unstable modes. It represents the temporal growth rate. B) The real part of the eigenvalues (σ_{R}) for the most unstable mode, representing the angular frequency. The orange line that spans $R_1 \in [10^{-3}, 10^2]$ represents the stability boundary computed numerically in chapter II.

In figure 3.7 we plot the imaginary (panel A) and real parts (panel B) of the most unstable eigenvalues in the region of instability for the fixed–free membranes in R_1-T_0 space. The red line marks the boundary where the eigenvalues change from all $\sigma_{\mathrm{I}} > 0$ (stable membranes) to at least one $\sigma_{\mathrm{I}} < 0$ (unstable membranes),

analogous to figure 3.5. As in the fixed–fixed case, the stability boundary moves to larger pretension (T_0) values with increasing membrane mass (R_1), but starting at much smaller R_1 now ($\geq 10^{-1}$). As R_1 decreases below 10^{-1}, the critical pretension reaches a lower plateau.

The stability boundary of the current study is compared against the boundary from the nonlinear study in chapter II (orange line). Their shapes are very similar and there is good agreement especially for $R_1 \in [10^{-0.75}, 10^{0.5}]$. As in figure 3.5, the discrepancy may be due to δ-smoothing used on the free vortex sheet of chapter II, the choice of the vortex wake ℓ_w, or the number of Chebyshev nodes $(m+1)$ on the membrane. In the unsteady simulations (orange line) we used $m = 40$ because the simulations require more computing time, but in the current work (red line) we used $m = 120$. The eigenvalue solver shows that the boundary slopes upward over $R_1 \in [10^2, 10^3]$, where it was difficult to obtain accurate results with the unsteady simulations.

The trends of the most unstable eigenvalues (colored dots) are similar to the fixed–fixed case (figure 3.4) in some ways: the growth rates σ_I generally become larger in magnitude at smaller T_0 and smaller R_1 (panel A), and the growth rates vary nonmonotonically with T_0 at intermediate R_1 ($[10^{0.5}, 10^{1.5}]$ for fixed–free, and smaller R_1 for fixed–fixed). A difference is the slight decrease in growth rates as R_1 decreases below 10^{-1} for the fixed–free case, which does not occur in the fixed–fixed case. For $R_1 \in [10^2, 10^3]$, the fixed–free growth rates are qualitatively similar to those in the fixed–fixed case above $T_0 = 10^{0.1}$. Below this value, however, the fixed–free growth rates jump by more than an order of magnitude. In both cases, the real parts of the eigenvalues (the angular frequencies σ_R, panel B) generally decrease with decreasing T_0 and with increasing R_1, particularly at the largest R_1. Below

$R_1 = 10^{1.5}$, the frequencies are very different: divergence ($\sigma_R \approx 0$) does not occur in the fixed–free case, but is common in the fixed–fixed case.

To consider the eigenmodes in the fixed–free case we again start with R_1 and $T_0 \gg 1$, so the fluid forcing is negligible and the eigenmodes are again solutions of (3.27), i.e., nontrivial linear combinations of $\cos(kx)$ and $\sin(kx)$, with $k = \pm\sigma\sqrt{R_1/T_0}$, but satisfying the boundary conditions (3.12) now. The k are now those for which the determinant of

$$\begin{pmatrix} \sin(-k) & \cos(-k) \\ \cos(k) & -\sin(k) \end{pmatrix} \tag{3.33}$$

is zero, which leads to $k = (n - 1/2)\pi/2$ for $n \in \mathbb{Z}_{>0}$, corresponding eigenvalues $\sigma = \pm k\sqrt{T_0/R_1}$, and eigenmodes now of the form

$$Y(x) = \sin\left(\left(n - \frac{1}{2}\right)\frac{\pi}{2}(x+1)\right), \tag{3.34}$$

for $n \in \mathbb{Z}_{>0}$ and $-1 \le x \le 1$. Each mode has one quarter wavelength less than that of the corresponding fixed–fixed mode, so that the trailing edge has zero slope.

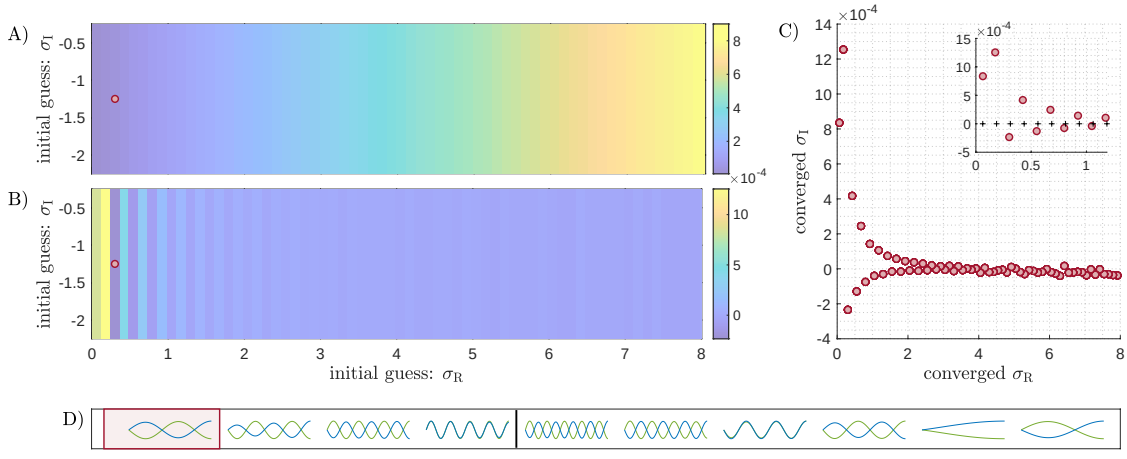

Figure 3.8: Fixed–free eigenvalues and eigenmodes with $R_1 = 10^3$ and $T_0 = 10^{0.8}$. Computed σ_R (panel A, values in colorbars at right) and computed σ_I (panel B, values in colorbars at right), both in the initial guess complex plane. C) The computed eigenvalues replotted as red dots in the (σ_R, σ_I) plane. The inset in panel C shows the ten computed eigenvalues (red $\circ$) that correspond to the eigenmodes shown in panel D. The analytical form of the eigenvalues is $\sigma = ((n - 1/2)\pi/2)\sqrt{T_0/R_1} = ((n - 1/2)\pi/2)\sqrt{10^{0.8}/10^3}$ for $n = 1, \ldots, 10$ (black plusses).

Figure 3.8 shows an example of how the computed eigenvalues (real parts in panel A and imaginary parts in panel B) vary over a grid of initial guesses in the complex plane, for a fixed–free membrane with $(R_1, T_0) = (10^3, 10^{0.8})$, in the large R_1 region near the stability boundary. The quantities plotted are analogous to those in figure 3.3. The grid of initial eigenvalue guesses in the complex plane covers $\sigma_{\mathrm{R}} \in (0, 8]$ and $\sigma_{\mathrm{I}} \in [-2, -0.5]$, spanning 640 values in the real direction and 4 values in the imaginary direction. As in figure 3.3, we see that for large R_1 (10^3) and moderately large T_0 $(10^{0.8})$ the eigenvalues obtained by the numerical method depend mainly on the real part of the initial eigenvalue guess. However, here we see that there is more variation in the computed eigenvalues with respect to the choice of initial σ_{R} compared to figure 3.3, where the vertical bands of constant real (panel A) and imaginary parts (panel B) of σ are wider. This may be due to the smaller value of T_0 considered in figure 3.8 ($10^{0.8}$ as opposed to $10^{1.5}$ in figure 3.3). As we decrease the membrane pretension (T_0) the number of distinct modes found (with our range of initial guesses) typically increases (e.g., figure 3.6A and B). The numerically computed eigenvalues from figure 3.8A and B are replotted as red dots in the $(\sigma_{\mathrm{R}}, \sigma_{\mathrm{I}})$ plane in panel C, and those at the smallest σ_{R}, shown in the inset, agree closely with the analytical form (3.30) with $k = (n - 1/2)\pi/2$ for $n \in \mathbb{Z}_{>0}$ (black plusses in inset; note there is close agreement in the imaginary part due to the small axis scale). Many eigenmodes are found with wavelengths decreasing down to the mesh scale, but in figure 3.8D we show the ten modes with largest wavelengths (i.e., $n = 1, \ldots, 10$ in (3.34)), those that are best resolved numerically. Starting from the left, the most unstable modes have $n = 3$, 5, 7, and 9, while $n = 10$, 8, 6, 4, 1 and 2 are stable. Except for $n = 1$, the modes with even and odd n have the opposite stability behavior. Here we omit the computed modes with highest

wavenumbers because they (and the corresponding eigenvalues) are not numerically converged. For the large-R_1, large-T_0 limit solved analytically in equation (3.34), we have a quadratic eigenvalue problem. When discretized by the numerical method in §3.3.1, we have $2m + 2$ eigenmodes $Y(x)$ varying from low wavenumber modes to very high wavenumber modes that oscillate on the mesh scale (due to the discretized second x-derivative). For more general R_1 and T_0, we have a nonlinear eigenvalue problem, but still have eigenmodes that oscillate on the mesh scale, and are thus not resolved (i.e., not close to a continuum solution). Therefore, we focus on the lower wavenumber eigenmodes—those with Y'_{RMS} (defined in (3.32)) below a threshold near 4π, or about four wavelengths for a sinusoidal $Y(x)$—which we can resolve well with $m = 120$ grid points.

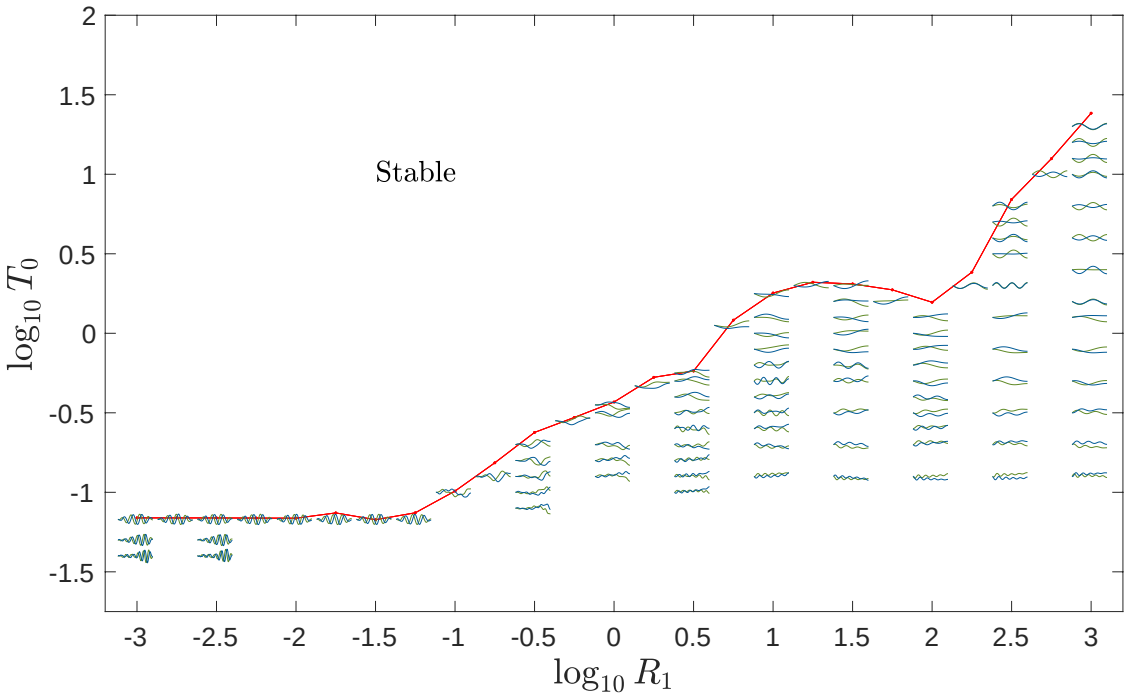

Figure 3.9: The shapes $Y(x)$ of the most unstable eigenmode as a function of R_1 and T_0 in the fixed–free case. The real part of $Y(x)$ is shown in green and the imaginary part of $Y(x)$ is shown in blue. Each shape is scaled, both vertically and horizontally, to fit within the plot. The shapes are superposed on the same stability boundary (red line) as in figure 3.7.

In figure 3.9 we examine the variations in the most unstable eigenmodes in the same (R_1, T_0) space as figure 3.7, corresponding to the eigenvalues shown there. There is a narrow band with $R_1 = 10^0$ and $10^{-0.65} < T_0 < 10^{-0.55}$ where our initial guesses all produced $\sigma_I > 0$ and so the modes are stable, and therefore none are shown in this range. Similar small bands of stability between unstable regions were also observed in [124, 128] for fixed–fixed membranes. The shapes do not change noticeably for the more irregular motions at $R_1 \in [10^{-3}, 10^{-1.25}]$ (the eigenvalues in figure 3.7 were also nearly constant in this region). At these smallest R_1 values the deflection at the free end is nearly zero. As we decrease T_0 for $R_1 \leq 10^{-2.5}$, the ripples move toward the trailing edge of the membrane while maintaining nearly zero deflection at that end. Close to the stability boundary, all the shapes for $R_1 \in [10^{0.75}, 10^2]$ are also nearly alike. At moderate values of R_1 ($[10^{-1}, 10^2]$) the maximum deflection occurs in most cases at the trailing edge of the membrane. At these and larger values of R_1, the mean slope of the membrane is nonzero. In a similar region of R_1 (i.e., $[10^{-1}, 10^{1.75}]$) fixed–fixed membranes become unstable with a single hump, losing stability via divergence. Fixed–free membranes, however, become unstable by flutter and divergence. When T_0 is below $10^{-0.2}$ the most unstable mode changes to a "wavier" profile—the mode wavenumber increases with decreasing T_0. Similar to the fixed–fixed case where even-numbered modes become unstable for large R_1, we see in figure 3.9 that heavy fixed–free membranes ($R_1 > 10^2$) with $T_0 \in [10^{0.2}, T_{0C}(R_1)]$, become unstable with an odd-numbered mode—the third mode (the first mode is stable). At $T_0 < 10^{0.2}$ we are no longer in the vacuum limit ($R_1 \gg 1$ but T_0 is not). Thus, the mode shape is not a simple sinusoidal function of the form (3.34), but the waviness still increases with decreasing T_0 for heavy membranes.

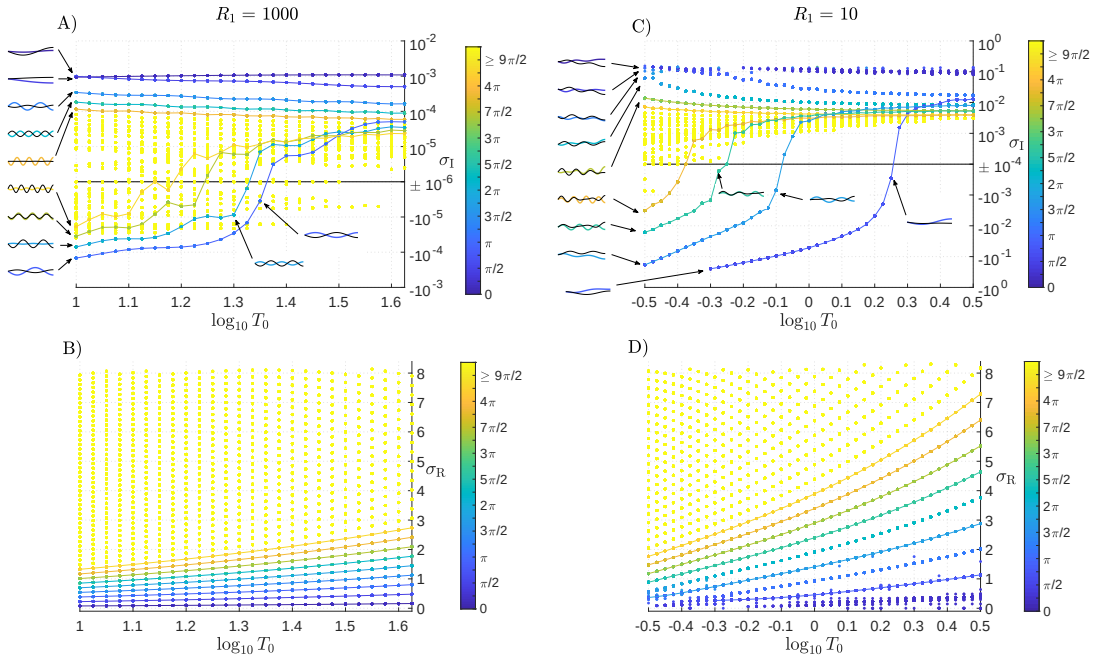

Figure 3.10: For two values of membrane mass (R_1), 10^3 (left column) and 10^1 (right column), the imaginary (A, C) and real parts (B, D) of the eigenvalues versus pretension (T_0) for fixed–free membranes. The coloring represents the RMS of the membrane's slope, Y'_{RMS}, for each (R_1, T_0) pair given by (3.32). The horizontal black line in the top panels located at A) $\sigma_I = \pm 10^{-6}$, C) $\sigma_I = \pm 10^{-4}$ distinguishes stable modes (above) and unstable modes (below). We also show typical modes that correspond to each branch with $Y'_{\text{RMS}} < 9\pi/2$.

We now consider the changes in the eigenvalues and associated eigenmode shapes as we pass through the stability boundary for a fixed mass density, the fixed–free analog of figure 3.6. In figure 3.10 the colors label Y'_{RMS}, given by (3.32). For the larger R_1, 1000 (panel A) the unstable modes are odd-numbered and they become unstable in order of increasing n. The third mode becomes unstable first, at $T_0 \approx 10^{1.36}$—consistent with figure 3.9. Then the fifth mode ($n = 5$) becomes unstable at $T_0 \approx 10^{1.33}$, the seventh mode at $T_0 \approx 10^{1.24}$, and the ninth mode at $T_0 \approx 10^{1.18}$. The even-numbered modes and the first mode remain stable for all values of T_0. Contrary to the fixed–fixed case with $R_1 = 1000$ (figure 3.6A) where the four branches with the largest positive σ_I correspond to modes $n = 1, 3, 5, 7$, the branches with largest

σ_{I} in the fixed–free case correspond to modes $n = 1, 2, 4, 6, 8$. This additional branch with opposite parity ($n = 1$) in panel A has a slightly smaller σ_{I} than the second mode at the smallest $T_0 = 10^1$ shown. Above a certain T_0 value the $n = 1$ branch acquires the largest $\sigma_{\mathrm{I}} > 0$.

We show the membrane shapes of the nine lowest wavenumber modes to the left of panel A at the lowest $T_0 = 10^1$, but also examples of membrane shapes at a couple of larger T_0 values for the first two unstable branches and observe that the mode shapes are almost unchanged. The Y'_{RMS} values that correspond to these nine lowest wavenumber modes are approximately those of the analytical eigenmodes in (3.34), $(n - 1/2)\pi/2$ for $n = 1, 2, \ldots, 9$. Even though higher wavenumber shapes (yellow dots) appear to become unstable at a larger T_0 value, such cases are not numerically resolved and are thus not used in determining T_{0C} here. At $R_1 = 1000$, the branches with the largest $\sigma_{\mathrm{I}} > 0$ are all continuous but at $R_1 = 10$, the same branches (blue dots at the top of panel C and bottom of panel D) are more scattered. There, the numerical method gives individual eigenvalues that do not seem to follow a particular branch, as was also found for fixed–fixed membranes at $R_1 = 10$. This could potentially be due to our choice for the range and density of the mesh of initial eigenvalue guesses. The loss of stability in figure 3.10C occurs at $T_0 \approx 10^{0.26}$. The imaginary parts of the eigenvalues (panel C) are about two orders of magnitude higher than in panel A. At $R_1 = 10$ we see four branches that fall below $\sigma_{\mathrm{I}} = 0$, each having approximately its own distinct value of Y'_{RMS}. If we consider smaller values of T_0 we would expect to observe more branches becoming unstable. As opposed to panel A, we see in panel C that the yellow dots (higher wavenumber modes) are mostly stable. Similar to the fixed–fixed case in figure 3.6 we see that the curves connecting the σ_{R} associated with a particular mode shape appear to be steeper in

panel D than in panel B.

In summary, the fixed–free stability boundary is lower than the fixed–fixed boundary at small and moderate values of R_1—so more membranes are stable—but resembles the upward-sloping portion of the fixed–fixed boundary at large R_1 ($\geq 10^2$). Similarly to fixed–fixed membranes (§3.4), when R_1 and T_0 dominate fluid pressure forces the eigenmodes tend to neutrally stable sinusoidal functions with odd-numbered modes becoming unstable, starting with the third mode. We find that in the small R_1 region (i.e., $R_1 < 10^{-1}$) the most unstable eigenmodes have small deflection at the trailing edge, despite its freedom to move in the vertical direction. The small-R_1 modes are very wavy shapes. For all R_1, the modes become wavier with decreasing T_0. At moderate and large R_1, the waves are superposed on a background shape with nonzero slope.

3.6 Free–free Membranes

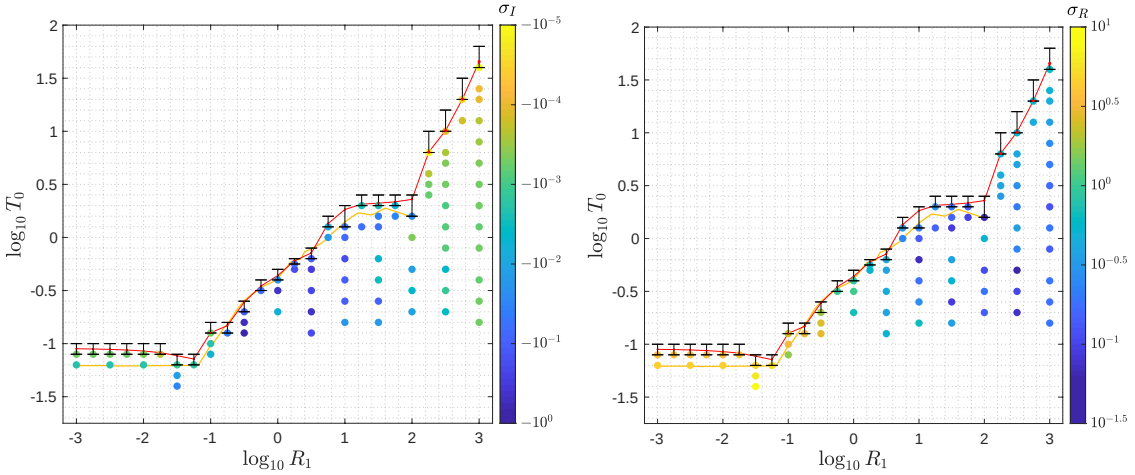

Figure 3.11: The region in R_1-T_0 space in which the free–free membrane is unstable. The red line and red dots indicate the position of the stability boundary computed using linear interpolation between σ_I of the smallest T_0 that gives a stable membrane and the σ_I of the largest T_0 that gives an unstable membrane (shown in the error bars). The color of the dots below the stability boundary labels: A) The imaginary part of the eigenvalue (σ_I) corresponding to the most unstable modes. It represents the temporal growth rate. B) The real part of the eigenvalues (σ_R) for the most unstable mode, representing the angular frequency. The orange line that spans $R_1 \in [10^{-3}, 10^2]$ represents the stability boundary computed numerically in chapter II.

We have found that allowing the trailing edge to deflect freely in the vertical direction dramatically changes the instability region and the membrane dynamics. As a natural next step, we now study the effect of making both ends free, satisfying the boundary conditions (3.13). The stability boundary (red line) and most unstable eigenvalues are shown in figure 3.11. The stability boundary is similar to the fixed–free case (figure 3.7): the critical pretension increases with mass when $R_1 > 10^2$, it decreases as we decrease R_1, and it plateaus when $R_1 \ll 1$. In figure 3.11 we show that there is close agreement for $R_1 \in [10^{-0.75}, 10^{0.5}]$ between the stability boundary computed here and in chapter II using unsteady simulations (orange line). For smaller R_1 ($[10^{-3}, 10^{-1}]$) and larger R_1 ($[10^{0.75}, 10^2]$), the red line has slightly higher T_0. As noted in §3.5 the difference in m (40 in chapter II versus 120 here) may be the main cause. As for the fixed–free case, we will show that the most unstable eigenmodes have higher wavenumbers at the smallest R_1, so numerical resolution is an issue there: in chapter II we found that the small- and large-amplitude motions were not converged with $m = 40$ for $R_1 < 10^{-1}$.

We can again use the imaginary (panel A) and real parts (panel B) of the eigenvalues to characterize the instability in (R_1, T_0) space. Within the region of instability (below the red line) a comparison with fixed–fixed (figure 3.4) and fixed–free membranes (figure 3.7) reveals that the colored dots (most unstable eigenvalues) have the same general behavior: the temporal growth rates (panel A) increase in magnitude with decreasing R_1 and T_0, but vary nonmonotonically with T_0 at moderate values of R_1 ($[10^0, 10^2]$). The growth rates of free–free heavy membranes ($R_1 \in [10^2, 10^3]$) are qualitatively similar to those in the fixed–free case in the same region. The angular frequencies (σ_R, panel B) are also larger for smaller R_1, but vary nonmonotonically with T_0. Similar to the fixed–free case, we observe that membranes exhibit the flut-

ter and divergence instability but do not lose stability solely by divergence (i.e. with $\sigma_{\mathrm{R}} \approx 0$) for any (R_1, T_0) pair. In the region $R_1 \leq 10^{-1.25}$ the eigenvalues just below the stability boundary are nearly constant; observed also in the fixed–free case (figure 3.7).

For $R_1, T_0 \gg 1$ the eigenvalues are the same as for the fixed–fixed case (3.30), with the addition of zero. The free–free eigenmodes are given by

$$Y(x) = \cos\left(\frac{(n-1)\pi}{2}(x+1)\right), \tag{3.35}$$

for $n \in \mathbb{Z}_{>0}$ and $-1 \leq x \leq 1$, where the amplitude is arbitrary.

Figure 3.12 shows an example of how the computed eigenvalues (real parts in panel A and imaginary parts in panel B) vary over a grid of initial guesses in the complex plane for a free–free membrane with $R_1 = 10^3$ and $T_0 = 10^{1.1}$, with the same mesh as in the fixed–free case of figure 3.8. We take R_1 and $T_0 \gg 1$ (vacuum limit) to compare with the analytical values (3.30) with $k = (n-1)\pi/2$ for $n \in \mathbb{Z}_{>0}$ (panel C). In panel D we show the eleven lowest wavenumber modes. Starting from the left, the most unstable modes are $n = 3$, 5, 7, 9, and 11 whereas $n = 1$, 10, 8, 6, 4, and 2 are stable. The sixth shape from the left that is displayed is flat ($n = 1$), with corresponding σ_{R} and $\sigma_{\mathrm{I}} \approx 10^{-8}$.

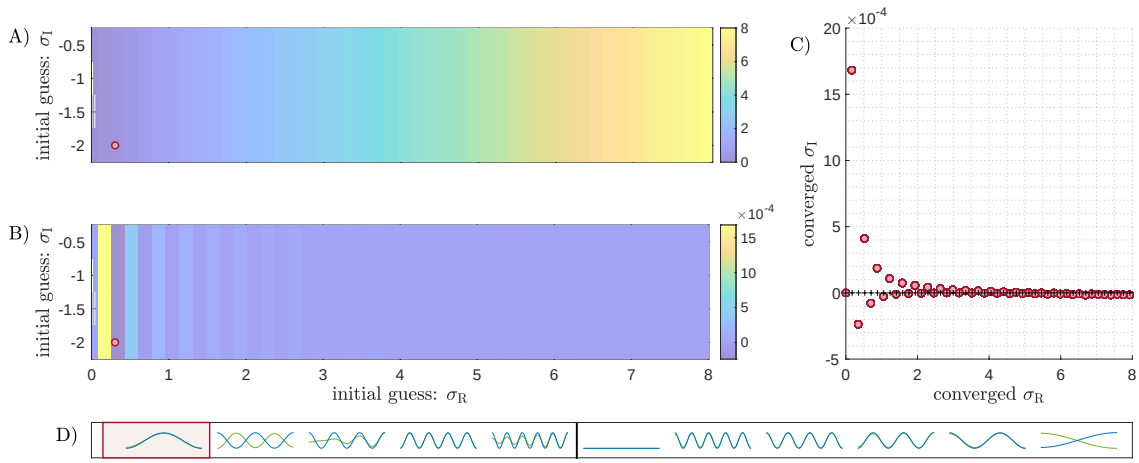

Figure 3.12: Free–free eigenvalues and eigenmodes with $R_1 = 10^3$ and $T_0 = 10^{1.1}$. Computed σ_R (panel A, values in colorbars at right) and computed σ_I (panel B, values in colorbars at right), both plotted in the initial guess complex plane. C) The distinct eigenvalues generated by the numerical method plotted as red dots in the (σ_R, σ_I) plane. The analytical form of the eigenvalues is $\sigma = ((n-1)\pi/2)\sqrt{T_0/R_1}$ for $n = 1, \ldots, 46$ (black plusses). D) The eleven lowest wavenumber eigenmodes ($\mathrm{Re}(Y(x))$ in green, $\mathrm{Im}(Y(x))$ in blue), from the most unstable (most negative σ_I) on the left to the most stable (largest positive σ_I) on the right. The vertical black line separates unstable modes (on its left) and stable modes (on its right).

In figure 3.13 we show the most unstable eigenmodes across (R_1, T_0) space. The mode shapes of light membranes ($R_1 \leq 10^{-1.75}$) just below the stability boundary seem very similar to fixed–free membranes with the same mass but have one less peak and one less trough. Decreasing the pretension values for membranes with $R_1 \leq 10^{-1.5}$, not only makes the membrane profile more wavy but also causes the ripples in the membrane shape to move rearward to the trailing edge. Mode shapes with nearly zero deflection at the free ends exist up to $R_1 = 10^{-0.75}$, slightly higher than in the fixed–free case (figure 3.9). When the mass density is between $10^{0.75}$ and 10^2 and the pretension is between 10^0 and $T_{0C}(R_1)$, the membranes are somewhat straighter than in the fixed–free case. Finally, heavy membranes ($R_1 > 10^2$) with T_0 between $10^{0.3}$ and $T_{0C}(R_1)$ (the stability boundary) all lose stability with the third mode, $n = 3$ in equation (3.35) (the highlighted mode in figure 3.12D).

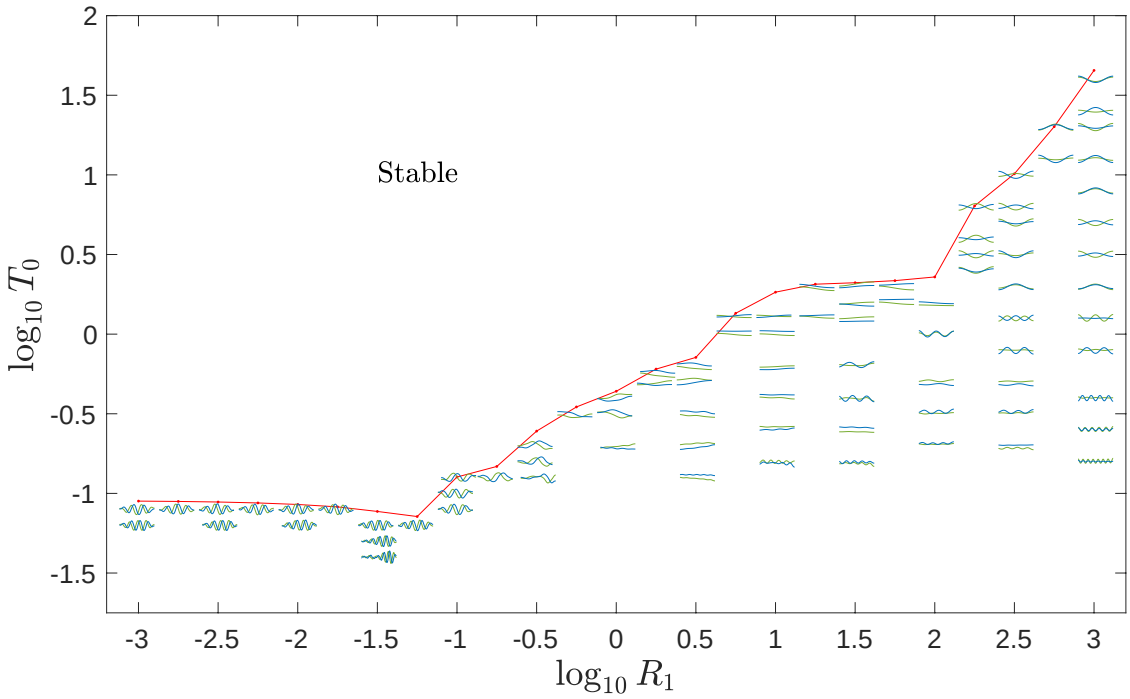

Figure 3.13: The shapes $Y(x)$ of the most unstable eigenmode as a function of R_1 and T_0 in the free–free case. The real part of $Y(x)$ is shown in green and the imaginary part of $Y(x)$ is shown in blue. Each shape is scaled, both vertically and horizontally, to fit within the plot. The shapes are superposed on the same stability boundary (red line) as in figure 3.11.

In figure 3.11 we studied how the most unstable eigenvalues change in the R_1-T_0 parameter space, and in figure 3.13 we investigated the trends in the corresponding most unstable eigenmodes. Now in figure 3.14 we show the changes in the eigenvalues and associated eigenmode shapes as we pass through the stability boundary for two fixed values of mass density, as for the fixed–fixed and fixed–free cases (figures 3.6 and 3.10, respectively). Each dot's color is used to label Y'_{RMS} (equation (3.32)). For the largest $R_1 = 1000$ (panel A) the unstable modes are odd-numbered. The first branch to become unstable is the third mode ($n = 3$ in equation (3.35)) at $T_0 \approx 10^{1.68}$—consistent with figure 3.13 (for the same R_1). Then the fifth mode ($n = 5$) becomes unstable at $T_0 \approx 10^{1.45}$, and the seventh mode at $T_0 \approx 10^{1.33}$. The even-numbered modes are all stable for the entire range of T_0 values considered

here. We show the membrane mode shapes that correspond to the nine lowest wavenumber modes to the left of panel A at the lowest $T_0 = 10^{1.275}$. The Y'_{RMS} values that correspond to these nine lowest wavenumber modes are approximately those of the analytical eigenmodes in (3.35), $(n-1)\pi/2$ for $n = 1, 2, \ldots, 9$. We also show instances of membrane shapes at a couple of larger T_0 values for the first two unstable branches and the flat mode. We see that in all cases, these mode shapes have the same features as at the smallest T_0. The branch corresponding to the flat mode ($n = 1$) in figure 3.14A oscillates about $\sigma_{\mathrm{I}} = \pm 10^{-6}$ at $T_0 \geq 10^{1.6}$ (while σ_{R} lies on $\pm 10^{-4}$)—it is essentially zero. As in the fixed–fixed and fixed–free cases at $R_1 = 1000$, the branches with the largest $\sigma_{\mathrm{I}} > 0$ are all continuous but at the smaller R_1 (i.e., 10), the same branches (blue dots at the top of panel C and bottom of panel D) appear more disordered. The loss of stability in figure 3.10C occurs at $T_0 \approx 10^{0.275}$. The values of σ_{I} in panel C are about two orders of magnitude higher than those in panel A (as for fixed–free membranes at the same membrane masses). The downward tendency of the darker orange branch when σ_{I} drops below 10^{-2} (panel C) suggests that the mode may be the next to become unstable as T_0 decreases. Contrary to panel A, we see in panel C that the yellow dots (higher wavenumber modes) are mostly stable. The free–free angular frequency (σ_{R}) behaves similarly to fixed–fixed and fixed–free membranes: the curves connecting σ_{R} associated with particular modes are steeper for $R_1 = 10$ (panel D) compared to $R_1 = 1000$ (panel B). The dotted part of the most unstable branch shown in figures 3.14C and D is used to bridge a gap in T_0 in which we did not find eigenvalues and eigenmodes for the lowest branch.

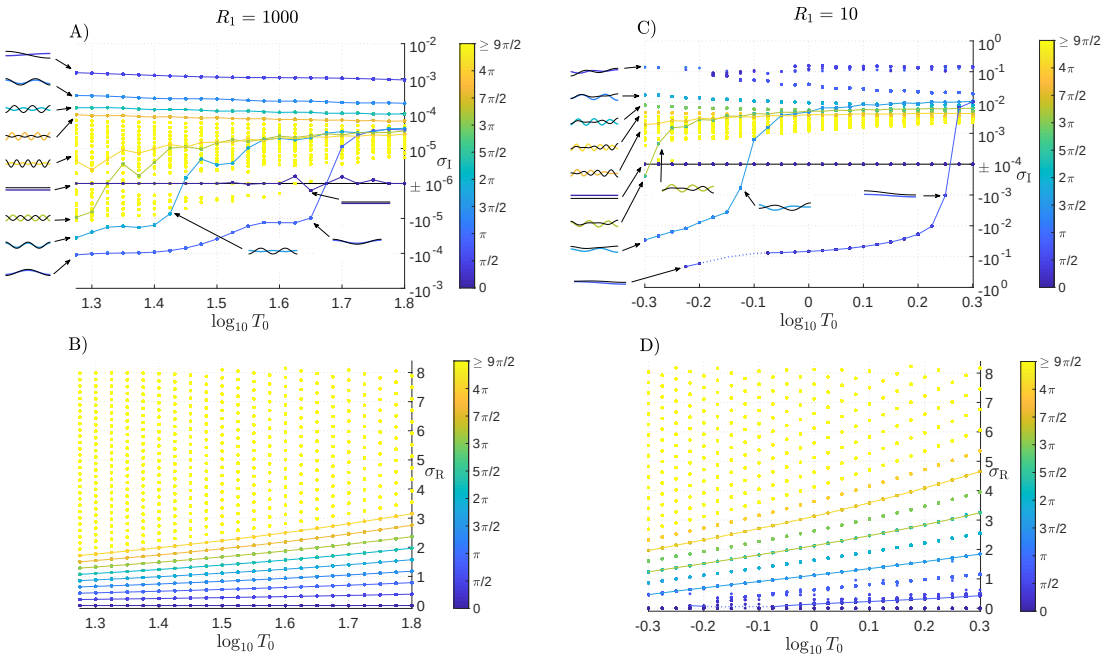

Figure 3.14: For two values of membrane mass (R_1), 10^3 (left column) and 10^1 (right column), the imaginary (A, C) and real parts (B, D) of the eigenvalues versus pretension (T_0) for free–free membranes. Numerical results are shown as points with color coded according to the value of the RMS of the membrane's slope for each (R_1, T_0) pair given by (3.32), as given in the colorbar. The horizontal black line in the top panels located at A) $\sigma_I = \pm 10^{-6}$, C) $\sigma_I = \pm 10^{-4}$ distinguishes stable modes (above) and unstable modes (below). We also show typical modes that correspond to each branch with $Y'_{\text{RMS}} < 9\pi/2$.

3.7 Comparison with Unsteady and Large-amplitude Simulations

We now compare the most unstable eigenmodes, in a few cases, with the corresponding small-amplitude motions as well as the eventual large-amplitude steady-state motions in the unsteady time-stepping simulations of chapter II. The main differences are that in the eigenvalue problem the free vortex wake has a finite length ℓ_w whereas in the unsteady simulations it grows from zero length, and has δ-smoothing to avoid chaotic dynamics. For fixed–fixed membranes, figure 3.15 compares eigenmodes (dashed green lines) with snapshots of time-stepping simulations in the small-amplitude growth regime (sequence of gray lines ending with black lines) and the time-stepping simulations' eventual large-amplitude steady states (blue lines). The

comparison is made at $R_1 = 10^{-1}$ with T_0 increasing: (A) $10^{-0.1}$, (B) 10^0, (C) $10^{0.1}$, and (D) $10^{0.2}$, the last value close to the stability boundary. Here we have a divergence instability, so the imaginary parts of the eigenmodes are zero; the green lines show the real parts. As T_0 increases, the small-amplitude membrane shapes change gradually, from ones with both downward and upward curvature (A) to a nearly fore-aft symmetric hump with upward curvature only (D). The close agreement between the green and black lines shows that the linearized model captures the small-amplitude unsteady dynamics well. Here the initial deflection is $y(x, 0) = 10^{-12} \sin(\pi x)$, but we find essentially the same agreement with a different form of the initial perturbation, in which the leading edge is moved slightly upward and then back to $y = 0$. In this case the membrane initially forms a small bump near the trailing edge as it evolves under the nonlinear membrane equation (3.5). Both types of initial deflections are much smaller than the gray shapes in figure 3.15, and eventually converge to them as the fastest growing mode outgrows the other modal components of the initial deflections. At large times, all the unsteady shapes converge to steady humps (blue lines), nearly fore-aft symmetric, despite the early-time differences. The magnitudes of the humps' deflections are set by the nonlinear stretching resistance in (3.5), the term proportional to the stretching modulus R_3. Here R_3 is set to 10 but only the magnitudes of the humps, and not their shapes, change much over the range $R_3 \geq 10$ [113].

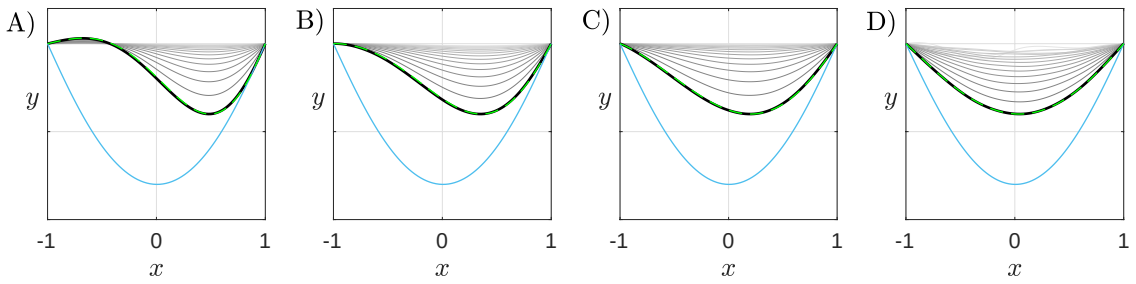

Figure 3.15: Fixed–fixed membranes at $R_1 = 10^{-1}$ and A) $T_0 = 10^{-0.1}$, B) $T_0 = 10^{0}$, C) $T_0 = 10^{0.1}$, and D) $T_0 = 10^{0.2}$. These membranes lose stability by divergence. We compare the most unstable modes obtained from the eigenvalue analysis (dashed green lines) to the membrane shapes of the time-stepping simulations in the small-amplitude (growth) regime—in each panel, 15 equally spaced snapshots are shown in the growth regime, gray and then black at the last time. The arbitrary amplitudes of the green lines are set to match those of the black lines. The light blue curves indicate shapes in the large-amplitude steady state regime.

We now investigate membranes with the leading edges fixed and the trailing edges free. Now the membranes lose stability through divergence and flutter, so the eigenmodes are complex. They are determined only up to a complex constant, with both a magnitude and a phase that need to be matched to a given time-stepping simulation of chapter II. In appendix E we give details about how the matching is done.

In figure 3.16, we compare two cases slightly below the stability boundary at $R_1 = 10^{-0.5}$: $T_0 = 10^{-0.8}$ (panels A, C, and E) and $T_0 = 10^{-0.7}$ (panels B, D, and F). In panels A and B, the gray lines again show sequences of snapshots from the time-stepping simulations. We fit the values $y(\alpha, t)$ for such a sequence to a function of the form $\mathrm{Re}\left([\mathrm{Re}(y_{\mathrm{nonlin}}(\alpha)) + i\mathrm{Im}(y_{\mathrm{nonlin}}(\alpha))]e^{i\sigma t}\right)$. First σ_{I} and σ_{R} are estimated. Then for each α, the real and imaginary parts of $y(\alpha, t)e^{-i\sigma t}$ are estimated (in amplitude-phase form; see appendix E), giving $\mathrm{Re}(y_{\mathrm{nonlin}}(\alpha))$ (red solid lines in panels A and B) and $\mathrm{Im}(y_{\mathrm{nonlin}}(\alpha))$ (green solid lines). The most unstable eigenmode $Y(x)$ is arbitrary up to a complex constant. The function $y_{\mathrm{nonlin}}(\alpha)$ contains a complex factor (magnitude and phase) that depends on the initial conditions of the time-stepping simulation. To account for this, we scale $Y(x)$ by the complex factor that gives

the best L^1-fit with $y_{\text{nonlin}}(\alpha) \approx y_{\text{nonlin}}(x)$ (see appendix E) and plot the resulting $\text{Re}(Y)$ and $\text{Im}(Y)$ as dotted black and blue lines respectively, in panels A and B. The fit between $Y(x)$ and $y_{\text{nonlin}}(x)$ is nearly as good as in the steady fixed–fixed cases (figure 3.15). The slight increase of error in the fit may be due to the extra steps involved in fitting the fixed–free eigenmodes because they are complex.

In panels C and D, we show 20 snapshots from the time-stepping simulations, but multiplied by our estimate of $e^{\sigma_1 t}$, which should remove the exponential growth. This shows the mode shapes much more clearly than in panels A and B. The rescaled shapes are equally spaced over our estimate of one time period. They appear to follow an up-down symmetric, periodic (as expected) oscillation with (A) seven and (B) five "necks" in their envelopes, respectively. Panels E and F show snapshots in the eventual large-amplitude periodic steady-state. The shapes are qualitatively similar to those in C and D, but the numbers of necks are reduced to four in both E and F. The shapes are nearly the same in both panels; as in the fixed–fixed case (figure 3.15) the differences in the small-amplitude shapes disappear at large amplitude. This may be because the T_0 term in (3.5) is subdominant to the R_3 term at large amplitudes, even at $T_{0C}(R_1)$, the largest T_0 where the membranes are unstable.

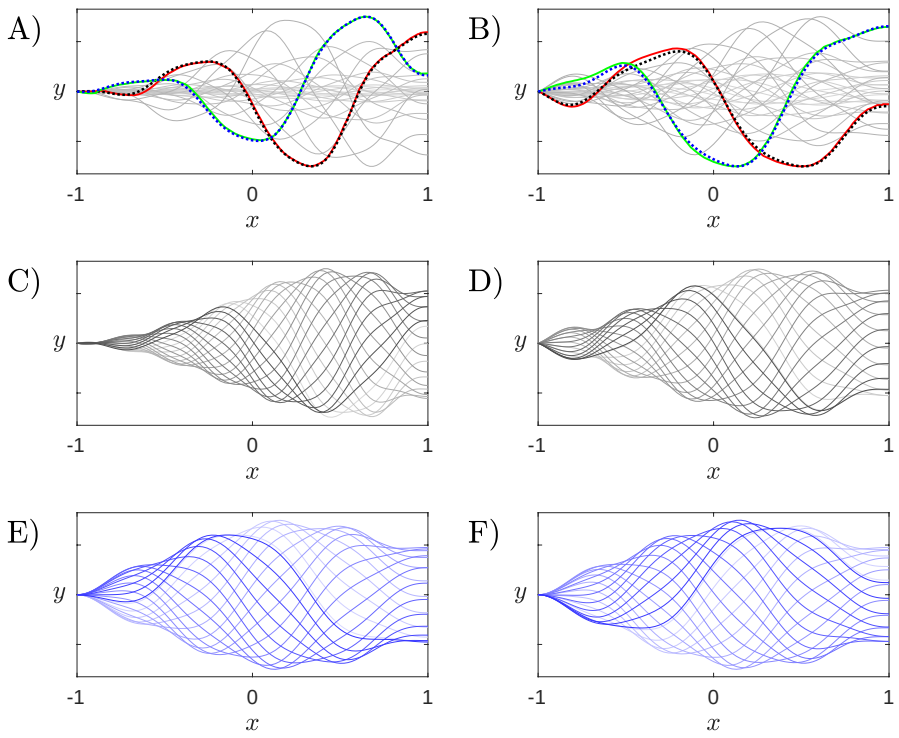

Figure 3.16: Fixed–free membranes at $R_1 = 10^{-0.5}$ and $R_3 = 10^{1.5}$, with $T_0 = 10^{-0.8}$ for A, C, E and $T_0 = 10^{-0.7}$ for B, D, and F. In panels A and B the solid red lines are $\mathrm{Re}(y_{\mathrm{nonlin}}(\alpha))$ estimated from the time-stepping simulation, which are close to $\mathrm{Re}(Y(x))$ from the eigenvalue problem (dotted black lines). The solid green lines are $\mathrm{Im}(y_{\mathrm{nonlin}}(\alpha))$, close to $\mathrm{Im}(Y(x))$ from the eigenvalue problem (dotted blue lines). The gray lines are a subset of snapshots in the linear growth regime. In panels C and D we show snapshots during the small-amplitude (growth) regime, but with the exponential growth removed. Panels E and F show snapshots during the steady-state large-amplitude motions. We show 20 equally spaced snapshots of membranes over a period, ranging from light blue at earlier times to dark blue at the last time.

We show the same comparisons at larger R_1 (10) in figure 3.17, at two T_0 values near the stability boundary. The wave numbers of the shapes are much reduced—only one neck appears in each envelope now—but otherwise many of the same features carry over from the previous figure. There is again good agreement between the eigenmodes and the versions estimated from the time-stepping simulations (panels A and B). The periodic parts of the small-amplitude motions have small but noticeable differences in panels C and D—in particular, the widths of the necks relative to the maximum widths of the envelopes. The large-amplitude motions (E and F) are again

nearly indistinguishable, however.

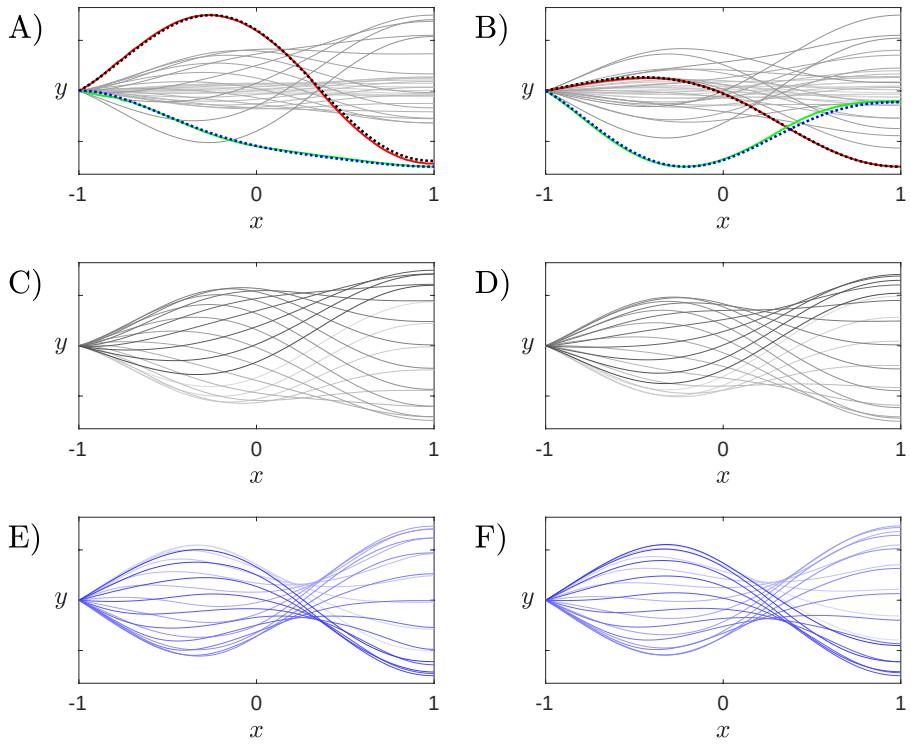

Figure 3.17: Same quantities as described in figure 3.16 but with $R_1 = 10^1$ and $R_3 = 10^{1.5}$, and $T_0 = 10^{-0.1}$ (for A, C, and E); $T_0 = 10^0$ (for B, D, and F).

We obtain similar levels of agreement in the free–free case; two examples are shown in appendix F.

3.8 Conclusions

To summarize, we have used a linearized model and a nonlinear eigenvalue solver to study small amplitude membrane motions, including the onset of membrane instability, in inviscid fluid flows. We characterized the different types of possible motions with respect to the two key dimensionless parameters—membrane mass and pretension—and for three sets of boundary conditions: "fixed–fixed," "fixed–free," and "free–free" leading and trailing edges. Previous work by other groups was limited to the fixed–fixed case, and a smaller range of membrane mass densities, and

our own previous time-stepping simulations in chapter II were unable to resolve the small-amplitude motions at small mass densities due to limited spatial resolution, and at large mass densities due to the very slow growth of instabilities.

For each of the three sets of boundary conditions, when membrane inertia and pretension dominate fluid pressure forces, the eigenmodes tend towards neutrally stable sinusoidal functions with half-integer or quarter-integer numbers of wavelengths. When the fluid forces are small but nonnegligible, the mode shapes are similar, but the even- (for fixed–fixed) or odd-numbered modes (for fixed–free and free–free) become unstable, starting with the second and third modes, respectively. For the fixed–fixed case, there are roughly two regimes: small membrane density, where divergence occurs and the most unstable mode becomes more fore-aft asymmetric as one moves further into the instability region; and large membrane density, where flutter and divergence occur with approximately sinusoidal modes. In both regimes, the most unstable modes become wavier at smaller T_0, akin to the most unstable beam modes at smaller bending rigidity in [3]. These results agree with those of [184] in the same parameter regimes.

The stability boundaries for the fixed–free and free–free cases resemble the fixed–fixed case at large membrane densities, showing an upward slope for $R_1 \geq 10^2$ (which we were not able to compute using time-stepping simulations). The fixed–free and free–free stability boundaries differ strongly from the fixed–fixed case at moderate and small membrane densities. There the membranes remain stable down to smaller pretension values, and eventually become unstable by flutter and divergence. For $10^{-3} \leq R_1 \leq 10^{-1}$, the most unstable mode is very wavy, and we were unable to resolve it with the time-stepping simulations in chapter II. Here we find that the most unstable eigenmodes have small deflection at the leading and trailing edges, despite

the free boundary conditions. For $10^{-1} \leq R_1 \leq 10^2$, the modes are wavy shapes (wavier at smaller T_0) superposed on background shapes with nonzero slopes (fixed–free) and/or deflections (free–free). By tracking the eigenmodes across the stability boundaries, we found that at moderate membrane densities, the modes resemble the sinusoidal shapes at large densities, but with more disorder, and the appearance of irregular bands of stable low-wavenumber modes that are difficult to associate with a particular branch.

Finally, we compared the eigenmodes with the membrane motions in the time-stepping simulations, and found very good agreement with the small-amplitude portion of the time-stepping simulations in examples with the three different boundary conditions. In all the examples, the large-amplitude motions qualitatively resembled those in the small amplitude regime in terms of the number of necks in the deflection envelopes, but had clear differences in the envelopes' shapes and the relative sizes of maxima and minima.

CHAPTER IV

Dynamics of Tethered Membranes in Inviscid Flow

4.1 Introduction

The majority of previous studies of membranes showed that when they are held with their ends fixed in a uniform oncoming fluid flow, they tend to adopt steady shapes with a single hump (when the flat state is unstable) [113, 158]. In the current chapter, we show that periodic and chaotic oscillations can occur in a simple physical setup. In our investigation we consider a passive case, i.e., we do not impose heaving or pitching motions [57, 78, 187, 191]. We also do not have any forcing of oscillations from leading-edge vortex shedding (vortex induced vibrations), which can be important in membranes that are driven by heaving and pitching motions or held at nonzero angle of attack [79, 143, 162].

In this chapter (as in the previous ones) we do not include gravity in our model in order to focus specifically on the basic flutter problem [154]. However, we need some restriction on the motion of the free membrane ends to ensure that the problem is well-posed (since membrane compression can lead to ill-posedness [188]). Such a restriction was realized experimentally by [87], with the membrane represented by an extensional spring that is tethered by steel wires to vertical supports. The membrane is thus free to move perpendicularly to its flat rest state, but remains

stretched between the supports, allowing for stable dynamics. The current chapter uses this tethered boundary condition to study membrane dynamics in a fluid flow. We study both small- and large-amplitude dynamics when the membrane is attached to tethers—i.e., inextensible rods that rotate freely—or mounted on springs.

We show that as the tether length is increased, the membrane dynamics change from static deflections with a single maximum, typical of the fixed–fixed case (similar to the shapes in [124, 127, 145, 191, 193, 194]) to a wide range of oscillatory motions that have some commonalities with flapping plates and flags [154]. We also study the stability properties of tethered membranes via a nonlinear eigenvalue problem. The nonlinearity makes it difficult to solve in certain regions of parameter space. Therefore we consider an approximate problem—an infinite membrane mounted on a periodic array of Hookean springs—that is easier to solve and allows us to obtain asymptotic scaling laws for the eigenmodes' dependences on membrane pretension and mass density.

The chapter is structured as follows. We begin in §4.2 by presenting the membrane and vortex-sheet model and in §4.2.1 we present the boundary conditions when the membranes are attached to inextensible-rod tethers. In §4.3 we present the results in the large-amplitude regime for this boundary condition. In §§4.3.1–4.3.2 we study the related case of membranes mounted on Hookean springs. In §4.4 we present a linearized, small-amplitude version of our model and study the stability properties (§4.4.1). We then study the stability behavior of an infinite periodic membrane mounted on a periodic array of springs and propose asymptotic scaling laws (§4.5). Finally, in §4.6, we summarize our findings.

4.2 Membrane and Vortex-sheet Model

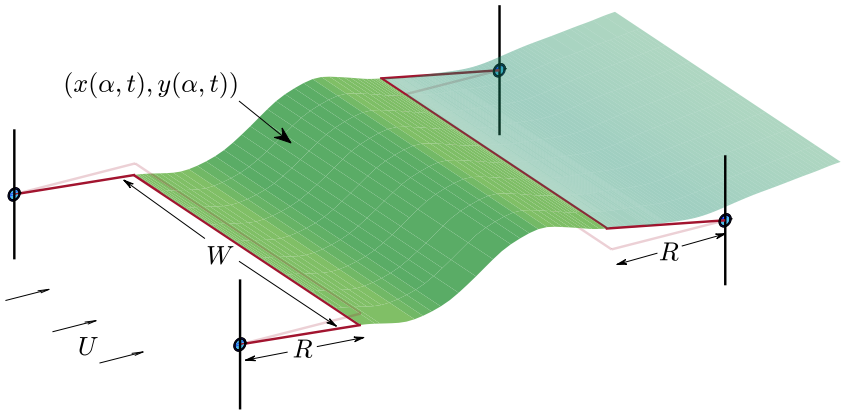

Figure 4.1: Schematic diagram of a flexible membrane (dark green surface) at an instant in time. U is the oncoming flow velocity and W is the membrane's spanwise width. The leading edge and the trailing edge of the membrane is attached to inextensible rods (red frames) that rotate freely about their hinged ends (small black/blue circles). There is also a vortex wake (light green surface) emanating from the membrane's trailing edge.

We model the dynamics of an extensible membrane that is nearly aligned with a two-dimensional background fluid flow that has speed U in the far field (see figure 4.1). The membrane is shown as a dark green surface with the vortex wake (light green surface) emanating from its trailing edge. Each membrane end is attached to a massless, open rigid frame of inextensible rods (red solid lines) that pivots freely at the hinges shown by small black/blue circles in figure 4.1 and therefore the membrane's ends are constrained to move along circles of radius R centered at the hinges. The motions of the membrane and open rod frames are assumed to be invariant in the spanwise direction (along W), and the effect of gravity is neglected for simplicity. The four clamping poles (black lines) at the end of the rod frame away from the membrane are sufficiently thin that their influence on the fluid flow is assumed to be negligible.

The membrane and flow models are the same as in chapter II but we repeat them briefly for completeness. The membrane dynamics are described by the unsteady ex-

tensible elastica equation with body inertia, stretching resistance, and fluid pressure loading, obtained by writing a force balance equation for a small section of membrane that lies between material coordinates α and $\alpha + \Delta\alpha$:

(4.1)

$$\rho_s h W \partial_{tt}\zeta(\alpha,t)\Delta\alpha = T(\alpha+\Delta\alpha)\hat{\mathbf{s}} - T(\alpha,t)\hat{\mathbf{s}} - [p]^+_-(\alpha,t)\hat{\mathbf{n}}W(s(\alpha+\Delta\alpha,t) - s(\alpha,t)).$$

Here ρ_s is the mass per unit volume of the undeflected membrane, h is the membrane's thickness, and W its spanwise width, all uniform along the length. In (4.1), $\zeta(\alpha,t) = x(\alpha,t)+iy(\alpha,t)$ denotes the membrane position in the complex plane, parameterized by the material coordinate α, $-L \le \alpha \le L$ (L is half the initial length) and time t. T is the tension in the membrane, $[p]^+_-$ is the pressure jump across it, $s(\alpha,t)$ is the local arc length coordinate, and the unit vectors tangent and normal to the membrane are $\hat{\mathbf{s}} = \partial_\alpha\zeta(\alpha,t)/\partial_\alpha s(\alpha,t) = e^{i\theta(\alpha,t)}$ and $\hat{\mathbf{n}} = i\hat{\mathbf{s}} = ie^{i\theta(\alpha,t)}$, respectively, with $\theta(\alpha,t)$ the local tangent angle and $\partial_\alpha s$ the local stretching factor. We use $+$ to denote the side towards which the membrane normal $\hat{\mathbf{n}}$ is directed, and $-$ for the other side. However, for the remainder of this chapter, we drop the $+$ and $-$ for ease of notation.

Dividing (4.1) by $\Delta\alpha$ and taking the limit $\Delta\alpha \to 0$, we obtain

$$\rho_s h W \partial_{tt}\zeta(\alpha,t) = \partial_\alpha(T(\alpha,t)\hat{\mathbf{s}}) - [p](\alpha,t)W\partial_\alpha s\hat{\mathbf{n}}, \tag{4.2}$$

where the membrane tension $T(\alpha,t)$ is given by linear elasticity [22, 123, 125] as

$$T(\alpha,t) = \overline{T} + EhW(\partial_\alpha s(\alpha,t) - 1). \tag{4.3}$$

Here E is the Young's modulus and $\overline{T}$ is the tension in the initial, undeflected equilibrium state. After nondimensionalizing length by L, time by L/U, and pressure by $\rho_f U^2$, where ρ_f is the density of the fluid and U is the oncoming flow velocity, equation (4.2) becomes the nonlinear, extensible membrane equation

$$R_1\partial_{tt}\zeta - \partial_\alpha((T_0 + R_3(\partial_\alpha s - 1))\hat{\mathbf{s}}) = -[p]\partial_\alpha s\hat{\mathbf{n}}. \tag{4.4}$$

In (4.4), $R_1 = \rho_s h/(\rho_f L)$ is the dimensionless membrane mass, $T_0 = \overline{T}/(\rho_f U^2 LW)$ is the dimensionless pretension, and finally, $R_3 = Eh/(\rho_f U^2 L)$ is the dimensionless stretching rigidity. We use (4.4) to study large-amplitude motions in §4.3. We use a linearized, small-amplitude version to study membrane stability in §§4.4 and 4.5.

We express the 2D flow past the membrane using $z = x + iy$, the complex representation of the xy flow plane. The complex conjugate of the fluid velocity at any point z not on the vortex sheets is a sum of the horizontal background flow with speed unity and the flow induced by the bound and free vortex sheets,

$$u_x(z) - iu_y(z) = 1 + \frac{1}{2\pi i}\int_{-1}^{1} \frac{\gamma(\alpha,t)}{z-\zeta(\alpha,t)}\partial_\alpha s \mathrm{d}\alpha + \frac{1}{2\pi i}\int_0^{s_{\max}} \frac{\gamma(s,t)}{z-\zeta(s,t)}\mathrm{d}s, \tag{4.5}$$

where s is the arc length along the free sheet starting at 0 at the membrane's trailing edge and extending to $s_{\max}$ at the free sheet's far end. To determine the bound vortex sheet strength γ we require that the fluid does not penetrate the membrane, which is known as the kinematic boundary condition. Here γ represents the jump in the component of the flow velocity tangent to the membrane from the $-$ to the $+$ side, i.e., $\gamma = -[(u_x, u_y)\cdot\hat{\mathbf{s}}]$. The normal components of the fluid and membrane velocities are equal along the membrane:

$$\begin{aligned}&\mathrm{Re}(\hat{\mathbf{n}}\partial_t\overline{\zeta}(\alpha,t)) = \\ &\mathrm{Re}\left(\hat{\mathbf{n}}\left(1 + \frac{1}{2\pi i}\int_{-1}^{1} \frac{\gamma(\alpha,t)}{z-\zeta(\alpha,t)}\partial_\alpha s \mathrm{d}\alpha + \frac{1}{2\pi i}\int_0^{s_{\max}} \frac{\gamma(s,t)}{z-\zeta(s,t)}\mathrm{d}s\right)\right),\end{aligned} \tag{4.6}$$

where $\hat{\mathbf{n}}$ is written as a complex scalar. Solving (4.6) for γ requires an additional constraint that the total circulation is zero for a flow started from rest. At each instant the part of the circulation in the free sheet, or alternatively, the strength of γ where the free sheet meets the trailing edge of the membrane, is set by the Kutta condition which makes velocity finite at the trailing edge. At every other point on the free sheet, γ is set by the criterion that circulation (the integral of γ) is conserved

at fluid material points of the free sheet. The vortex sheet strength $\gamma(\alpha, t)$ is coupled to the pressure jump $[p](\alpha, t)$ across the membrane using a version of the unsteady Bernoulli equation written at a fixed material point on the membrane:

$$\partial_\alpha s \partial_t \gamma + \partial_\alpha \left(\gamma(\mu - \tau)\right) + \gamma(\partial_\alpha \tau - \nu\kappa\partial_\alpha s) = \partial_\alpha [p], \tag{4.7}$$

where μ is the average flow velocity tangent to the membrane, τ and ν are the tangential and normal components of the membrane velocity, respectively, and $\kappa(\alpha, t) = \partial_\alpha \theta / \partial_\alpha s$ is the membrane's curvature. At the trailing edge, $[p]|_{\alpha=1} = 0$. The derivation of (4.7) can be found in appendix A.

4.2.1 Boundary Conditions: Inextensible-rod Tethers

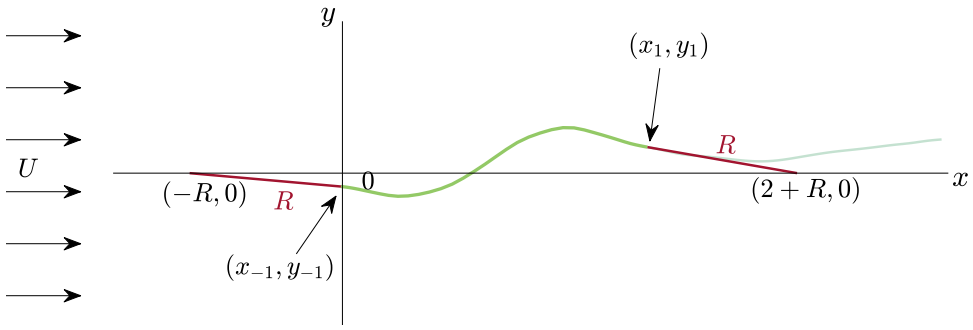

Figure 4.2: Slice through the membrane in figure 4.1. Schematic diagram of a flexible membrane (green line) at an instant in time. The leading edge of the membrane with position $(x(-1,t), y(-1,t))$ is attached to an inextensible rod frame (red line) whose motion is restricted to a circle of radius R (length of rod frame) and whose other end is fixed at $(-R, 0)$ for all time. The membrane's trailing edge with position $(x(1,t), y(1,t))$ is attached to another rod frame whose other end is fixed at $(2+R, 0)$ for all time. There is also a vortex wake emanating from the membrane's trailing edge (light green line).

A slice through the membrane and rod frame in the 2D flow plane is shown schematically in figure 4.2. The rod frames pivot freely about the points $(-R, 0)$ and $(2+R, 0)$, respectively. Because the frames are inextensible, the membrane ends are constrained to move along circular arcs of radius R. This is enforced by requiring

$$(x_{-1} - (-R))^2 + y_{-1}^2 = R^2 \quad \text{and} \quad (x_1 - (2+R))^2 + y_1^2 = R^2, \tag{4.8}$$

for all time, where $x_{\pm 1} = x(\pm 1, t)$ and $y_{\pm 1} = y(\pm 1, t)$ are four unknowns that denote the x- and y-coordinates of the membrane ends, respectively. Two equations for the four unknowns are (4.8) and the remaining two equations require the membrane and rod frames to be tangent where they meet:

$$\left.\frac{\partial_\alpha y}{\partial_\alpha x}\right|_{\alpha=-1} = \frac{y_{-1} - 0}{x_{-1} - (-R)} \quad \text{and} \quad \left.\frac{\partial_\alpha y}{\partial_\alpha x}\right|_{\alpha=1} = \frac{0 - y_1}{(2+R) - x_1}, \tag{4.9}$$

again for all time. Equations (4.9) follow from balancing the forces on an infinitessimal length of membrane near the membrane ends; because its mass is infinitessimal, the tension forces on it from the rods and from the adjacent portion of the membrane must be aligned. The rod tether length R is an important parameter that influences the dynamics of the membrane. With short rods ($R \to 0$), we will show that the membrane dynamics are similar to fixed–fixed membranes, whereas with longer rods the dynamics resemble free–free membranes but without the large-scale translational motions seen in chapter II.

4.3 Large-amplitude Results

We simulate the membrane starting from an initial condition in which the membrane is perturbed from the flat horizontal equilibrium state: it has a linear profile with a small nonzero slope,

$$\zeta(\alpha, 0) = (\alpha + 1)(1 + i\sigma), \tag{4.10}$$

for $\sigma = 10^{-3}$. We evolve the membrane and vortex sheet wake forward in time using a numerical method similar to those in [4] and chapter II.

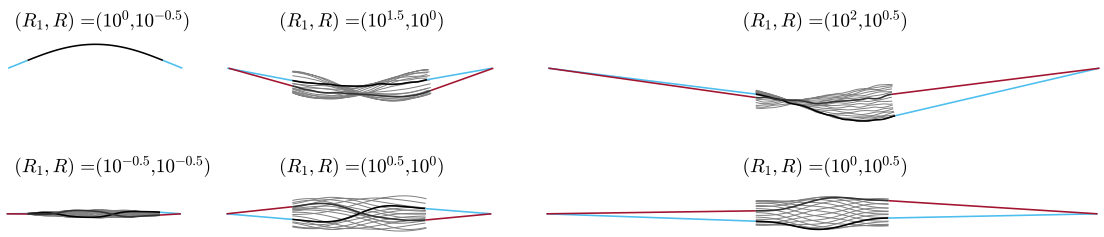

Figure 4.3: Examples of membrane (black) and rod (red and blue) snapshots at two different times, superposed on a larger set of membrane snapshots (gray) within a period. Each column corresponds to a rod length R: $10^{-0.5}$ (left column), 10^0 (middle column), and $10^{0.5}$ (right column). Here $R_3 = 10^{1.5}$ and $T_0 = 10^{-2}$.

In figure 4.3 we show snapshots of membranes and rods for a fixed stretching rigidity ($R_3 = 10^{1.5}$) and pretension ($T_0 = 10^{-2}$), at six pairs of (R_1, R) values that give typical dynamics. In each case, two of the snapshots show the rods (blue in one and red in the other) together with the membranes (black lines). The remaining 16 snapshots show only the membranes (gray lines), equally spaced in time within a period of motion. R increases from left to right: $10^{-0.5}$ (left column), 10^0 (middle column), and $10^{0.5}$ (right column). The membrane deflection may be very small, particularly at small R_1 (bottom left case), and may be steady, particularly at small R (top left case). In the bottom row, middle column case (i.e., $R_1 = 10^{0.5}$ and $R = 10^0$) and in the bottom row, right column case (i.e., $R_1 = 10^0$ and $R = 10^{0.5}$) it is evident that the inextensible rods may deflect upwards or downwards.

We characterize the large-amplitude dynamics using three main quantities. One is the time-averaged deflection of the membrane, defined as

$$\langle y_{\rm defl} \rangle \equiv \frac{1}{t_2} \int_{t_1}^{t_1+t_2} \left(\max_{-1 \le \alpha \le 1} y(\alpha, t) - \min_{-1 \le \alpha \le 1} y(\alpha, t) \right) {\rm d}t. \tag{4.11}$$

Here, as in chapter II, t_1 and t_2 are sufficiently large (typically 50–100) that $\langle y_{\rm defl} \rangle$ changes by less than 1% with further increases in these values. So, $\langle y_{\rm defl} \rangle$ is the maximum membrane deflection minus the minimum membrane deflection, averaged over time.

The second quantity used to characterize the large-amplitude dynamics is the time period. This is computed using the peak frequency in the power spectrum computed using the fast Fourier transform (`fft` function in MATLAB). The power spectrum is obtained from a time series of the membrane's midpoint when the membrane has reached steady-state large-amplitude dynamics. The third quantity is the time-averaged number of zero crossings along the membrane, computed using the same temporal data as the power spectrum. Apart from the number of zero crossings, we also use the time-averaged number of local extrema as a different measure of the 'waviness' of the membrane shape.

In figure 4.4 we show typical membrane snapshots in R-R_3 space, while fixing $T_0 = 10^{-2}$ and $R_1 = 10^{-0.5}$. At each (R, R_3) value, the set of snapshots is normalized by the maximum deflection of the snapshots to show the motions more clearly and scaled to fit within a colored rectangle at the (R, R_3) value. Each snapshot has the corresponding R value at its horizontal midpoint, and the R_3 value at its average vertical position. Colors represent the time-averaged deflection defined by (4.11). In the lower-left corner the snapshots are omitted because steady-state membrane motions were not obtained. Two main types of membrane behaviors are seen: at small R, a steady single-hump shape that is fore-aft symmetric, similar to membranes that have both the leading and trailing edges fixed at zero deflection; at moderate-to-large R, an oscillatory motion. The framed panel on the right-hand side of figure 4.4 shows the transition between these states in finer detail, between $R = 10^{-0.65}$ and $10^{-0.57}$. The red dashed lines show where larger increments of R are taken, from $10^{-0.65}$ to $10^{-0.7}$ (where only single hump solutions are obtained for any R_3) and from $R = 10^{-0.57}$ to $10^{-0.5}$ (where only flapping membranes are observed, for any R_3). In the framed panel we see that the initial condition of nonzero slope [equation (4.10)]

may evolve to single-hump shapes that are concave up, concave down, or to oscillatory motions when R is changed slightly. In the left panel, the oscillatory motions are mostly close to periodic and fore-aft symmetric, with some deviations particularly at $R = 10^{-0.5}$ and $10^{1.5}$, where a less wavy shape becomes more common.

For very large stretching rigidity $R_3 \gtrsim 10^3$ the code reaches the steady-state regime only if we decrease the membrane discretization size to $m = 40$ (from $m = 120$ below the red dividing line). As we observed in chapter II, in many cases varying the stretching rigidity R_3 alters the overall deflection magnitudes but leaves the membranes' shapes nearly unchanged.

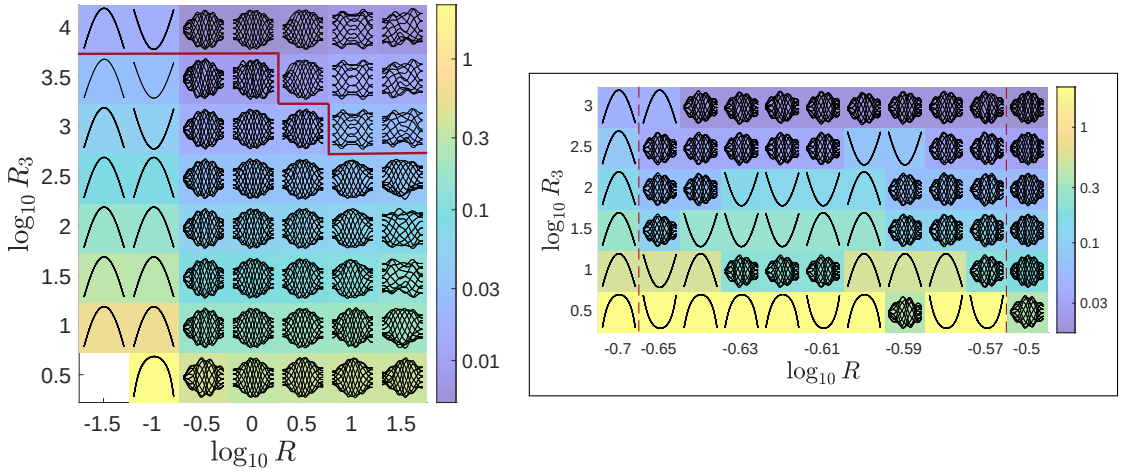

Figure 4.4: (Inextensible rods) Snapshots of large-amplitude membrane motions in R-R_3 space for fixed $T_0 = 10^{-2}$ and $R_1 = 10^{-0.5}$. Colors represent the time-averaged deflection of the membranes defined by (4.11). For rods with length $R \leq 10^{-1}$ the membranes behave similarly to those with fixed–fixed ends, yielding a single hump solution, whereas when $R \geq 10^{-0.5}$ the membranes oscillate as in some cases with free–free ends. At each (R, R_3) value, the set of snapshots is scaled to fit within a colored rectangle centered at that value and normalized by the maximum deflection of the snapshots to show the motions more clearly. The red solid line separates membranes with $m = 40$ points (above) and $m = 120$ points (below). In the framed figure we look at a finer grid between $R = 10^{-0.7}$ and $10^{-0.5}$, to investigate dynamics near the transition between the single-hump solution and the flapping state occurs. The red dashed lines indicate a jump in the increment of R values.

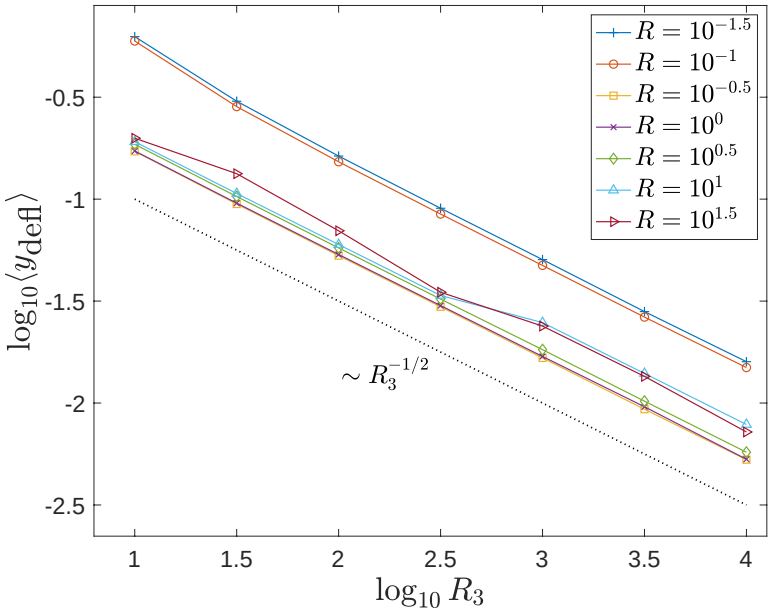

Figure 4.5: (Inextensible rods) Time-averaged deflections of the membranes (defined by (4.11)) versus R_3 for various R and fixed $R_1 = 10^{0.5}$, $T_0 = 10^{-2}$. The dotted black line indicates the scaling $R_3^{-1/2}$.

In figure 4.5 we show how the time-averaged deflection quantitatively depends on R_3 at several fixed values of $R \in \{10^{-1.5}, 10^{-1}, \ldots, 10^{1.5}\}$, for $R_1 = 10^{0.5}$ and $T_0 = 10^{-2}$ here. The $\langle y_{\mathrm{defl}}\rangle \sim R_3^{-1/2}$ dependence at large R_3 is the same for other mass ratios from $R_1 = 10^{-0.5}$ to $R_1 = 10^2$, again with $T_0 = 10^{-2}$. This was observed also for fixed–fixed, fixed–free, and free–free membranes in chapter II. We include the explanation for how the scaling $\langle y_{\mathrm{defl}}\rangle \sim R_3^{-1/2}$ arises from the y-component of the membrane equation (4.4) with small deflections. We assume that $\partial_\alpha y \ll 1$ and $\partial_\alpha x \approx 1$. Then $\partial_\alpha s - 1 = \sqrt{(\partial_\alpha x)^2 + (\partial_\alpha y)^2} - 1 \approx \partial_\alpha y^2/2$ and $\hat{s}_y \approx \partial_\alpha y$. With these approximations, the y-components of the T_0 and R_3 terms in (4.4) are linear and cubic in deflection, respectively:

$$\partial_\alpha(T_0 \hat{s}_y) \approx T_0 \partial_{\alpha\alpha} y; \quad \partial_\alpha(R_3(\partial_\alpha s - 1)\hat{s}_y) \approx R_3 \partial_\alpha((\partial_\alpha y)^3/2). \tag{4.12}$$

The R_1 term that multiplies $\partial_{tt} y$ is also linear in deflection. The pressure jump is linear in the bound vortex sheet strength because the left-hand side of (4.7) $\approx$

$\partial_t\gamma + \partial_\alpha\gamma$ with small deflections. The bound vortex sheet strength is linear in the deflection by the linearized version of (4.6),

(4.13)
$$\partial_t y(\alpha,t) \approx \frac{1}{2\pi}\fint_{-1}^{1} \frac{\gamma(\alpha',t)}{x(\alpha,t)-x(\alpha',t)}\,\mathrm{d}\alpha' - \frac{1}{2\pi}\int_0^{\Gamma_+(t)} \frac{x(\alpha,t)-x(\Gamma',t)}{(x(\alpha,t)-x(\Gamma',t))^2+\delta(\Gamma',t)^2}\,\mathrm{d}\Gamma',$$

in which the second integral consists of bound vorticity advected from the trailing edge, so it has the same dependence on deflection as the bound vorticity. Here, with small deflections, we have assumed that $\partial_\alpha x \approx 1$, and then the linearization is the same as in [10, 113]. Without viscous stresses, horizontal membrane deformations arise only through nonlinear terms in the elastic and pressure forces associated with large deflections, so it is reasonable to neglect them, and this is consistent with the simulation results. Balancing the terms that are linear in deflection with the product of R_3 and a term that scales with deflection cubed gives $\langle y_{\mathrm{defl}}\rangle \sim R_3^{-1/2}$. The slight increase in $\langle y_{\mathrm{defl}}\rangle$ between $R_3 = 10^{2.5}$ and 10^3 when $R = 10^1$ (light blue line with upward-pointing triangle) and $R = 10^{1.5}$ (dark red line with right-pointing triangle) arises because for $R_3 = 10^{2.5}$ the discretization size of the membrane is $m = 120$ whereas for $R_3 = 10^3$ it is $m = 40$.

Table 4.1: Table of plots showing snapshots of large-amplitude membrane motions in R_1-R space for two values of stretching rigidity R_3 ($10^{1.5}$ in left column, 10^3 in right column) and two value of pretension T_0 (10^{-1} in top row, 10^{-2} in bottom row). Colors represent the time-averaged deflection defined by (4.11).

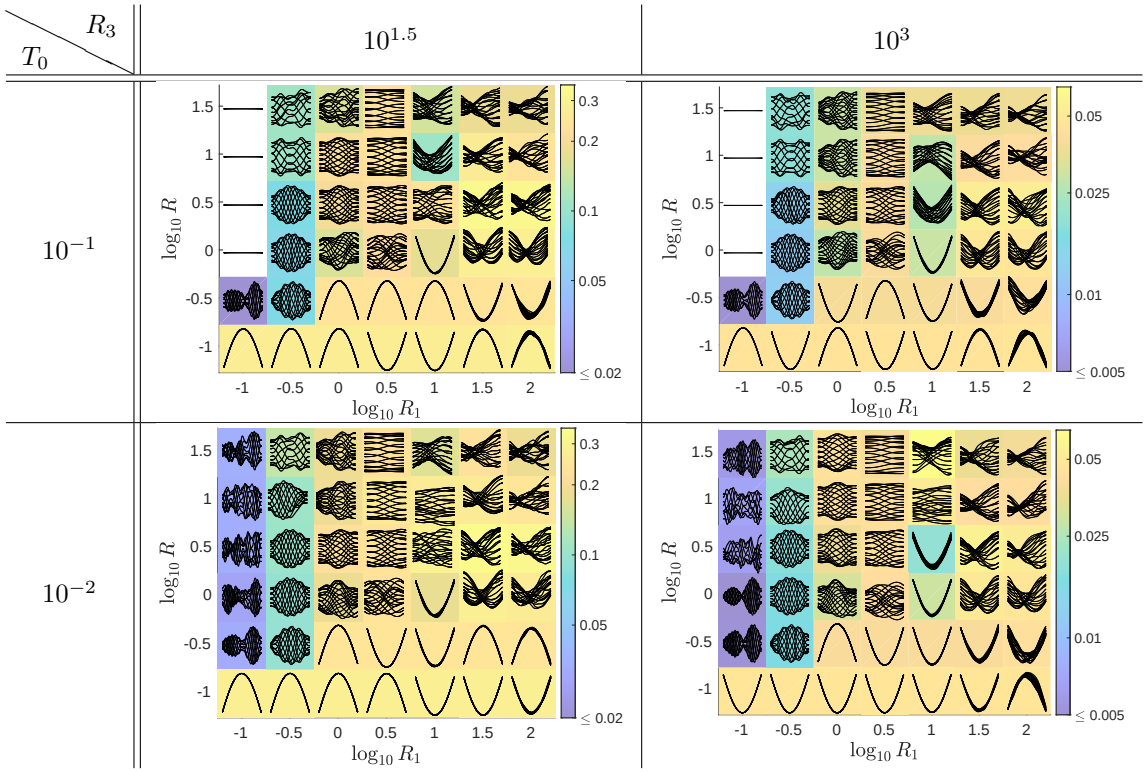

In figure 4.4 we saw that the motions do not change considerably with R_3 (apart from their amplitudes) except in the narrow transition region shown in the inset. We also find that the motions do not depend much on T_0 except close to the critical value of T_0 below which the flat state is unstable. In table 4.1 we show membrane snapshots in the full four-dimensional parameter space R_1-T_0-R_3-R, collected into four subpanels, each with a particular value of T_0 and R_3 (labeled at top and left, respectively), and with a range of values of R_1 and R within each subpanel. There is more variation within a given subpanel than between corresponding points in different subpanels, indicating that R and R_1 have a stronger effect on the dynamics than T_0 and R_3. The white background and flat lines at $R_1 = 10^{-1}$ and $R \geq 10^0$ when $T_0 = 10^{-1}$ (top row) indicate stable membranes, so the deflection there is zero.

From this comparison we see that, as in the previous figure, the deflections decrease with increasing R_3 (values in color bars at right) but often the snapshot shapes do not change much, at the same (R_1, R) values. Some membranes with moderate values of R_1 (10^0 and 10^1) have more prominent differences as R_3 is changed, sometimes by altering the location of a transition between different types of dynamics. Decreasing the value of T_0 can cause stable membranes to become unstable (e.g., at $R_1 = 10^{-1}$), but otherwise decreasing T_0 has a small effect, mainly to increase the deflection slightly at a given R_3. Below 10^{-2}, the T_0 term in the membrane equation (4.4) becomes insignificant, as noted in chapter II.

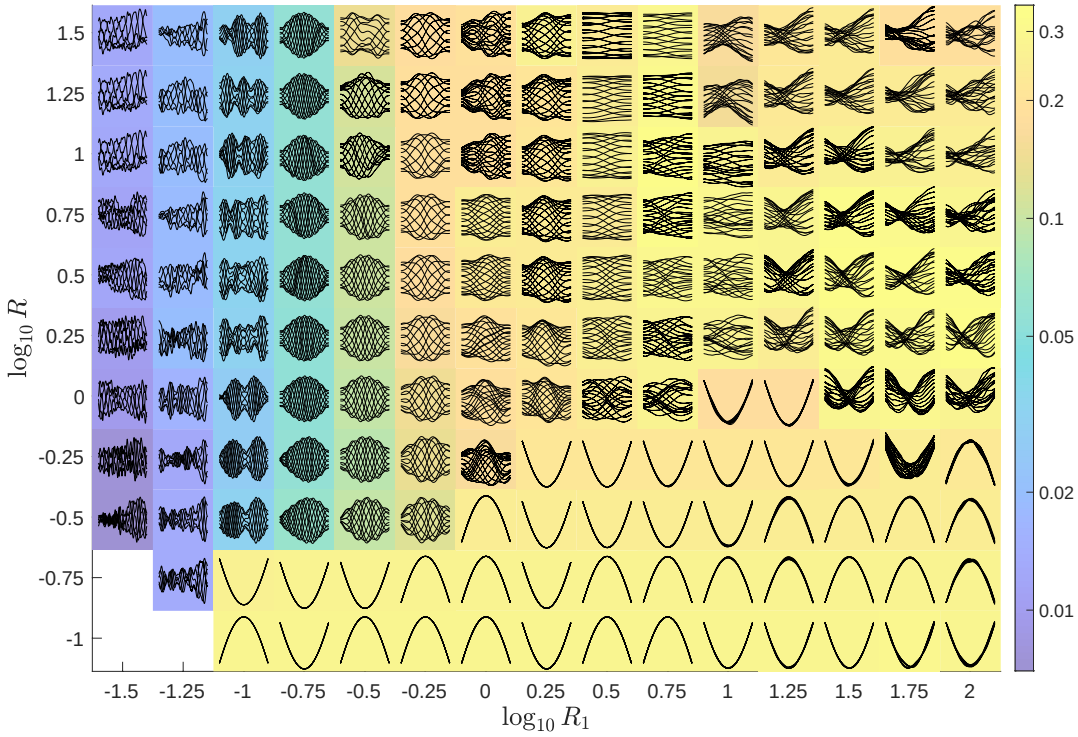

Figure 4.6: (Inextensible rods) Membrane profiles in the large-amplitude steady-state regime, in R_1-R space for fixed $T_0 = 10^{-2}$ (dimensionless pretension) and $R_3 = 10^{1.5}$ (dimensionless stretching rigidity). The colored background represents the time-averaged deflection of the membranes defined by (4.11).

In figure 4.6, we focus on the lower left subpanel of table 4.1, but double the density of values of R_1 and R, and decrease the lower limit of R_1, to obtain a more compre-

hensive picture of the dynamics. The motions in figure 4.6 have the largest deflection amplitudes at the largest $R_1 = 10^2$. As mentioned in chapter II, we hypothesize that at large R_1 membrane inertia allows the membrane to maintain its momentum for longer times against restoring fluid forces, and obtain larger deflections (with longer periods, as we will show) before reversing direction. The same has been observed for flutter with bending rigidity [10,31]. As R_1 decreases, the membrane deflection amplitudes progressively decrease until the motions become difficult to resolve numerically (for $R_1 \lesssim 10^{-1}$). In this region, we find chaotic membrane oscillations with very small amplitudes and high spatial frequencies. To obtain numerically-converged motions with respect to the spatial grid when $R_1 \leq 10^{-1}$ we use more discretization points. In the lower-left corner in figure 4.6, i.e., $(R_1, R) = (10^{-1.5}, 10^{-1})$, $(10^{-1.5}, 10^{-0.75})$, and $(10^{-1.25}, 10^{-1})$, snapshots are omitted because steady-state membrane motions were not obtained.

Decreasing the membrane mass ratio (R_1) generally tends to introduce more oscillating states and fewer single-hump solutions for R values in the range $(10^{-0.75}, 10^{0.25})$. For large R_1 (heavy membranes) the maximum deflection of the membrane occurs close to either the leading or trailing edge of the membrane. However, at $R_1 \in [10^{-0.75}, 10^{0.25}]$ the maximum membrane deflection seems to occur close to the midpoint of the membrane, with the deflection at the endpoints decreasing with decreasing R_1 in this region.

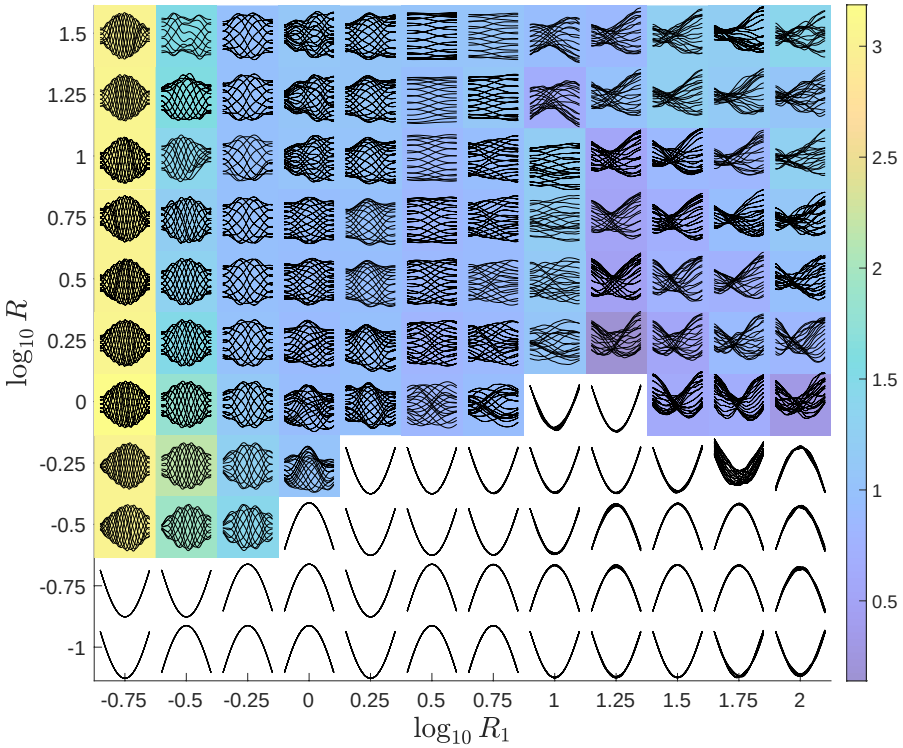

Figure 4.7: (Inextensible rods) Colors represent the time-averaged number of zero-crossings (values in color bar at right) for membrane flutter in the R_1-R parameter space for fixed $T_0 = 10^{-2}$ and $R_3 = 10^{1.5}$. Note that R_1 is the dimensionless membrane mass, T_0 is the dimensionless pretension, and R_3 is the dimensionless stretching modulus. We also define R to be the length of the inextensible rods at either end of the membrane. The white background corresponds to membranes with no zero-crossings. At each (R_1, R) value the set of snapshots is normalized by the maximum deflection of the snapshots to show the motions more clearly.

We now quantify the membrane shapes in terms of the time-averaged number of 'zero crossings'. Our definition is the number of crossings that a membrane makes with the line connecting its two endpoints, averaged over time—excluding the endpoints. This is one way to measure the 'waviness' of a shape that is not sinusoidal and whose wavelength is thus not well defined (chapter II, [7]). We first focus on moderate-to-large values of R_1 where the membranes have fewer zero-crossings (figure 4.7). Decreasing R_1 from the largest value (10^2), the average number of zero crossings changes non-monotonically. In most cases it decreases until about $R_1 = 10^{1.25}$ for $R \in [10^0, 10^1]$. Further decreases in R_1 give rise to more periodic

motions with slightly larger numbers of zero-crossings. Independent of R_1, when T_0 and R_3 are fixed at 10^{-2} and $10^{1.5}$, respectively, and when the rods have a length of $\leq 10^{-0.75}$ then the membrane behaves similarly to the fixed–fixed case, where a single-hump solution is obtained. We use a white background for membranes with no zero-crossings (single hump solutions).

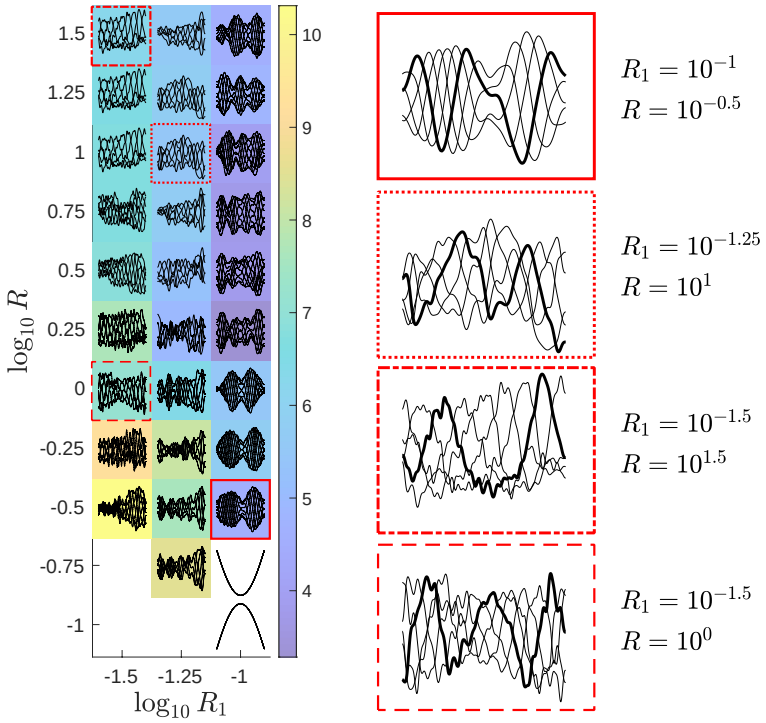

Figure 4.8: (Inextensible rods) Colors represent the time-averaged number of zero-crossings (values in color bar at right) for membrane flutter in the R_1-R parameter space for fixed $T_0 = 10^{-2}$ and $R_3 = 10^{1.5}$ for light membranes ($R_1 \leq 10^{-1}$). Snapshots of these large-amplitude membrane motions are superposed to show the motions clearly in this region.

In figure 4.8 we present the zero-crossings in the small R_1 ($\leq 10^{-1}$) region, where higher spatial frequency components occur with decreasing R_1. The motions also become more irregular at the smallest R_1 values, where we increase the spatial grid density to resolve the fine undulations that appear on the membranes. On the right-hand side of figure 4.8 we show four panels with examples of sequences of membrane snapshots, equally spaced in time (with the thicker black line representing

the membrane at the last time), to emphasize that even though the number of zero-crossings is a good measure of waviness it also misses some features of the shapes. For example, we see that the shape at $R_1 = 10^{-1.5}$ and $R = 10^0$ (bottom row of right-most column) has small undulatory features that are not reflected in the number of zero-crossings. In the small-R_1 region, the numbers of zero-crossings (shown by the colors) vary more rapidly compared to figure 4.7. In the lower-left corner, snapshots are omitted because steady-state membrane motions were not obtained.

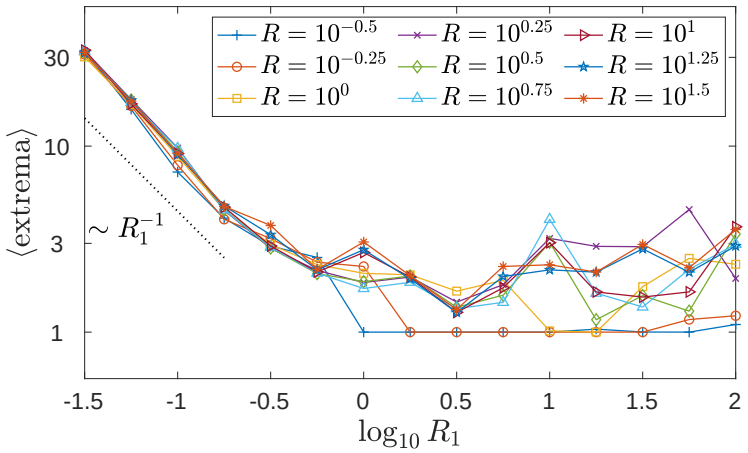

Figure 4.9: (Inextensible rods) Time-averaged number of local extrema of the membranes versus the dimensionless mass density R_1 for various R and fixed $R_3 = 10^{1.5}$ and $T_0 = 10^{-2}$. The dotted black line at small R_1 indicates the scaling R_1^{-1}.

To quantify the small undulatory features on the membranes, we calculate the time-averaged number of local extrema of deflection. In figure 4.9 we show that for fixed $R_3 = 10^{1.5}$, $T_0 = 10^{-2}$, and various fixed values of R, the time-averaged number of local extrema for small R_1 scales as R_1^{-1} approximately. At moderate-to-large values of R_1 (i.e., $[10^0, 10^2]$) and R small, the membranes tend to fore-aft symmetric, single-hump solutions and therefore the average number of extrema is one. For the oscillatory shapes that occur at larger values of R in the same region of R_1, the average number of local extrema is not large (i.e., between 1 and 5).

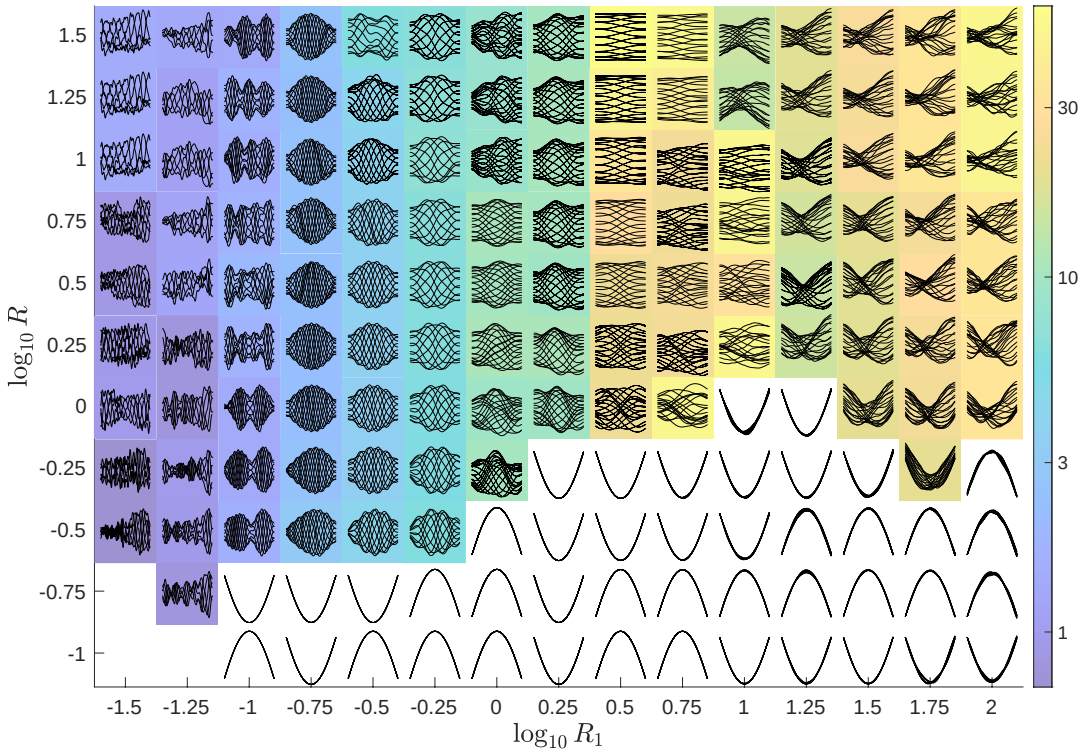

Figure 4.10: (Inextensible rods) Colors represent the dominant periods (values in color bar at right) of large-amplitude motions for various R_1 and R, and fixed $T_0 = 10^{-2}$ and $R_3 = 10^{1.5}$. The data in the bottom-left corner are obtained for a shorter time and so we neglect the computational results for those values of R_1 and R.

We have considered the amplitude of membrane deflection and its spatial frequency (in terms of zero crossings and numbers of extrema). The third main quantity we consider is the temporal period. We compute the power spectra of the time series of the membrane's midpoint, $y(1/2, t)$, using the fast Fourier transform. We identify the dominant frequency as that corresponding to the largest local maximum in the power spectrum (in a few cases excluding the peak closest to zero, which represents the time scale of the entire time series, and occurs because of the discontinuity in $y(1/2, t)$ at the beginning and end of the time series). The background color in figure 4.10 represents the dominant period, defined as the reciprocal of the dominant frequency, and is white for the steady single-hump solutions since the dominant period is undefined in the steady case. Similar to figures 4.6 and 4.8, in the lower-

left corner, snapshots are omitted because steady-state membrane motions were not obtained.

We find different types of power spectra in different regions of R_1-R space, corresponding to the different motions illustrated in figure 4.10. At small R_1 ($\lesssim 10^{-1}$) the motions are more chaotic and there, the power spectra have a broad band of frequencies. At small-to-moderate values of R_1—between $10^{-0.75}$ and $10^{0.25}$—the motions are periodic and thus the power spectra have a discrete set of peaks. At moderate values of R_1—between $10^{0.5}$ and 10^{1}—the peak frequencies are decreased. Finally, for large values of R_1 ($\geq 10^{1.25}$) the motions become somewhat chaotic again (as at the smallest R_1), and with little dependence on R except at values greater than 10^1, where there is a slight increase in the dominant period.

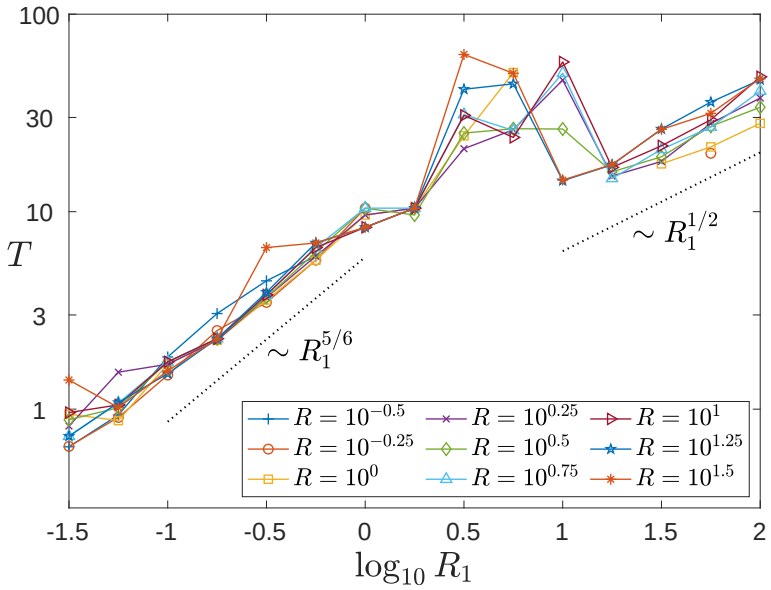

Figure 4.11: Plots of the dominant period (T) versus mass density R_1 for various R and fixed $R_3 = 10^{1.5}$ and $T_0 = 10^{-2}$. The dotted black line at large R_1 shows the scaling $R_1^{1/2}$ and the dotted black line at small R_1 shows the scaling $R_1^{5/6}$.

In figure 4.11 we show how the dominant period varies with R_1 for various fixed values of R. The trend at the largest R_1 is approximately $T \sim R_1^{1/2}$ (admittedly over a short range of R_1). This scaling arises when one approximates the normal component

of the membrane equation (4.4) by its y-component, and chooses a characteristic time scale t_0 so that $R_1\partial_{tt}y$ balances other terms that depend on y but not its time derivatives (i.e., the R_3 and T_0 terms and some of the fluid pressure terms). At large R_1, $R_1\partial_{tt}y$ is comparable to the other terms when $R_1/T^2 \sim 1$ giving a typical period $T \sim R_1^{1/2}$. For some values of R, when $10^{0.25} < R_1 < 10^{1.25}$ and $R_1 > 10^{1.5}$, the period increases to > 30 as can be seen in figure 4.11. This range of moderate R_1 is a transition region, and at smaller R_1, (here, $10^{-1.5} \leq R_1 < 10^{0.25}$), another power law behavior is observed: $T \sim R_1^{5/6}$.

4.3.1 Hookean Springs

The inextensible rods are a particular choice of tether motivated by the experiment of [87]. In this section we briefly explore some alternative tethers involving Hookean springs. In the first case, we replace the inextensible rods at the ends of the membrane with springs of rest length zero that obey Hooke's law [69]. We illustrate schematically this alternative configuration in figure 4.12. The four prescribed dimensionless parameters are: membrane mass R_1, stretching rigidity R_3, pretension T_0, and spring stiffness k_s.

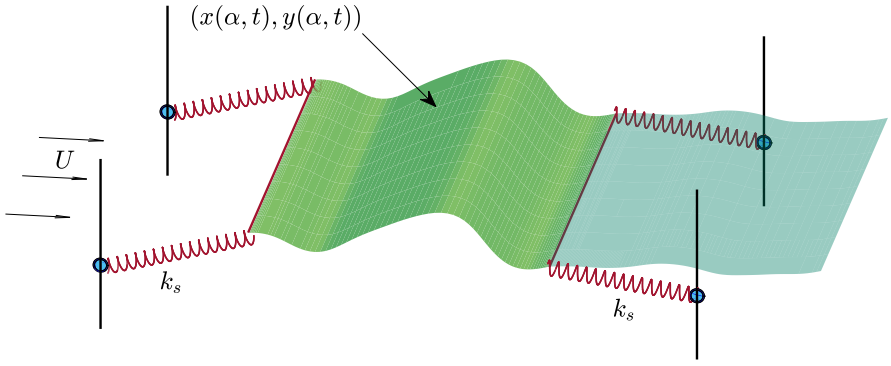

Figure 4.12: Schematic diagram of a flexible membrane (green surface) at an instant in time. U is the oncoming flow velocity. There is also a vortex wake (light green surface) emanating from the membrane's trailing edge. The leading edge of the membrane with position $(x(-1,t), y(-1,t))$ is attached to springs (red coils) of spring constant k_s whose other ends are fixed at $(0,0)$ for all time. The membrane's trailing edge with position $(x(1,t), y(1,t))$ is attached to another spring whose other end is fixed at $(2,0)$.

We solve for the four endpoint unknowns ($x_{\pm1}$, $y_{\pm1}$) with four boundary conditions. At the membrane-spring contact, the tension forces must be equal in magnitude and direction to avoid infinite acceleration at the membrane ends, as for the rod tethers. Here the forces are equal in magnitude when:

$$k_s\sqrt{x_{-1}^2+y_{-1}^2}=T_{-1} \quad \text{and} \quad k_s\sqrt{(x_1-2)^2+y_1^2}=T_1. \tag{4.14}$$

Here $T_{\pm1}$ is the tension force at $\alpha=\pm1$ and $\sqrt{x_{-1}^2+y_{-1}^2}$ is the stretch of the spring (change in length from its rest length, zero). The directions of the tensions in the membrane and springs are equal if the slopes of the membrane and springs are equal:

$$\left.\frac{\partial_\alpha y}{\partial_\alpha x}\right|_{\alpha=-1}=\frac{y_{-1}-0}{x_{-1}-0} \quad \text{and} \quad \left.\frac{\partial_\alpha y}{\partial_\alpha x}\right|_{\alpha=1}=\frac{0-y_1}{2-x_1}. \tag{4.15}$$

When we simulate the spring-tethered membrane for various k_s, we find that for sufficiently large k_s, the membrane behaves like the fixed–fixed case, converging to a steady single-hump shape when the flat state is unstable. As we decrease k_s, the single hump solution continues until a threshold value of k_s (near unity) where the membrane develops a sharp spike at the trailing edge at early times and the simulations fail to converge beyond a short time. Unlike the inextensible-rod tethers, here the springs are too soft to ensure that the membrane remains under tension during the dynamics, and the membrane equation is ill-posed under compression [188].

4.3.2 Vertical Hookean Springs

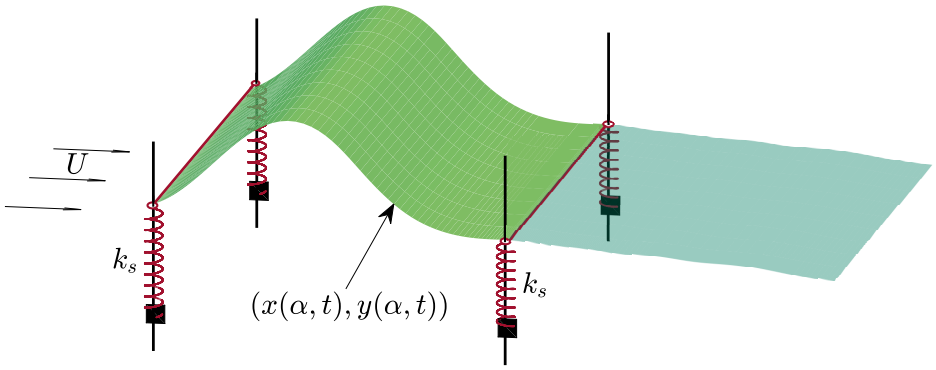

Figure 4.13: Schematic diagram of a flexible membrane (green surface) at an instant in time. U is the oncoming flow velocity. There is also a vortex wake (light green surface) emanating from the membrane's trailing edge. The leading edge of the membrane with position $(0, y(-1,t))$ is attached to vertical springs (red coils) of spring constant k_s whose other end is fixed at (0,0) for all time. The membrane's trailing edge with position $(2, y(1,t))$ is attached to another vertical spring whose other end is fixed at $(2,0)$.

More interesting dynamics occur with springs in an alternative configuration, in which the springs are attached to massless rings that slide along vertical poles, shown in figure 4.13. This is the same as the free–free boundary condition except that the vertical motion is not free but instead resisted by springs. As in the free–free case, the vertical poles ensure that the membrane does not experience significant compression, and thus stable long-time oscillatory dynamics can occur. We will show that this boundary condition is equivalent to that of the inextensible-rod tethers in the limit of small deflections, so it provides an alternative way to understand the effect of the rods. Both the rods and vertical springs allow for a difference in resistance to transverse and in-plane motions, and hence allow for stable oscillatory large-amplitude flutter.

Here, by balancing the vertical forces on the rings, we obtain the mixed boundary

conditions:

$$T_{-1}\left.\frac{\partial_\alpha y}{\partial_\alpha s}\right|_{\alpha=-1} - k_s y_{-1} = 0 \quad \text{and} \quad -T_1\left.\frac{\partial_\alpha y}{\partial_\alpha s}\right|_{\alpha=1} - k_s y_1 = 0. \tag{4.16}$$

The free–free case corresponds to $k_s = 0$ (chapter II). The fixed–fixed case ($y(-1,t) = y(1,t) = 0$) occurs when $k_s \to \infty$. The remaining boundary conditions are $x_{\pm1} = 2$, due to the poles.

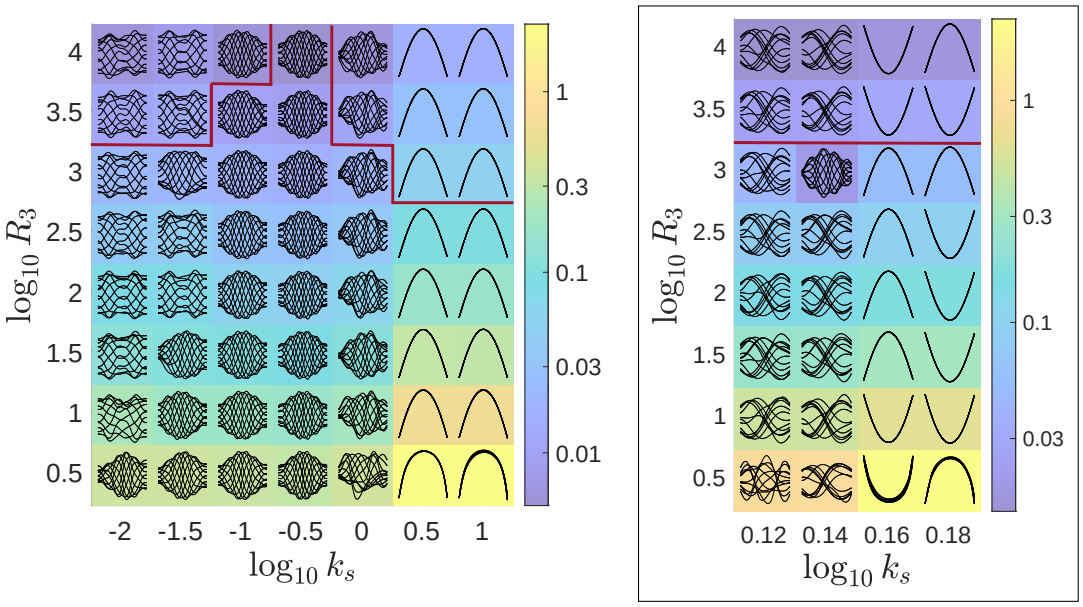

Figure 4.14: (Vertical springs) Snapshots of large-amplitude membrane motions in k_s-R_3 space for fixed $T_0 = 10^{-2}$ and $R_1 = 10^{-0.5}$. Colors represent the time-averaged deflection of membranes defined by (4.11). Oscillatory ($k_s \le 10^0$) and steady single-hump solutions ($k_s \ge 10^{0.5}$) are obtained. At each (k_s, R_3) value, the set of snapshots is scaled to fit within a colored rectangle at the (k_s, R_3) value and normalized by the maximum deflection of the snapshots to show the motions more clearly. The framed panel at right shows a finer grid between $k_s = 10^{0.12}$ and $10^{0.18}$, near the transitional k_s value. The red line separates membranes with $m = 40$ points (above) and $m = 80$ points (below).

In figure 4.14 we show membrane snapshots in the k_s-R_3 parameter space for fixed $T_0 = 10^{-2}$ and $R_1 = 10^{-0.5}$. The shapes are superposed on colors that represent the time-averaged deflections of the membranes [equation (4.11)]. As for the rod tethers, the stretching rigidity R_3 mainly affects the deflection of the membrane, not its shape. For $R_3 = 10^{0.5}$ and $k_s \in [10^{0.5}, 10^1]$ the deflections are so large that vortex shedding might not be confined to the trailing edge in reality, but we include these results

to illustrate the model's behavior. The red line separates simulations with $m = 80$ points (below) and $m = 40$ (above); the smaller value is needed when $R_3 \geq 10^3$ to reach the steady-state regime. When $k_s \geq 10^{0.5}$ the membranes reach the single hump state, as in the fixed–fixed case, and for the rods with $R \leq 10^{-1}$ in figure 4.4.

There is a critical value of k_s at which the membrane transitions from the steady single-hump solutions to oscillatory motions. In the framed panel on the right-hand side of figure 4.14, we show the dynamics close to the transition. From $k_s = 10^0$ to $10^{0.12}$ the membrane shapes become less wavy. At $k_s = 10^{0.12}$ and $10^{0.14}$ they have only one "neck" in their deflection envelopes, apart from $(k_s, R_3) = (10^{0.12}, 10^{0.5})$ and $(10^{0.14}, 10^3)$.

4.4 Linearized Membrane Model

In this section we analyze the small-amplitude behavior of the system described in §4.2. We are able to present the small-amplitude motions of the membranes at a wide range of parameter values (membrane mass and pretension) by computing the eigenvalues and eigenmodes in detail, and after further simplifications, obtain asymptotic scaling laws. The modes resemble the large-amplitude motions qualitatively, and quantitatively in some cases. We consider small deflections $y(x,t)$ from the straight configuration, aligned with the flow. Since the membrane stretching factor is $\partial_\alpha s \approx 1 + \partial_x y^2/2$, to linear order $\alpha \approx s \approx x$, all α-derivatives in (4.4) are x-derivatives, and $\zeta(\alpha,t) \approx \zeta(x,t) = x + iy(x,t)$. At linear order, the tangent and normal vectors are:

$$\hat{\mathbf{s}} \approx (1, \partial_x y)^\top, \quad \hat{\mathbf{n}} \approx (-\partial_x y, 1)^\top. \tag{4.17}$$

The linearized version of the membrane equation (4.4) is

$$R_1 \partial_{tt} y - T_0 \partial_{xx} y = -[p]. \tag{4.18}$$

When considering the linearized problem the term in the tension force $T(\alpha,t) = T_0 + R_3(\partial_\alpha s - 1)$ involving R_3 (dimensionless stretching rigidity) is neglected since it is of quadratic order, and so the linear dynamics are governed by the dimensionless membrane mass R_1 and the dimensionless pretension T_0.

The linearized conditions from §§4.2.1 and 4.3.2 are:

$$\text{Inextensible rods:} \quad x(-1,t) = 0,\ x(1,t) = 2, \tag{4.19}$$
$$\partial_x y(-1,t) = \frac{1}{R} y(-1,t),\ \partial_x y(1,t) = -\frac{1}{R} y(1,t),$$

$$\text{Vertical Hookean springs:} \quad T_0 \partial_x y(-1,t) - k_s y(-1,t) = 0, \tag{4.20}$$
$$-T_0 \partial_x y(1,t) - k_s y(1,t) = 0.$$

We note that the boundary conditions in (4.19) are equivalent to (4.20) with $1/R = k_s/T_0$. In chapter II the boundary conditions were (i) fixed–fixed: $y(\pm 1,t) = 0$, (ii) fixed–free: $y(-1,t) = 0$, $\partial_x y(1,t) = 0$, and (iii) free–free: $\partial_x y(\pm 1,t) = 0$.

The dynamics of the membrane are coupled to the fluid flow through the pressure jump term $[p](x,t)$. The linearized version of the pressure jump equation (4.7) is

$$\partial_t \gamma + \partial_x \gamma = \partial_x [p]. \tag{4.21}$$

The set of equations is closed by relating the vortex sheet strength $\gamma(x,t)$ back to the membrane position $y(x,t)$, through the kinematic condition [equation (4.6)], which in linearized form is:

$$\partial_t y(x,t) = -\partial_x y(x,t) + \frac{1}{2\pi} \int_{-1}^{1} \frac{v(x',t)}{\sqrt{1-x'^2}(x-x')}\, \mathrm{d}x' + \frac{1}{2\pi} \int_{1}^{\ell_w+1} \frac{\gamma(x',t)}{x-x'}\, \mathrm{d}x', \tag{4.22}$$

$-1 < x < 1$. Here, we use that $\partial_t \overline{\zeta}(x,t) \approx -i\partial_t y$ and from (4.17), the normal velocity component is $\mathrm{Re}(\hat{\mathbf{n}} \partial_t \overline{\zeta}) \approx \partial_t y$. The general solution $\gamma(x,t)$ has inverse square-root singularities at $x = \pm 1$ and so we define $v(x,t)$, the bounded part of $\gamma(x,t)$, by

$\gamma = v/\sqrt{1-x^2}$. The second integral in (4.22) represents the velocity induced by the vortex sheet wake, which extends downstream from the membrane on the interval $1 < x < \ell_w + 1$, $y = 0$. Therefore, the eigenvalue problem assumes a free vortex wake of a given fixed length ℓ_w, which we take to be large, 39 here, as in chapter III. In that work, we found that the modes are essentially unchanged at larger values of ℓ_w. This long flat wake corresponds to starting with a deflection that is sufficiently small that we remain in the small-amplitude regime for large times.

The circulation in the wake,

$$\Gamma(x,t) = -\int_x^{\ell_w+1} \gamma(x',t)\,\mathrm{d}x', \tag{4.23}$$

is conserved along material points of the wake by Kelvin's circulation theorem. At linear order, the wake moves at the constant speed (unity) of the free stream; self-interaction is negligible.

At each time t, the total circulation in the wake, $\Gamma(1,t)$, is set by the Kutta condition, i.e.,

$$v(1,t) = 0. \tag{4.24}$$

Using the system of equations (4.18), (4.21), (4.22), and (4.24) we solve for the following unknowns: the motion of the membrane and the strength of the vortex sheets along the membrane and in the wake.

For the linearized system, we may write solutions in the following form:

(4.25)

$$y(x,t) = Y(x)e^{i\sigma t}, \quad \gamma(x,t) = g(x)e^{i\sigma t}, \quad v(x,t) = V(x)e^{i\sigma t}, \quad \Gamma(1,t) = \Gamma_0 e^{i\sigma t},$$

where Y, g, V, and Γ_0 are components of eigenmodes with complex eigenvalues $\sigma = \sigma_\mathrm{R} + i\sigma_\mathrm{I} \in \mathbb{C}$. The real parts of the eigenvalues are the angular frequencies and

the imaginary parts are the temporal growth rates. If $\sigma_{\mathrm{I}} > 0$, small perturbations decay exponentially and the mode is stable, while if $\sigma_{\mathrm{I}} < 0$, small perturbations grow exponentially and the mode is unstable. If $\sigma_{\mathrm{I}} = 0$ the mode is neutrally stable. We wish to identify the region of R_1-T_0 space in which unstable eigenmodes exist, and when there are multiple unstable modes, identify the fastest growing mode.

Since Γ is conserved at material points of the free vortex sheet as they move downstream (at speed 1), and the material point at location $x \geq 1$ at time t was at location $x = 1$ at time $t - (x - 1)$ we can write

$$\Gamma(x,t) = \Gamma_0 e^{i\sigma(t-(x-1))} = \Gamma_0 e^{-i\sigma(x-1)} e^{i\sigma t}, \quad 1 < x < \ell_w + 1, \tag{4.26}$$

$$\gamma(x,t) = \partial_x \Gamma(x,t) = -i\sigma\Gamma_0 e^{-i\sigma(x-1)} e^{i\sigma t}, \quad 1 < x < \ell_w + 1, \tag{4.27}$$

using $\Gamma(1,t)$ from (4.25). Inserting the eigenmodes (4.25) into the governing equations (4.18) and (4.22), yields

$$-\sigma^2 R_1 Y = T_0 \partial_{xx} Y - i\sigma \int_{-1}^{1} g \, \mathrm{d}x - g, \tag{4.28}$$

and

$$i\sigma Y = -\partial_x Y + \frac{1}{2\pi} \int_{-1}^{1} \frac{V(x')}{\sqrt{1-x'^2}(x-x')} \, \mathrm{d}x' - \frac{1}{2\pi} i\sigma\Gamma_0 \int_{1}^{\ell_w+1} \frac{e^{-i\sigma(x'-1)}}{x-x'} \, \mathrm{d}x', \ -1 < x < 1, \tag{4.29}$$

respectively. Because σ appears in the exponential in the second integral in (4.29), this is a nonlinear eigenvalue problem. We solve the nonlinear eigenvalue problem iteratively by the same method as in chapter III.

4.4.1 Eigenmode Analysis of Membranes Attached to Vertical Hookean Springs

For the small-amplitude analysis we focus on membranes attached to vertical Hookean springs, equivalent to rods (shown by equations (4.19) and (4.20) with $1/R = k_s/T_0$).

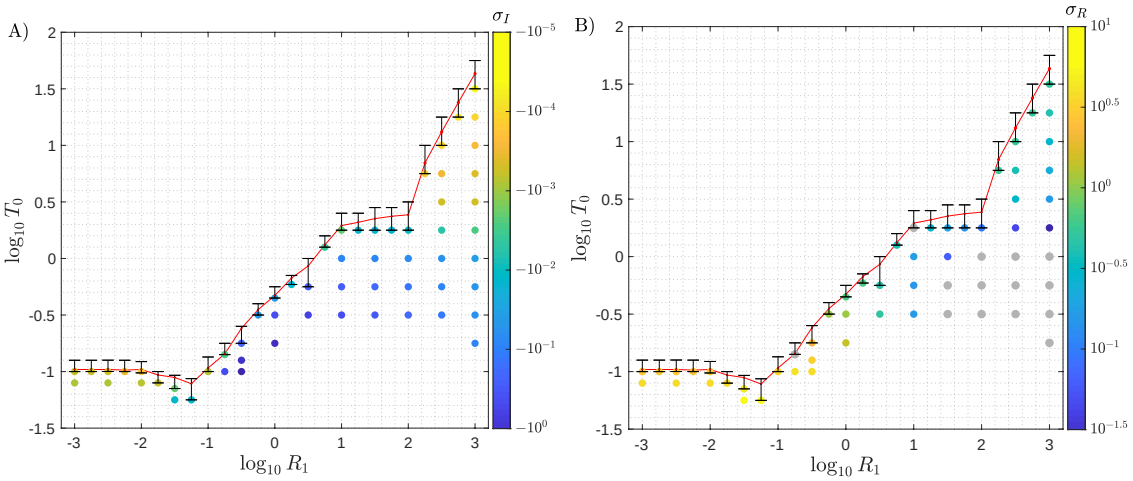

Figure 4.15: (Vertical springs) The region in R_1-T_0 space in which membranes are unstable. The springs attached at the leading and trailing edges of the membrane have spring constant $k_s = 10^{-1}$. The red line and red dots indicate the position of the stability boundary computed using linear interpolation between σ_I of the smallest T_0 that gives a stable membrane and the σ_I of the largest T_0 that gives an unstable membrane (shown in the error bars). The color of the dots below the stability boundary labels: A) The imaginary part of the eigenvalue (σ_I) corresponding to the most unstable modes. It represents the temporal growth rate. B) The real part of the eigenvalues (σ_R) for the most unstable mode, representing the angular frequency. The gray dots correspond to modes that lose stability by divergence and have $\sigma_\mathrm{R} \leq 10^{-9}$.

In figure 4.15 we plot the imaginary (figure 4.15A) and real parts (figure 4.15B) of the most unstable eigenvalues in the region of instability for membranes attached to springs with spring constant $k_s = 10^{-1}$ in R_1-T_0 space. The red line marks the boundary where the eigenvalues change from all $\sigma_\mathrm{I} > 0$ (stable membranes) to at least one $\sigma_\mathrm{I} < 0$ (unstable membranes). The stability boundary moves to larger pretension (T_0) values with increasing membrane mass (R_1), starting at $R_1 = 10^{-1.25}$. As R_1 decreases below $10^{-1.75}$ the critical pretension reaches a lower plateau. Below and to the right of the red line is the unstable region. The red dots that mark the stability boundary are computed by linear interpolation of σ_I between neighboring T_0 values (shown by the horizontal black bars) that bracket the boundary: all σ_I are positive at the larger of the T_0 values and above, but one σ_I is negative at the smaller of the T_0 values. The gray dots in figure 4.15B indicate negative σ_I and nearly zero σ_R ($\sigma_\mathrm{R} \leq 10^{-9}$) for the most unstable eigenmode, which corresponds to divergence

without flutter; they occur at $(R_1, T_0) = (10^{-0.75}, 10^{-0.85})$, $(10^1, 10^{0.25})$, and several cases with $R_1 \geq 10^{1.5}$ and $T_0 \leq 10^0$. The colored dots in figure 4.15B indicate a nonzero real part (value in color bar at right) for the most unstable eigenmode, corresponding to flutter and divergence.

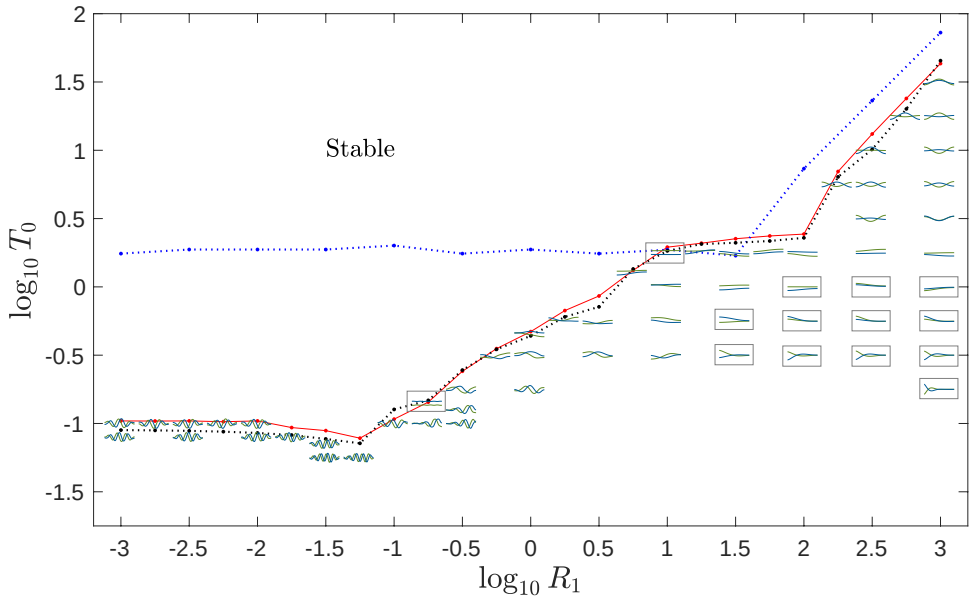

Figure 4.16: (Vertical springs) The shapes $Y(x)$ of the most unstable eigenmode as a function of R_1 and T_0 with springs that have a spring stiffness of $k_s = 10^{-1}$. The real part of $Y(x)$ is shown in green and the imaginary part of $Y(x)$ is shown in blue. Each shape is scaled, both vertically and horizontally, to fit within the plot. Modes exhibiting a divergence instability have a gray rectangle outline. The shapes are superposed on the same stability boundary (red line) as in figure 4.15. The blue dotted line represents the stability boundary for fixed–fixed membranes and the black dotted line represents the stability boundary for free–free membranes from chapter III. We include them here for comparison.

In figure 4.16 we examine the variations in the most unstable eigenmodes in the same (R_1, T_0) space as figure 4.15, corresponding to the eigenvalues shown there. We also include our results from chapter III (figures 3.5 and 3.13) for the stability boundary when both ends of the membrane are fixed (dotted blue line) and when both ends of the membrane are free (dotted black line). The real part of the eigenmode $Y(x)$ is shown in green and the imaginary part of $Y(x)$ is shown in blue. We place gray rectangles around the modes that lose stability by divergence. The shapes do

not change noticeably for the wavier motions at $R_1 \in [10^{-3}, 10^{-2}]$. At these small R_1 values the deflection at the trailing edge is nearly zero. With R_1 increased to $(10^{-1}, 10^{-0.25})$, however, the maximum deflection occurs at the trailing edge of the membrane in most cases. Here and at some larger values of R_1, the mean slope of the membrane is nonzero. When $R_1 \in [10^{1.25}, 10^3]$ and $T_0 = 10^{0.25}$ the modes are nearly alike and their growth rates (σ_{I}, figure 4.15A) and angular frequencies (σ_{R}, figure 4.15B) are almost equal.

In the limit $R_1, T_0 \gg 1$, the fluid pressure is negligible and the linearized membrane equation reduces to the homogeneous wave equation

$$R_1 \partial_{tt} y - T_0 \partial_{xx} y = 0, \tag{4.30}$$

which after substituting the form of $y(x,t)$ from (4.25) becomes

$$-\sigma^2 R_1 Y - T_0 \partial_{xx} Y = 0. \tag{4.31}$$

The eigenmodes are combinations of $\cos(kx)$ and $\sin(kx)$, with $k = \pm\sigma\sqrt{R_1/T_0}$, satisfying the two boundary conditions in (4.20). We find k by determining where the determinant of the matrix

$$\begin{pmatrix} -kT_0 \sin(-k) - k_s \cos(-k) & kT_0 \cos(-k) - k_s \sin(-k) \\ kT_0 \sin(k) - k_s \cos(k) & -kT_0 \cos(k) - k_s \sin(k) \end{pmatrix} \tag{4.32}$$

vanishes, which occurs if $k \sin(k) - (k_s/T_0)\cos(k) = 0$ or $k\cos(k) + (k_s/T_0)\sin(k) = 0$. The numerical solutions of these two nonlinear equations for $k_s = 10^{-1}$ and $T_0 = 10^1$ are:

(4.33)

$$k = 0.0998,\ 1.5771,\ 3.1448,\ 4.7145,\ 6.2848,\ 7.8553,\ 9.4258,\ 10.9965,\ 12.5672.$$

The eigenmodes are given by

$$Y(x) = \cos(k(x+1)) + \left(\frac{k_s}{T_0}\right)\frac{1}{k}\sin(k(x+1)), \tag{4.34}$$

with k from (4.33), for $-1 \leq x \leq 1$. Heavy membranes ($R_1 > 10^2$) with T_0 between $10^{0.25}$ and $T_{0C}(R_1)$ (i.e., the stability boundary) all lose stability with the third mode, $k = 3.1448$ in (4.34).

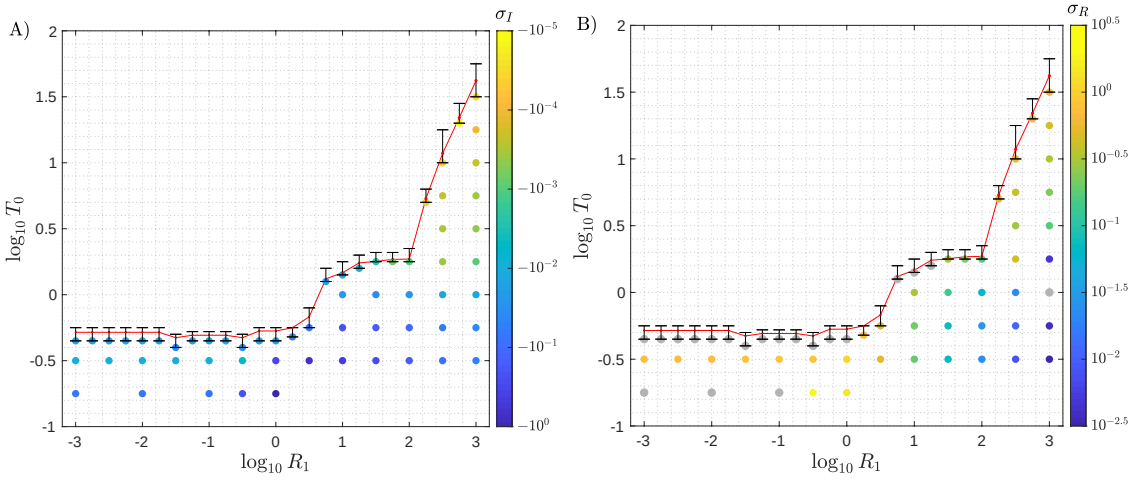

Figure 4.17: (Vertical springs) Same as figure 4.15 but with $k_s = 10^0$.

We now consider the analogous results when the Hookean spring constant is increased to $k_s = 10^0$. The stability boundary is shown as the red dots connected by red lines in figures 4.17A and 4.17B. As with $k_s = 10^{-1}$, the stability boundary moves to larger pretension (T_0) values with increasing membrane mass (R_1), starting at $R_1 = 10^2$. Now the critical pretension reaches a lower plateau at $R_1 = 10^0$ and below. The gray dots in figure 4.17B again indicate divergence without flutter (negative σ_{I} and nearly zero σ_{R} ($\leq 10^{-9}$) for the most unstable eigenmode). We observe this for all $R_1 \leq 10^0$ and $R_1 \in [10^{0.75}, 10^{1.25}]$ close to the stability boundary, as well as for $(R_1, T_0) = (10^3, 10^0)$ and $R_1 \in [10^{-3}, 10^{-1}]$ with $T_0 = 10^{-0.75}$. Therefore, an increase in the spring stiffness not only changes the location and shape of the stability boundary but also leads to more instances of the divergence instability at smaller R_1 and fewer at larger R_1.

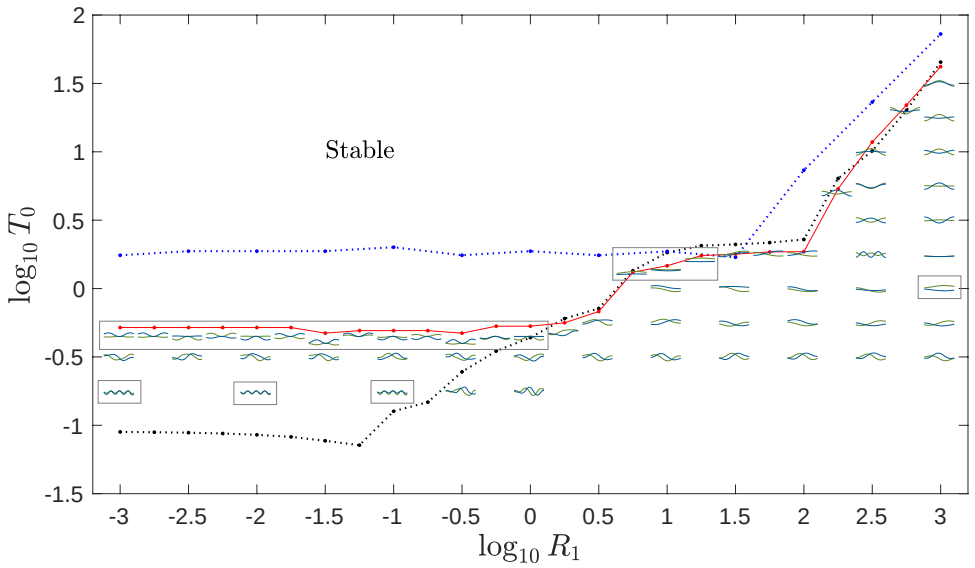

Figure 4.18: (Vertical springs) Same as figure 4.16 but with $k_s = 10^0$.

The corresponding eigenmodes are shown in figure 4.18. The critical pretension for $R_1 < 10^0$ is larger for $k_s = 10^0$ than for $k_s = 10^{-1}$ and lies almost midway between the stability boundary for fixed–fixed membranes ($k_s \to \infty$, blue dotted line) and for free–free membranes ($k_s = 0$, black dotted line). The mode shapes of light membranes $R_1 \leq 10^0$ close to the stability boundary have three extrema and are mostly symmetric. The shapes do not vary noticeably with R_1 at these R_1 values. The eigenvalues in figure 4.17 were also nearly constant in this region for fixed T_0. In general, as T_0 decreases the most unstable mode changes to a "wavier" profile at small R_1. However, there are exceptions: the membrane modes at $R_1 \geq 10^1$ and $T_0 = 10^0$ all have a similar shape (small but nonzero mean slope) but the associated eigenvalues vary more significantly there, as can be seen from figure 4.17.

Using $k_s = 10^0$ and $T_0 = 10^1$ we have that the determinant of (4.32) vanishes when

(4.35)

$$k = 0.3111,\ 1.6320,\ 3.1731,\ 4.7335,\ 6.2991,\ 7.8667,\ 9.4354,\ 11.0047,\ 12.5743.$$

When the mass density is between $10^{0.75}$ and 10^2 (especially close to the boundary), the membranes are similar in shape to those with $k_s = 10^{-1}$. The modes for heavy membranes ($R_1 > 10^2$), with T_0 between $10^{0.5}$ and $T_{0C}(R_1)$, all lose stability again with the third mode, $k = 3.1731$ in (4.34).

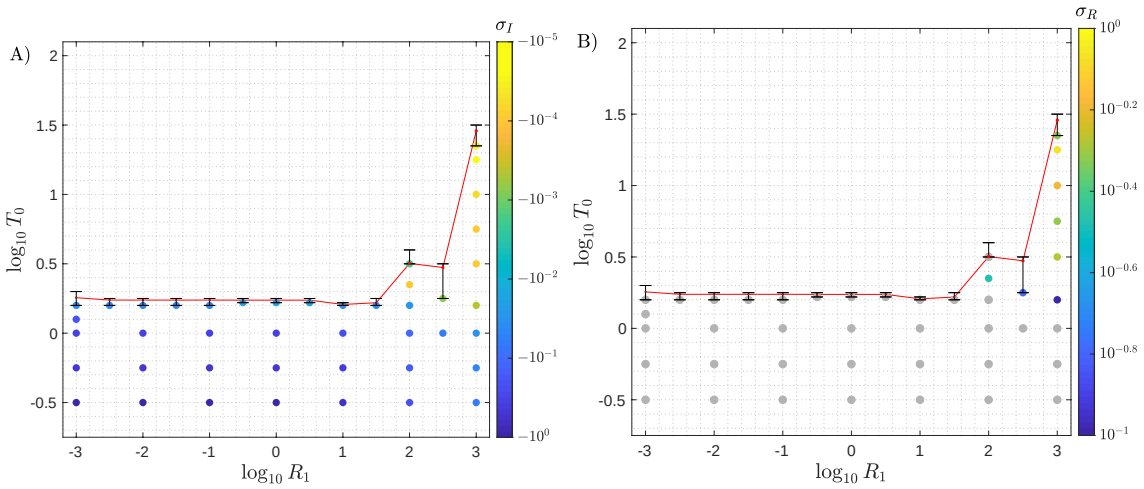

Figure 4.19: (Vertical springs) Same as figure 4.15 but with $k_s = 10^1$.

Increasing k_s further to 10^1 we approach the small-amplitude dynamics of a membrane whose edges are both fixed at zero deflection. In figure 4.19 the colored dots give the imaginary (figure 4.19A) and real parts (figure 4.19B) of the most unstable eigenvalues (with corresponding eigenmodes shown later, in figure 4.20). There are now many more cases of divergence without flutter (gray dots in figure 4.19B). At $R_1 > 10^2$ with $T_0 > 10^0$, divergence with flutter occurs (colored dots in figure 4.19B).

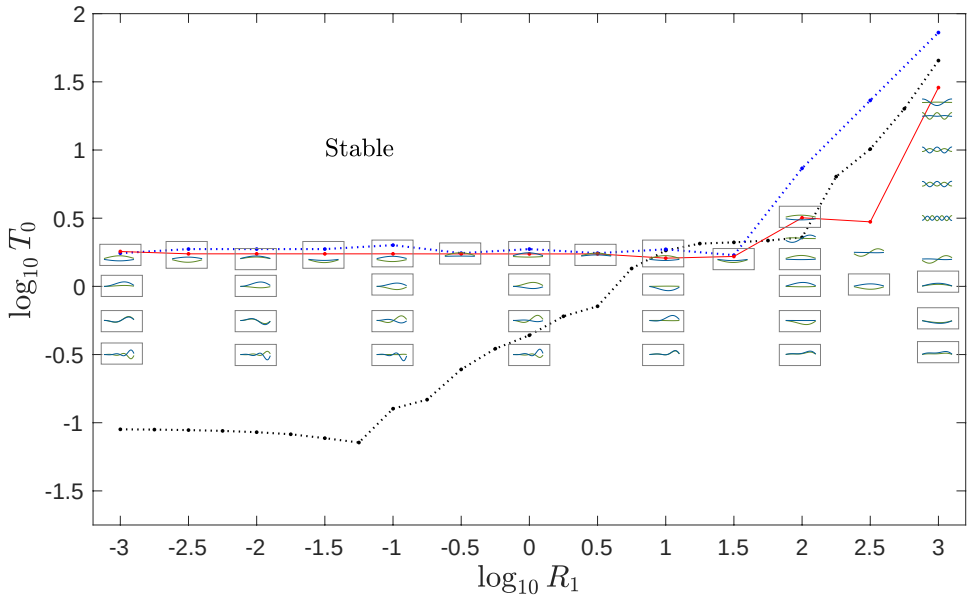

Figure 4.20: (Vertical springs) Same as figure 4.16 but with $k_s = 10^1$.

In figure 4.20 we see that the critical pretension for $R_1 \leq 10^{1.5}$ is almost the same as the stability boundary for fixed–fixed membranes ($k_s \to \infty$, blue dotted line in figure 4.18). We place gray rectangles around the modes that lose stability by divergence. The shapes are also similar to the ones seen for a fixed–fixed membrane: For $R_1 < 10^2$ and T_0 just below T_{0C}, the unstable eigenmode is a single-hump shape that is nearly fore-aft symmetric. As the pretension is decreased further below T_{0C} (at $T_0 = 10^0$ and $R_1 < 10^{2.5}$) the divergent eigenmode becomes asymmetric, its maximum deflection point shifting towards the trailing edge. As the membrane mass (R_1) is increased to $10^{2.5}$, the maximum camber point moves towards the midchord and the membrane shape becomes almost fore-aft symmetric. At a smaller T_0 ($10^{-0.25}$) the membranes still lose stability by divergence but there is now an inflection point approximately at the membrane's midchord, with the maximum point on the membrane being closer to the aft part. Even though the membrane mode shapes generally look very similar to the fixed–fixed membranes in chapter III (figure 3.5) when $k_s = 10^1$,

this is not the case for $R_1 > 10^{2.5}$. The critical pretension in figure 4.20 starts to increase when $R_1 \gtrsim 10^2$ as opposed to a smaller mass, i.e., $R_1 \gtrsim 10^{1.5}$ for fixed–fixed membranes, and the mode shapes there are also very different. As for the other k_s values, here we use $k_s = 10^1$ and for a fixed value of T_0 determine the value of k such that the determinant of (4.32) is equal to zero. In figure 4.20 the first membrane that becomes unstable just below the stability boundary (at $T_0 = 10^{1.35}$) is approximately the third sinusoidal mode ($k = 3.28$). At $T_0 = 10^1$ and $10^{0.5}$ the most unstable modes are approximately the fifth and seventh sinusoidal modes ($k = 6.44$ and 9.74, respectively). The trend of odd-numbered modes does not continue when $T_0 < 10^{0.5}$.

To summarize, we have found that the stability boundary has an upward slope for large R_1, whereas for small-to-moderate R_1 values, the critical T_0 is smaller. At small R_1 the critical pretension for instability reaches a plateau value that depends on the spring stiffness. When R_1 and T_0 are dominant over fluid pressure forces, the membrane eigenmodes tend to neutrally-stable sinusoidal functions. Increasing the spring stiffness k_s introduces more divergence instabilities, in agreement with the fixed–fixed case studied in chapter III. In general, the most unstable modes become more wavy at smaller T_0 and small R_1. The nonlinear eigenvalue problem for the linearized membrane model has allowed us to extend results from the large-amplitude model in §4.3 to a wider range of R_1-T_0 space. Next, we study a more analytically tractable model—that of an infinite, periodic array of springs attached to an infinite membrane. This model allows us to compute solutions for a much wider range of parameters and obtain asymptotic scaling laws.

4.5 Periodic Array of Springs on an Infinite Membrane

We have seen that the eigenvalue problem for a membrane tethered with springs (or rods) interpolates between the fixed–fixed and free–free cases. The vortex sheet wake results in a nonlinear eigenvalue problem, requiring an iterative solver that is time-consuming, particularly at small T_0. We now consider a simplified model with spatially periodic solutions that will allow us to derive asymptotic scaling laws. We assume the membrane extends to infinity upstream and downstream, and is tethered by an infinite, periodic array of Hookean springs (with stiffness k_s). The horizontal spacing between the springs (unity) is analogous to the length of the finite membrane in the previous section. This problem is shown schematically in figure 4.21, where the green surface represents a section of the infinite membrane at an instant in time and the pairs of red coils on either side of the membrane span represent the springs. The membrane has period L. By taking L larger than the distance between the springs, the infinite periodic membrane may have different deflections at streamwise-adjacent spring locations, as occurs for the tethered finite membrane. As L increases, the membrane can assume a wider range of shapes, but the eigenvalue problem becomes more costly to solve. We choose $L = 4$ as a compromise between these competing considerations. The flow velocity is again uniform at infinity (far above and below the membrane). With an infinite membrane there is no free vortex wake, and the nonlinear eigenvalue problem is reduced to a quadratic eigenvalue problem, which has analytic solutions for the eigenvalues when $k_s = 0$. In [128] a related approximate model was considered—an infinite membrane with two- and three-harmonic truncations that were used to approximate fixed–fixed boundary conditions.

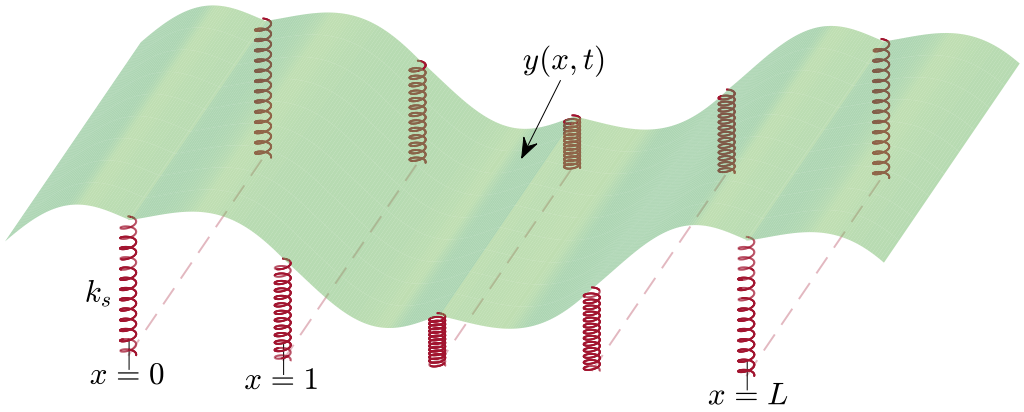

Figure 4.21: Schematic diagram of a section of an infinite, flexible membrane (green surface) at an instant in time. Here L is the x-period of the membrane, $y(x,t)$ is the membrane deflection and the red springs of stiffness k_s are spaced one unit apart. The distance between springs is smaller than the membrane's period ($L > 1$, $L \in \mathbb{N}$).

The system of governing equations is:

$$R_1 \partial_{tt} y - T_0 \partial_{xx} y = -[p] - k_s y(x,t)\delta_1(x), \tag{4.36}$$

$$\partial_t y + \partial_x y = \frac{1}{2\pi} \int_{-\infty}^{\infty} \frac{\gamma(x',t)}{x - x'} \, \mathrm{d}x', \tag{4.37}$$

$$\partial_t \gamma + \partial_x \gamma = \partial_x [p]. \tag{4.38}$$

In (4.36), $\delta_1(x)$ is a periodic Dirac delta function with period one, resulting in a spring force at each integer x, and proportional to $y(x,t)$, the vertical deflection there. We next write the membrane position, vortex sheet strength, and pressure jump across the membrane, each as a Fourier series with period L, and the periodic Dirac delta function as a Fourier series with period one:

$$y(x,t) = \sum_{k=-\infty}^{\infty} \hat{y}_k e^{i(2\pi k/L)x} e^{i\sigma t}, \quad \gamma(x,t) = \sum_{k=-\infty}^{\infty} \hat{\gamma}_k e^{i(2\pi k/L)x} e^{i\sigma t}, \tag{4.39}$$

$$[p](x,t) = \sum_{k=-\infty}^{\infty} \widehat{[p]}_k e^{i(2\pi k/L)x} e^{i\sigma t}, \quad \delta_1(x) = \sum_{k=-\infty}^{\infty} e^{i(2\pi k)x}, \tag{4.40}$$

respectively, where $\hat{y}_k$, $\hat{\gamma}_k$, $\widehat{[p]}_k$ are complex Fourier coefficients to be found.

Using equations (4.39) and (4.40), the membrane equation (4.36) can be written

as

$$\sum_{k=-\infty}^{\infty}\left(-\sigma^2 R_1\hat{y}_k + T_0\left(\frac{2\pi k}{L}\right)^2\hat{y}_k\right)e^{i(2\pi k/L)x} = -\sum_{k=-\infty}^{\infty}\widehat{[p]}_k e^{i(2\pi k/L)x}$$

$$-k_s\sum_{k'=-\infty}^{\infty}\hat{y}_{k'}e^{i(2\pi k'/L)x}\sum_{k''=-\infty}^{\infty}e^{i(2\pi k'')x}, \tag{4.41}$$

having divided throughout by the common factor $e^{i\sigma t}$. Substituting equations (4.39) into (4.37), we obtain

$$\sum_{k=-\infty}^{\infty}\left(i\sigma + i\frac{2\pi k}{L}\right)\hat{y}_k e^{i(2\pi k/L)x}e^{i\sigma t} = \sum_{k=-\infty}^{\infty}-\frac{i}{2}\mathrm{sgn}\left(\frac{2\pi k}{L}\right)\hat{\gamma}_k e^{i(2\pi k/L)x}e^{i\sigma t}, \tag{4.42}$$

which implies that

$$i\left(\sigma + \frac{2\pi k}{L}\right)\hat{y}_k = -\frac{i}{2}\mathrm{sgn}\left(\frac{2\pi k}{L}\right)\hat{\gamma}_k. \tag{4.43}$$

Similarly, if we substitute equations (4.39) and (4.40) into (4.38), we get

$$i\left(\sigma + \frac{2\pi k}{L}\right)\hat{\gamma}_k = i\frac{2\pi k}{L}\widehat{[p]}_k. \tag{4.44}$$

Using equations (4.43) and (4.44) in (4.37) and in (4.38), we obtain

$$\hat{\gamma}_k = -2\mathrm{sgn}\,(k)\left(\sigma + \frac{2\pi k}{L}\right)\hat{y}_k, \tag{4.45}$$

$$\widehat{[p]}_k = -\frac{L}{\pi|k|}\left(\sigma + \frac{2\pi k}{L}\right)^2\hat{y}_k, \tag{4.46}$$

respectively, where we use that $\mathrm{sgn}\,(2\pi k/L) = \mathrm{sgn}(k)$ and thus write (4.41), in terms of $\hat{y}_k$ only, as

$$\sum_{k=-\infty}^{\infty}\left(-\sigma^2 R_1 + T_0\left(\frac{2\pi k}{L}\right)^2\right)\hat{y}_k e^{i(2\pi k/L)x} = \sum_{k=-\infty}^{\infty}\frac{L}{\pi|k|}\left(\sigma + \frac{2\pi k}{L}\right)^2\hat{y}_k e^{i(2\pi k/L)x}$$

$$-k_s\sum_{k'=-\infty}^{\infty}\hat{y}_{k'}\left(\sum_{k''=-\infty}^{\infty}e^{i(2\pi(k''L+k')/L)x}\right). \tag{4.47}$$

We match coefficients of $e^{i(2\pi k/L)x}$ in (4.47) and obtain

$$\left(-R_1 - \frac{L}{\pi|k|}\right)\sigma^2\hat{y}_k - \frac{4k}{|k|}\sigma\hat{y}_k + \left(\frac{2\pi k}{L}\right)^2\left(T_0 - \frac{L}{\pi|k|}\right)\hat{y}_k + k_s\sum_{k'\equiv k \bmod L}\hat{y}_{k'} = 0, \tag{4.48}$$

for $k = -N, \ldots, -1, 1, \ldots, N$. The last sum in (4.48) includes those k' that are equal to k plus a multiple of L. If we make the truncation approximation that $\hat{y}_k = 0$ for $|k| > N$ then (4.48) is a system of $2N+1$ equations in $2N+1$ unknowns $\hat{y}_k$. In the derivation we assumed $k \neq 0$. From (4.43) we see that $\hat{y}_0 = 0$ (Hilbert transform of a constant is equal to zero). Therefore, we insert 0 for $\hat{y}_0$ in the system of equations and remove $\hat{y}_0$ from the unknowns, resulting in $2N$ equations in $2N$ unknowns.

Equation (4.48) is a quadratic eigenvalue problem of the form

$$(A_2\sigma^2 + A_1\sigma + A_0)\hat{\mathbf{y}} = 0, \tag{4.49}$$

where A_2 and A_1 are diagonal matrices, A_0 is a rank-L matrix, and $\hat{\mathbf{y}}$ is the eigenvector of Fourier coefficients $\{\hat{y}_k, k = -N, \ldots, -1, 1, \ldots, N\}$. Using `polyeig` in MATLAB we solve for the eigenvalues σ and determine the fastest growing eigenmode, i.e., corresponding to the most negative σ_{I}.

In figure 4.22 we show the imaginary parts of the most unstable modes for the periodic membrane problem, over one period $0 \leq x \leq 4$, and thus with 4 subintervals between springs shown. In a few examples (at the corners) in panels A–D, we show the locations of the springs by small red lines. In many (but not all cases), the shapes seem to repeat 4 times. This is particularly true at larger k_s, where the springs are stronger and impose a period-1 component more strongly in the eigenmode. The real parts are similar and are omitted. Membranes that lose stability by divergence without flutter are again outlined with gray rectangles. We compute the relative error in the eigenvalues when $N = 2^8$ and 2^9:

$$\text{relative error} = \left| \frac{\sigma_{2^8} - \sigma_{2^9}}{\sigma_{2^9}} \right|. \tag{4.50}$$

The maximum relative error is small for the cases in figure 4.22: 0.0437 when $R_1 = 10^{-4}$ (figure 4.22A), 0.0269 when $R_1 = 10^{-1}$ (figure 4.22B), 0.00267 when $R_1 = 10^{0}$

(figure 4.22C), and 1.31×10^{-5} when $R_1 = 10^4$ (figure 4.22D).

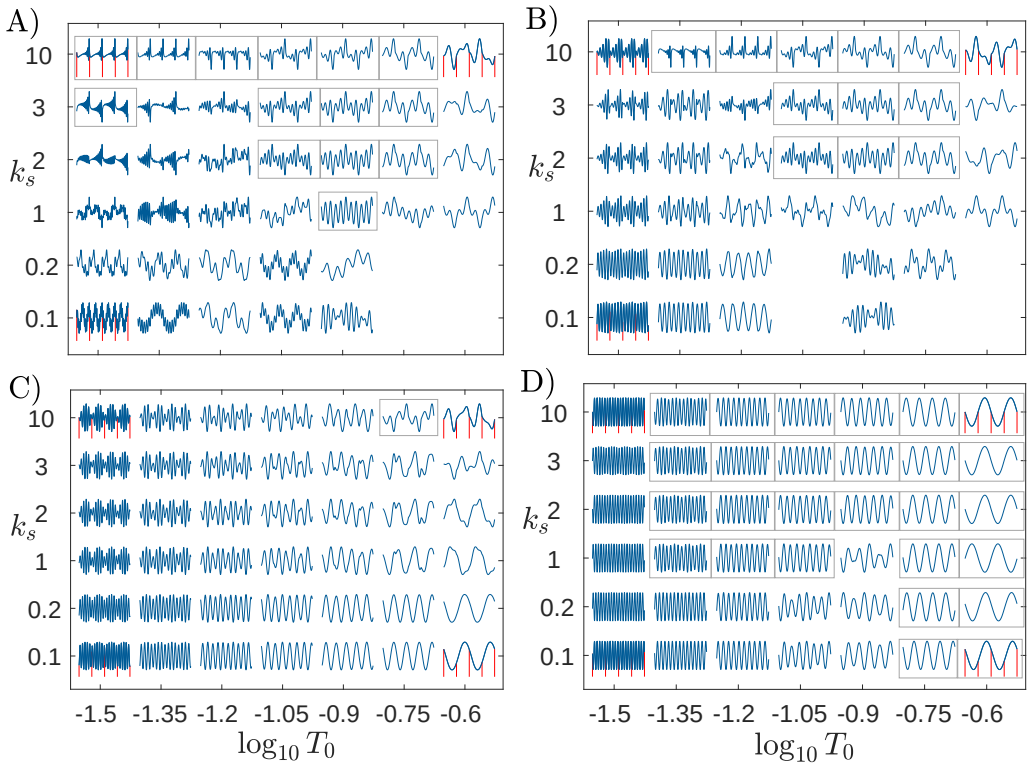

Figure 4.22: Imaginary part of the most unstable eigenmode [Im($y(x)$)] in T_0-k_s parameter space for A) $R_1 = 10^{-4}$, B) $R_1 = 10^{-1}$, C) $R_1 = 10^0$, and D) $R_1 = 10^4$. Modes exhibiting a divergence instability with $\sigma_{\mathrm{R}} \leq 10^{-9}$ have a gray rectangle outline. In all the panels, we use $N = 2^9$.

The periodic membrane modes do not align precisely with those in the membrane-vortex-wake model due to the different membrane boundary conditions (periodic versus finite with a trailing vortex wake). However, there are many qualitative similarities. In both cases, the modes become sharper (or wavier) as we decrease T_0. At large R_1 the membranes are more sinusoidal with single bumps between the springs at large values of T_0 (in figure 4.22D for the periodic membrane). At small R_1 (figures 4.22A and 4.22B), the membranes are less sinusoidal and less symmetric. Another similarity at small R_1 is that increasing the spring stiffness k_s causes the maximum deflection point of the membrane to move downstream (to the right) with sharp peaks close to the spring locations (figures 4.22A and 4.22B as well as fig-

ure 4.16). Also true for both models is that the stability boundary shifts to lower T_0 at small R_1 and small k_s. As a result, at some locations in the lower right of panels A and B, membranes are omitted because all modes are stable, unlike at the corresponding locations in panels C and D (where R_1 is larger).

The membrane deflections at the springs increase when R_1 and T_0 increase relative to k_s. This can be seen by moving from left to right in some of the rows of figures 4.22A–C (i.e., increasing T_0 at fixed k_s), such as $k_s = 10^0$ in panel C. The same trend is seen moving from panel A to B to C to D, at the same location in each panel, i.e., increasing R_1 with k_s and T_0 fixed. A similar phenomenon was seen in the membrane-vortex-wake model.

In figure 4.23 we plot the imaginary parts of the most unstable eigenvalues as colored dots in the region of instability for membranes attached to a periodic array of springs with spring constants $k_s = 0$ (figure 4.23A), $k_s = 10^{-1}$ (figure 4.23B), $k_s = 10^0$ (figure 4.23C), and $k_s = 10^1$ (figure 4.23D). When $k_s = 0$, equations (4.48) become decoupled scalar quadratic equations which can be solved analytically. The resulting σ_{I} are plotted in figure 4.23A. In figures 4.23B–D, $k_s \neq 0$, and we use the aforementioned MATLAB eigenvalue solver. With 2^9 modes, the results are resolved only in a small portion of figure 4.23A—a subset of the region within the red rectangle. The axis limits of panels B–D coincide with the red rectangle. Both the analytical results in panel A and the computed results in panels B–D are much easier to obtain than in the case of the membrane-vortex-wake model, so the data in all the panels of figure 4.23 are much more extensive than in figures 4.15, 4.17, and 4.19, a key advantage of the infinite-membrane model.

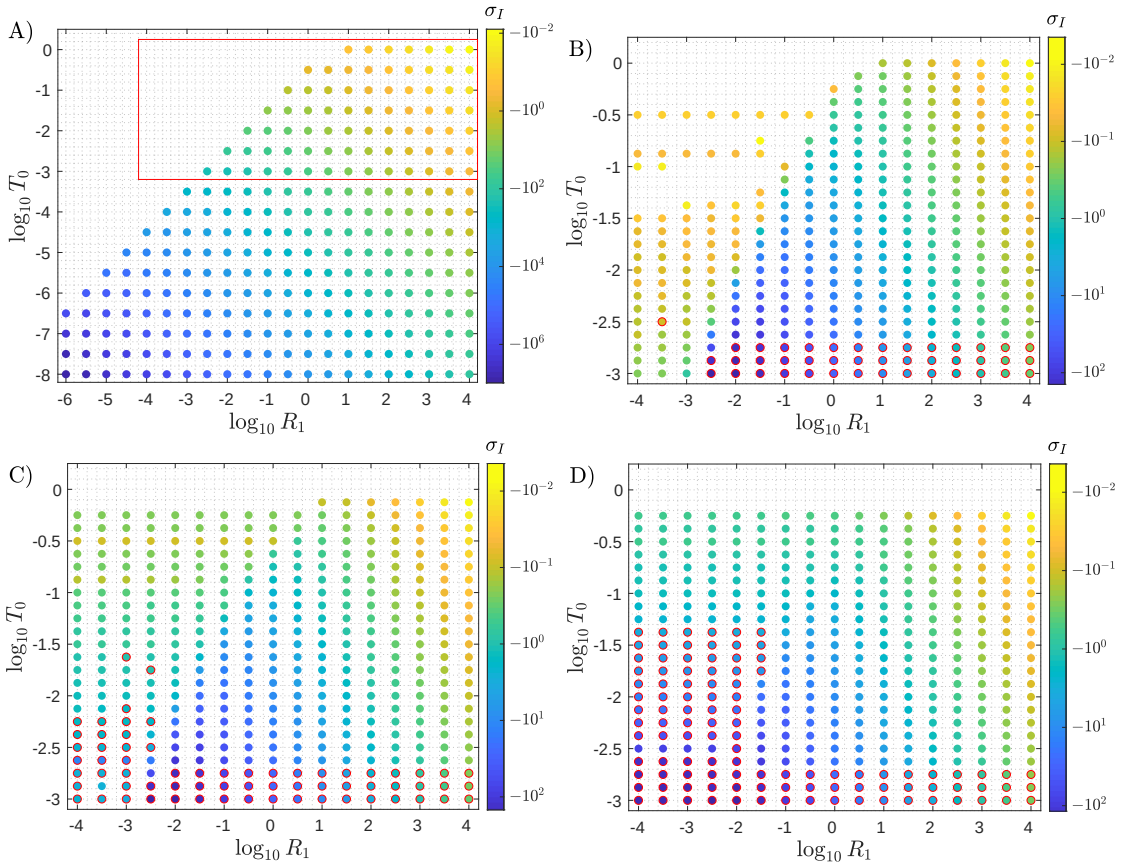

Figure 4.23: (Infinite, periodic membrane) The region in R_1-T_0 space in which membranes are unstable. The color of the dots in the instability region labels the imaginary part of the eigenvalues (σ_{I}) corresponding to the most unstable modes. It represents the growth rate. The springs have stiffness values of: A) $k_s = 0$ (analytical result), B) $k_s = 10^{-1}$, C) $k_s = 10^{0}$, and D) $k_s = 10^{1}$. The numerical results shown in panels B–D are with $N = 2^9$. The red rectangle in panel A indicates the region we consider in panels B–D to facilitate comparison. The red outline on some of the colored dots indicates the cases where convergence with respect to N (as defined by (4.50)) was not obtained.

For this periodic problem, we see that the stability boundary at large R_1 plateaus, independent of the value of k_s, i.e., the critical pretension (T_0) is the same for all $R_1 \gtrsim 10^1$ instead of increasing with increasing mass as in the vortex-wake model (figures 4.15, 4.17, and 4.19). Although the stability boundaries differ at large R_1, here the vortex-wake model's eigenvalues are only slightly unstable [$\sigma_{\mathrm{I}} = O(10^{-5})$] compared to neutrally stable ($\sigma_{\mathrm{I}} = 0$) in the infinite membrane model.

We see that for smaller R_1 ($< 10^0$), the stability boundary in figure 4.23A is close to the diagonal line $T_0 = R_1$, and we will show this asymptotically in the next

section. In panels B–D ($k_s \neq 0$), this line is no longer the stability boundary, but is instead the location of a sharp change in σ_{I}, shown by the sharp change in colors moving across this line, particularly in panel B and less so in C and D.

From the colors of the dots in all the panels we see that if we fix R_1 and decrease T_0, the growth rate σ_{I} becomes larger in magnitude (value in color bar at right). If we fix T_0 and increase R_1 above T_0, the growth rate σ_{I} becomes smaller in magnitude which implies slower growth of instabilities.

In figure 4.23B, $k_s = 10^{-1}$ as in figure 4.15A for the membrane-vortex-wake model. There are two main points of qualitative agreement between the models in this case. One is that a lower plateau of the stability boundary occurs at small R_1; another is that the growth rates are much lower for $R_1 < T_0$. At this k_s value (10^{-1}) and at small R_1 and T_0 close to the stability boundary (e.g., at $T_0 = 10^{-0.5}$ and $10^{-0.875}$, for $R_1 \lesssim 10^{-2}$), there are also a few narrow bands of instability (lines of yellow dots) between stable regions, which was not observed in the membrane-vortex-wake model (figure 4.15A). Moving to figure 4.23C, k_s is increased to 10^0, and the stable regions in panel B surrounding the isolated bands become unstable in panel C, with larger growth rates than in the bands. Therefore, the stability boundary in panel C is almost at constant T_0 for all R_1, with a very small increase when $R_1 \geq 10^1$. An upward shift in the lower plateau is also seen in the vortex-wake model with the same increase in k_s, moving from figure 4.15A to figure 4.17A. Increasing k_s further to 10^1 (figure 4.23D) in the periodic membrane model these trends continue: the stability boundary is horizontal at $T_{0C} \approx 10^{-0.25}$ (a factor of ≈ 3 smaller than T_{0C} in the small-to-moderate R_1 region of figure 4.19), and the growth rates have increased further where $R_1 < T_0$. In figures 4.23B–D as T_0 decreases, $N = 2^9$ is eventually too small to resolve the most unstable eigenmodes. These cases are shown by red

outlines around the colored dots, and become more prevalent as we move from panel B to C to D. These cases correspond to an eigenvalue relative error (as defined in equation (4.50))$> 3 \times 10^{-2}$ (chosen somewhat arbitrarily; other values give a similar classification of nonconvergence).

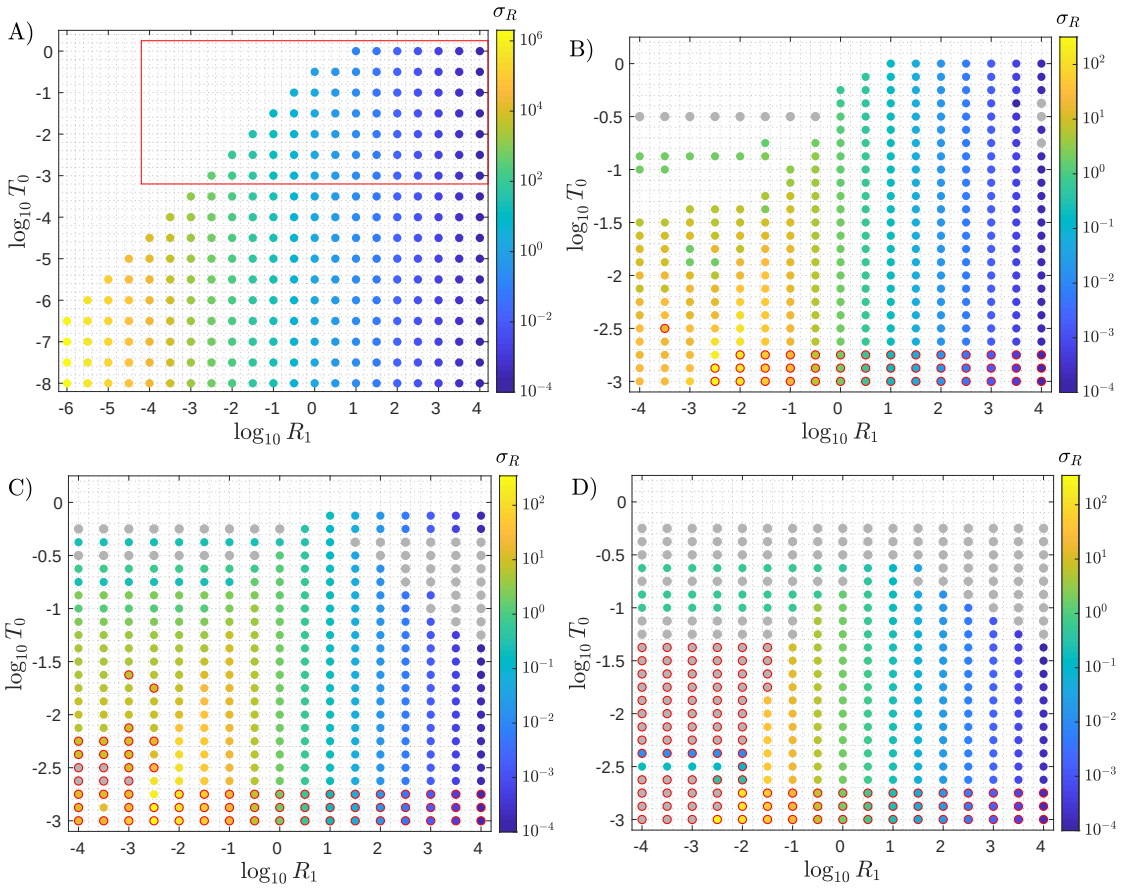

Figure 4.24: (Infinite, periodic membrane) The region in R_1-T_0 space in which membranes are unstable. The color of the dots in the instability region labels the real part of the eigenvalues (σ_{R}) corresponding to the most unstable modes. It represents the angular frequency. The springs have stiffness values of: A) $k_s = 0$ (analytical result), B) $k_s = 10^{-1}$, C) $k_s = 10^{0}$, and D) $k_s = 10^{1}$. The numerical results shown in panels B–D are with $N = 2^9$. The gray dots correspond to modes that lose stability by divergence and have $\sigma_{\mathrm{R}} \leq 10^{-9}$. The red rectangle in panel A indicates the region we consider in panels B–D to facilitate comparison. The red outline on some of the colored/gray dots indicates the cases where convergence with respect to N (as defined by (4.50)) was not obtained.

In figure 4.24 we plot the corresponding real parts of the eigenvalues for the most unstable modes. Increasing the spring stiffness k_s introduces more divergence modes (the gray dots, $\sigma_{\mathrm{R}} \leq 10^{-9}$). Note that this also occurs in the vortex-wake model,

figures 4.15, 4.17, and 4.19. σ_{R} varies more strongly with R_1 than with T_0. There is almost no variation with T_0 in figure 4.24A, and little variation in panels B–D—mainly when $T_0 > R_1$. Here, as T_0 decreases, σ_{R} increases but non-monotonically, particularly at the isolated bands of dots in panel B that become bands of non-monotonic change in σ_{R} in panels C and D, including changes between divergence (gray dots) and flutter and divergence (colored dots). Next we discuss more quantitatively how the real and imaginary parts of the eigenvalues depend on R_1 and T_0, including asymptotic scaling laws.

4.5.1 Analytical Results and Scaling Laws in the Instability Region

In this section we find analytically the eigenvalues and the corresponding eigenmodes (sinusoidal functions)—in the special case of $k_s = 0$. From these analytical solutions we derive asymptotic approximations for how the maximum growth rate, corresponding angular frequency, and dominant wave number depend on R_1 and T_0 when these parameters are small and large. We also study how the scaling laws behave when $k_s \neq 0$, where numerical solutions are required.

With $k_s = 0$ equation (4.48) reduces to

$$\left[\left(-R_1 - \frac{L}{\pi|k|}\right)\sigma^2 - \frac{4k}{|k|}\sigma + \left(\frac{2\pi k}{L}\right)^2\left(T_0 - \frac{L}{\pi|k|}\right)\right]\hat{y}_k = 0, \tag{4.51}$$

for $k = -\infty, \ldots, -1, 1, \ldots, \infty$. Solving (4.51) for σ, we obtain

$$\sigma = -\frac{2k}{|k|\,(R_1 + L/(\pi|k|))} \pm \sqrt{D_k}, \tag{4.52}$$

where

$$D_k := \frac{4}{(R_1 + L/(\pi|k|))^2}\left[1 + \left(R_1 + \frac{L}{\pi|k|}\right)\left(\frac{\pi k}{L}\right)^2\left(T_0 - \frac{L}{\pi|k|}\right)\right]. \tag{4.53}$$

The term in brackets can be written as $(L(-R_1 + T_0) + \pi R_1 T_0|k|)$ multiplied by a positive factor. Therefore D_k can be negative only for $T_0 < R_1$. When R_1 is small

the R_1T_0 term is negligible, so the stability boundary follows $T_0 = R_1$ as shown in figure 4.23A.

In (4.52) there are two possible eigenvalues for each R_1 and T_0 combination (due to the square root) that correspond to a complex-conjugate pair. We can then find k for the most unstable mode by setting the derivative of (4.53) with respect to k to zero and solving for k:

$$k_{\max} = \pm \frac{L(R_1 - 5T_0) + L\sqrt{R_1^2 + 14R_1T_0 + T_0^2}}{4\pi R_1 T_0}. \tag{4.54}$$

Since the discriminant in (4.53) is symmetric about $k = 0$, we have a symmetric pair of $k_{\max}$ in (4.54). For the periodic membrane, $k_{\max}$ must be an integer, but equation (4.54) is not necessarily an integer. Restricting $k_{\max}$ to integer values, we find that it is given by one of the integers nearest to the value in (4.54).

With this model we are able to obtain asymptotic scaling laws in the instability region for a wide range of R_1 and T_0 values. Unstable membrane modes are realized when the argument of the radical in (4.52) is negative, i.e., $D_k < 0$ in (4.53). We will now present the asymptotic scaling laws for $k_{\max}$, σ_{R}, and σ_{I} in different limits within the instability region. As we do so, we will refer to the summary in table 4.2. We study three asymptotic regimes that correspond to moving within the unstable region of figure 4.23A (or figure 4.24A) in three different directions. Moving rightward off to infinity, we have $R_1 \to \infty$ with fixed $T_0 \leq T_{0C}$, the first row of table 4.2. Moving diagonally downward and leftward, parallel to the stability boundary, we have $R_1 \to 0$ with $T_0 = cR_1$, for a fixed c between 0 and 1, the second row of table 4.2. Moving vertically downward instead, we have $T_0 \to 0$ with fixed R_1, the third row of table 4.2. Moving across each row, we give the asymptotic behavior of the three main quantities of interest.

Table 4.2: Summary of asymptotic scalings for the dominant wavenumber ($k_{\max}$), the real part of the eigenvalue (σ_{R}), and the imaginary part of the eigenvalue (σ_{I}) in the small- and large-R_1 and small-T_0 regimes, in the instability region.

Regimes \ Quantities	$k_{\max}$	σ_{R}	σ_{I}
$R_1 \to \infty$ (fixed $T_0 \le T_{0C}$)	$\max\left(\frac{L}{2\pi T_0}, 1\right)$	$\frac{2}{R_1}$	$\max\left(\frac{1}{\sqrt{R_1 T_0}}, \frac{2\pi}{L\sqrt{R_1}}\sqrt{\frac{L}{\pi} - T_0}\right)$
$R_1 \to 0$ ($T_0 = cR_1$, $0 < c < 1$)	$\frac{LC}{4\pi T_0}$	$\frac{2C}{R_1(C+4c)}$	$\frac{\sqrt{C^3(4-4c-C)}}{2R_1(C+4c)\sqrt{c}}$
$T_0 \to 0$ (fixed R_1)	$\frac{L}{2\pi T_0}$	$\frac{2}{R_1}$	$\frac{1}{\sqrt{R_1 T_0}}$

In the first column of table 4.2, we give the asymptotic forms of $k_{\max}$ by taking the appropriate limits in (4.54). In the first and third rows, we obtain

$$k = k_{\max} \to \frac{L}{2\pi T_0}. \tag{4.55}$$

In the second row, setting $T_0 = cR_1$ and taking $R_1 \to 0$, we have

$$k = k_{\max} = \pm\frac{LC}{4\pi c R_1} = \pm\frac{LC}{4\pi T_0} \quad \text{where} \quad C = (1-5c) + \sqrt{1+14c+c^2}. \tag{4.56}$$

In figure 4.25 we plot the dominant wavenumber versus T_0 for various fixed values of R_1 (one per line) and for four values of spring stiffness: $k_s = 0$ (figure 4.25A), $k_s = 10^{-1}$ (figure 4.25B), $k_s = 10^{0}$ (figure 4.25C), and $k_s = 10^{1}$ (figure 4.25D). When $k_s = 0$, we have the analytical result in (4.54) (actually, the nonzero integer closest to it, as mentioned previously). We also still assume that the membrane has period $L = 4$, as in the $k_s \neq 0$ case discussed previously. In panel A, we find that the wavenumber does not vary significantly with R_1 except when $R_1 \ll 1$ and we are close to the stability boundary, i.e., $T_0 \approx R_1$ for small R_1. The lines in panel A with $R_1 \le 10^{-2}$ curve downwards towards a vertical asymptote as they approach the stability boundary, but $k_{\max}$ is bounded below by 1, the endpoint of each line. The

dotted black line in figure 4.25A shows that the dominant wave number for various fixed R_1 values follows the scaling T_0^{-1}. Representative mode shapes at various (R_1, T_0) pairs are shown for $x \in [0, L]$, with the colors of the modes corresponding to the value of R_1. They are sinusoidal modes with wavelength that increases with T_0.

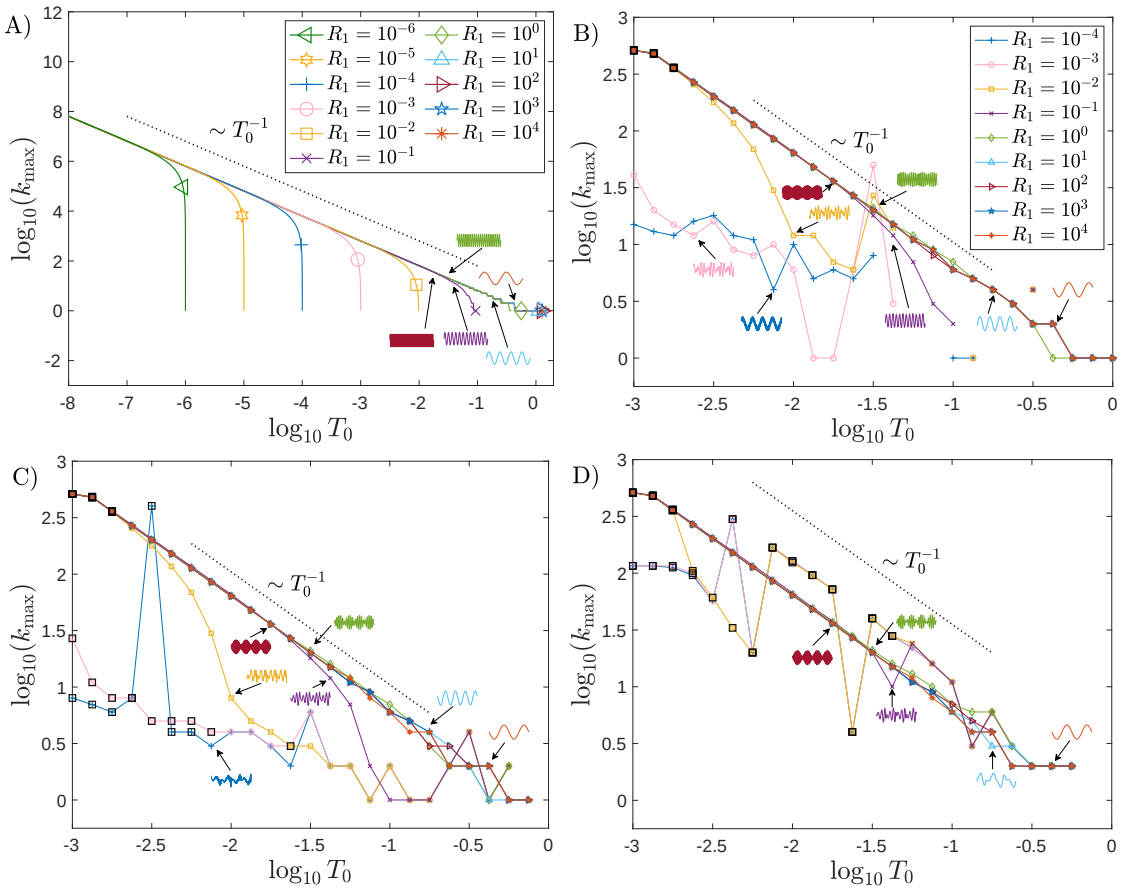

Figure 4.25: (Infinite, periodic membrane) Plots showing the membrane's dominant wavenumber versus T_0 for various fixed R_1 values at four values of spring constants: A) $k_s = 0$ (analytical results), B) $k_s = 10^{-1}$, C) $k_s = 10^{0}$, and D) $k_s = 10^{1}$. We show typical examples of the imaginary part of the eigenmode shapes. The dotted black line shows the scaling T_0^{-1}.

In panels B–D, $k_s \neq 0$, and the eigenmodes are found computationally. They are a superposition of multiple sinusoidal modes. For the most unstable mode we define the dominant wavenumber to be that of the sinusoidal component with the largest amplitude (the k for which $|\hat{y}_k|$ is largest [see equation (4.39)]). In figures 4.25B–D we find that at large R_1 ($\gtrsim 10^0$), where the spring force is relatively less significant, the

lines scale as T_0^{-1} and do not vary significantly with R_1, similarly to the case without springs in panel A. At smaller R_1, the lines deviate greatly from this behavior, and do not seem to follow any specific power law. The data points outlined with black squares are cases that are not resolved (using the same definition as for the red circles in figures 4.23 and 4.24—when the eigenvalue relative error [equation (4.50)] $> 3 \times 10^{-2}$). These occur mostly at small T_0, when the dominant wavenumber $k_{\max}$ is very large, so good resolution would require a larger N than is feasible computationally. The deviations at small R_1 coincide with changes in the eigenmodes similar to those seen in figure 4.22 when R_1 and T_0 are small relative to k_s. In particular, the mode shapes are less sinusoidal and less symmetric than at large R_1. For example, as the spring stiffness k_s increases, moving from panel B to C to D, the envelopes of deflection for the green modes at $(R_1, T_0) = (10^0, 10^{-1.5})$ and the red modes at $(R_1, T_0) = (10^2, 10^{-1.75})$ are decreased near the springs at $x = 0, 1, \ldots, L = 4$. The light blue modes at $(R_1, T_0) = (10^1, 10^{-0.75})$ are sinusoidal in panels A–C but change to a non-sinusoidal shape at largest k_s (panel D), and the dominant wavenumber there is also decreased compared to the sinusoidal cases in panels A–C. The orange mode (at $(R_1, T_0) = (10^4, 10^{-0.375})$) has larger R_1 and therefore retains a sinusoidal shape even at the largest k_s value. Moving to much smaller R_1, such as the purple mode ($(R_1, T_0) = (10^{-1}, 10^{-1.375})$) we again have a transition from a sinusoidal shape at $k_s = 0$ to a shape that is less sinusoidal as k_s increases (from panels B to D) and less fore-aft symmetric, with peaks of deflection just upstream of the spring locations, unlike the more fore-aft symmetric red and green shapes at larger R_1.

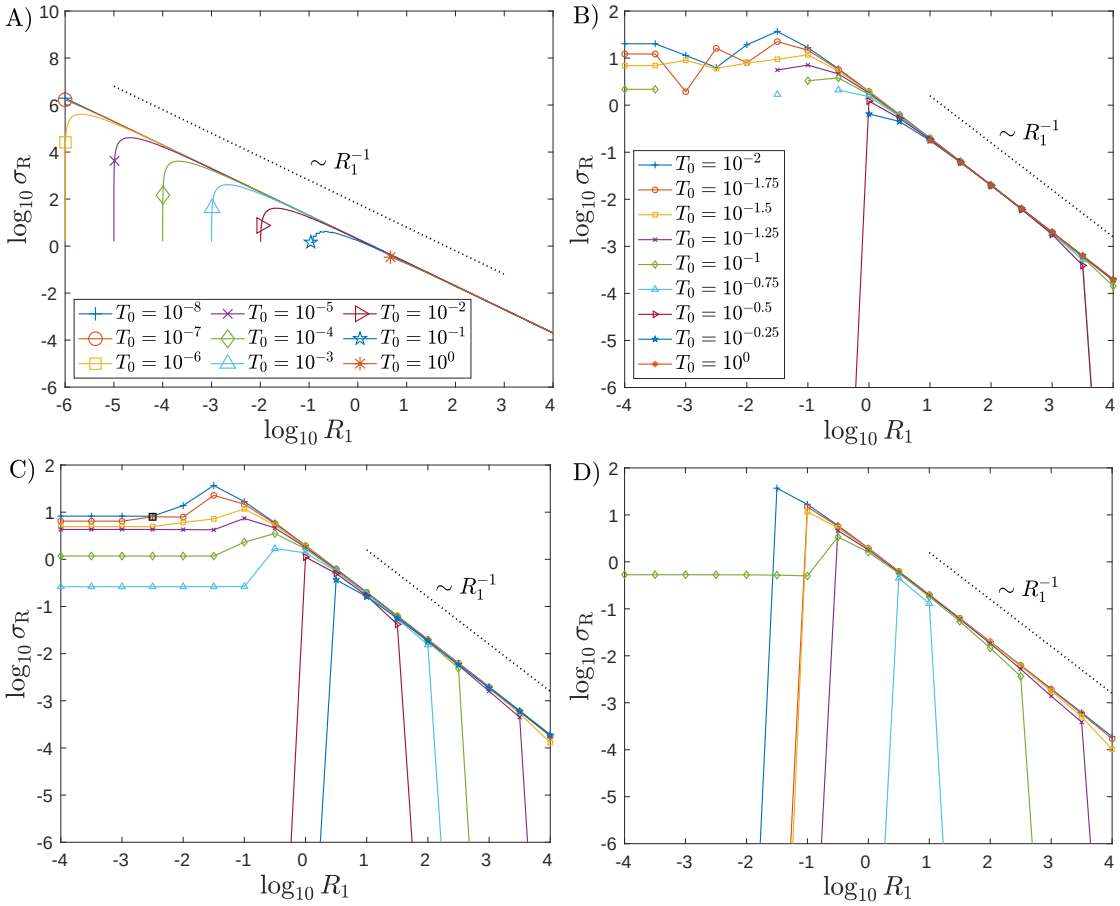

Figure 4.26: (Infinite, periodic membrane) Plots showing the real parts of the eigenvalues for spring constants: A) $k_s = 0$ (analytical result), B) $k_s = 10^{-1}$, C) $k_s = 10^{0}$, and D) $k_s = 10^{1}$. Panels B–D share the same legend, and result from computations with $N = 2^9$. The dotted black line at moderate-to-large values of R_1 shows the scaling R_1^{-1}.

We now present the real parts of the eigenvalues within the instability region, with three asymptotic behaviors given in the three rows of the second column of table 4.2. For each row, we find the dominant behaviors of σ_{R} by inserting the values of $k_{\max}$ from the first column of that row into the first term on the right side of (4.52), which is σ_{R}. When we take the appropriate limits for each row (shown on the left side of table 4.2), we obtain the expressions for σ_{R} in the second column of table 4.2.

Figure 4.26 plots the values of the real parts of the eigenvalues (σ_{R}) with respect to the membrane mass (R_1) for various fixed T_0 (one value per line) and for the same four spring stiffness constants as in figure 4.25, one per panel. As with figure 4.25A,

the values in figure 4.26A, with $k_s = 0$, are obtained analytically through (4.52), and are obtained computationally for the remaining panels. Most of the data lie nearly on the straight line given by $2/R_1$, corresponding to the first and third rows in the second column of table 4.2. For each $T_0 \leq 10^{-1}$, the corresponding line curves downward and becomes nearly vertical at the stability boundary. A vertical asymptote would occur if $k_{\max}$ could decrease to 0 (as in (4.54) when $R_1 \to T_0$), but it is bounded below by 1 (as in figure 4.25A), and consequently σ_{R} also has a positive lower bound at the stability boundary.

When k_s is increased from 0 to 10^{-1} we obtain different behaviors, shown in figure 4.26B. When $R_1 \gg 1$, the data follow the same $2/R_1$ behavior as in panel A for T_0 relatively large but below the stability boundary. At other (R_1, T_0) pairs, the springs cause different behaviors. Disconnected lines or points are observed (e.g., at $T_0 = 10^{-1.25}$, 10^{-1}, $10^{-0.75}$) where the membrane switches between being stable and unstable. These correspond to the isolated bands of unstable modes seen in figure 4.23B.

In figure 4.26 (panels B, C, and D), some membranes lose stability by divergence, shown by the sharp drop in some of the graphs to values below 10^{-6} (for example, $T_0 = 10^{-0.5}$ in panels B and C and $T_0 = 10^{-1.25}$ and $T_0 = 10^{-0.75}$ in panel D). The graphs continue to the left or right R_1 limits of the plots with values $\approx 10^{-12}$ (not visible), indicating instability by divergence throughout these regions. Divergence occurs for ranges of small and large R_1 that are generally more extensive at larger T_0 until the stability boundary is reached. When $T_0 = 10^{-0.25}$ and $10^{-0.5}$ in panel D all membranes lose stability by divergence. Therefore, the lines for these two cases do not appear in the panel. Another striking effect of $k_s \neq 0$ is the plateaus on the left sides of panels B–D, at small R_1. Here the values of σ_{R} drop to a plateau instead of

a vertical asymptote as in panel A. The values of σ_{R} for each plateau decrease with increasing T_0 in most cases in panels B and C.

The small square with the black outline in panel C shows a case with an eigenvalue that is not converged. More of these cases occur in panel D where divergence occurs (below the lower limit of the panel, and so not shown).

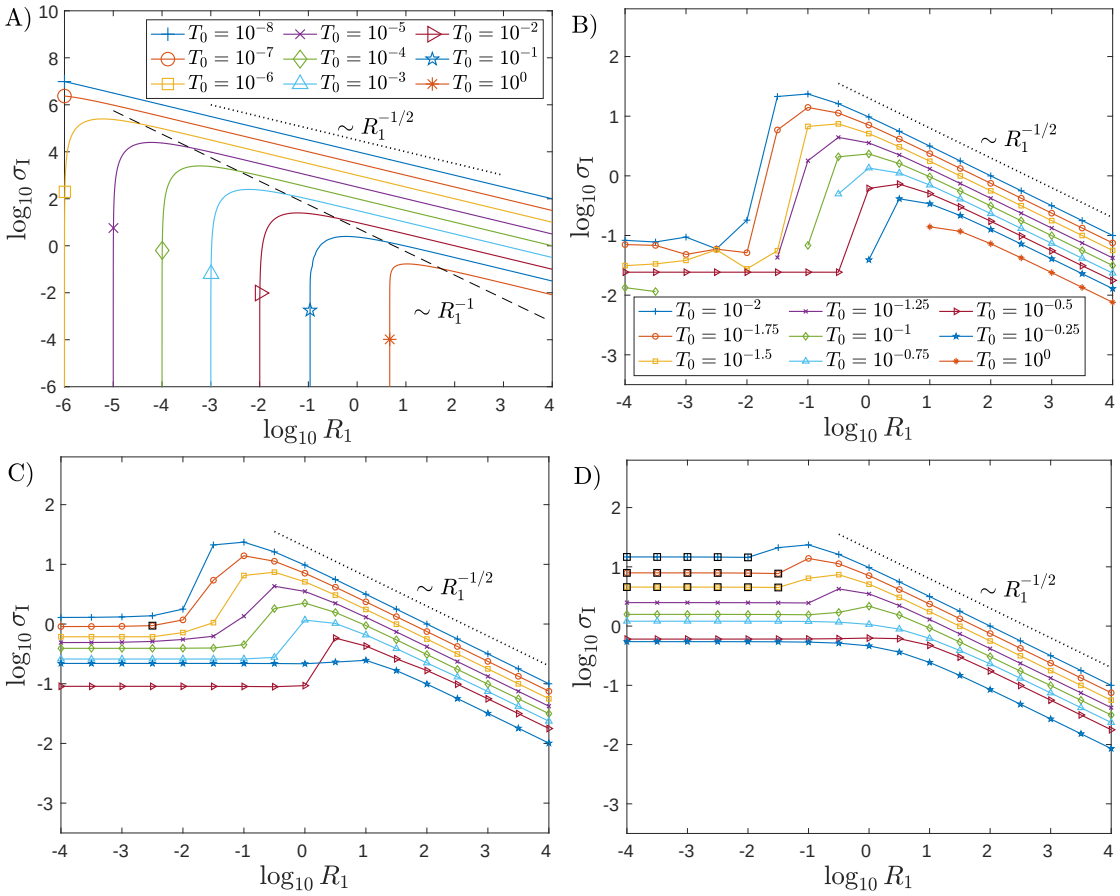

Figure 4.27: (Infinite, periodic membrane) Plots showing the imaginary parts of the eigenvalues for spring constants: A) $k_s = 0$ (analytical result), B) $k_s = 10^{-1}$, C) $k_s = 10^{0}$, and D) $k_s = 10^{1}$. Panels B–D share the same legend, and for the numerical results shown we use $N = 2^9$. The dotted black line at moderate-to-large values of R_1 shows the scaling $R_1^{-1/2}$.

Finally, we present the imaginary parts of the eigenvalues in the unstable region and investigate the same three asymptotic regimes as for the other two quantities in table 4.2. For each regime, we derive the dominant behaviors of σ_{I} by substituting the $k_{\max}$ values shown in the first column of table 4.2 in the second term on the right

side of (4.52), which is $\pm i\sigma_{\mathrm{I}}$ if $D_k < 0$, i.e., the mode is unstable.

In figure 4.27 we plot the imaginary parts of the eigenvalues (σ_{I}) versus the membrane mass (R_1) for various fixed values of T_0 and for the same spring stiffness constants, one per panel, as in figures 4.25 and 4.26. In figure 4.27A at large R_1 for fixed T_0, σ_{I} follows the $R_1^{-1/2}$ scaling shown by the dotted line. The lines are equispaced at large R_1, consistent with the scaling $T_0^{-1/2}$ for fixed R_1. Both behaviors are consistent with the asymptotic scaling law $\sigma_{\mathrm{I}} \sim 1/\sqrt{R_1 T_0}$ at large R_1 or at small T_0, the first and third rows, respectively, of the third column of table 4.2. As in figure 4.26A, each line curves downward to a vertical asymptote as it approaches the stability boundary at a certain R_1 value. The dashed line shows the R_1^{-1} scaling of σ_{I} when $T_0 = cR_1$, $0 < c < 1$ and $R_1 \to 0$, given analytically in the second row of the third column of table 4.2.

Panels B–D show the results with three nonzero k_s values, and have many similarities with the corresponding results for σ_{R} (figures 4.26B–D). For example, the lines end in panel B where the membrane switches between being stable and unstable. Another similarity, when $k_s \neq 0$, is that σ_{I} plateaus on the left sides of panels B–D, at small R_1. Here, when $T_0 \to R_1^-$ the lines of σ_{I} initially curve downward (but not towards a vertical asymptote as in figure 4.27A) and then tend to a constant value at small R_1 in most cases. These lines curve downward less sharply as k_s increases, and the region of downward curving disappears completely in some cases in panel D. Another qualitative similarity with figure 4.26 is that the growth rate $|\sigma_{\mathrm{I}}|$ decreases with increasing T_0 in most cases. As previously, the small squares with the black outline in figures 4.27C and 4.27D correspond to (R_1, T_0) pairs where the eigenvalue is not converged with respect to N but we still include them here to distinguish them from stable membranes where a marker is omitted altogether.

There is no indication in figures 4.27B–D of a switch in behavior corresponding to the changes from divergence with flutter to divergence without flutter shown by the sudden drops in σ_{R} in figures 4.26B–D. In other words, the imaginary parts of the eigenvalues change smoothly despite the sharp changes in the real parts. The orange line with asterisks, $T_0 = 10^0$, is not present in figures 4.27C and 4.27D because the critical T_0 for instability drops below 10^0 as k_s increases to 10^0 and 10^1.

4.6 Conclusions

In this chapter we have studied the flutter instability of thin membranes whose leading and trailing edges are attached to inextensible rods of length R and Hookean springs of stiffness constant k_s. We looked at different parts of the four-dimensional parameter spaces (R_1, R_3, T_0, R) and (R_1, R_3, T_0, k_s). We found that when membranes are attached to rods with small length R or to springs of moderate-to-large stiffness k_s, they exhibit large (but physically reasonable) deflections that converge to states of steady deflection with single humps that are almost fore-aft symmetric. When R is moderate-to-large and k_s small, we find a wide range of unsteady dynamics, somewhat similar to those seen in studies of flapping plates or flags (or fixed–free and free–free membranes in chapter II). In either of the two regimes, deflections scale as $R_3^{-1/2}$, when the stretching modulus R_3 is large. The large-amplitude dynamics depend most strongly on the membrane mass density R_1 and less strongly on the pretension T_0. At the largest R_1 studied we find the smallest oscillation frequencies and largest membrane deflections corresponding to somewhat chaotic and asymmetrical membrane motions. Here the dominant time period scales as $R_1^{1/2}$. As R_1 decreases, the membrane motions become more periodic and symmetrical, and with larger spatial frequency components (sharper curvatures and more zero crossings).

At $R_1 \lesssim 10^{-1.25}$ the motions become more chaotic again, with much finer spatial features that are difficult to resolve numerically and so a finer mesh on the membrane is required there. Our study shows that the boundary conditions (inextensible rods and vertical Hookean springs) allow for a smooth transition between types of membrane dynamics that were observed when both membrane ends are fixed at zero deflection or when one or both ends are free to move in the vertical direction.

To study the onset of membrane instability and small-amplitude membrane motions, we used a linearized model and a nonlinear eigenvalue solver—similar to the one in chapter III. In this regime, the nonlinear R_3 term in (3.5) is negligible so we characterized the different types of motions with respect to the other two key dimensionless parameters—membrane mass and pretension. In the small-amplitude model we focused on the vertical Hookean springs, equivalent to inextensible rods via $1/R = k_s/T_0$. When membrane inertia and pretension dominate fluid pressure forces, the eigenmodes tend toward neutrally stable sinusoidal functions. As we increase k_s, we transition from membranes that resemble the free–free case to membranes that resemble the fixed–fixed case. There are roughly two regimes: small membrane density, where divergence occurs and the most unstable mode becomes more fore-aft asymmetric as one moves further into the instability region, and large membrane density, where flutter and divergence occur with approximately sinusoidal modes. In both regimes, the most unstable modes become wavier at smaller T_0, akin to the most unstable beam modes at smaller bending rigidity in [3]. The stability boundaries with $k_s = 10^{-1}$ and 10^0 are very similar at large membrane densities, showing an upward slope for R_1. This upward slope for R_1 is also seen with $k_s = 10^1$ but it starts at a larger R_1.

To derive asymptotic scaling laws theoretically, we introduced a simplified model

with spatially periodic solutions by assuming that the membrane extends to infinity upstream and downstream and is tethered by an infinite, periodic array of Hookean springs, all with stiffness k_s. This model corresponds to a standard eigenvalue problem, and is much faster to compute than the nonlinear eigenvalue problem of the membrane-vortex-wake model. We can thus study much wider ranges of the key parameters R_1, T_0, and k_s. When $k_s = 0$ we can compute asymptotic scaling laws for the real and imaginary parts of the eigenvalues, and the dominant wave number of the most unstable eigenmodes. We find that as R_1 increases from small to large, the dominant wave number scaling varies from R_1^{-1} to R_1^0 for the periodic membrane within the instability region. In the large amplitude simulations, the time-averaged number of extrema of deflection also changes from R_1^{-1} to R_1^0 scalings as R_1 increases from small to large. For the periodic membrane, the frequency σ_{R} scales as R_1^{-1} at both small and large R_1, while the large-amplitude dominant frequency transitions scales as $R_1^{-5/6}$ and $R_1^{-1/2}$, respectively. At small R_1, the large-amplitude results are mostly independent of T_0 within the instability region, while the periodic membrane results do depend on T_0. For the periodic membrane, we also considered the small-amplitude growth rate σ_{I}. At large R_1, it decays as $R_1^{-1/2}$ for a fixed T_0; at small R_1 and $T_0 = cR_1$ for $0 < c < 1$, it decays as R_1^{-1}. When k_s is increased to a nonzero value, both σ_{R} and σ_{I} plateau at small R_1.

There are qualitative similarities in the shapes of the stability boundaries for the periodic membrane and membrane-vortex-wake models. At small R_1, the stability boundaries have a plateau at a certain T_0 value, that decreases as k_s decreases. At large R_1, the periodic membrane has a flat stability boundary, while that with the vortex wake is upward sloping, corresponding to unstable modes at larger T_0, albeit with very slow growth rates. At all R_1, as k_s increases divergence modes become

more common near the stability boundary in both models.

The membrane modes from the two models also share many features. For example, the mode shapes become wavier at smaller T_0 in both models. Additionally, by tracking the eigenmodes across the three parameter space of R_1, T_0, and k_s, we found that at larger R_1, the modes are more sinusoidal and fore-aft symmetric in both models. At small-to-moderate R_1, the modes are more asymmetric, with peak deflections shifted downstream.

CHAPTER V

Membrane Flutter in Three-dimensional Inviscid Flow

5.1 Introduction

In this chapter, we develop a model and computational method to study the large-amplitude dynamics of rectangular membranes in a three-dimensional (3D) inviscid flow. To our knowledge the present chapter is the first 3D study of this problem.

We compute the stability boundary locations and the large-amplitude dynamics for a range of membrane mass density, pretension, and stretching rigidity values, for 12 combinations of boundary conditions at the membrane edges. With free side edges we find good agreement with previous 2D results even though different discretization methods were used. Here we also use a flat-wake approximation [86] and find good agreement between membranes with large aspect ratio in 3D flow and membranes in 2D flow with wake roll-up. Computing wake roll-up with high precision in 3D is challenging as the vortex sheet may undergo complex twisting and shearing deformations that make meshing difficult [46]. Fast algorithms (e.g., tree codes) for the evolution of vortex sheets in three dimensions have been developed by [47, 85, 105, 150, 201].

We find that the 3D dynamics in the 12 cases naturally fall into four groups that are determined by only the leading and trailing edge conditions. Within each group the conditions at the side edges can still have some qualitative effects on the mem-

brane dynamics. For example, the side-edge conditions can determine the variety of spanwise curvature distributions and whether membranes are steady versus unsteady, periodic versus chaotic—depending on the group and the physical parameter values. The deflection amplitudes and oscillation frequencies have scalings similar to those in the 2D case.

The structure of this chapter is as follows. §5.2 describes our large-amplitude membrane-vortex-sheet model. Unlike chapters II–IV, here we consider a membrane surface held in a 3D inviscid flow with 12 different sets of boundary conditions. We solve this nonlinear model using Broyden's method and an unsteady vortex lattice algorithm. §5.3 describes the numerical method. We apply a small initial perturbation to the membrane in the direction transverse to the flow and compute the subsequent dynamics, which have large-amplitude deflections if the membrane is unstable. In §5.4 we perform convergence studies and validate our model by comparing the current results with our previous 2D studies of fixed–fixed, fixed–free, and free–free membranes. §5.5 describes the computed membrane dynamics and how these vary with key parameters such as the membrane mass, pretension, and stretching rigidity. We find that the membrane dynamics naturally form four groups based on the boundary conditions at the leading and trailing edges. §5.6 gives the conclusions.

5.2 Large-amplitude Membrane-vortex-sheet Model

We consider the motion of an extensible membrane held in a 3D fluid flow with velocity $U\widehat{\mathbf{e}}_x$ in the far field (see figure 5.1). In the undeformed state the membrane is flat and parallel to the flow in the plane $z = 0$. As in [9], the membrane obeys linear elasticity but undergoes large deflections, so geometrically nonlinear terms enter the force expression. The membrane has a small thickness h and to leading

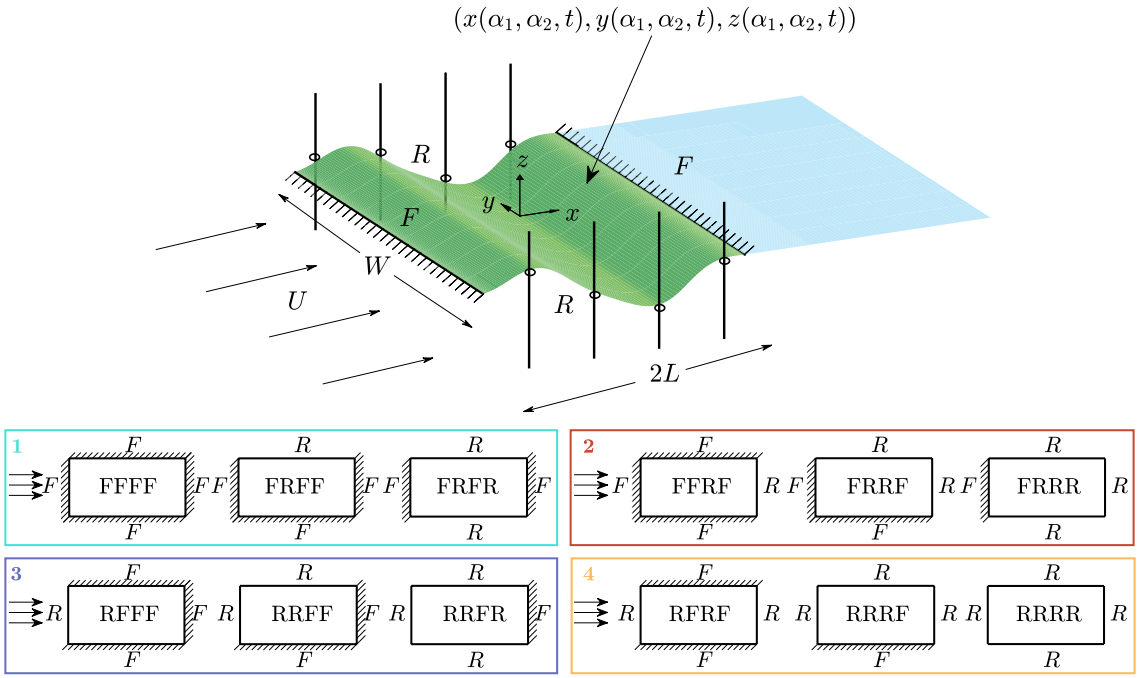

Figure 5.1: Schematic diagram (in perspective view) showing a three-dimensional membrane (dark green surface) with fixed leading and trailing edges and free side edges. Along a free edge, points are fixed to massless rings that slide without friction along vertical poles. $U\widehat{\mathbf{e}}_x$ is the oncoming flow velocity, W is the membrane's spanwise width, and $2L$ is the membrane's chord. There is also a flat vortex wake (light blue surface) that emanates from the membrane's trailing edge. In the lower portion of the figure, we also show schematically (in top view) the 12 distinct boundary conditions explored in the current work. The diagonal marks indicate a fixed (F) boundary and other boundaries are free (R). The arrows indicate the far-field flow direction which is the same for each configuration.

order the deformations do not vary through the thickness, so they can be described by the middle surface, midway through the thickness. The middle surface is a geometric surface, a three-component vector parametrized by two spatial coordinates and time: $\mathbf{r}(\alpha_1,\alpha_2,t) = (x(\alpha_1,\alpha_2,t), y(\alpha_1,\alpha_2,t), z(\alpha_1,\alpha_2,t)) \in \mathbb{R}^3$, where the spatial coordinates $\alpha_1 \in [-L, L]$ and $\alpha_2 \in [-W/2, W/2]$ are the material coordinates, the x and y coordinates of each point in the initially flat state (with a uniform in-plane tension— a "pretension"—applied by the boundaries).

Each of the four membrane edges is either fixed at zero deflection or free to move in the z direction, perpendicular to the oncoming flow. Then there are $2^4 = 16$ possible boundary conditions but since the problem is symmetrical with respect to reflection

in the x-z plane, we only need to consider 12 distinct boundary conditions, which can be denoted: FFFF, FRFF/FFFR, FRFR, FFRF, FRRF/FFRR, FRRR, RFFF, RRFF/RFFR, RRFR, RFRF, RRRF/RFRR, and RRRR (with symmetrical pairs identified). Here F stands for a *fixed* edge and R stands for a *free* edge. The first letter in each label is the leading-edge boundary condition type and the following letters are the boundary conditions moving clockwise around the rectangular membrane looking down from larger z values (bottom of figure 5.1), as in [54]. Thus, the second and fourth letters are the side-edge boundary conditions and the third letter is the trailing-edge boundary condition. We will see in the results sections that the dynamics in the 12 cases are naturally classified into four groups, based on whether the leading and trailing edges are fixed or free. Each group is placed in one of the four colored rectangles in the lower portion of figure 5.1. We present the results for each group in the four subsections of §5.5.2, numbered with the numbers listed at the upper left corner of each group's rectangle in figure 5.1. We list the equations for three examples from the set of 12 boundary conditions (and the others are analogous):

$$\text{FRFR:} \quad z(-L,\alpha_2,t)=0,\ z(L,\alpha_2,t)=0, \tag{5.1}$$
$$\partial_{\alpha_2} z(\alpha_1,-W/2,t)=0,\ \partial_{\alpha_2} z(\alpha_1,W/2,t)=0,$$

$$\text{FRRR:} \quad z(-L,\alpha_2,t)=0,\ \partial_{\alpha_1} z(L,\alpha_2,t)=0, \tag{5.2}$$
$$\partial_{\alpha_2} z(\alpha_1,-W/2,t)=0,\ \partial_{\alpha_2} z(\alpha_1,W/2,t)=0,$$

$$\text{RRRR:} \quad \partial_{\alpha_1} z(-L,\alpha_2,t)=0,\ \partial_{\alpha_1} z(L,\alpha_2,t)=0, \tag{5.3}$$
$$\partial_{\alpha_2} z(\alpha_1,-W/2,t)=0,\ \partial_{\alpha_2} z(\alpha_1,W/2,t)=0.$$

Whether the edge is fixed or free affects only the out-of-plane (z-) component of the membrane motion at the edge. In all cases, no in-plane motion of the membrane

edges is allowed, i.e., the x- and y-coordinates of the edges are fixed (see figure 5.1):

Upstream/downstream edges:

$$\{x(\pm L, \alpha_2, t) = \pm L,\ y(\pm L, \alpha_2, t) = \alpha_2\}, -\frac{W}{2} \leq \alpha_2 \leq \frac{W}{2}, \tag{5.4}$$

$$\text{Side edges: } \left\{x\left(\alpha_1, \pm\frac{W}{2}, t\right) = \alpha_1,\ y\left(\alpha_1, \pm\frac{W}{2}, t\right) = \pm\frac{W}{2}\right\}, -L \leq \alpha_1 \leq L. \tag{5.5}$$

We start with the stretching energy per unit undeformed area for a thin sheet with isotropic elasticity (described in appendix G and [9, 41]):

$$w_s = \frac{h}{2}\frac{E}{1+\nu}\left(\frac{1}{1-\nu}(\epsilon_{11}^2 + \epsilon_{22}^2) + \frac{2\nu}{1-\nu}\epsilon_{11}\epsilon_{22} + 2\epsilon_{12}^2\right), \tag{5.6}$$

where E is Young's modulus, ν is Poisson's ratio, h is the membrane's thickness, and the strain tensor is

$$\epsilon_{ij}(\alpha_1, \alpha_2, t) = \overline{e}\delta_{ij} + \frac{1}{2}\left(\partial_{\alpha_i}\mathbf{r} \cdot \partial_{\alpha_j}\mathbf{r} - \delta_{ij}\right). \tag{5.7}$$

Here $\overline{e}$ denotes a constant prestrain corresponding to the pretension applied at the boundaries and δ_{ij} is the identity tensor, with $i, j \in \{1, 2\}$. We take the variation of the stretching energy

$$W_s = \iint w_s \mathrm{d}\alpha_1 \mathrm{d}\alpha_2 \tag{5.8}$$

with respect to the position $\mathbf{r}$ to obtain the stretching force per unit material area, i.e., $-\delta w_s/\delta\mathbf{r}$.

Integrating by parts to move derivatives off of $\delta\mathbf{r}$ terms, we obtain

$$\begin{aligned}\delta W_s = \frac{Eh}{1+\nu}\oint \Bigg[&\left(\frac{1}{1-\nu}\epsilon_{11}\left(\frac{\partial\mathbf{r}}{\partial\alpha_1}\cdot\delta\mathbf{r}\right) + \frac{\nu}{1-\nu}\epsilon_{22}\left(\frac{\partial\mathbf{r}}{\partial\alpha_1}\cdot\delta\mathbf{r}\right) + \epsilon_{12}\left(\frac{\partial\mathbf{r}}{\partial\alpha_2}\cdot\delta\mathbf{r}\right)\right)\upsilon_1 \\ &+ \left(\frac{1}{1-\nu}\epsilon_{22}\left(\frac{\partial\mathbf{r}}{\partial\alpha_2}\cdot\delta\mathbf{r}\right) + \frac{\nu}{1-\nu}\epsilon_{11}\left(\frac{\partial\mathbf{r}}{\partial\alpha_2}\cdot\delta\mathbf{r}\right) + \epsilon_{12}\left(\frac{\partial\mathbf{r}}{\partial\alpha_1}\cdot\delta\mathbf{r}\right)\right)\upsilon_2\Bigg]\,\mathrm{d}\sigma \\ &- \frac{Eh}{1+\nu}\iint\Bigg[\frac{\partial}{\partial\alpha_1}\left(\frac{1}{1-\nu}\epsilon_{11}\frac{\partial\mathbf{r}}{\partial\alpha_1} + \frac{\nu}{1-\nu}\epsilon_{22}\frac{\partial\mathbf{r}}{\partial\alpha_1} + \epsilon_{12}\frac{\partial\mathbf{r}}{\partial\alpha_2}\right) \\ &+ \frac{\partial}{\partial\alpha_2}\left(\frac{1}{1-\nu}\epsilon_{22}\frac{\partial\mathbf{r}}{\partial\alpha_2} + \frac{\nu}{1-\nu}\epsilon_{11}\frac{\partial\mathbf{r}}{\partial\alpha_2} + \epsilon_{12}\frac{\partial\mathbf{r}}{\partial\alpha_1}\right)\Bigg]\cdot\delta\mathbf{r}\,\mathrm{d}\alpha_1\mathrm{d}\alpha_2.\end{aligned} \tag{5.9}$$

The first integral in (5.9) can be used to obtain the free edge boundary conditions. It is a boundary integral with respect to $\mathrm{d}\sigma$, arc length along the boundary in the α_1-α_2 plane; (υ_1, υ_2) is the outward normal in this plane. The integrand in the second integral in (5.9) gives the stretching force per unit material area,

$$\begin{aligned}\mathbf{f}_s = -\frac{\delta w_s}{\delta \mathbf{r}} = \frac{Eh}{1+\nu}\Bigg[&\frac{\partial}{\partial\alpha_1}\left(\frac{1}{1-\nu}\epsilon_{11}\frac{\partial \mathbf{r}}{\partial\alpha_1} + \frac{\nu}{1-\nu}\epsilon_{22}\frac{\partial \mathbf{r}}{\partial\alpha_1} + \epsilon_{12}\frac{\partial \mathbf{r}}{\partial\alpha_2}\right)\\ &+\frac{\partial}{\partial\alpha_2}\left(\frac{1}{1-\nu}\epsilon_{22}\frac{\partial \mathbf{r}}{\partial\alpha_2} + \frac{\nu}{1-\nu}\epsilon_{11}\frac{\partial \mathbf{r}}{\partial\alpha_2} + \epsilon_{12}\frac{\partial \mathbf{r}}{\partial\alpha_1}\right)\Bigg].\end{aligned} \tag{5.10}$$

The membrane dynamics are governed by the balance of momentum for a small material element with area $\Delta\alpha_1\Delta\alpha_2$:

$$\rho_s h\Delta\alpha_1\Delta\alpha_2\partial_{tt}\mathbf{r} = \mathbf{f}_s\Delta\alpha_1\Delta\alpha_2 - [p](\alpha_1,\alpha_2,t)\hat{\mathbf{n}}\sqrt{\det[\partial_{\alpha_i}\mathbf{r}\cdot\partial_{\alpha_j}\mathbf{r}]}\Delta\alpha_1\Delta\alpha_2, \tag{5.11}$$

where ρ_s is the mass per unit volume of the membrane, uniform in the undeformed state; $[p](\alpha_1,\alpha_2,t)$ is the fluid pressure; $\hat{\mathbf{n}}$ is the unit normal vector,

$$\hat{\mathbf{n}} = (\partial_{\alpha_1}\mathbf{r}\times\partial_{\alpha_2}\mathbf{r})/\|\partial_{\alpha_1}\mathbf{r}\times\partial_{\alpha_2}\mathbf{r}\|, \tag{5.12}$$

and $\det[\partial_{\alpha_i}\mathbf{r}\cdot\partial_{\alpha_j}\mathbf{r}]$ is the determinant of the metric tensor, so $\sqrt{\det[\partial_{\alpha_i}\mathbf{r}\cdot\partial_{\alpha_j}\mathbf{r}]}\Delta\alpha_1\Delta\alpha_2$ is the area of the material element in physical space.

We nondimensionalize the governing equations by the density of the fluid ρ_f, the half-chord L, and the imposed fluid flow velocity U. The dimensionless time, space, and pressure jump variables (denoted by tildes) are:

$$\tilde{t} = \frac{t}{L/U}, \quad (\tilde{\mathbf{r}},\widetilde{\alpha_1},\widetilde{\alpha_2}) = \frac{(\mathbf{r},\alpha_1,\alpha_2)}{L}, \quad \widetilde{[p]} = \frac{[p]}{\rho_f U^2}. \tag{5.13}$$

The membrane equation (5.11) becomes

$$\begin{aligned}\frac{\rho_s h U^2}{L}\widetilde{\partial_{tt}\mathbf{r}} = \frac{Eh}{L(1+\nu)}\Bigg[&\widetilde{\partial_{\alpha_1}}\left(\frac{1}{1-\nu}\widetilde{\epsilon_{11}}\widetilde{\partial_{\alpha_1}\mathbf{r}} + \frac{\nu}{1-\nu}\widetilde{\epsilon_{22}}\widetilde{\partial_{\alpha_1}\mathbf{r}} + \widetilde{\epsilon_{12}}\widetilde{\partial_{\alpha_2}\mathbf{r}}\right)\\ &+\widetilde{\partial_{\alpha_2}}\left(\frac{1}{1-\nu}\widetilde{\epsilon_{22}}\widetilde{\partial_{\alpha_2}\mathbf{r}} + \frac{\nu}{1-\nu}\widetilde{\epsilon_{11}}\widetilde{\partial_{\alpha_2}\mathbf{r}} + \widetilde{\epsilon_{12}}\widetilde{\partial_{\alpha_1}\mathbf{r}}\right)\Bigg]\\ &-\rho_f U^2\widetilde{[p]}\hat{\mathbf{n}}\sqrt{\det[\widetilde{\partial_{\alpha_i}\mathbf{r}}\cdot\widetilde{\partial_{\alpha_j}\mathbf{r}}]}.\end{aligned} \tag{5.14}$$

Dividing (5.14) by $\rho_f U^2$ throughout yields

$$\begin{aligned}\frac{\rho_s h}{\rho_f L}\widetilde{\partial_{tt}\mathbf{r}} = \frac{Eh}{\rho_f U^2 L(1+\nu)}\Bigg[&\widetilde{\partial_{\alpha_1}}\left(\frac{1}{1-\nu}\widetilde{\epsilon_{11}}\widetilde{\partial_{\alpha_1}\mathbf{r}} + \frac{\nu}{1-\nu}\widetilde{\epsilon_{22}}\widetilde{\partial_{\alpha_1}\mathbf{r}} + \widetilde{\epsilon_{12}}\widetilde{\partial_{\alpha_2}\mathbf{r}}\right)\\ &+\widetilde{\partial_{\alpha_2}}\left(\frac{1}{1-\nu}\widetilde{\epsilon_{22}}\widetilde{\partial_{\alpha_2}\mathbf{r}} + \frac{\nu}{1-\nu}\widetilde{\epsilon_{11}}\widetilde{\partial_{\alpha_2}\mathbf{r}} + \widetilde{\epsilon_{12}}\widetilde{\partial_{\alpha_1}\mathbf{r}}\right)\Bigg]\\ &-\widetilde{[p]}\hat{\mathbf{n}}\sqrt{\det[\widetilde{\partial_{\alpha_i}\mathbf{r}}\cdot\widetilde{\partial_{\alpha_j}\mathbf{r}}]}.\end{aligned} \tag{5.15}$$

Thus, the dimensionless membrane equation (dropping tildes) is

$$\begin{aligned}R_1\partial_{tt}\mathbf{r} - K_s\{&\partial_{\alpha_1}\left(\epsilon_{11}\partial_{\alpha_1}\mathbf{r} + \nu\epsilon_{22}\partial_{\alpha_1}\mathbf{r} + (1-\nu)\epsilon_{12}\partial_{\alpha_2}\mathbf{r}\right)\\ &+\partial_{\alpha_2}\left(\epsilon_{22}\partial_{\alpha_2}\mathbf{r} + \nu\epsilon_{11}\partial_{\alpha_2}\mathbf{r} + (1-\nu)\epsilon_{12}\partial_{\alpha_1}\mathbf{r}\right)\}\\ &= -[p]\hat{\mathbf{n}}\sqrt{(\partial_{\alpha_1}\mathbf{r}\cdot\partial_{\alpha_1}\mathbf{r})(\partial_{\alpha_2}\mathbf{r}\cdot\partial_{\alpha_2}\mathbf{r}) - (\partial_{\alpha_1}\mathbf{r}\cdot\partial_{\alpha_2}\mathbf{r})^2},\end{aligned} \tag{5.16}$$

where $R_1 = \rho_s h/(\rho_f L)$ is the dimensionless membrane mass density, $K_s = R_3/(1-\nu^2)$ is a dimensionless stretching stiffness written in terms of $R_3 = Eh/(\rho_f U^2 L)$, the dimensionless stretching rigidity, and we have written out the determinant under the square root explicitly in (5.16). The prestrain $\bar{e}$ in (5.7) is the strain in a membrane under uniform tension $T_0 = K_s\bar{e}$, the "pretension," one of the main control parameters here, as in our 2D study (chapter II). We assume that the thickness ratio h/L is small, but ρ_s/ρ_f may be large, so R_1 may assume any non-negative value. As in chapter II, we have neglected bending rigidity, denoted as R_2 in [10]. In the extensible regime studied here, R_3 is finite, so $R_2 = R_3 h^2/(12L^2) \to 0$ in the limit $h/L \to 0$. For simplicity and for ease of comparison with the 2D case we set the Poisson ratio ν (the transverse contraction due to axial stretching) to zero.

We solve for the flow using the vortex lattice method, a type of panel method [88] that solves for the 3D inviscid flow past a thin body by posing a vortex sheet on the body to satisfy the no-flow-through or kinematic condition. The vortex sheet is advected into the fluid at the body's trailing edge, thus avoiding a flow singularity

there [88]. The velocity $\mathbf{u}$ is a uniform background flow $\widehat{\mathbf{e}}_x$ plus the flow induced by a distribution of vorticity $\boldsymbol{\omega}$, via the Biot-Savart law [149]:

$$\mathbf{u}(\mathbf{x}) = \widehat{\mathbf{e}}_x + \frac{1}{4\pi}\iiint_{\mathbb{R}^3} \boldsymbol{\omega}(\mathbf{x}', t) \times (\mathbf{x} - \mathbf{x}')/\|\mathbf{x} - \mathbf{x}'\|^3 \mathrm{d}\mathbf{x}'. \tag{5.17}$$

The vorticity is a vortex sheet on the body and wake. With the body surface parametrized by α_1 and α_2, we define a local coordinate basis by $\{\widehat{\mathbf{s}}_1, \widehat{\mathbf{s}}_2, \hat{\mathbf{n}}\}$:

$$\widehat{\mathbf{s}}_1 = \frac{\partial_{\alpha_1}\mathbf{r}}{\|\partial_{\alpha_1}\mathbf{r}\|}; \qquad \widehat{\mathbf{s}}_2 = \frac{\partial_{\alpha_2}\mathbf{r}}{\|\partial_{\alpha_2}\mathbf{r}\|}; \qquad \hat{\mathbf{n}} \text{ from (5.12)}. \tag{5.18}$$

Thus $\widehat{\mathbf{s}}_1$ and $\widehat{\mathbf{s}}_2$ span the body's local tangent plane and $\hat{\mathbf{n}}$ is its normal vector. $\widehat{\mathbf{s}}_1$ and $\widehat{\mathbf{s}}_2$ are also the tangents to the material lines $\alpha_2 =$ constant and $\alpha_1 =$ constant, respectively. When the body experiences in-plane shear, $\widehat{\mathbf{s}}_1$ and $\widehat{\mathbf{s}}_2$ are not orthogonal, but they do not become parallel except for singular deformations that we do not consider.

For the vortex sheet on the body, the vorticity takes the form

$$\boldsymbol{\omega}(\mathbf{x}, t) = \boldsymbol{\gamma}(\alpha_1, \alpha_2, t)\delta(n) = \gamma_1(\alpha_1, \alpha_2, t)\delta(n)\widehat{\mathbf{s}}_1 + \gamma_2(\alpha_1, \alpha_2, t)\delta(n)\widehat{\mathbf{s}}_2,$$

with $\delta(n)$ the Dirac delta distribution and n the signed distance from the vortex sheet along the sheet normal. The vorticity is concentrated at the vortex sheet, $n = 0$, and $\boldsymbol{\gamma}$ is the jump in the tangential flow velocity across the vortex sheet [149]. The vorticity can be written similarly in the wake vortex sheet, but a different parametrization is used since α_1 and α_2 are only defined on the body. The nonlinear kinematic equation states that the normal component of the body velocity equals that of the flow velocity at the body [149]:

$$\hat{\mathbf{n}} \cdot \partial_t \mathbf{r} = \hat{\mathbf{n}} \cdot \left(\widehat{\mathbf{e}}_x + \frac{1}{4\pi} \Xint{=}\!\!\!\!\!\!\iint_{S_B + S_W} \boldsymbol{\gamma}(\mathbf{x}', t) \times (\mathbf{r} - \mathbf{x}')/\|\mathbf{r} - \mathbf{x}'\|^3 \mathrm{d}S_{\mathbf{x}'} \right) \tag{5.19}$$

where S_B and S_W are the body and wake surfaces respectively. Since $\mathbf{r}$ and $\mathbf{x}'$ lie on S_B, the integral in (5.19) is singular, defined as a principal value integral.

The pressure jump across the membrane $[p](\alpha_1, \alpha_2, t)$ can be written in terms of the vortex sheet strength components γ_1 and γ_2 using the unsteady Bernoulli equation written at a fixed material point on the membrane. The formula and its derivation are lengthy so they are given in appendix H, but the form of the pressure jump formula is

$$\partial_{\alpha_1}[p] = G(\mathbf{r}, \gamma_1, \gamma_2, \mu_1, \mu_2, \tau_1, \tau_2, \nu_v). \tag{5.20}$$

Here μ_1 and μ_2 are the tangential components of the average of the flow velocity on the two sides of the membrane, i.e., the dot products of $\widehat{\mathbf{s}}_1$ and $\widehat{\mathbf{s}}_2$ with the term in parentheses on the right side of (5.19). τ_1, τ_2, and ν_v are the components of the membrane's velocity in the $\{\widehat{\mathbf{s}}_1, \widehat{\mathbf{s}}_2, \hat{\mathbf{n}}\}$ basis:

$$\tau_1(\alpha_1, \alpha_2, t) = \partial_t \mathbf{r} \cdot \widehat{\mathbf{s}}_1; \qquad \tau_2(\alpha_1, \alpha_2, t) = \partial_t \mathbf{r} \cdot \widehat{\mathbf{s}}_2; \qquad \nu_v(\alpha_1, \alpha_2, t) = \partial_t \mathbf{r} \cdot \hat{\mathbf{n}}. \tag{5.21}$$

(5.20) generalizes the 2D formula from appendix A to the case of an extensible body in a 3D flow. We integrate it from the trailing edge using the Kutta condition

$$[p](\alpha_1 = 1, \alpha_2, t) = 0, \tag{5.22}$$

to obtain $[p](\alpha_1, \alpha_2, t)$ at all points on the membrane.

In summary, equations (5.16), (5.19), and (5.20) are a coupled system of equations for $\mathbf{r}$, $\boldsymbol{\gamma}$, and $[p]$ that we can solve with suitable initial and boundary conditions to compute the membrane dynamics.

5.3 Numerical Method

We solve equations (5.16), (5.19), and (5.20) using an implicit iterative time-stepping approach. At the initial time $t = 0$ the membrane has a very small uniform slope $\partial_{\alpha_1} z / \partial_{\alpha_1} x$ of 10^{-3}, or 10^{-5} if the small-amplitude regime is the focus of interest,

and the free vortex wake has length zero. The background flow speed is increased smoothly from 0 to 1 using a saturating exponential function with a time constant 0.2.

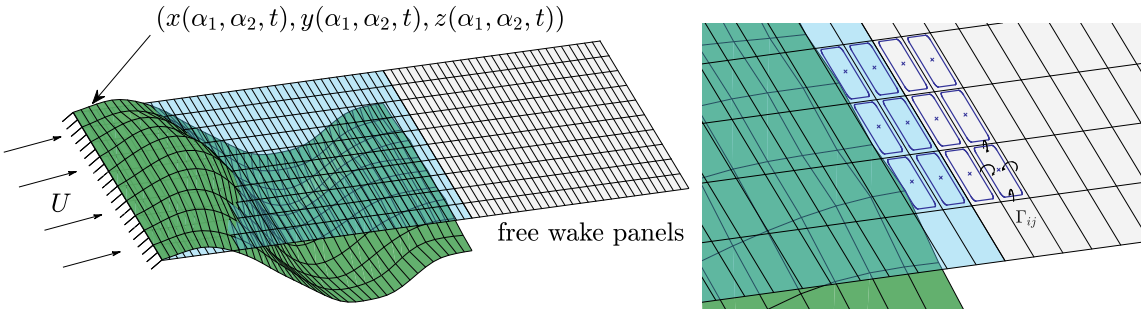

Figure 5.2: Discretization of the membrane surface into panels with vortex rings. On the left, we show an example of an FRRR deformed membrane (dark green surface) used for computing the inertial and elasticity terms, together with the flat membrane panels (light blue surface) and flat wake panels (light gray surface) used for the kinematic condition. On the right, we show a zoomed-in version of the same membrane with a subset of the vortex rings (blue rounded rectangles) on top of the flat membrane and flat wake panels. The curved arrows illustrate the velocity induced by positive Γ according to the right-hand rule.

We discretize the membrane with a uniform rectangular grid of $M+1$ and $N+1$ points in the α_1 and α_2 directions respectively. The membrane grid becomes deformed in physical space; an example is shown by the black lines on the green membrane surface in figure 5.2. The vortex sheet is discretized as a lattice of vortex rings, one per membrane grid cell. Each vortex ring consists of four vortex filaments, one along each side of the grid cell. This discretization is a type of vortex-lattice method [66, 88]. To speed up the computations, we approximate the vortex sheet geometries as flat, a common approach in vortex-lattice methods [66,88]. This occurs in the kinematic equation (5.19), which we solve for $\boldsymbol{\gamma}$ on the body assuming the body position and velocity (i.e., $\mathbf{r}$, $\partial_t \mathbf{r}$, and $\hat{\mathbf{n}}$) and $\boldsymbol{\gamma}$ on the wake are known. The values of $\mathbf{r}$, $\partial_t \mathbf{r}$, and $\hat{\mathbf{n}}$ in (5.19) are those of the true membrane except in the vortex sheet integrals, where they and $\mathbf{x}'$ correspond to the body in its flat position with uniform pretension in the $z = 0$ plane and points in the wake are those of the body's trailing edge, advected at speed 1 in the x-direction. The approximate body

and wake vortex sheets lie on the light blue and light gray regions respectively in figure 5.2. The vortex sheets are approximated by lattices of rectangular vortex rings that lie on the boundaries of the rectangular grid cells. Each line segment in the grid is the support of two vortex lines, one from the vortex ring of each neighboring grid cell. The inset at the right of figure 5.2 shows a schematic example of 12 vortex rings in a 3-by-4 portion of the lattice that runs across the membrane's trailing edge. The vortex rings are shown as blue rounded rectangles slightly inside each black rectangular boundary, but they actually run along the black edges. The circular arrows show the velocity induced by a single vortex ring marked Γ_{ij}.

The net circulation along each lattice line segment is the difference of the circulations in the two neighboring vortex rings. The net circulation per unit length in the $\widehat{\mathbf{s}}_1$ direction converges to γ_1 in the limit of small mesh spacing in that direction, and similarly for γ_2:

(5.23)
$$\gamma_1|_{x_{i+1/2},y_j} \approx -\frac{\Gamma|_{x_{i+1/2},y_{j+1/2}} - \Gamma|_{x_{i+1/2},y_{j-1/2}}}{y_{j+1/2} - y_{j-1/2}};\ \gamma_2|_{x_i,y_{j+1/2}} \approx \frac{\Gamma|_{x_{i+1/2},y_{j+1/2}} - \Gamma|_{x_{i-1/2},y_{j+1/2}}}{x_{i+1/2} - x_{i-1/2}}$$

using centered difference approximations. We linearly interpolate these expressions to obtain γ_1 and γ_2 values at the panel edge midpoints from these expressions to values at the panel corners $\{x_i, y_j\}$ and thus obtain $\partial_{\alpha_1}[p]$ in (5.20).

We solve for the strengths of the vortex rings by imposing (5.19) at a set of $\mathbf{r}$ (in the integral), called the control points or collocation points in vortex-lattice methods, and here located at the centers of each vortex ring (shown as crosses in the inset at the right of figure 5.2). [65, 205] also placed the control points at the centers of their vortex rings, quadrilaterals and triangles respectively. Other methods shift the vortex rings and control points downstream by one-quarter mesh spacing, which reproduces certain formulas for the lift and moment on a flat plate [66, 73, 77, 88, 120]. Such meth-

ods are considered low-order methods, in contrast to higher-order methods that use curved body panel geometries and nonconstant polynomial representations for the distribution of circulation or velocity potential on each panel [29, 200]. We proceed with the low-order method described here for simplicity and because we find remarkably good agreement with 2D results using a different discretization method based on Chebyshev polynomials and including the non-flat geometries of the body and wake vortex sheets, including wake roll-up (chapter II). We also find good agreement among results with different mesh sizes, although they indicate spatial convergence below first order (see §5.4).

The integral in (5.19) is replaced by a sum that gives the velocity induced by the four sides of all the vortex rings. From [88], the velocity induced at a point $\mathbf{x}_p$ by a straight vortex line segment with circulation Γ that runs from $\mathbf{x}_1$ to $\mathbf{x}_2$ is

(5.24)
$$\mathbf{u} = \frac{\Gamma}{4\pi|\mathbf{r}_1 \times \mathbf{r}_2|^2}\left(\frac{(\mathbf{r}_2-\mathbf{r}_1)\cdot\mathbf{r}_1}{\|\mathbf{r}_1\|} - \frac{(\mathbf{r}_2-\mathbf{r}_1)\cdot\mathbf{r}_2}{\|\mathbf{r}_2\|}\right)\cdot(\mathbf{r}_1\times\mathbf{r}_2);\ \mathbf{r}_1 \equiv \mathbf{x}_p - \mathbf{x}_1,\ \mathbf{r}_2 \equiv \mathbf{x}_p - \mathbf{x}_2.$$

When discretized, (5.19) becomes a linear system of equations for the vortex ring strengths. The key advantage of approximating the body and wake vortex sheets as flat is that we can precompute all the matrix entries in the linear system (the "influence coefficients," i.e., sums of the coefficients of Γ in (5.24)), before the time-stepping iterative solver for the membrane position. For an M-by-N lattice of vortex rings on the body and an M_w-by-N lattice in the wake (typically $M_w \gg M$), the cost of computing the influence coefficients would be $O(MM_wN^2)$ per iteration within each time step for general membrane and wake shapes, but for flat vortex sheets this can be reduced to a one-time cost of $O(MM_wN)$ (actually less) using repetition in relative positions of control points and vortex rings in the flat wake to change from N^2 to N. We also avoid an even larger cost to evolve the vortex wake position,

$O(M_w^2 N^2)$, though this could be reduced using fast summation methods [105]. The right-hand-side vector for the linear system consists of the remaining terms in (5.19), the body velocity and the background flow, using the actual (non-flat) membrane position, and interpolated to give values at the control points.

The algorithm alternates between computing the membrane position at the current time step and updating the vortex wake circulation for the next time step. To compute the membrane position at the current time step, the distribution of circulation in the vortex wake is assumed to be known from the previous steps of the algorithm, and is zero initially. We then use a quasi-Newton iterative method (Broyden's method [140]) to solve for the x, y, and z components of the membrane position on the interior points of the α_1-α_2 grid, resulting in $3(M-1)(N-1)$ unknowns for the iterative solver.

Broyden's method solves a nonlinear system of equations $\mathbf{f}(\mathbf{x}) = \mathbf{0}$. In our case $\mathbf{x}$ is a vector whose entries are the x, y, and z components of the membrane position $\mathbf{r}$ on the interior points of the α_1-α_2 grid. $\mathbf{f}$ is a vector given by the three components of the membrane equation (5.16), discretized at the interior α_1-α_2 grid points using second-order finite differences for the temporal and spatial derivatives of the membrane position. One-sided spatial differentiation formulas are used near boundaries and backward temporal differentiation formulas are used, with the given initial values for the membrane position and background flow, and zero initial bound circulation (see appendix I for details). $\mathbf{f}$ requires the membrane position boundary values, which are either prescribed (for a fixed boundary) or deduced from the guesses for the values at the interior mesh points (for a free boundary). At each time step Broyden's method produces a sequence of iterates that converges to the solution for $\mathbf{x}$ starting from an initial guess, which we choose to be the membrane position at the previous time

step. Usually convergence is obtained in just a few iterations.

Given the free wake position and circulation and the guess for $\mathbf{r}$, we compute $\partial_t \mathbf{r}$ and $\hat{\mathbf{n}}$ and then compute the membrane circulation values by solving the linear system with influence coefficients corresponding to the discretized kinematic equation (5.19). The membrane circulation (and other quantities derived from it and $\mathbf{r}$) are used to compute $\partial_{\alpha_1}[p]$ in the membrane equation (5.16), by integrating (5.20) from the trailing edge using the trapezoidal rule. All quantities on the right hand side of (5.20) can be evaluated using the guess for $\mathbf{r}$ and the circulations of the vortex rings on the membrane. Some quantities (e.g., γ_1 and γ_2) are computed on the panel edge midpoints and others (e.g., μ_1 and μ_2) on the panel centers; these are extrapolated to the corner points of each panel, where $\partial_{\alpha_1}[p]$ is evaluated. Before integrating $\partial_{\alpha_1}[p]$, we decouple it into two parts, as explained at the end of appendix H. We integrate one part analytically and the other part numerically using the trapezoidal rule, and apply $[p] = 0$ at the trailing edge. We use this decoupled approach because it gives much better agreement with our previous 2D computations.

When Broyden's method converges, we obtain the membrane position at the current time step and the circulation values on the membrane. The next step is to update the wake circulation values for the next time step. This is done by moving the vortex rings in the wake and the last row of the vortex rings on the body downstream at speed 1. This is a flat-wake approximation of the more general statement that lines in the wake vortex sheet move at the average of the tangential components of the flow velocity on the two sides of the wake vortex sheet [149]. This turns out to be equivalent to the condition that the pressure jump is zero across the wake, and advecting the last row of vortex rings on the membrane into the wake at the trailing-edge flow velocity imposes $[p] = 0$ at the trailing edge, known as the unsteady Kutta

condition, which makes flow velocity finite at the trailing edge [88, 149]. The time step is set equal to the streamwise grid spacing, so to move downstream at speed 1 each vortex ring in the wake and along the membrane trailing edge in figure 5.2 simply shift to the next panel downstream.

In the next section we study the convergence of this numerical method as the membrane grid is refined, and compare the large-span 3D solutions with 2D membrane solutions computed using the method in chapter II.

5.4 Validation of the 3D Model and Algorithm

We now study the effect of spatial grid refinement on membrane dynamics in test cases using a square membrane at four different combinations of boundary conditions and physical parameters. We then compare 3D results in the quasi-2D limit (large span, free side edges) with results at same parameters using our previous 2D algorithm that had several differences: a Chebyshev-Lobatto mesh and Chebyshev differentiation matrices were used; the kinematic and Kutta conditions were imposed with a Chebyshev-Galerkin method and non-flat vortex sheets; and the full (non-flat) dynamics of the vortex sheet wake was computed (chapter II). Three cases are compared: (i) fixed–fixed (2D) and FRFR (3D), (ii) fixed–free (2D) and FRRR (3D), (iii) free–free (2D) and RRRR (3D).

5.4.1 Spatial Convergence for a Square Membrane

Ours and most other implementations of the vortex-lattice method are considered low-order methods, as flat rather than curved body panel geometries are used, as well as vortex rings rather than nonconstant polynomial distributions of circulation on each panel [29, 122, 200]. First-order spatial accuracy was found for certain quantities by [62, 111] using similar versions of the vortex-lattice method. We study the

spatial convergence of our method in four test cases with the following boundary conditions and (R_1, T_0, R_3) values, one from each of the colored boxes in figure 5.1: an FFFF membrane with $(R_1, T_0, R_3) = (10^{-0.5}, 10^{-0.5}, 10^{0})$, an FFRF membrane with $(10^{0.5}, 10^{-0.75}, 10^{1})$, an RFFF membrane with $(10^{0.5}, 10^{-0.5}, 10^{1})$, and an RFRF membrane with $(10^{0}, 10^{-0.75}, 10^{1})$. All membranes have aspect ratio one ($W/2L = 1$). We compute the dynamics of the membrane up to a time $t_p \in [20, 30]$ at which large-amplitude oscillatory motion occurs, and record the maximum of $|z(\alpha_1, \alpha_2, t)|$ over the membrane surface and time.

In table 5.1 we present the maximum $|z|$ values for four different streamwise mesh spacings $\mathrm{d}x$ together with the change in $\max|z|$ between two successive $\mathrm{d}x$ values, and the estimated order of convergence using three successive $\mathrm{d}x$ values:

(5.25)
$$\Delta \max|z| \equiv \left|\max|z|_{\mathrm{d}x} - \max|z|_{\mathrm{d}x/2}\right|, \qquad \text{Order} \equiv \log_2 \frac{\left|\max|z|_{\mathrm{d}x} - \max|z|_{\mathrm{d}x/2}\right|}{\left|\max|z|_{\mathrm{d}x/2} - \max|z|_{\mathrm{d}x/4}\right|}.$$

We fix the spanwise mesh spacing $\mathrm{d}y = 2/10$ (so ten panels cover the span), and recall that $\mathrm{d}t = \mathrm{d}x$ in all cases, so the time step and streamwise mesh spacing are refined together.

In general RFFF membranes take a long time to reach the large-amplitude regime (across R_1), so the computations with $\mathrm{d}x = 2/160$ and $2/320$ were omitted because they were very expensive to compute (due to the large wake size needed). Although the order of convergence is below one in many cases, the $\Delta \max|z|$ values are quite small. We guess that $\Delta \max|z|$ is a reasonable estimate of the error in each case, the difference between the computed solution and the solution in the limit $\mathrm{d}x \to 0$. As a compromise between computational effort and accuracy, we use $\mathrm{d}x = 2/40$ ($M = 40$) in most cases (i.e., throughout §5.5), but we present a few comparisons between $\mathrm{d}x = 2/40$, $2/80$, and $2/160$ in the next subsection and find that the results are

Table 5.1: $\mathrm{d}x$-convergence with fixed $\mathrm{d}y = 2/10$ for four cases with boundary conditions and t_p listed at the top, and (R_1, T_0, R_3) below, for membranes with aspect ratio 1. The change in $\max|z|$ between successive $\mathrm{d}x$ values and the estimated order of convergence are defined in (5.25).

	FFFF, $t_p = 30$			FFRF, $t_p = 22$		
	$(10^{-0.5}, 10^{-0.5}, 10^{0})$			$(10^{0.5}, 10^{-0.75}, 10^{1})$		
$\mathrm{d}x$	$\max\|z\|$	$\Delta\max\|z\|$	Order	$\max\|z\|$	$\Delta\max\|z\|$	Order
2/40	0.5596	0.0171	1.89	0.2169	7.71×10^{-3}	1.55
2/80	0.5425	4.60×10^{-3}	1.46	0.2092	2.64×10^{-3}	0.63
2/160	0.5379	1.67×10^{-3}	...	0.2066	1.71×10^{-3}	...
2/320	0.5363	...	...	0.2048	...	...

	RFFF, $t_p = 22$			RFRF, $t_p = 20$		
	$(10^{0.5}, 10^{-0.5}, 10^{1})$			$(10^{0}, 10^{-0.75}, 10^{1})$		
$\mathrm{d}x$	$\max\|z\|$	$\Delta\max\|z\|$	Order	$\max\|z\|$	$\Delta\max\|z\|$	Order
2/40	0.2417	4.72×10^{-3}	—	0.2891	9.85×10^{-3}	0.57
2/80	0.2369	—	—	0.2989	6.64×10^{-3}	0.38
2/160	—	—	...	0.3056	5.09×10^{-3}	...
2/320	—	...	...	0.3107	...	...

qualitatively similar.

Table 5.2: $\mathrm{d}y$-convergence with fixed $\mathrm{d}x = 2/40$ for a membrane with aspect ratio 1. The error and order of convergence shown are computed using (5.25) but varying $\mathrm{d}y$ instead of $\mathrm{d}x$. The (R_1, T_0, R_3) values are the same as in table 5.1.

	FFFF, $t_p = 30$			FFRF, $t_p = 22$		
	$(10^{-0.5}, 10^{-0.5}, 10^{0})$			$(10^{0.5}, 10^{-0.75}, 10^{1})$		
$\mathrm{d}y$	$\max\lvert z\rvert$	$\Delta\max\lvert z\rvert$	Order	$\max\lvert z\rvert$	$\Delta\max\lvert z\rvert$	Order
2/10	0.5596	0.0119	2.05	0.2169	7.56×10^{-3}	2.29
2/20	0.5715	2.87×10^{-3}	6.13	0.2093	1.54×10^{-3}	8.62
2/40	0.5744	4.11×10^{-5}	...	0.2078	3.93×10^{-6}	...
2/80	0.5744	...	...	0.2078	...	...
	RFFF, $t_p = 22$			RFRF, $t_p = 20$		
	$(10^{0.5}, 10^{-0.5}, 10^{1})$			$(10^{0}, 10^{-0.75}, 10^{1})$		
$\mathrm{d}y$	$\max\lvert z\rvert$	$\Delta\max\lvert z\rvert$	Order	$\max\lvert z\rvert$	$\Delta\max\lvert z\rvert$	Order
2/10	0.2417	2.14×10^{-3}	0.08	0.2891	7.59×10^{-3}	1.70
2/20	0.2438	2.02×10^{-3}	5.54	0.2815	2.34×10^{-3}	1.63
2/40	0.2418	4.35×10^{-5}	...	0.2792	7.58×10^{-4}	...
2/80	0.2418	...	...	0.2784	...	...

Table 5.2 shows the $\max|z|$ values at four choices of the spanwise mesh spacing $\mathrm{d}y$, with $\mathrm{d}x$ fixed at 2/40 and the other parameters the same as in table 5.1. The $\mathrm{d}y$ convergence is much faster than the $\mathrm{d}x$ convergence, presumably because $\mathrm{d}x$ sets the resolution near the membrane trailing edge, a particularly sensitive region due to the vortex shedding there [4, 5, 66]. $\Delta\max|z|$ is uniformly small in table 5.2, at most 4.4% of the last $\max|z|$ value (with $\mathrm{d}y = 2/80$). For computational efficiency with reasonable accuracy we use $\mathrm{d}y = 2/10$ ($N = 10$) in most cases (i.e., throughout

§5.5). Other recent vortex lattice works have also found that a modest number of grid points in the spanwise direction is sufficient for good accuracy (e.g., [108], [88, p. 429], and [129, figure 6]).

5.4.2 Comparisons of 2D and 3D Results with Different Mesh Sizes

We now compare 3D results with free side edges with results from our 2D algorithm (chapter II) in cases with both small- and large-amplitude dynamics. We begin by comparing the 2D fixed–fixed case with the 3D FRFR case (fixed leading and trailing edges, free side edges). We simulate both cases by starting with a flat membrane at $t = 0$, and for $t > 0$ we keep the leading edge fixed at $z = 0$ and move the trailing edge slightly away from and back to $z = 0$:

$$z_{2D}(1,t) = z_{3D}(1,\alpha_2,t) = 2\sin\left(\sigma\left(\frac{t}{\eta}\right)^3 \mathrm{e}^{-(t/\eta)^3}\right), \quad -\frac{W}{2L} \le \alpha_2 \le \frac{W}{2L}, \tag{5.26}$$

where σ is a small constant, 10^{-6}–10^{-3}, and $\eta = 0.2$.

On the left side of figure 5.3, the panels plot the z-deflection of the membrane center (in 3D) or midpoint (in 2D) versus time at three choices of (R_1, T_0, R_3) (listed in the caption) in panels (a)–(c). The 2D membrane has a Chebyshev-Lobatto mesh with 41 points. In 3D, the number of panels in the streamwise direction (M) is 40, 80, or 160, with the aspect ratio $W/2L = 4$, and the number of panels in the spanwise direction (N) is 10 in each case. The perturbation size, σ in (5.26), is 10^{-6}. In panels (a)–(c), the 3D graphs become closer to the 2D graph as M increases.

To the right of each set of time plots, membrane snapshots are shown, equally spaced in time, for 2D (green lines) and 3D (with the same colors as in the time plots, for each M), where the line shows the midspan profile. In all three examples, the membranes tend to a steady single-hump shape at large times, as shown for the 2D case in chapter II. In figure 5.3 there is good qualitative agreement in all the

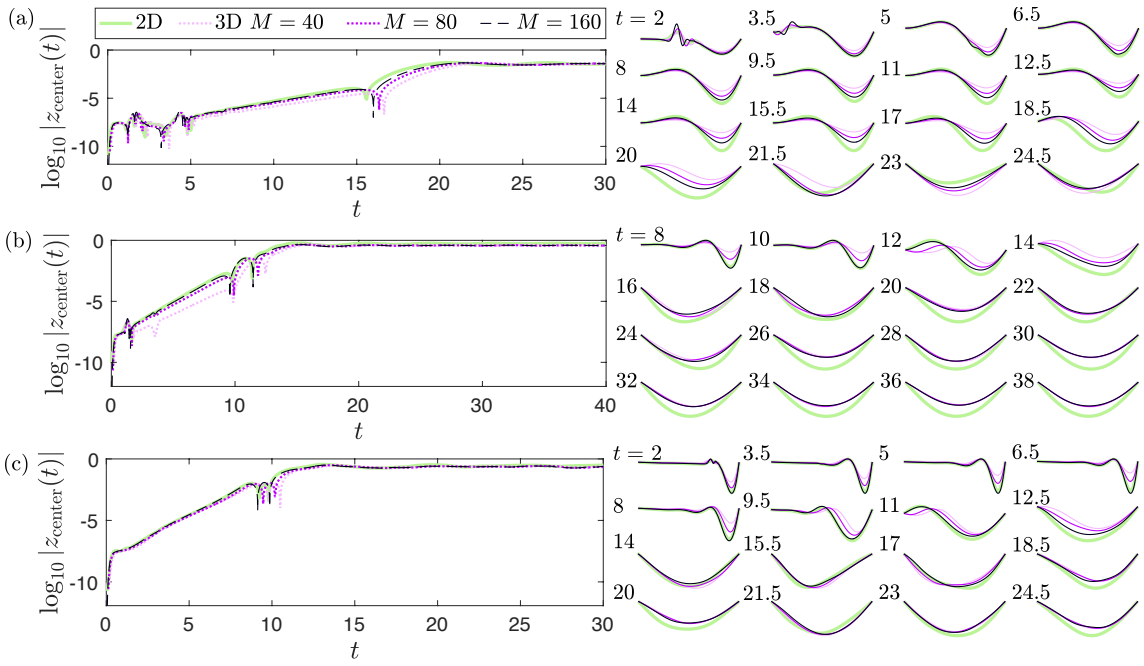

Figure 5.3: Comparisons of fixed–fixed (2D) and FRFR (3D) computations at three choices of (R_1, T_0, R_3): (a) $(10^0, 10^{-0.25}, 10^3)$, (b) $(10^{-0.5}, 10^{-0.5}, 10^1)$, and (c) $(10^{0.25}, 10^{-0.75}, 10^{1.5})$. Recall that R_1 is the dimensionless membrane mass, T_0 is the dimensionless pretension, and R_3 is the dimensionless stretching rigidity. The panels at left show plots of $\log_{10}|z_{\text{center}}|$ versus time. At right, snapshots of membranes at equally spaced times (labeled at top left) are shown. The plots and snapshots are green for 2D membranes and light pink ($M = 40$), dark pink ($M = 80$), or black ($M = 160$) for 3D membranes. Here the aspect ratio $W/2L = 4$, $N = 10$, and $\sigma = 10^{-6}$ in (5.26).

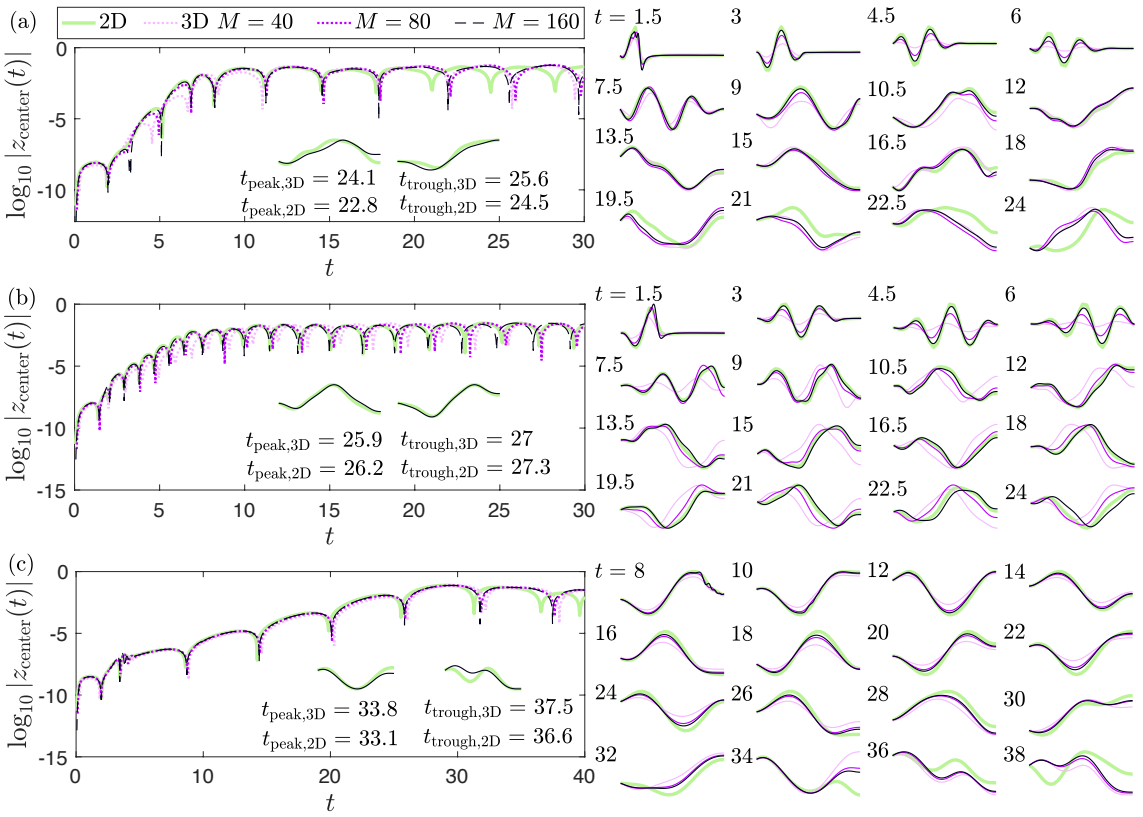

Figure 5.4: Comparisons of fixed–free (2D) and FRRR (3D) computations at three choices of (R_1, T_0, R_3): (a) $(10^0, 10^{-1}, 10^2)$, (b) $(10^{-0.5}, 10^{-1}, 10^2)$, and (c) $(10^{0.5}, 10^{-0.5}, 10^2)$. The panels at left show plots of $\log_{10}|z_{\text{center}}|$ versus time. At right, snapshots of membranes at equally spaced times (labeled at top left) are shown. The plots and snapshots are green for 2D membranes and light pink ($M = 40$), dark pink ($M = 80$), or black ($M = 160$) for 3D membranes. Here the aspect ratio $W/2L = 4$, $N = 10$, and $\sigma = 10^{-6}$ in (5.27).

membranes' motions, and good quantitative agreement in most cases, particularly between $M = 160$ (black lines) and 2D (green lines) in the small-amplitude (growth) regime. At later times, the 3D snapshots tend to converge, while the 2D snapshot is noticeably displaced from them, particularly in panel (b). The differences between 2D and 3D may be due in part to algorithmic differences, and to differences in the flows due to the finite span in 3D.

Next we compare the 2D fixed–free case with the 3D FRRR case. Now the trailing edge is free, and a small transient perturbation is applied at the leading edge:

$$z_{2D}(-1,t) = z_{3D}(-1,\alpha_2,t) = \sin\left(\sigma\left(\frac{t}{\eta}\right)^3 \mathrm{e}^{-(t/\eta)^3}\right), \quad -\frac{W}{2L} \le \alpha_2 \le \frac{W}{2L}. \tag{5.27}$$

Figure 5.4 compares the membranes' center-point deflections and snapshots similarly to figure 5.3 but at three different choices of (R_1, T_0, R_3), given in the figure 5.4 caption. In the fixed–free case, oscillatory motions occur at large amplitude (chapter II), and they tend to be periodic rather than chaotic at the $O(1)$ values of R_1 used in figure 5.4. Again, there is good qualitative agreement in all cases, and good quantitative agreement particularly in the linear growth regime. At large times in panels (a) and (c) the three 3D cases are clustered together and are somewhat separate from the 2D case. In panel (b) the $M = 160$ and 2D case are relatively close, even at large times. Within each panel the graphs have somewhat different periods of oscillation at large amplitude, including some abrupt changes in the period, e.g., the 2D graph near the final time in panel (c). However, if we compare the snapshots at qualitatively similar times, i.e., at nearby peaks and troughs of the $\log_{10}|z_{\text{center}}(t)|$ plots, instead of at the same times, then we find better agreement. Comparisons of the 2D case and the 3D case with $M = 160$ at nearby peaks and troughs are shown below the time plots, and show better agreement than in the late-time comparisons on the right side of the figure.

Finally, we compare the free–free 2D case with 3D RRRR cases. Now the membrane starts with a small nonzero slope:

$$z_{2D}(\alpha_1, 0) = z_{3D}(\alpha_1, \alpha_2, 0) = \sigma\alpha_1 \ , \quad -\frac{W}{2L} \le \alpha_2 \le \frac{W}{2L}, \tag{5.28}$$

for $\sigma = 10^{-3}$. In figure 5.5 we again compare the membranes' deflections and snapshots for three different (R_1, T_0, R_3) combinations (in the figure caption) with $R_1 = O(1)$ that have qualitatively different dynamics. With all edges free, the membrane can move uniformly upward or downward yet keep the same shape, so there is a translational z motion to consider along with the evolution of the membrane shape. Therefore, on the left side we plot the membrane deflection versus time, defined here

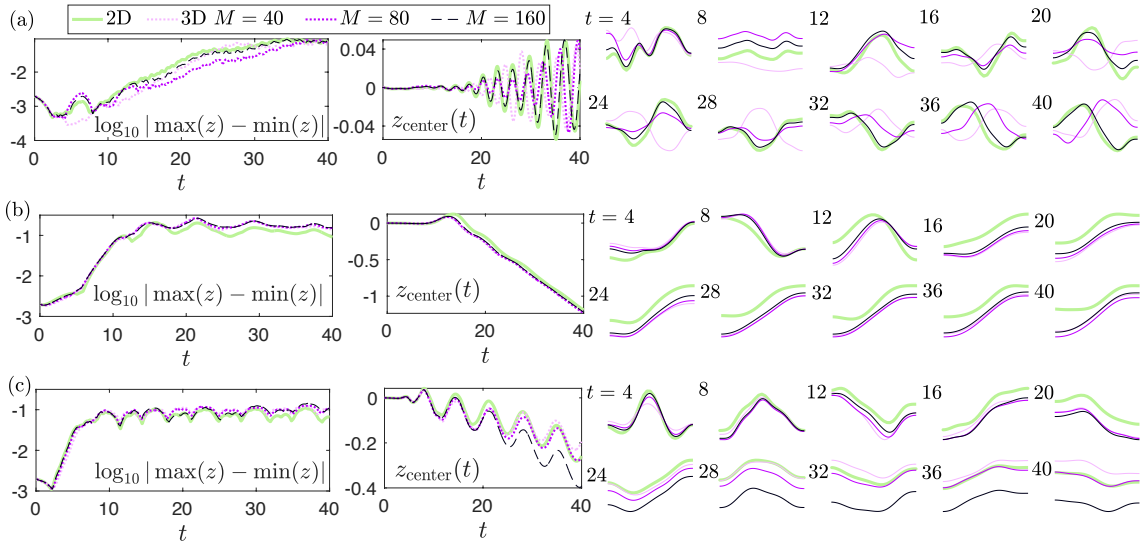

Figure 5.5: Comparisons of free–free (2D) and RRRR (3D) computations at three choices of (R_1, T_0, R_3): (a) $(10^{-0.5}, 10^{-0.75}, 10^{1})$, (b) $(10^{0.5}, 10^{-0.5}, 10^{2})$, and (c) $(10^{-0.25}, 10^{-0.8}, 10^{2})$. The panels at left show plots of $\log_{10} |\max(z) - \min(z)|$ and z_{center} versus time. At right, snapshots of membranes at equally spaced times (labeled at top left) are shown. The plots and snapshots are green for 2D membranes and light pink ($M = 40$), dark pink ($M = 80$), or black ($M = 160$) for 3D membranes. Here the aspect ratio $W/2L = 4$, $N = 10$, and $\sigma = 10^{-3}$ in (5.28).

as $|\max(z) - \min(z)|$, with max and min taken over α_1 (and α_2 for 3D), and we also plot $z_{\text{center}}(t)$, which shows the net translational motion. Panel (a) shows an oscillatory motion of z_{center}, (b) shows a steady translation, and (c) shows a combination of the two. As in the fixed–fixed and fixed–free cases, in each panel the agreement in the deflection $|\max(z) - \min(z)|$ is generally best at early times, and at later times there is a more noticeable difference, particularly between the 2D and 3D plots in panels (b) and (c). The snapshots at the right show that in many cases the shapes agree well but there is a translational shift, particularly at $t = 8$ in (a) (where the shift is small, $\approx 10^{-3}$) and at larger times in (c). As in the fixed–free case, there are noticeable phase shifts among the motions at later times for the oscillatory case in panel (a).

In summary, the comparisons of 3D motions at $M = 40$, 80, and 160 and the 2D motion have shown good qualitative agreement in the types of dynamics—steady or

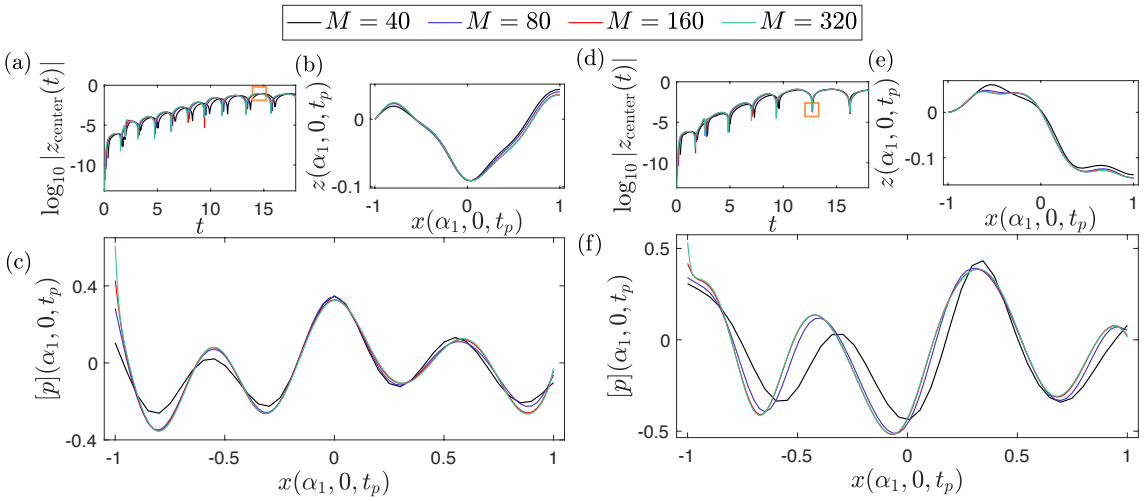

Figure 5.6: Two examples of how the pressure distribution changes with increasing numbers of streamwise panels. Panels (a)–(c) show plots of $\log_{10}|z_{\text{center}}|$ versus time and $z(\alpha_1, 0, t_p)$ and $[p](\alpha_1, 0, t_p)$ versus $x(\alpha_1, 0, t_p)$, respectively, for an FRRR membrane with $R_1 = 10^{-0.25}$, $T_0 = 10^{-0.75}$, and $R_3 = 10^1$ at times t_p where $|z_{\text{center}}(t)|$ has a peak that is closest to 14.5 (enclosed in the orange square), for each M. Panels (d)–(f) show the same quantities for an FRRR membrane with $R_1 = 10^0$, $T_0 = 10^{-0.75}$, and $R_3 = 10^1$, for the troughs in $|z_{\text{center}}(t)|$ nearest to $t_p \approx 12.6$. The plots are black for $M = 40$, blue for $M = 80$, red for $M = 160$, and green for $M = 320$. Here the aspect ratio $W/2L = 4$, $N = 10$, and $\sigma = 10^{-4}$ in (5.27).

oscillatory, with or without translation—and good quantitative agreement as well in the magnitudes of the deflections, the frequencies of oscillations, and many detailed aspects of the dynamics.

Inviscid simulations of airfoils and flapping plates in 2D and 3D have shown that the largest computational errors tend to occur in flow quantities near the trailing edge [2, 5, 66, 88]. The Kutta condition makes the flow velocity and pressure jump finite there, but their spatial derivatives across the edge are infinite there in general [5], and the numerical solution is sensitive to the mesh near the trailing edge [5, 66]. For the present simulations, this sensitivity can be seen in the pressure jump distribution near the trailing edge. In figure 5.6 we plot the pressure jump versus streamwise location along the membrane midspan, $y = 0$, for two different examples of FRRR membranes in the large-amplitude regime, at R_1, T_0, and R_3 given in the figure caption, and for various M listed at the top. Both cases reach oscillatory large-amplitude states,

shown by the center deflection versus time in panels (a) and (d) respectively. In panels (b) and (e) we compare the midspan deflections that occur at $|z_{\text{center}}|$ peaks near $t = 14.5$ and troughs near 12.6, respectively—the peaks and troughs that occur in the orange boxes of panels (a) and (d). For each M the times of the peaks/troughs are slightly different due to phase shifts, as in the snapshot comparisons in the left panels of figure 5.4. Panels (c) and (f) show the midspan pressure jump distributions at these times. The pressure jump distributions are more oscillatory and have larger deviations at these M than the deflections ((b) and (e)), perhaps because in the membrane equation (5.16) $[p]$ is balanced by terms that include second derivatives of deflection, so z is smoother than $[p]$. The pressure jump distributions in (c) and (f) only approximately reach zero at the trailing edge, more closely for larger M, which also resemble the generic square-root behavior there, as well as the generic inverse-square-root behaviors at the leading edge [4, 5, 55]. Although the deviations from $M = 40$ to 320 are significant, the overall form of the $[p]$ and z distributions at $M = 40$ are reasonable approximations to those at $M = 320$.

Now we briefly present a comparison of dynamics in 2D and 3D using different numbers of panels across the span for 3D: $N = 10$, 20, and 40. Figure 5.7 shows comparisons of (a) fixed–fixed, (b) fixed–free, and (c) free–free 2D cases with the corresponding 3D cases at $M = 40$ and aspect ratio 4. The 3D plots converge more rapidly here with increasing N than with increasing M in the previous figures, similarly to tables 5.1 and 5.2. In the remainder of this work we use $N = 10$.

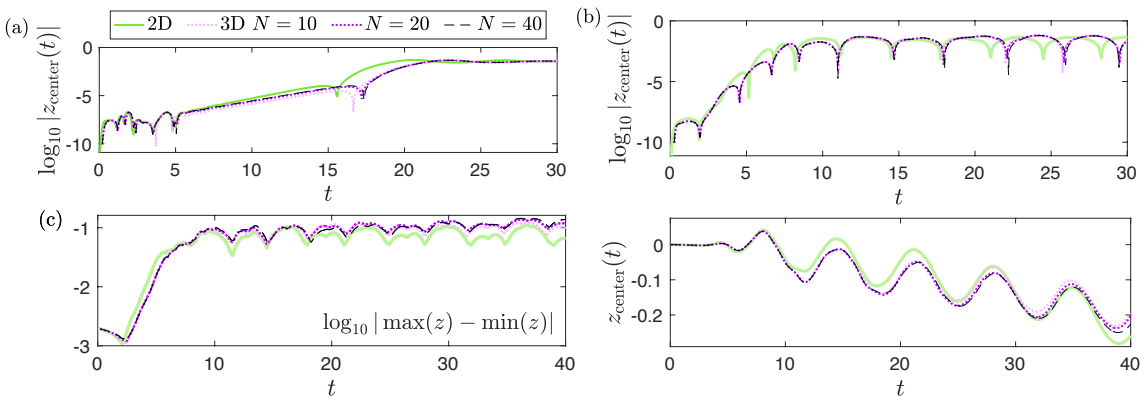

Figure 5.7: Comparisons of 2D and 3D membrane deflections at three boundary conditions and (R_1, T_0, R_3) values: (a) fixed–fixed versus FRFR at $(10^0, 10^{-0.25}, 10^3)$; (b) fixed–free versus FRRR at $(10^0, 10^{-1}, 10^2)$ and (c) free–free versus RRRR at $(10^{-0.25}, 10^{-0.8}, 10^2)$, where both $\log_{10}|\max(z) - \min(z)|$ and z_{center} are plotted, at left and right respectively. The plots are green for 2D membranes and light pink ($N = 10$), dark pink ($N = 20$), or black ($N = 40$) for 3D membranes. Here 41 Chebyshev-Lobatto points are used in 2D and for the 3D cases $W/2L = 4$, $M = 40$, and $\sigma = 10^{-6}$, 10^{-6}, and 10^{-3} respectively in (a)–(c).

We have compared the small- and large-amplitude dynamics in 2D and 3D at several (R_1, T_0, R_3) values, and shown the effect of varying the numbers of streamwise and spanwise panels in 3D, M and N, at aspect ratio 4. Next, we compare the dynamics across a much larger set of R_1 and T_0 values, but restricted to the small-amplitude regime (where R_3 has a negligible effect). We also show the effect of increasing the 3D membrane aspect ratio from 1 to 8, approaching the 2D limit.

5.4.3 Comparison of Stability Boundaries and Mode Shapes in 2D and 3D

The small-amplitude membrane dynamics can be organized in terms of the stability boundary in R_1-T_0 space. We again apply the small perturbations (5.26)–(5.28) to the FRFR, FRRR, and RRRR membranes, across a grid of values in R_1-T_0 space. At each R_1 we find exponential decay in membrane deflections above a critical T_0 and exponential growth below this T_0 (followed by large-amplitude, nonlinear dynamics). The stability boundary is the curve of critical T_0 versus R_1, and is found by interpolating between neighboring T_0 points with positive and negative growth

rates.

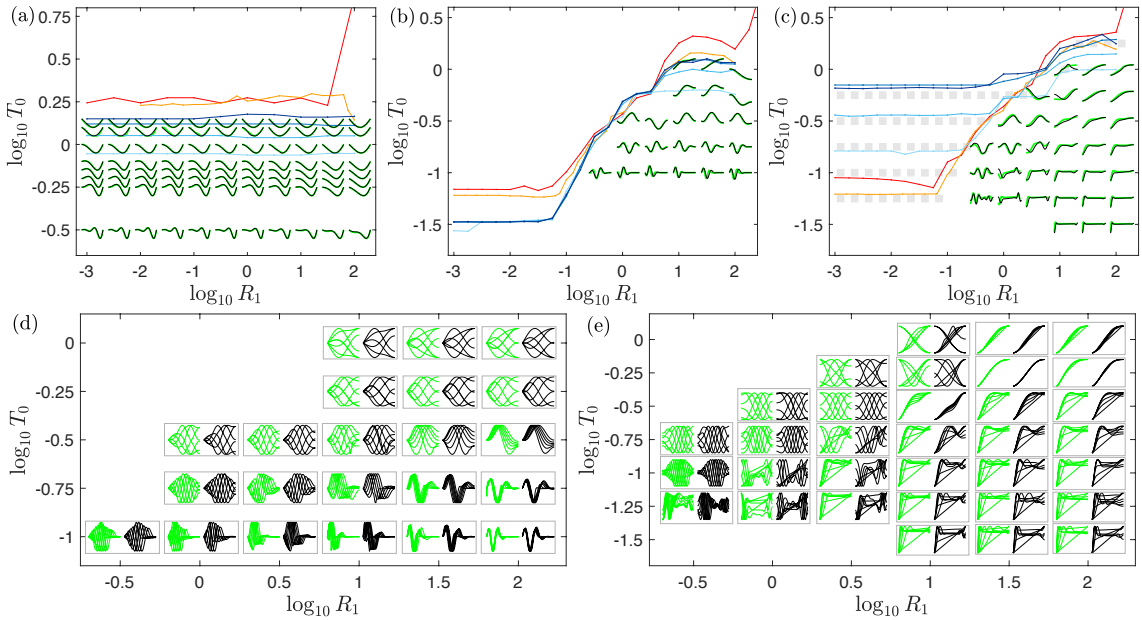

Figure 5.8: Comparisons of stability boundaries in 2D (orange from chapter II; red from chapter III) and 3D with aspect ratios 1, 2, 4, and 8 (ranging from light blue to dark blue) for (a) fixed–fixed and FRFR, (b) fixed–free and FRRR, and (c) free–free and RRRR cases. Below the stability boundary, 3D midspan profiles with aspect ratio 8 (black) are compared with 2D profiles (green) during the linear growth regime. Here $R_3 = 10^1$, $N = 10$, $M = 40$ (for FRFR and FRRR membranes) and $M = 80$ (for RRRR membranes) for all aspect ratios.

In figure 5.8 we compare the stability boundaries in the 2D fixed–fixed (a), fixed–free (b) and free–free (c) cases with the 3D FRFR, FRRR, and RRRR cases respectively, with 3D aspect ratios 1, 2, 4, and 8. Two stability boundaries are shown for the 2D case. The orange lines, from chapter II, are calculated from the growth rates in time-stepping simulations starting from small perturbations, as in the 3D cases here. The red lines, from chapter III, are calculated by linearizing the 2D equations and solving the nonlinear eigenvalue problem; the imaginary parts of the eigenvalues are the growth rates. The eigenvalue method was able to identify very small positive growth rates at $R_1 \geq 10^2$, too small to be distinguishable from no growth or very slow decay in the time-stepping method. Here the red line has a sharply upward slope (similar to [184]), unlike the orange line. The stability boundaries for the 3D

cases with aspect ratios 1, 2, 4, and 8 range from light blue to dark blue. In (a) and at large R_1 in (b) and (c) the boundaries tend towards the 2D boundaries as aspect ratio increases. As in studies of 3D flexible plates [18, 42, 43], more bodies are unstable at high aspect ratio, i.e., the stability boundary moves up as the aspect ratio increases. In the region of instability for aspect ratio 8, we compare the aspect-ratio-8 midspan snapshots at small amplitude (black lines) with the 2D snapshots (green lines) over a range of R_1 and T_0. In (a), all the membranes lose stability by divergence without flutter, so the membranes' deflections grow exponentially without change of shape. The snapshots show the eigenmode shapes, which become more fore-aft asymmetric as T_0 decreases, although at large amplitude the membranes tend to single-hump shapes that are nearly fore-aft symmetric as in figure 5.3. The agreement is uniformly very good between 2D and 3D in panel (a).

Panel (b) shows the same comparison for the 2D fixed–free and 3D FRRR cases. The modes are somewhat underresolved for $T_0 < 10^{-1}$ and the growth rates in 2D and 3D do not agree well, so we omit the membrane snapshots in this region of the parameter space. Even with a much finer mesh, the fastest growing 2D modes are difficult to resolve in this region using an eigenvalue solver (chapter III). This underresolution may affect the apparent lack of convergence of the 3D stability boundaries with increasing aspect ratio to the 2D boundaries at small R_1. At moderate R_1 ($\in [10^{-0.5}, 10^{0.5}]$), interestingly, the stability boundaries approximately coincide at all aspect ratios, while at larger R_1 the stability boundaries shift upward with increasing aspect ratio similarly to panel (a). Unlike in panel (a), here the snapshots oscillate and change shape in the small-amplitude growth regime. In panel (d) we show sets of six snapshots for the 2D (green) and 3D (black) cases during time intervals between two consecutive peaks or troughs in the graph of $z_{\text{center}}(t)$. The

snapshots are normalized to have uniform maximum deflections. The agreement between 2D and 3D is very good in all cases. The third snapshots in each sequence are overlaid in the instability region in panel (b). In (b) and (d) the values of $\log_{10} R_1$ and $\log_{10} T_0$ for each set of snapshots are the multiples of 0.5 and 0.25 respectively that intercept each set.

Panels (c) and (e) show the same comparison for the 2D free–free and 3D RRRR cases. The stability boundaries and resolution issues are similar to those in panel (b), but here adequate resolution is obtained down to smaller T_0. At small R_1 values, the 3D stability boundaries actually move away from the 2D boundaries as the aspect ratio increases. This is due to special cases with very small but positive growth rates over a large range of T_0 at small R_1. Cases with aspect ratio 8 and growth rates < 0.04 are marked in panel (c) by gray boxes. Such cases only occur close to the stability boundary at large R_1, as expected, but occur over a large range of T_0 from the dark blue line to the orange (2D) line at small R_1. Below the orange line, the 3D growth rates abruptly become much larger, so setting aside the cases with very slow growth, we have better agreement in the stability boundary for 2D and 3D with aspect ratio 8. There is nothing obviously wrong with these slow-growth cases (such as very jagged shapes or nonphysical motions); unlike most of the results in this section, they may be a case where the 3D large-span dynamics are qualitatively different from the 2D dynamics.

The agreement between the snapshots in 2D (green) and 3D (black) in panels (c) and (e) is generally very good, though not quite as good as in (b) and (d), particularly in some cases at $T_0 = 10^{-1}$ and $10^{-1.25}$ that are clearly underresolved. In (c) and (e) higher resolution is used: $M = 80$ for RRRR and 81 Chebyshev-Lobatto points are used in 2D, versus 40 and 41 respectively in (a), (b), and (d). In four cases

at the upper right of (c) and (e) $|z_{\text{center}}|$ grows without oscillating, similarly to a divergence instability, so the six snapshots are equally spaced over a large portion of the small-amplitude regime.

We have presented a broad range of evidence of good qualitative agreement between 2D and 3D dynamics, even with fairly modest 3D mesh sizes ($M = 40$ and $N = 10$ in most cases) and other significant computational differences. In 2D we used a Chebyshev-Lobatto mesh, computed wake roll-up, and used a Galerkin method for the kinematic equation and Kutta condition, with a non-flat body and wake in the kinematic condition. In 3D we used a uniform mesh, flat approximate vortex sheets on the body and wake, and a collocation method for the kinematic condition. We now proceed to study and classify the dynamics of 3D membranes with square aspect ratio at all 12 of the boundary conditions in figure 5.1.

5.5 Membrane Dynamics Across Parameter Space for 12 Boundary Conditions

We now broadly classify membrane dynamics with respect to R_1, T_0, and R_3 at all 12 combinations of fixed and free boundary conditions at the edges. In a few cases the large-amplitude dynamics do not seem to depend very strongly on aspect ratio, so we set it to 1 here, but it would be good to explore this parameter in future work.

To find where the membranes are unstable, we apply the perturbation (5.28) with $\sigma = 10^{-5}$ for all 12 boundary conditions at a large number of R_1 and T_0 values, and as before we find the critical T_0 at each R_1 by interpolation of growth rates.

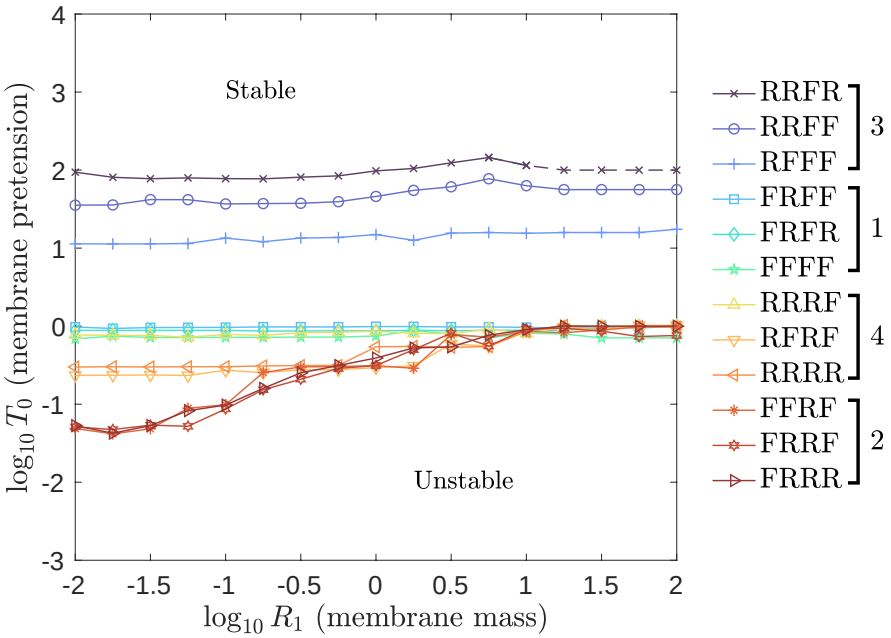

Figure 5.9: Stability boundaries for the 12 boundary conditions, listed at right, and placed in four groups that depend on only the leading and trailing edge conditions, as in figure 5.1.

Figure 5.9 shows the stability boundaries for the 12 boundary conditions, listed at right. Based on the locations of the boundaries and the qualitative features of membranes' large-amplitude dynamics (presented later), the 12 boundary conditions naturally fall into four groups, listed at right in figure 5.9 and shown in figure 5.1, and determined by only the leading and trailing edge conditions. The conditions at these edges seem to determine the qualitative behaviors of the membranes' dynamics more strongly than the side-edge conditions. However, the side edges can still have important effects, particularly for the large-amplitude results we will present.

In the 2D versus 3D comparisons, we have already shown one stability boundary from three of the four groups: FRFR from group 1, FRRR from group 2, and RRRR from group 4. The other stability boundaries within these groups are similar—nearly flat in group 1, upward sloping in group 2, and either flat or upward sloping in group 4, though the flatness at small R_1 for RRRR is affected by the slow-growth

cases in figure 5.8(c). Perhaps due to these cases, there is more variability in the boundaries of group 4 at small R_1, while the boundaries are more uniform across groups 1 and 2. The data for group 3, with the leading edge free and trailing edge fixed, are completely new, and stand out from the other groups in two respects. The group 3 stability boundaries are orders of magnitude higher in T_0 than the other groups'. There is also about an order-of-magnitude variation of the critical T_0 within group 3, higher (less stable) with more side edges free. At large R_1 it is difficult to distinguish slow growth and slow decay, particularly for RRFR, so the stability boundary is dashed to indicate this lack of certainty.

5.5.1 Large-amplitude Scaling Laws

We now study how key quantities—the typical magnitudes of deflections, and for unsteady cases, frequencies of oscillations—depend on R_1, T_0, and R_3. In our 2D work (chapters II–IV) we also studied the typical spatial wave numbers of membrane deformations, but these are somewhat difficult to quantify precisely without higher spatial resolution, which is more feasible computationally in 2D. However, there is sometimes a correlation between wave numbers and frequencies, which are computed here.

In figure 5.10 we show how the time-averaged deflection depends on R_3 at several fixed values of R_1 (listed in the legends of the top panels) and T_0 for all 12 boundary conditions. We define the time-averaged deflection of the membrane as the maximum membrane deflection minus the minimum deflection, averaged over time:

$$\langle z_{\text{defl}} \rangle \equiv \frac{1}{t_2} \int_{t_1}^{t_1+t_2} \left(\max_{-1<\alpha_1,\alpha_2<1} z(\alpha_1, \alpha_2, t) - \min_{-1<\alpha_1,\alpha_2<1} z(\alpha_1, \alpha_2, t) \right) \mathrm{d}t \tag{5.29}$$

where t_1 and t_2 are sufficiently large that $\langle z_{\text{defl}} \rangle$ changes by less than 1% with further increases in these values. As in the 2D studies (chapters II and IV), deflection scales

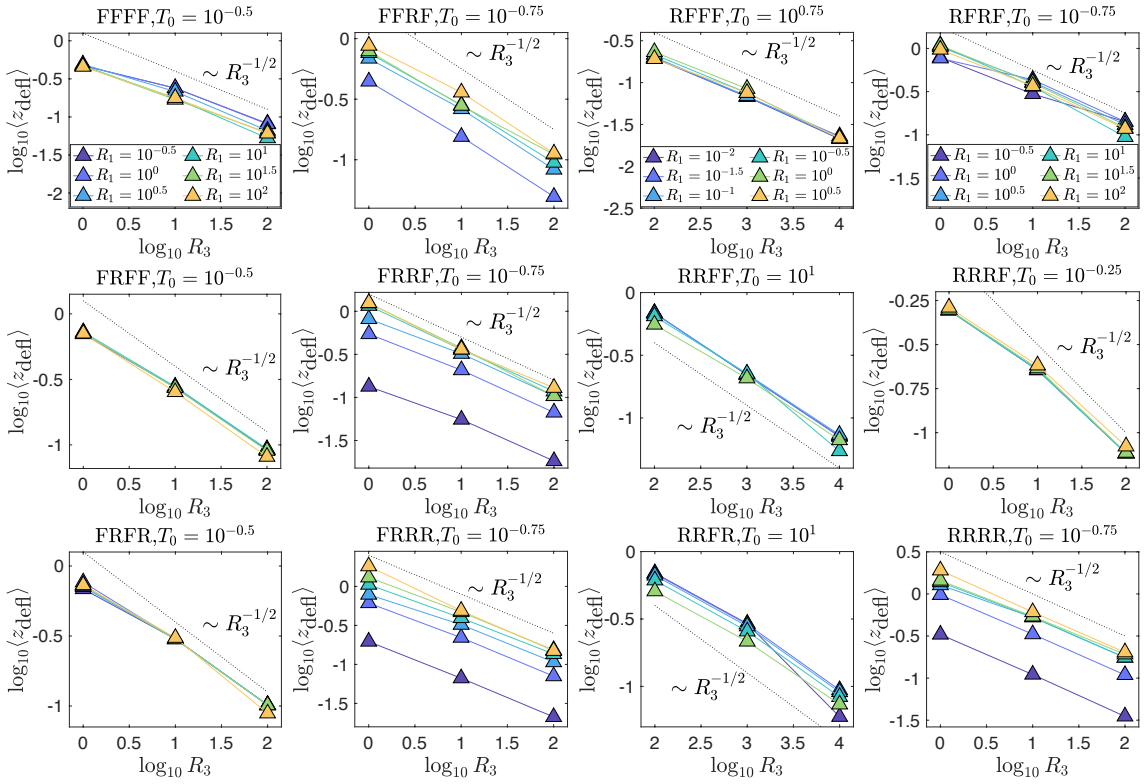

Figure 5.10: Time-averaged deflections of the membranes (defined by (5.29)) versus R_3 for various R_1 (listed in the top panel of each column except column 2 which uses the same values as column 1) and fixed T_0 for all 12 boundary conditions. Recall that R_1 is the dimensionless membrane mass, T_0 is the dimensionless pretension, and R_3 is the dimensionless stretching rigidity. Columns 1–4 correspond to groups 1–4 in figures 5.1 and 5.9. The dotted black line in each subpanel indicates the scaling $R_3^{-1/2}$.

as $1/\sqrt{R_3}$ at moderate and large R_3 in all 3D cases. The scaling begins at larger R_3 for the third column, so the R_3 range there is a factor of 10^2 higher than in the other columns. At $R_3 = 10^2$, the deflection magnitudes are generally much higher in column 3 than in the other columns. Selected T_0 values are shown in figure 5.10 but the same scaling holds at other T_0 values, two of which are shown in appendix J. We briefly explain the $1/\sqrt{R_3}$ scaling similarly to chapter II. We expand terms in the z component of the membrane equation (5.16) in the limit of small deflections, by inserting Taylor series for z and its derivatives. T_0 and R_3 enter through the $\overline{e}$ and K_s terms respectively. T_0 multiplies $(\partial^2_{\alpha_1} + \partial^2_{\alpha_2})z$ and R_3 multiplies a term that is cubic in derivatives of z. Using the kinematic and pressure jump equations, (5.19) and (5.20), we find that γ_2 is linear in z and therefore so is $[p]$ and the $[p]$ term in (5.16). At steady state, the amplitude is set by a balance of the destabilizing $[p]$ term and the stabilizing R_3 term; the T_0 term is similar in magnitude to these terms near the stability boundary, and becomes insignificant at smaller T_0. Balancing $R_3 O(|z|^3)$ and the $O(|z|)$ pressure term, we have $|z| \sim R_3^{-1/2}$.

In the third column, smaller R_1 values (listed in the top panel) are used compared to the other columns, because the third-column cases did not reach large amplitude within 350 times units at the larger R_1. In a few cases data are omitted because membranes were stable (FFRF with $R_1 = 10^{-0.5}$) or did not attain steady-state motions by $t = 350$ (RRFF and RRFR with $R_1 = 10^{0.5}$).

The other main quantity we measure is the membranes' frequency of oscillation. This is calculated as the reciprocal of the period of oscillation, the time between successive peaks in $z_{\text{center}}(t)$ near the end of the computation (typically $t = 350$). We plot the frequency data in figure 5.11, similarly to the amplitude data in the previous figure, but now versus R_1, the most important parameter for frequency,

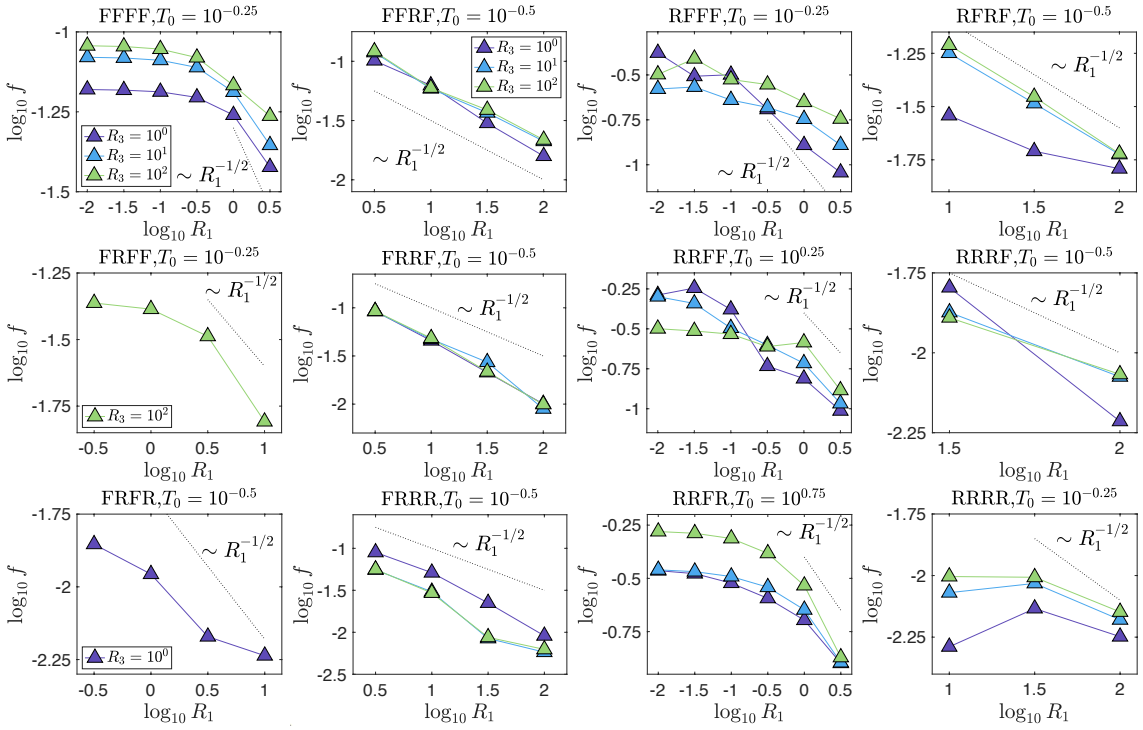

Figure 5.11: Plots of mean frequency $\log_{10} f$ versus mass density $\log_{10} R_1$ with various R_3 and fixed T_0 values for all 12 boundary conditions. Columns 1–4 correspond to groups 1–4 in figures 5.1 and 5.9. The dotted black line in each subpanel indicates the scaling $R_1^{-1/2}$.

at various fixed values of T_0 and R_3 (listed in the titles and in the legends in the first two columns, respectively). Unlike the amplitude, the membranes' shapes and frequencies do not vary much with R_3. In most cases with large R_1 ($\in [10^1, 10^2]$) and some cases with moderate R_1 ($\in [10^0, 10^1]$), the frequency approximately scales as $1/\sqrt{R_1}$, as in the large-amplitude 2D studies (chapters II and IV). The scaling can be explained in 2D or 3D by balancing the $R_1 \partial_{tt} z$ term in the membrane equation with the other terms, which are independent of R_1. Assuming a period of oscillation T, we have $R_1 \partial_{tt} z \sim R_1 z/T^2 \sim O(z)$ for the remaining terms (i.e., the $[p]$ term), so at large R_1 the frequency $= 1/T \sim 1/\sqrt{R_1}$.

There is more variability in the frequency dependence on R_1 than in the amplitude dependence on R_3, for a few main reasons. At large R_1, the oscillation period is longer, so longer times are needed to reach a steady state, and the estimates of period

and frequency are based on smaller and perhaps noisier data sets. The oscillations are periodic in some cases but chaotic in others, and in the latter cases the frequency is only a rough estimate of the long-time average. Finally, the oscillatory motion may change qualitatively (e.g., the membrane shapes may change) as R_1 increases in the ranges considered here, which may cause deviations from the simple $1/\sqrt{R_1}$ scaling law.

At small R_1 the frequency typically plateaus here (in the first and third columns). A different behavior was seen in 2D simulations of tethered membranes in chapter IV which were similar to the 2D free–free case. There the frequencies scaled as $R_1^{-5/6}$ at small R_1 and the shapes had very sharp spatial features that required hundreds of points in the streamwise direction to resolve, much higher resolution than we use here in 3D. In the corresponding case here, the fourth column of figure 5.11, we have a limited set of data at small R_1 (at different T_0 than in the fourth column) that show increasing frequencies as R_1 decreases, but it is difficult to characterize the scaling behavior. At small R_1 one might expect a plateau if the limit $R_1 \to 0$ is a regular perturbation problem, e.g., if the membrane shape does not change much in the limit $R_1 \to 0$, as seems to occur in the first and third columns. However, if the membrane becomes ever wavier as R_1 decreases, the frequency may also diverge, consistent with the 2D tethered membrane data in chapter IV and the closely related problem of a fixed–free flag with bending rigidity [8]. The fourth and second columns respectively are similar to these cases.

The highest frequencies occur in the third column, and these are much higher than in the first column at the same R_1. The third-column frequencies are only moderately higher than those in the second column at the R_1 where both are given, $10^{0.5}$.

One interesting difference with 2D that we will discuss further in the next section is that in 3D we find many cases of oscillatory membranes with leading and trailing edges fixed, corresponding to the frequencies in the first column. In 2D, all physically-reasonable fixed–fixed cases assumed steady single-hump shapes. In the first column data are only presented at $R_3 = 10^2$ in the lower two panels, because the membranes did not oscillate at $R_3 = 10^0$ and 10^1 across the full range of R_1 shown at these T_0.

5.5.2 Large-amplitude Dynamics

We have presented basic scaling relationships for the amplitudes and frequencies of steady-state large-amplitude membrane motions. In this section we characterize the types of motions—e.g., a shape that is steady, or with periodic or chaotic oscillations—across all 12 boundary conditions. We consider in turn each of the four groups in figure 5.1, determined by the conditions at the leading and trailing edges. We use three values of the stretching rigidity parameter R_3: 10^0, 10^1, and 10^2. Somewhat below 10^0, deflections become unrealistically large in some cases. At $R_3 = 10^2$, the motions generally approximate the large-R_3 asymptotic regime.

We consider values of T_0 that are relatively close to the stability boundary, within 1–1.5 orders of magnitude of it. At much smaller T_0, the iterative method in our computational method tends to stagnate without converging at an early time step. In some cases, the stagnation occurs after a sharp angular feature appears in the membrane shape. Presumably larger T_0 inhibits the formation of such features. By contrast, our 2D algorithm from chapters II and IV was able to compute at arbitrarily small T_0, where the T_0 term became insignificant compared to the R_3 term in the total stretching force. There we found only modest changes in the dynamics as T_0 increased from zero to the stability boundary, so possibly the 3D results here indicate what would happen at very small T_0, but we defer this question to future work.

In each case we consider a wide range of membrane mass R_1, from small to large.

1. Leading and Trailing Edges Fixed (FFFF, FRFF, FRFR)

We begin with membranes whose leading and trailing edges are fixed at zero deflection (group 1 in figures 5.1 and 5.9). Figure 5.12 shows typical motions and where they occur in parameter space. Each row of the top 3-by-3 array of panels corresponds to different side-edge conditions (FFFF, FRFF, or FRFR), and each column to a different R_3 value (10^0, 10^1, or 10^2). The different colors in each panel indicate where different types of motions occur in R_1-T_0 space, with representative examples below. Purple is used for steady single-hump shapes, green for small oscillations (periodic or not) about single-hump shapes, and yellow for up-down symmetric oscillations, usually periodic. Small black dots indicate periodic cases. Blue is used for cases that had slowly decaying oscillations at $t = 350$, and could approach the green or purple states at later times. Such cases occur at large R_1 and the oscillations tend to be less periodic than at smaller R_1. A few white regions in the upper corners of the FFFF panels indicate motions that were still in the exponential growth regime at $t = 350$, while cases in the white region in the FRFR panel at $R_3 = 10^0$ failed to converge at an early time. The three rows at the bottom of figure 5.12 show representative examples of the membrane motions in the purple, green, and yellow regions. Just to the right of small rectangles with these colors, the motions are shown by sequences of 11 midspan snapshots (overlaid), and then further to the right, smaller sequences of four 3D snapshots, arrayed horizontally. All these sequences are for FFFF cases, but single 3D snapshots from the same type of motion with other side-edge conditions are shown at the far left in each row.

As noted previously, only steady single-hump shapes (purple) occur in 2D with fixed leading and trailing edges (chapter II), whereas steady-state oscillations are

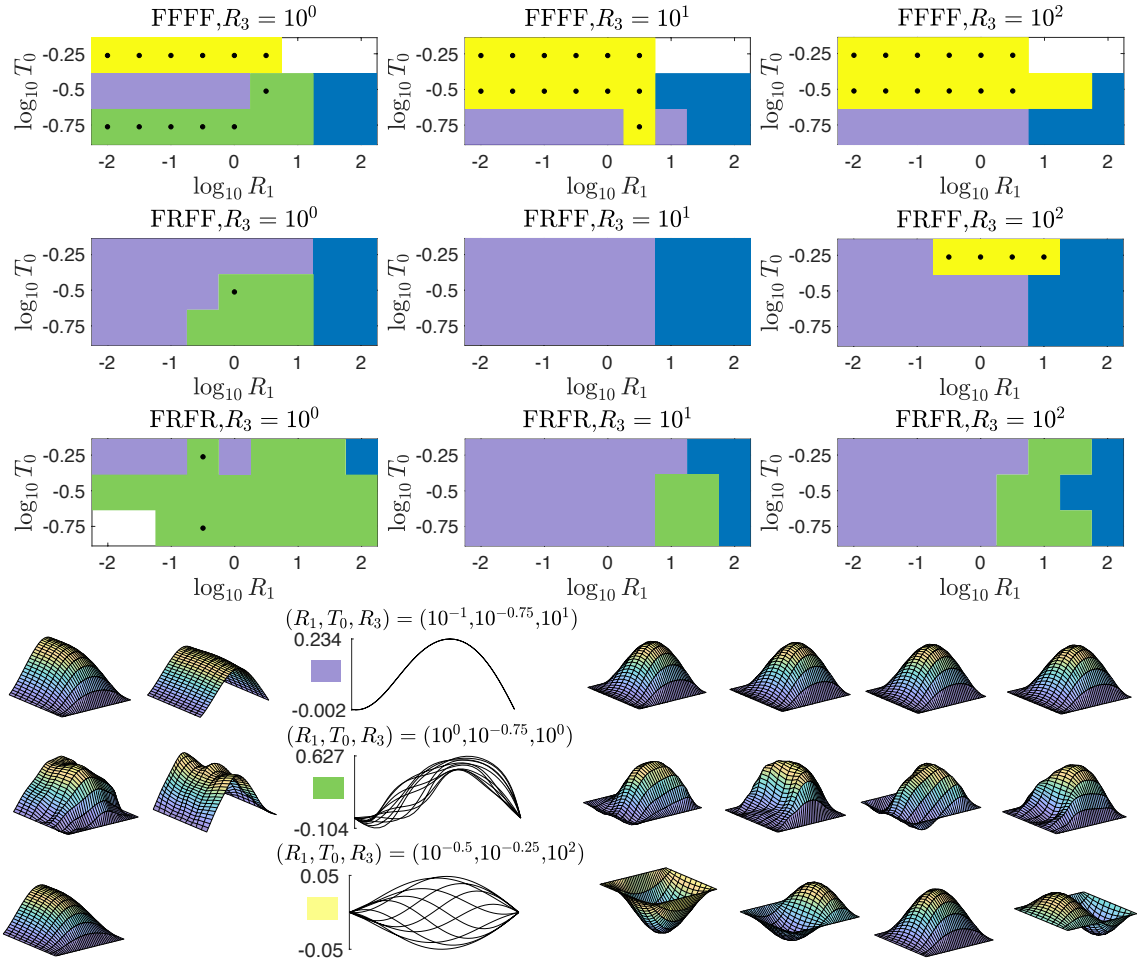

Figure 5.12: Typical membrane dynamics with fixed leading and trailing edges. The color plots classify the different membrane dynamics across a grid of (R_1, T_0) values for three values of R_3 $(10^0, 10^1, 10^2)$ with black dots indicating periodic motions. Recall that R_1 is the dimensionless membrane mass, T_0 is the dimensionless pretension, and R_3 is the dimensionless stretching rigidity. Representative examples of motions in the purple, green, and yellow regions are shown in the bottom three rows, identified by small colored rectangles. To the right of the rectangles are overlaid sequences of 11 midspan snapshots in black, for FFFF boundary conditions. To the right of the midspan snapshots are a smaller representative sequence of four 3D snapshots, from left to right with increasing time. To the left of the midspan snapshots are single 3D snapshots representing similar cases with other side-edge conditions (FRFF and FRFR).

surprisingly common in 3D, particularly with all four edges fixed. Here up-down symmetric periodic motions (yellow) are much more common than with the other side-edge conditions, which typically have moderately small or no oscillations about a single-hump shape. The yellow motion includes a traveling wave of deflection that moves *upstream*, unlike in the 2D fixed–free and free–free cases (chapter II). Compared to the steady purple shape, the green motion has more variability not just in time but also in the spanwise direction, exemplified by the snapshot to the left of the small green rectangle in the second row from the bottom. In experiments, oscillatory cases with fixed leading and trailing edges have been reported mainly at nonzero angle of attack, where leading edge vortex shedding seems particularly significant [146, figure 4].

2. Leading Edge Fixed and Trailing Edge Free (FFRF, FRRF, FRRR)

The typical motions are qualitatively different in the second group (group 2 in figures 5.1 and 5.9), with the leading edge fixed and the trailing edge free. Hence we classify the motions somewhat differently in figure 5.13, with colors denoting the number of times the midspan profile crosses $z = 0$ (not including the leading edge), time-averaged. This classifies the spatial waviness of the profiles. Here R_3 is fixed at 10^1; at other R_3 the deflection amplitude varies but the numbers of zero crossings are almost unchanged. The numbers of zero crossings decrease almost monotonically as R_1 increases, and chaotic states (without black dots) with larger amplitudes and more up-down asymmetry become more common, similarly to the 2D results in chapter II. In the white regions at the upper left of each panel, membranes are stable. In the white regions at the lower right, the computations did not converge when the membranes reached large amplitude but before they attained a steady-state motion, so results are not reported.

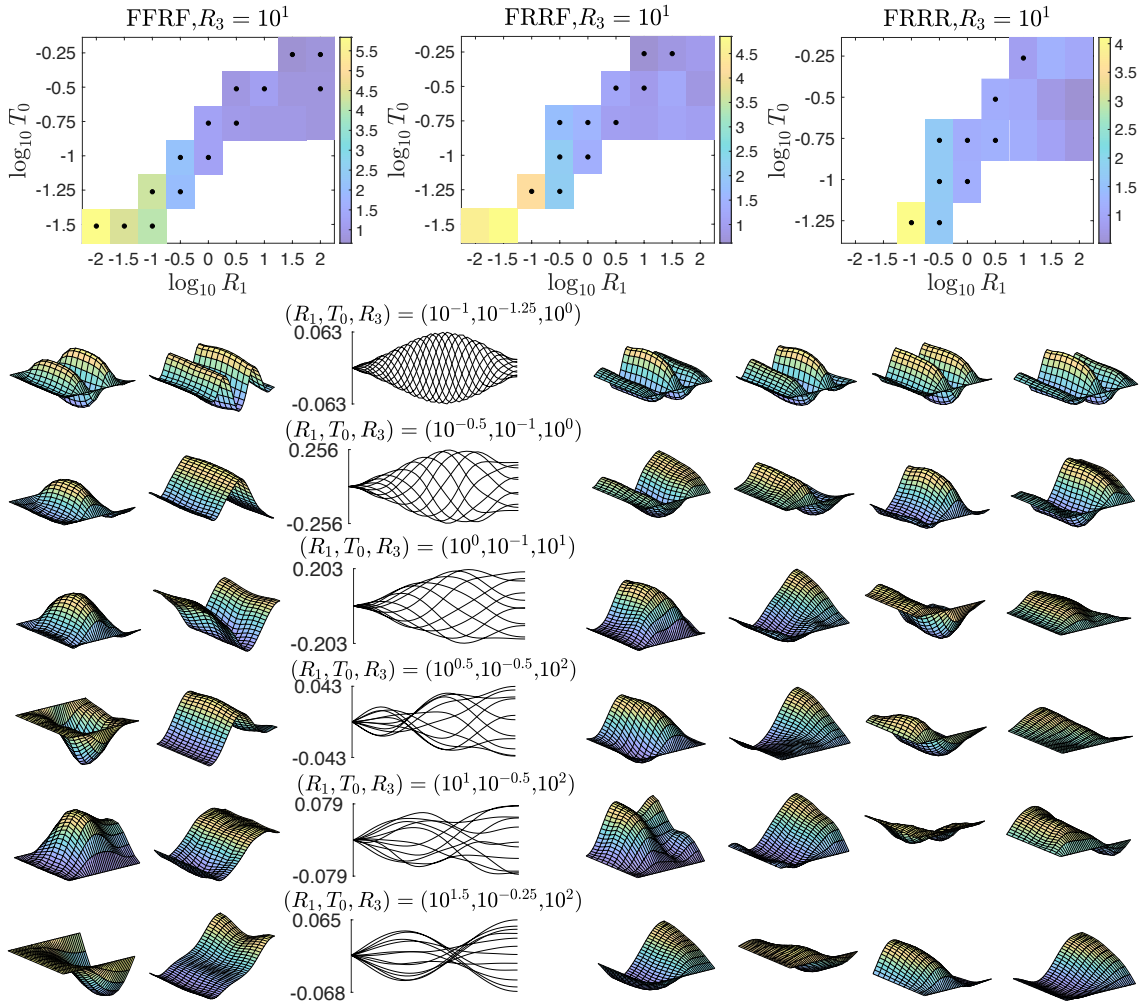

Figure 5.13: Typical membrane dynamics with fixed leading edges and free trailing edges. The color plots in the top row show the time-averaged number of zero-crossings of the membranes' midspan profiles at various (R_1,T_0) values for $R_3 = 10^1$. The black dots indicate periodic motions. Representative examples of motions at a sequence of R_1 values from 10^{-1} to $10^{1.5}$ are shown in the bottom six rows. Overlaid sequences of 11 midspan snapshots are shown in black, for FRRF boundary conditions. To the right of the midspan snapshots are a smaller representative sequence of four 3D snapshots, from left to right with increasing time. To the left of the midspan snapshots are single 3D snapshots representing similar cases with other side-edge conditions (FFRF and FRRR).

Typical membrane motions are shown in the rows at the bottom, one for each R_1 in a sequence from 10^{-1} to $10^{1.5}$. Here the motions resemble different modes of a flapping flag [3,8,31], with traveling waves that pass downstream, unlike for group 1. Another difference here is that the side-edge conditions do not change the type of motion. As in chapter II, at small R_1 the deflection envelope has small amplitude near the trailing edge. At large R_1 (e.g., $10^{1.5}$) the traveling waves become more like standing waves, with fixed nodes and antinodes.

3. Leading Edge Free and Trailing Edge Fixed (RFFF, RRFF, RRFR)

Next, we consider membranes whose leading edge is free and trailing edge is fixed (group 3 in figures 5.1 and 5.9). We showed in figure 5.9 that here the critical pretensions for instability are much larger than in the other cases. The space of motions is qualitatively different than for groups 1 and 2. We identify just three types of motions, with approximately periodic, up-down symmetric oscillations in most cases, characterized by three typical midspan profiles shown in the bottom three rows: a low-mode shape with at most a single interior z extremum (light purple), a higher mode shape with one or two interior z extrema (yellow), and a low-mode shape with a multi-valued z profile near the trailing edge at certain times (dark purple). This last motion is more common at smaller R_1 and does not appear with both side edges fixed or at the largest R_3 (right column), where the first motion dominates. White regions are again cases in which the computations did not converge when the membranes reached large amplitude but before they attained a steady-state motion. Another special feature of group 3 is that the small-amplitude growth rates are generally much less than in the other groups, so data are omitted for $R_1 > 10^0$ because the amplitudes were growing and had not yet reached a steady state at $t = 350$. In some cases at $R_1 = 10^{1.5}$ and 10^2 (not shown) the amplitude neither

grows nor decays noticeably after the initial perturbations, as also occurred in some 2D cases at large R_1 in chapter II.

The motions of group 3 seem more likely to violate the physical assumptions of the model than the other groups. The oscillation amplitude is highest at the leading edge, so leading-edge vortex shedding is probably important unless the oscillation amplitudes are very small (i.e., at $R_3 = 10^3$ and 10^4, where the motions are similar to those in the $R_3 = 10^2$ column, light purple generally). Vortex shedding would probably occur in multiple locations upstream of the trailing edge for the dark purple motions, due to large deflection amplitudes and slopes.

4. Leading and Trailing Edges Free (RFRF, RRRF, RRRR)

Group 4 consists of membranes with the leading and trailing edges free (figures 5.1 and 5.9). With fewer of the edges fixed, we find a wider variety of dynamics. In figure 5.15 we use seven categories to classify the motions, with representative examples in the seven rows at the bottom, each labeled using a small rectangle with a certain color and symbol that is repeated at data points in this category in the 3-by-3 array of color plots above. The first three rows represent categories of steady shapes with one, two, or three internal inflection points, respectively. The fourth row represents a category of motions with small oscillations about one of the steady shapes. To identify these cases, we decompose the midspan deflection $z(\alpha_1, 0, t)$ as the sum of its time-average and the remainder, the unsteady part. Motions are in the fourth category if the maximum minus the minimum of the unsteady deflection is nonzero but much less than the maximum minus the minimum of the time-averaged deflection. The fifth row represents unsteady motions whose unsteady part is comparable to or larger than the steady part (in the same sense as for the fourth category). The sixth row is for a special type of unsteady motion with all edges free (RRRR) that is

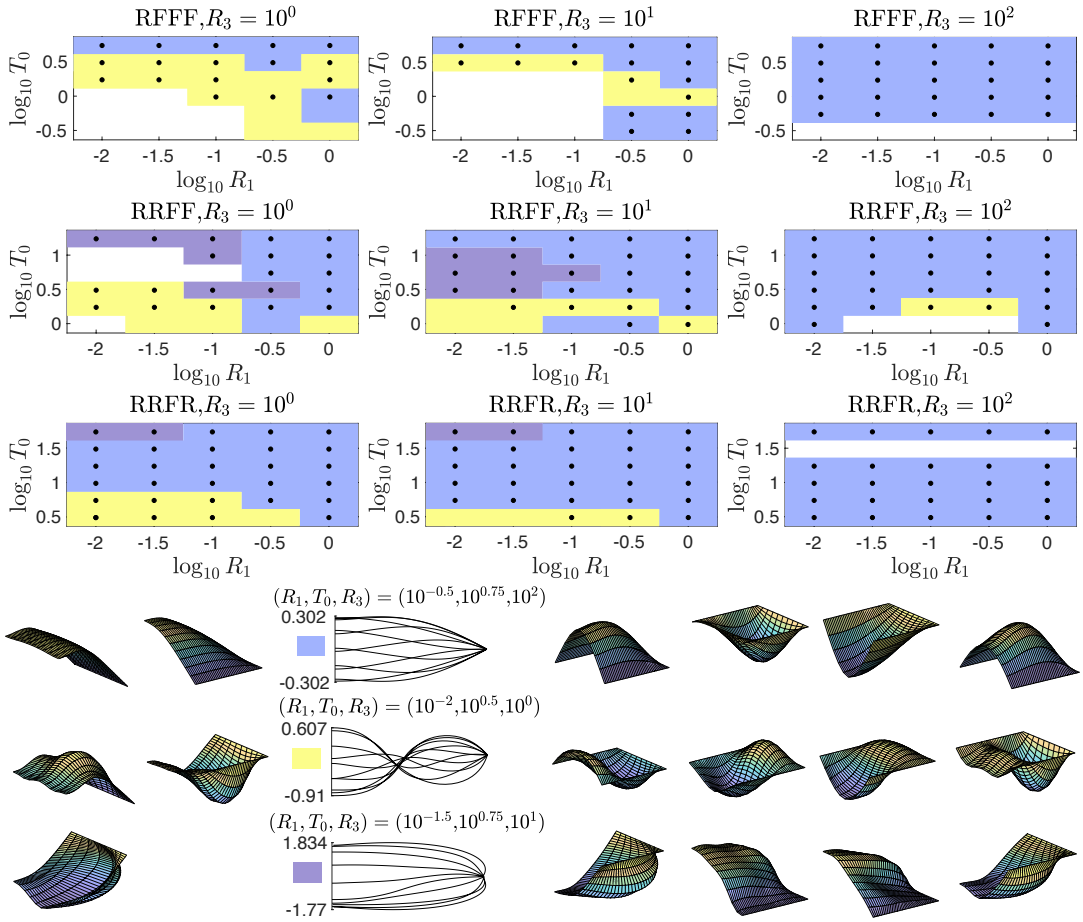

Figure 5.14: Typical membrane dynamics with free leading edges and fixed trailing edges. The color plots classify the different membrane dynamics across a grid of (R_1, T_0) values for three values of R_3 $(10^0, 10^1, 10^2)$ with black dots indicating periodic motions. Representative examples of motions in the light purple, yellow, and dark purple regions are shown in the bottom three rows, identified by small colored rectangles. To the right of the rectangles are overlaid sequences of 11 midspan snapshots in black, for RFFF boundary conditions (top two rows) and RRFF boundary conditions (bottom row). To the right of the midspan snapshots are a smaller representative sequence of four 3D snapshots, from left to right with increasing time. To the left of the midspan snapshots are single 3D snapshots representing similar cases with other side-edge conditions (RRFR and RRFF).

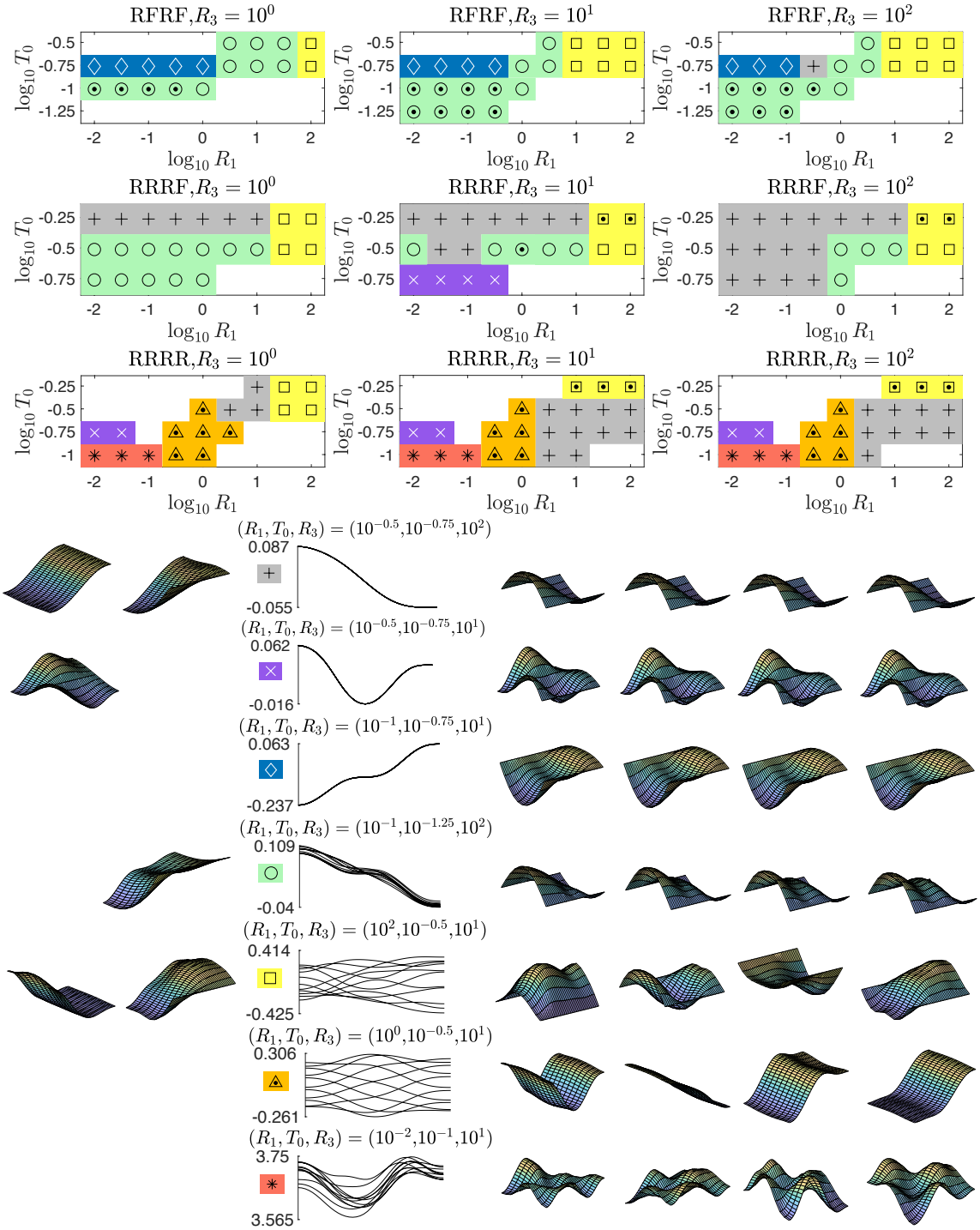

Figure 5.15: Typical membrane dynamics with free leading and trailing edges. The color plots classify the different membrane dynamics across a grid of (R_1, T_0) values for three values of R_3 $(10^0, 10^1, 10^2)$ with black dots indicating periodic motions. Representative examples of motions in all the colored regions are shown in the bottom seven rows, identified by small colored rectangles with symbols. To the right of the rectangles are overlaid sequences of 11 midspan snapshots in black, for RFRF (rows 1, 3, 4, and 5), RRRF (row 2), and RRRR boundary conditions (rows 6 and 7). To the right of the midspan snapshots are a smaller representative sequence of four 3D snapshots, from left to right with increasing time. To the left of the midspan snapshots are single 3D snapshots representing similar cases with other side-edge conditions (RRRF and RRRR).

time-periodic. These motions have translational and deformational dynamics with $O(1)$ frequencies, and their translational motions are more precisely time-periodic than those at large R_1. The seventh row is for another special type of unsteady RRRR motion that has both large spanwise and large chordwise curvatures.

The sixth and seventh categories occur only for the RRRR case, which seems to have a wider variety of motions because it is free to translate in z. As in the 2D case (chapter II), the translational motion is distinct from but coupled to the shape deformation dynamics, and the combination of the two results in more types of dynamics. Other categories of motions that occur only with certain edge conditions are the second and third, the steady states with two or three interior inflection points respectively. The second occurs for RRRF and RRRR and the third for RFRF, both mainly at small R_1. The fourth category, small oscillations about a steady shape, occurs only with one or both side edges fixed (RFRF and RRRF). The first category, a steady shape with a single inflection point, occurs with all side edge conditions, but in the RRRR case it translates either up or down in z at almost constant speed, with occasional reversals in direction (as in figure 2.20 in chapter II). The fifth category, of general unsteady motions, occurs with all side edge conditions at large R_1. Here motions tend to be more asymmetrical and irregular and have larger oscillation amplitudes. The large body mass may allow the body to maintain its momentum against resisting fluid forces for longer times.

5.6 Conclusions

We have developed a model and numerical method to compute small- and large-amplitude dynamics of thin membranes in 3D inviscid flows. We provided numerical evidence that indicates convergence of our method with respect to spatial grid re-

finement. The 3D solutions agree remarkably well with those computed in 2D flows with different discretization techniques, particularly when the aspect ratio in 3D is large.

With fixed or free boundary conditions at each of the four edges, we have 16 combinations of boundary conditions for rectangular membranes, reduced to 12 when symmetric cases are accounted for. We computed the dynamics in all 12 cases with various values of the three key physical parameters: membrane mass (R_1), pretension (T_0), and stretching rigidity (R_3). The 12 cases fit naturally into four groups that are determined by the leading- and trailing-edge boundary conditions. Within each group there are strong similarities in the shapes and locations of the stability boundaries, the typical magnitudes of membranes' deflections and their oscillation frequencies in unsteady cases, and the typical shapes of the membranes at the midspan location. The side-edge boundary conditions can cause small or large qualitative differences in the dynamics within each group. The differences are relatively small for the fixed-free case (group 2); the midspan shape is almost unchanged at a free side edge or gradually scaled to flat at a fixed side edge. The differences are larger for the fixed-fixed and free-fixed cases (groups 1 and 3); changes in side-edge conditions lead to the appearance or disappearance of certain types of oscillation modes. In group 4 (free-free) the side edges have an even larger effect, for example by allowing or preventing translational motions that lead to a wider variety of dynamics.

As in 2D, the deflection magnitudes scale as $R_3^{-1/2}$ and the oscillation frequencies scale as $R_1^{-1/2}$ at large values of R_3 and R_1 respectively. The stability boundaries and dynamics in groups 1, 2, and 4 have many resemblances to the 2D cases with same leading and trailing edge conditions studied in chapter II. The fixed-free case in 3D is very similar to the 2D case in terms of increasing waviness with decreasing

R_1, a more limited effect of T_0 on the shapes, and R_3 mainly setting the amplitudes of oscillation but not the shapes. The free-free case in 3D has some of the same types of states as in 2D: periodic oscillatory states and vertical translational states that may be nearly steady with a non-zero mean slope, or undergo periodic or chaotic oscillations.

However, there are important qualitative differences in 3D. Unlike the 2D fixed-fixed case where all membranes converge to steady single-hump shapes, the 3D version (group 1) has cases with small and large unsteady oscillations, particularly when both side edges are fixed. The 3D results contradicted our intuition from the 2D study that more fixed edges leads to fewer unsteady states. The 3D free-free case (group 4) has complicated spanwise curvature distributions, particularly with one or both side edges free. There are more types of motions here than in the 2D free-free case. We did not study the 2D analog of group 3, free-fixed, but the variations with side-edge conditions here show that 3D effects can be significant. Taken together these results validate the use of 2D models for a good qualitative understanding of membrane motions and scaling with parameters, but also show that certain important phenomena can only be seen with the 3D model.

Future work could investigate several topics, for example: the effect of aspect ratio; a nonzero Poisson ratio; including non-flat vortex sheets in the kinematic condition and computing wake roll-up (e.g., using a treecode [105]) and consequences on membrane dynamics, especially at large mass density ratio and small stretching rigidity (figures 2.17 and 2.23 in chapter II); the types of motions at smaller T_0, which would require altering the algorithm to be able to compute steady state motions in this regime; mixed fixed and free boundary conditions on a single edge; and different membrane shapes.

APPENDICES

APPENDIX A

Pressure Jump Equation in 2D Flows

In this appendix we derive the equation for the pressure jump $[p](\alpha, t)$ across the membrane, given by (2.19), as in [6] but for an extensible body. We use vector notation instead of complex notation.

The Euler momentum equation given by

$$\partial_t \boldsymbol{u}(\boldsymbol{x}, t) + \boldsymbol{u}(\boldsymbol{x}, t) \cdot \nabla \boldsymbol{u}(\boldsymbol{x}, t) = -\nabla p(\boldsymbol{x}, t), \tag{A.1}$$

determines the velocity of the fluid flow $\boldsymbol{u}(\boldsymbol{x}, t)$ at a point $\boldsymbol{x}$ in the fluid. We want to calculate the fluid pressure at a point in the fluid that is adjacent to and follows a material point $\boldsymbol{X}(\alpha, t)$ on the membrane. The rate of change of fluid velocity at such a point is

$$\frac{\mathrm{d}}{\mathrm{d}t}\boldsymbol{u}(\boldsymbol{X}(\alpha, t), t) = \partial_t \boldsymbol{u}(\boldsymbol{x}, t)|_{\boldsymbol{x}=\boldsymbol{X}(\alpha,t)} + (\partial_t \boldsymbol{X}(\alpha, t) \cdot \nabla)\, \boldsymbol{u}(\boldsymbol{x}, t)|_{\boldsymbol{x}=\boldsymbol{X}(\alpha,t)}. \tag{A.2}$$

We replace the first term in (A.1) using the same term in (A.2) (the first term on the right hand side). This yields the pressure gradient at a point that moves with $\boldsymbol{X}(\alpha, t)$. Since the fluid velocity is discontinuous across the membrane, we actually need to do this separately for points that tend toward $\boldsymbol{X}(\alpha, t)$ from each side of the membrane. We obtain

$$\frac{\mathrm{d}}{\mathrm{d}t}\boldsymbol{u}(\boldsymbol{X}(\alpha, t), t)^{\pm} + \left((\boldsymbol{u}(\boldsymbol{x}, t) - \partial_t \boldsymbol{X}) \cdot \nabla \boldsymbol{u}(\boldsymbol{x}, t) \Big|_{\boldsymbol{x}=\boldsymbol{X}(\alpha,t)} \right)^{\pm} = -(\nabla p(\boldsymbol{x}, t)|_{\boldsymbol{x}=\boldsymbol{X}(\alpha,t)})^{\pm}, \tag{A.3}$$

using + for the side toward which the membrane normal $\hat{\mathbf{n}}$ is directed and − for the other side.

Next, we decompose the fluid velocity into components tangential and normal to the membrane. The normal component matches that of the membrane, ν in (2.21). The tangential component of the fluid velocity may be written in terms of its jump across the membrane, the same as the vortex sheet strength γ [149],

$$\left(\boldsymbol{u}^{+}-\boldsymbol{u}^{-}\right)\cdot\hat{\mathbf{s}}=-\gamma, \tag{A.4}$$

and the average of the tangential components of the fluid velocity on the two sides of the membrane, denoted μ. Combining the tangential and normal components we have

$$\boldsymbol{u}^{\pm}=\left(\mu\mp\frac{\gamma}{2}\right)\hat{\mathbf{s}}+\nu\hat{\mathbf{n}}. \tag{A.5}$$

We take the difference of (A.3) on the + and − sides:

$$\begin{aligned}&\frac{\mathrm{d}}{\mathrm{d}t}\left(\boldsymbol{u}^{+}(\boldsymbol{X}(\alpha,t),t)-\boldsymbol{u}^{-}(\boldsymbol{X}(\alpha,t),t)\right)+\left((\boldsymbol{u}^{+}(\boldsymbol{x},t)-\partial_t\boldsymbol{X})\cdot\nabla\boldsymbol{u}^{+}(\boldsymbol{x},t)\Big|_{\boldsymbol{x}=\boldsymbol{X}(\alpha,t)}\right)\\&-\left((\boldsymbol{u}^{-}(\boldsymbol{x},t)-\partial_t\boldsymbol{X})\cdot\nabla\boldsymbol{u}^{-}(\boldsymbol{x},t)\Big|_{\boldsymbol{x}=\boldsymbol{X}(\alpha,t)}\right)=-(\nabla p(\boldsymbol{x},t)^{+}-\nabla p(\boldsymbol{x},t)^{-})|_{\boldsymbol{x}=\boldsymbol{X}(\alpha,t)}.\end{aligned} \tag{A.6}$$

We then take the tangential component of (A.6), term by term. Using (A.5),

$$\hat{\mathbf{s}}\cdot\frac{\mathrm{d}}{\mathrm{d}t}(\boldsymbol{u}^{+}(\boldsymbol{X}(\alpha,t),t)-\boldsymbol{u}^{-}(\boldsymbol{X}(\alpha,t),t))=\hat{\mathbf{s}}\cdot\partial_t(-\gamma(\alpha,t)\hat{\mathbf{s}}(\alpha,t))=-\partial_t\gamma(\alpha,t). \tag{A.7}$$

Using

$$\partial_t\boldsymbol{X}=\tau\hat{\mathbf{s}}+\nu\hat{\mathbf{n}}, \tag{A.8}$$

and (A.5),

$$\hat{\mathbf{s}}\cdot\left[(\boldsymbol{u}^{\pm}(\boldsymbol{x},t)-\partial_t\boldsymbol{X})\cdot\nabla\boldsymbol{u}^{\pm}(\boldsymbol{x},t)\right]\Big|_{\boldsymbol{x}=\boldsymbol{X}(\alpha,t)}=\left(\mu\mp\frac{\gamma}{2}-\tau\right)\left[\partial_s\left(\mu\mp\frac{\gamma}{2}\right)-\nu\kappa\right]. \tag{A.9}$$

The difference of the + and − terms on the right hand side of (A.9) is

$$-(\mu-\tau)\partial_s\gamma-\gamma(\partial_s\mu-\nu\kappa). \tag{A.10}$$

The tangential component of the right hand side of (A.6) is

$$-\partial_s[p]^+_-(\boldsymbol{x},t)|_{\boldsymbol{x}=\boldsymbol{X}(\alpha,t)}. \tag{A.11}$$

Combining (A.7), (A.10), and (A.11), the tangential component of (A.6) is

$$\partial_t\gamma+(\mu-\tau)\partial_s\gamma+\gamma(\partial_s\mu-\nu\kappa)=\partial_s[p]^+_-, \tag{A.12}$$

or using α-derivatives,

$$\partial_\alpha s\partial_t\gamma+(\mu-\tau)\partial_\alpha\gamma+\gamma(\partial_\alpha\mu-\partial_\alpha s\nu\kappa)=\partial_\alpha[p]^+_-. \tag{A.13}$$

APPENDIX B

Numerical Approximations

Vortex sheet computations can become expensive for long-time simulations. For a membrane in an oncoming flow (unidirectional and steady far upstream), the vortex wake is advected away from the membrane and it is possible to decrease resolution of the far-field wake (similarly to [4]) with only a small effect on the membrane and near-membrane wake dynamics.

We briefly describe the numerical approximations used to compute the wake dynamics in this work. For computational efficiency we use a higher resolution near the membrane's trailing edge, and we prune the vortex wake in the far-field. Once the free vortex sheet gets longer than one thousand points, we retain only the points of the free vortex sheet at local extrema of the circulation, to approximately maintain the zeroth and and first moments of vorticity but using a small number of points. Because this portion of the sheet is far from the membrane, this approximation has a negligible effect on the dynamics. Examples are shown in figures 2.17 and 2.23, where the prescribed membrane parameters are $(R_1, R_3) = (10^{0.5}, 10^1)$ and $(R_1, R_3) = (10^0, 10^{0.5})$, respectively.

We also use a point insertion/deletion scheme, but only sufficiently far from the membrane's trailing edge (e.g., implemented only more than 80 wake points from the trailing edge). As the free wake evolves, the distance between two consecutive points

can increase beyond a given parameter d_1 (a fixed fraction of the wake smoothing parameter δ), and if this occurs, we insert new points using cubic interpolation to maintain wake resolution [4, 95, 131]. Similarly, at each time step, we check the distance between three consecutive points and if the distance between the first and third point is less than a specified threshold value d_2, then we delete the point in between the two to reduce the computational cost. During both processes, we always ensure that the total circulation is conserved for all times to satisfy Kelvin's circulation theorem.

APPENDIX C

Membrane Frequencies in the Free–free Case

Since we have determined where in the parameter space the membrane is unstable, we can characterize the large-amplitude dynamics using the mean frequency and study how it depends on R_1 and R_3. We focus on the region where reliable frequency data can be obtained. As we have done previously, we compute the power spectrum from a plot of the circulation versus time, when the membrane has reached large-amplitude dynamics. In figure C.1, we see that in general the frequency decreases with increasing R_1. For $R_1 = 10^{0.5}$ and R_3 ranging from 10^2 to 10^4, the membranes translate steadily (see figure 2.19) and the wake circulation tends to zero at large times. Therefore the power spectra for those cases are zero and we omit them.

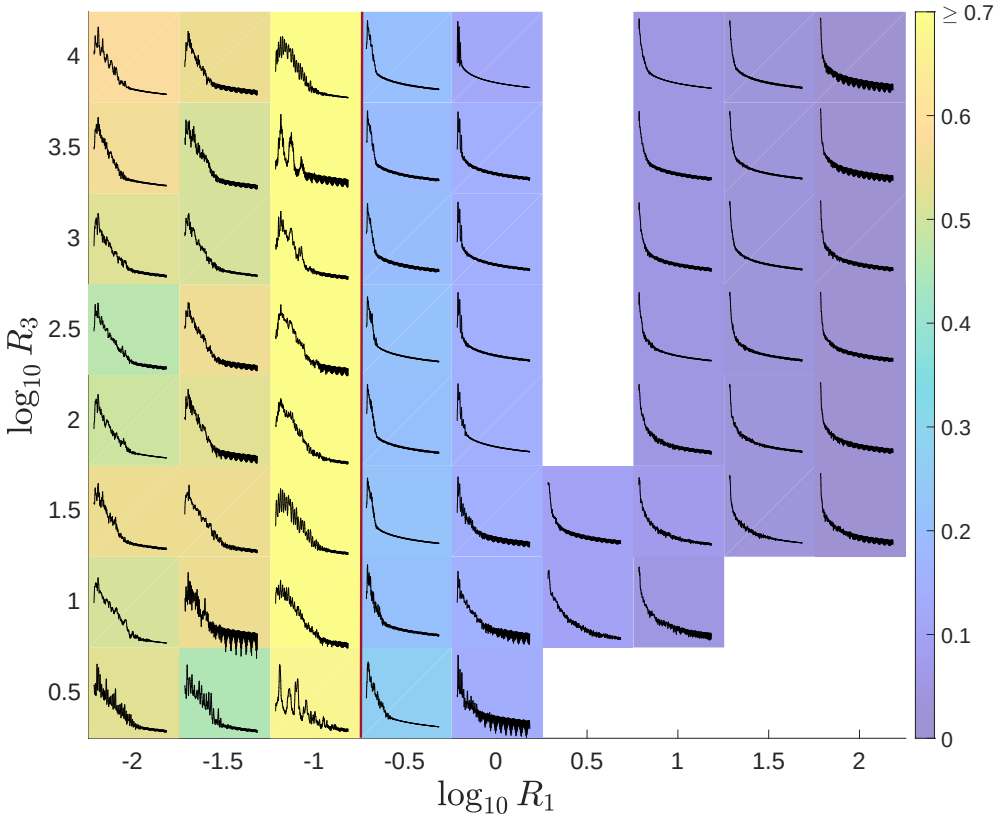

Figure C.1: (Free–free.) Surface plot of the mean frequency computed from the time series of the circulation, once the membranes have entered the large-amplitude regime, with $T_0 = 10^{-2}$. The corresponding power spectra for each of the membranes are also shown on the surface plot. The data in the right bottom corner are obtained for a shorter time and so, we neglect the computational results for those values of R_1 and R_3.

APPENDIX D

Convergence with Respect to Number of Chebyshev Nodes

In this work we have computed the membrane eigenmodes and eigenvalues using $m = 120$ (121 Chebyshev points on the membrane) and a free vortex wake of length $\ell_w = 39$. We consider here the effect of varying the former. The effect of varying the vortex wake length was explored in [3, Sec. V], and here we find that the results in the unstable regime are basically unchanged when ℓ_w is as large as 39, given the exponential decay of circulation in the wake (except right on the stability boundary, but there is still algebraic decay of the induced velocity by an alternating-sign wake).

To compare the eigenmodes obtained when using $m = 80$ versus 120, we remove the arbitrary phase shift from the eigenmode solver by finding $\phi \in [0, 2\pi]$ that solves

$$\min_{\phi} \int_{-1}^{1} |Y_{80}(x) - Y_{120}(x)e^{i\phi}| \, \mathrm{d}x. \tag{D.1}$$

To perform the subtraction in (D.1) we interpolate Y_{80} using shape-preserving piecewise cubic interpolation onto the 120-point grid. In figure D.1 we compare the real (panel A) and imaginary parts (panel B) of the fixed–free eigenmodes when using $m = 80$ and 120 across an array of (R_1, T_0) pairs. The eigenmodes agree well except in some cases at the smallest values of T_0 for each R_1, where the modes are also more wavy and difficult to resolve numerically.

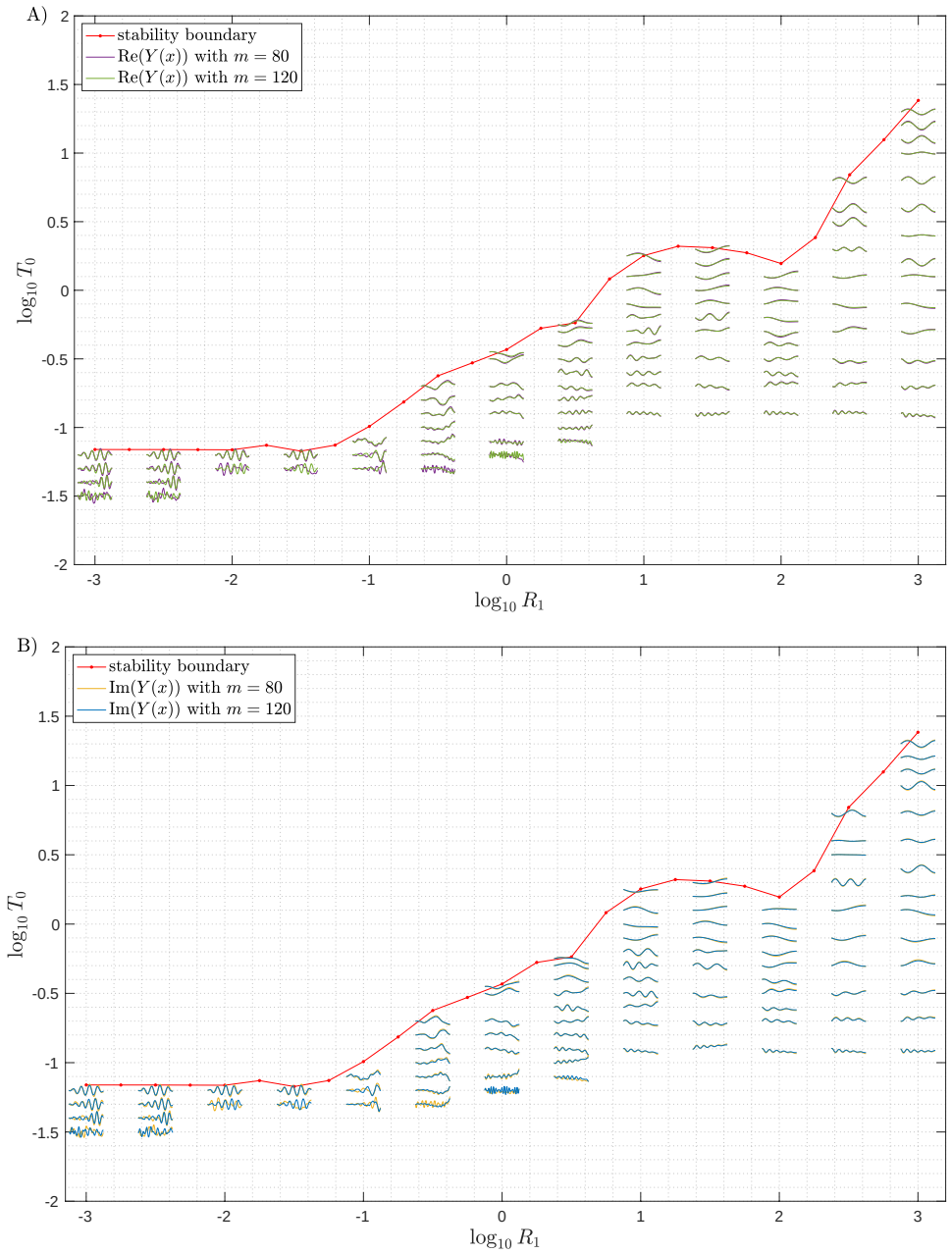

Figure D.1: Comparison between the A) real and B) imaginary parts of the eigenmodes with fixed–free boundary conditions, using grids with $m = 80$ and $m = 120$. Each shape is scaled in both vertical and horizontal directions to fit within the plot. The red dots indicate the position of the stability boundary (same as in figure 3.9).

In figure D.2 we present the relative error in the eigenvalues when $m = 80$ and 120. This quantity is computed as

$$\text{relative error} = \left| \frac{\sigma_{80} - \sigma_{120}}{\sigma_{120}} \right|. \tag{D.2}$$

The errors are typically 10^{-2}–10^{-5} near the stability boundary, and gradually increase to 10^{-1}–10^{0} as we decrease T_0, eventually reaching a point where the solutions are underresolved (as in figure D.1).

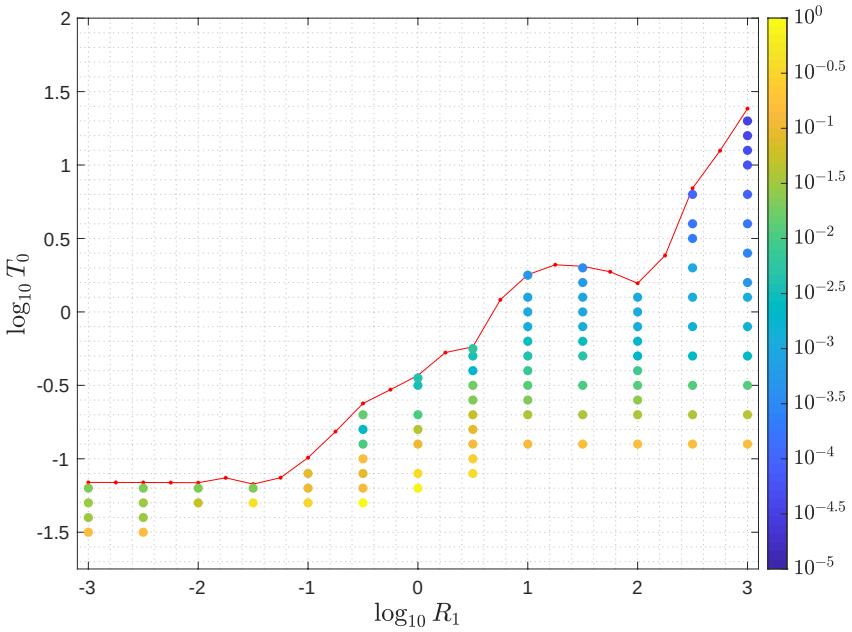

Figure D.2: At each (R_1, T_0) in the instability region (below red line), the relative error (D.2) in the eigenvalues when using $m = 80$ and $m = 120$ Chebyshev points on the fixed–free membrane is plotted as a colored dot.

Figure D.3 shows three examples of the computed eigenvalues using grids of initial guesses with $m = 80$ (green diamonds), 120 (red circles), and 240 (blue crosses). Panel A corresponds to a fixed–free membrane at a moderate value of R_1 ($10^{0.5}$) and $T_0 = 10^{-0.25}$. The eigenvalues agree well except for an additional stable eigenmode found when $m = 240$ (small blue cross located at $(\sigma_{\mathrm{R}}, \sigma_{\mathrm{I}}) \approx (0.29, 0.13)$). Panel B corresponds to a fixed–free membrane with a larger value of R_1 (10^{3}), and $T_0 = 10^{0.8}$. The eigenvalues agree well at the three values of m when $\sigma_{\mathrm{R}} \lesssim 2.5$, approximately the 15 lowest modes. As σ_{R} increases, the modes are eventually underresolved and the eigenvalues deviate significantly, beginning with $m = 80$ (green diamonds). Panel C corresponds to a free–free membrane at $R_1 = 10^{0.5}$ as in panel A, but with T_0 slightly

smaller, $10^{-0.5}$. As in panel A, there are extra stable eigenvalues (with $\sigma_{\mathrm{R}} < 2$ and $\sigma_{\mathrm{I}} > 0.1$) most with $m = 240$ (blue crosses) and one with $m = 80$ (green diamond). These eigenvalues are similar to those in the irregular bands of stable eigenvalues in figures 3.6, 3.10, and 3.14 when $R_1 = 10$. We have good agreement among the eigenvalues that are unstable or close to neutrally stable. In each case, the most unstable modes (i.e. the modes associated with smallest—or most negative—σ_{I}) change little when m increases from 120 to 240, and they are the focus of this paper.

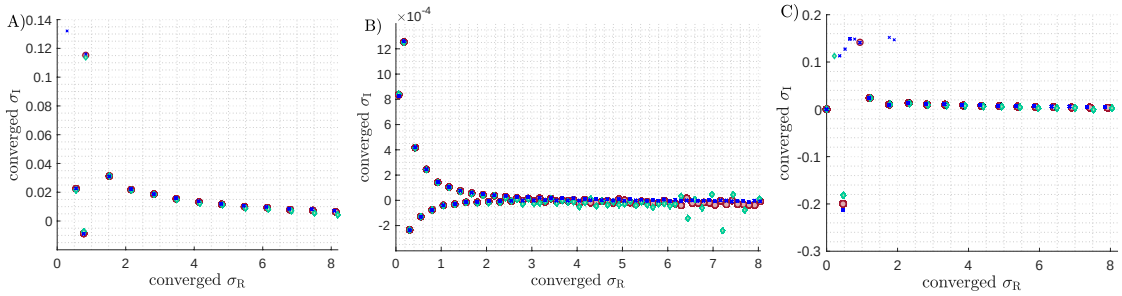

Figure D.3: Spectrum of eigenvalues for $m = 80$ (green diamonds), 120 (red circles), and 240 (blue crosses) for a fixed–free membrane at A) $(R_1, T_0) = (10^{0.5}, 10^{-0.25})$, B) $(R_1, T_0) = (10^{3}, 10^{0.8})$, and a free–free membrane at C) $(R_1, T_0) = (10^{0.5}, 10^{-0.5})$.

APPENDIX E

Method for Comparing the Eigenvalue Analysis Results to Time-stepping Simulations

Here we outline the method for comparing mode shapes obtained using the eigenvalue analysis developed in the current paper and mode shapes obtained from the time-stepping simulations in [113].

We first determine the regime of exponential growth in the nonlinear simulations by plotting the trailing edge deflection as a function of time, i.e., $y(1,t)$. The time it takes to reach the large-amplitude steady state regime depends on the magnitude of the initial perturbation. To extend the time spent in the small-amplitude regime, we start with a very small perturbation, $\mathcal{O}(10^{-12})$. This is important particularly when the growth rate is large, i.e. for unstable membranes that are far from the stability boundary in parameter space.

During this exponential growth (with flutter) regime, we approximate the computed $y(\alpha,t)$ as

$$y(\alpha,t) \approx \mathrm{Re}\left([\mathrm{Re}(y_{\mathrm{nonlin}}(\alpha)) + i\mathrm{Im}(y_{\mathrm{nonlin}}(\alpha))]e^{i\sigma t}\right). \tag{E.1}$$

To obtain σ and $y_{\mathrm{nonlin}}(\alpha)$, we first obtain σ_{I} as the negative of the slope of $\ln(|y|)$ versus time (figure E.1A) and subsequently compute $y(\alpha,t)e^{\sigma_1 t}$. For each grid point $1,\ldots,m+1$ in $\alpha \in [-1,1]$, this is a function that oscillates sinusoidally in time but

does not grow (figure E.1B). We estimate the frequency f of these functions as the reciprocal of the time between the peaks of the sinusoidal function. The frequency should be the same for all $\alpha \in [-1, 1]$ according to our Ansatz, and the computed values vary only slightly due to numerical errors. We use the average over α as our estimate of the single, global frequency. We then define $\sigma_{\mathrm{R}} := 2\pi f$ and denote the amplitudes of these sinusoidal functions $R(\alpha)$. We denote by $t_{\mathrm{peak}}(\alpha)$ the times at which they reach their peaks and define the phase as $\phi(\alpha) := -\sigma_{\mathrm{R}} \cdot t_{\mathrm{peak}}(\alpha)$. Thus, we have:

$$\mathrm{Re}(y_{\mathrm{nonlin}}(\alpha)) = R(\alpha)\cos(\phi(\alpha)), \tag{E.2}$$

$$\mathrm{Im}(y_{\mathrm{nonlin}}(\alpha)) = R(\alpha)\sin(\phi(\alpha)). \tag{E.3}$$

We show in figure E.1C the reconstructed data $\mathrm{Re}\left([\mathrm{Re}(y_{\mathrm{nonlin}}(\alpha)) + i\mathrm{Im}(y_{\mathrm{nonlin}}(\alpha))]e^{i\sigma t}\right)$ (black dashed line) compared to $y(\alpha, t)$ (cyan solid lines) at three times.

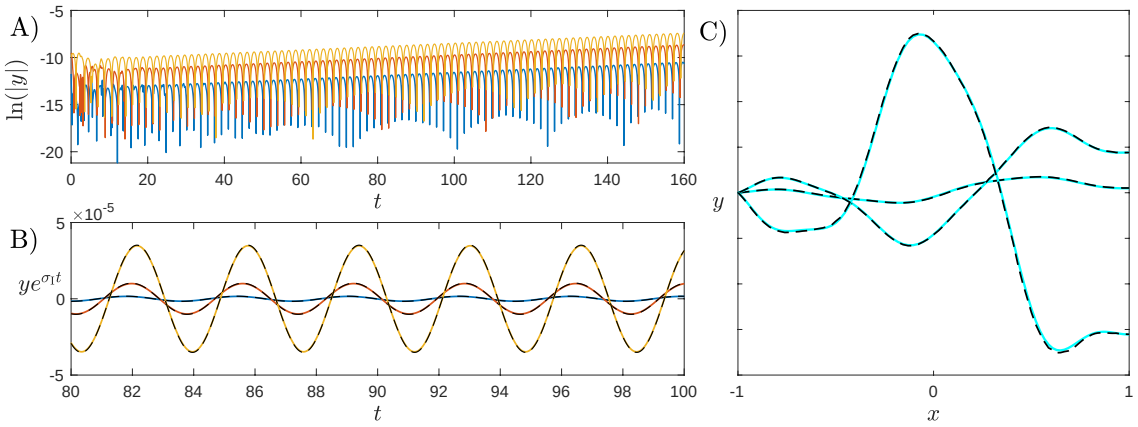

Figure E.1: Example of the comparison method using fixed–free membrane data with $(R_1, T_0) = (10^{-0.5}, 10^{-0.7})$. A) $\ln(|y|)$ versus time for the 10th (blue), 30th (red), and 100th (yellow) grid points on the membrane. B) A portion of the time series of $ye^{\sigma_1 t}$ at the 10th (blue), 30th (red), and 100th (yellow) grid points. This corresponds to part of the small-amplitude regime but with the growth removed. The black dashed lines represent the constructed $R(\alpha)\cos(\sigma_{\mathrm{R}} t + \phi(\alpha))$ at the same grid points. C) The reconstructed data $\mathrm{Re}\left([\mathrm{Re}(y_{\mathrm{nonlin}}(\alpha)) + i\mathrm{Im}(y_{\mathrm{nonlin}}(\alpha))]e^{i\sigma t}\right)$ (black dashed lines) compared against the data $y(\alpha, t)$ (cyan solid lines) at the times $t = 20, 100, 160$. The initial perturbation here is $\zeta(\alpha, 0) = \eta\sin(\pi\alpha)$ where η is chosen as 0.0001. Note that the axes are not to scale.

Finally, we choose a phase ϕ that gives the best match between $Y(x)$ from the

eigenvalue analysis described in §3.3 and $y_{\text{nonlin}}(\alpha)$ from the nonlinear simulations. We do this by solving the following optimization problem:

$$\min_{\phi} \int_{-1}^{1} \left| \frac{[\text{Re}(y_{\text{nonlin}}(x)) + i\text{Im}(y_{\text{nonlin}}(x))]}{\max(|[\text{Re}(y_{\text{nonlin}}(x)) + i\text{Im}(y_{\text{nonlin}}(x))]|)} - \frac{Y(x)e^{i\phi}}{\max(|Y(x)e^{i\phi}|)} \right| \text{d}x \tag{E.4}$$

for $\phi \in [0, 2\pi]$.

APPENDIX F

Comparison of Eigenmodes and Time-stepping Simulations with Free–free Boundary Conditions

In figure F.1, we compare the eigenmodes to the time-stepping simulations for two cases of free–free membranes: $(R_1, T_0) = (10^1, 10^{0.1})$ (panels A, C, and E) and $(10^{1.5}, 10^{0.2})$ (panels B, D, and F) at $R_3 = 10^{1.5}$ in both cases. The comparison methods for fixed–free membranes (see appendix E) are used again here. In A and B we see close agreement between the real and imaginary parts of the eigenmodes obtained from the two methods. In panels C and D a point of inflection occurs close to the midpoint of the membrane, and migrates closer to the leading edge at large amplitude (panels E and F). The small- and large-amplitude shapes are similar in terms of the number of local maxima and minima of deflection (typically one of each).

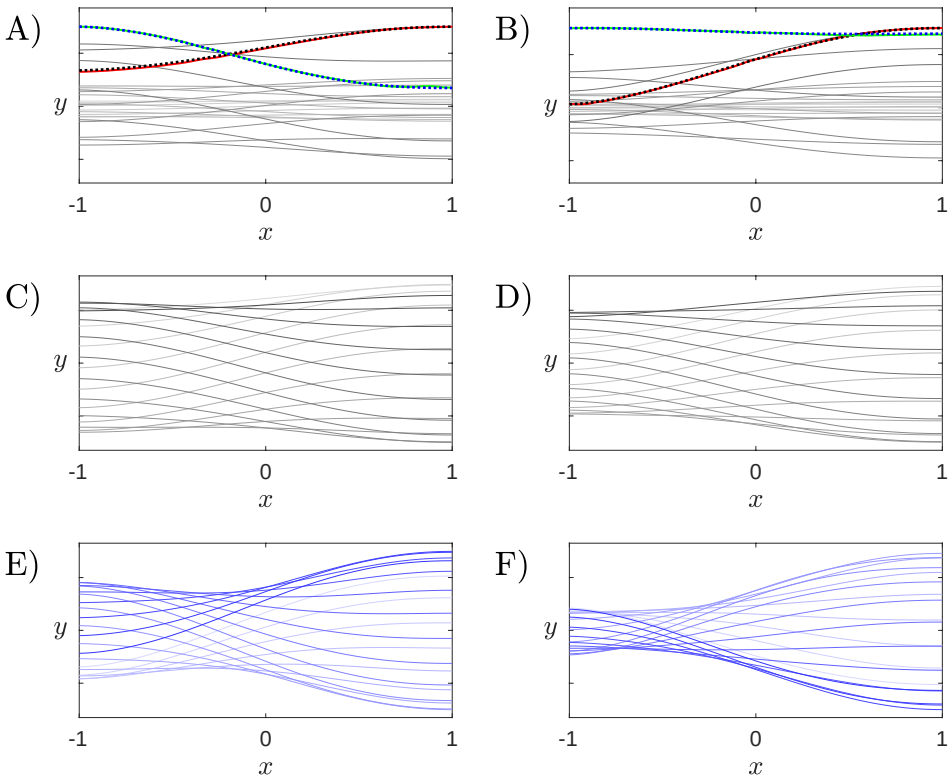

Figure F.1: Free–free membranes at $(R_1, T_0) = (10^1, 10^{0.1})$ for A, C, E and at $(R_1, T_0) = (10^{1.5}, 10^{0.2})$ for B, D, and F, with $R_3 = 10^{1.5}$ in both cases. These membranes lose stability by flutter and divergence. In panels A and B the solid red lines are $\mathrm{Re}(y_{\mathrm{ynonlin}}(\alpha))$ estimated from the time-stepping simulation, which are close to $\mathrm{Re}(Y(x))$ from the eigenvalue problem (dotted black lines). The solid green lines are $\mathrm{Im}(y_{\mathrm{ynonlin}}(\alpha))$, close to $\mathrm{Im}(Y(x))$ from the eigenvalue problem (dotted blue lines). The gray lines are a subset of snapshots in the linear growth regime. In panels C and D we show the snapshots during the small-amplitude (growth) regime, but with the exponential growth removed. Panels E and F show snapshots during the steady-state large-amplitude motions. Shades of gray (and blue) increase from light to dark as 20 membrane positions cycle through a period.

APPENDIX G

Thin-membrane Elasticity

We compute the stretching energy of the membrane using the position $\mathbf{r}(\alpha_1, \alpha_2, t)$. The membrane has thickness $h \ll L, W$, the lateral dimensions. We assume the stretching strain is constant through the thickness, accurate to leading order in h [41].

We denote the flat prestrained configuration of the membrane central surface by $\boldsymbol{\alpha} \equiv (\alpha_1, \alpha_2, 0) = \mathbf{r}(\alpha_1, \alpha_2, 0)$. A small line of material connecting two material points $\boldsymbol{\alpha}$ and $\tilde{\boldsymbol{\alpha}}$ in the flat prestrained configuration is $\mathrm{d}\boldsymbol{\alpha} = \boldsymbol{\alpha} - \tilde{\boldsymbol{\alpha}}$. We assume that the prestrained state is obtained from the zero-energy state by applying a uniform prestrain $\overline{e}$. Thus in the zero-energy state the small line of material is $\mathrm{d}\boldsymbol{\alpha}/(1+\overline{e})$, the prestrain having been removed by dividing by $(1+\overline{e})$.

One of the most common measures of deformation in nonlinear elasticity is the difference between the squared length of a material line in the deformed and zero-energy configurations [97, 170]:

$$\|\mathrm{d}\mathbf{r}\|^2 - \frac{1}{(1+\overline{e})^2}\|\mathrm{d}\boldsymbol{\alpha}\|^2 = 2\epsilon_{ij}\,\mathrm{d}\alpha_i \mathrm{d}\alpha_j\ , \quad \epsilon_{ij} = \frac{1}{2}\left(a_{ij} - \frac{1}{(1+\overline{e})^2}\delta_{ij}\right) \tag{G.1}$$

where $\mathrm{d}\mathbf{r} = \mathbf{r}(\alpha_1, \alpha_2, 0) - \mathbf{r}(\tilde{\alpha}_1, \tilde{\alpha}_2, 0)$ and ϵ_{ij} is the (Green-Lagrange) strain tensor, written in terms of the metric tensor

$$a_{ij} = \partial_{\alpha_i}\mathbf{r} \cdot \partial_{\alpha_j}\mathbf{r} = \frac{\partial r_k}{\partial \alpha_i}\frac{\partial r_k}{\partial \alpha_j}, \quad i, j = 1, 2. \tag{G.2}$$

and the identity tensor δ_{ij}.

For an isotropic membrane with Young's modulus E, Poisson ratio ν, and thickness h, the elastic energy per unit midsurface area [9] is

$$w_s = \frac{h}{2}\bar{A}^{mnop}\epsilon_{mn}\epsilon_{op}\ , \quad \bar{A}^{mnop} = \frac{E}{1+\nu}\left(\frac{\nu}{1-\nu}\delta_{mn}\delta_{op} + \delta_{mo}\delta_{np}\right) \tag{G.3}$$

where $\bar{A}^{mnop}$ is the elasticity tensor for an isotropic material [97]. For small-to-moderate prestrains, the focus of this work, the strain tensor in (G.1) is approximately

$$\epsilon_{ij}(\alpha_1, \alpha_2, t) = \overline{e}\delta_{ij} + \frac{1}{2}\left(\partial_{\alpha_i}\mathbf{r}\cdot\partial_{\alpha_j}\mathbf{r} - \delta_{ij}\right), \quad i,j = 1,2. \tag{G.4}$$

APPENDIX H

Derivation of Pressure Jump Equation in 3D Flow

In this appendix we derive an expression for the pressure jump $[p](\alpha_1, \alpha_2, t)$ across the membrane in terms of the membrane vortex sheet strength and other quantities, as a generalization of appendix A.

The Euler momentum equation given by

$$\partial_t \boldsymbol{u}(\boldsymbol{x}, t) + \boldsymbol{u}(\boldsymbol{x}, t) \cdot \nabla \boldsymbol{u}(\boldsymbol{x}, t) = -\nabla p(\boldsymbol{x}, t) \tag{H.1}$$

couples the fluid velocity $\boldsymbol{u}(\boldsymbol{x}, t)$ and the pressure $p(\boldsymbol{x}, t)$. We calculate the fluid pressure at a point that is adjacent to and follows a material point $\boldsymbol{r}(\alpha_1, \alpha_2, t)$ on the membrane. The rate of change of fluid velocity at such a point is

$$\frac{\mathrm{d}}{\mathrm{d}t}\boldsymbol{u}(\boldsymbol{r}(\alpha_1, \alpha_2, t), t) = \partial_t \boldsymbol{u}(\boldsymbol{x}, t)|_{\boldsymbol{x}=\boldsymbol{r}(\alpha_1,\alpha_2,t)} + (\partial_t \boldsymbol{r}(\alpha_1, \alpha_2, t) \cdot \nabla)\, \boldsymbol{u}(\boldsymbol{x}, t)|_{\boldsymbol{x}=\boldsymbol{r}(\alpha_1,\alpha_2,t)}. \tag{H.2}$$

We use (H.2) to replace the first term in (H.1) and write the pressure gradient at a point that moves with $\boldsymbol{r}(\alpha_1, \alpha_2, t)$. To obtain the jump in fluid pressure at a material point on the membrane, we write (H.1) (modified by (H.2)) separately at points in the fluid that approach the membrane from either side:

$$\begin{aligned} \frac{\mathrm{d}}{\mathrm{d}t}\boldsymbol{u}(\boldsymbol{r}(\alpha_1, \alpha_2, t), t)^{\pm} + \left((\boldsymbol{u}(\boldsymbol{x}, t) - \partial_t \boldsymbol{r}) \cdot \nabla \boldsymbol{u}(\boldsymbol{x}, t)\Big|_{\boldsymbol{x}=\boldsymbol{r}(\alpha_1,\alpha_2,t)} \right)^{\pm} \\ = -(\nabla p(\boldsymbol{x}, t)|_{\boldsymbol{x}=\boldsymbol{r}(\alpha_1,\alpha_2,t)})^{\pm}, \end{aligned} \tag{H.3}$$

using + for the side toward which the membrane normal $\hat{\mathbf{n}}$ is directed and − for the other side.

Next, we decompose the fluid velocity into components tangential and normal to the membrane. The normal component matches that of the membrane, ν_v. The tangential component of the fluid velocity may be written in terms of its jump across the membrane, using the vortex sheet strength components γ_1, γ_2 [149], and the average of the tangential components of the fluid velocity on the two sides of the membrane, denoted μ_1 and μ_2. The subscripts $\{1, 2\}$ denote the components in the $\widehat{\mathbf{s}}_1$ and $\widehat{\mathbf{s}}_2$ directions, respectively. The fluid velocity can be written

$$\boldsymbol{u}^{\pm} = \left(\mu_1 \pm \frac{\gamma_2}{2}\right)\widehat{\mathbf{s}}_1 + \left(\mu_2 \mp \frac{\gamma_1}{2}\right)\widehat{\mathbf{s}}_2 + \nu_v \hat{\mathbf{n}}. \tag{H.4}$$

We take the difference of (H.3) on the + and − sides:

$$\begin{aligned} &\frac{\mathrm{d}}{\mathrm{d}t}\left(\boldsymbol{u}^+(\boldsymbol{r}(\alpha_1,\alpha_2,t),t) - \boldsymbol{u}^-(\boldsymbol{r}(\alpha_1,\alpha_2,t),t)\right) \\ &+ \left((\boldsymbol{u}^+(\boldsymbol{x},t) - \partial_t \boldsymbol{r}) \cdot \nabla \boldsymbol{u}^+(\boldsymbol{x},t)\Big|_{\boldsymbol{x}=\boldsymbol{r}(\alpha_1,\alpha_2,t)}\right) \\ &- \left((\boldsymbol{u}^-(\boldsymbol{x},t) - \partial_t \boldsymbol{r}) \cdot \nabla \boldsymbol{u}^-(\boldsymbol{x},t)\Big|_{\boldsymbol{x}=\boldsymbol{r}(\alpha_1,\alpha_2,t)}\right) \\ &= -(\nabla p(\boldsymbol{x},t)^+ - \nabla p(\boldsymbol{x},t)^-)|_{\boldsymbol{x}=\boldsymbol{r}(\alpha_1,\alpha_2,t)}. \end{aligned} \tag{H.5}$$

We then take the $\widehat{\mathbf{s}}_1$ components of (H.5), term by term. The $\widehat{\mathbf{s}}_1$ component of the right hand side of (H.5) is $-\partial_{s_1}[p]^+_-$ which we will ultimately integrate to obtain $[p]^+_-$. $-\partial_{s_1}[p]^+_-$ is equal to the $\widehat{\mathbf{s}}_1$ components of the terms on the left hand side of (H.5), which we now compute. Using (H.4), the $\widehat{\mathbf{s}}_1$ component of the first term on the left-hand side of (H.5) is

$$\begin{aligned} \widehat{\mathbf{s}}_1 \cdot \frac{\mathrm{d}}{\mathrm{d}t}(\boldsymbol{u}^+(\boldsymbol{r}(\alpha_1,\alpha_2,t),t) - \boldsymbol{u}^-(\boldsymbol{r}(\alpha_1,\alpha_2,t),t)) &= \widehat{\mathbf{s}}_1 \cdot \partial_t(-\gamma_1\widehat{\mathbf{s}}_2 + \gamma_2\widehat{\mathbf{s}}_1) \\ &= \partial_t\gamma_2 - \partial_t\gamma_1(\widehat{\mathbf{s}}_1 \cdot \widehat{\mathbf{s}}_2) - \gamma_1(\widehat{\mathbf{s}}_1 \cdot \partial_t\widehat{\mathbf{s}}_2), \end{aligned} \tag{H.6}$$

where we use $\widehat{\mathbf{s}}_i \cdot \widehat{\mathbf{s}}_i = 1$ and $\widehat{\mathbf{s}}_i \cdot \partial_t \widehat{\mathbf{s}}_i = 0$ for $i = 1, 2$.

For $\widehat{\mathbf{s}}_i \cdot [(\boldsymbol{u}^{\pm}(\boldsymbol{x}, t) - \partial_t \boldsymbol{r}) \cdot \nabla \boldsymbol{u}^{\pm}(\boldsymbol{x}, t)]$ where $i = 1, 2$, we first write $\boldsymbol{u}^{\pm} - \partial_t \boldsymbol{r}$ as $A\widehat{\mathbf{s}}_1 + B\widehat{\mathbf{s}}_2$. Then we compute the dot product between that and $\nabla \boldsymbol{u}^{\pm}$ and obtain $A\partial_{s_1}\boldsymbol{u}^{\pm} + B\partial_{s_2}\boldsymbol{u}^{\pm}$. If we substitute $\boldsymbol{u}^{\pm}$, we get an expression of the form $C\widehat{\mathbf{s}}_1 + D\widehat{\mathbf{s}}_2$, which we can finally dot with $\widehat{\mathbf{s}}_1$ and $\widehat{\mathbf{s}}_2$.

Using

$$\partial_t \boldsymbol{r} = \tau_1 \widehat{\mathbf{s}}_1 + \tau_2 \widehat{\mathbf{s}}_2 + \nu_v \hat{\mathbf{n}}, \tag{H.7}$$

and (H.4), we find that the $\widehat{\mathbf{s}}_1$ components of the second and third terms on the left-hand side of (H.5) are

$$\begin{aligned}
&\widehat{\mathbf{s}}_1 \cdot \left[(\boldsymbol{u}^{\pm}(\boldsymbol{x}, t) - \partial_t \boldsymbol{r}) \cdot \nabla \boldsymbol{u}^{\pm}(\boldsymbol{x}, t)\right] \Big|_{\boldsymbol{x}=\boldsymbol{r}(\alpha_1,\alpha_2,t)} \\
&\quad = \left(\mu_1 \pm \frac{\gamma_2}{2} - \tau_1\right) \left[\partial_{s_1}\left(\mu_1 \pm \frac{\gamma_2}{2}\right) + \left(\partial_{s_1}\left(\mu_2 \mp \frac{\gamma_1}{2}\right)\right) \widehat{\mathbf{s}}_1 \cdot \widehat{\mathbf{s}}_2 \right. \\
&\qquad \left. + \left(\mu_2 \mp \frac{\gamma_1}{2}\right) \widehat{\mathbf{s}}_1 \cdot \partial_{s_1} \widehat{\mathbf{s}}_2 + \nu_v \widehat{\mathbf{s}}_1 \cdot \partial_{s_1} \hat{\mathbf{n}}\right] \\
&\quad + \left(\mu_2 \mp \frac{\gamma_1}{2} - \tau_2\right) \left[\partial_{s_2}\left(\mu_1 \pm \frac{\gamma_2}{2}\right) + \left(\partial_{s_2}\left(\mu_2 \mp \frac{\gamma_1}{2}\right)\right) \widehat{\mathbf{s}}_1 \cdot \widehat{\mathbf{s}}_2 \right. \\
&\qquad \left. + \left(\mu_2 \mp \frac{\gamma_1}{2}\right) \widehat{\mathbf{s}}_1 \cdot \partial_{s_2} \widehat{\mathbf{s}}_2 + \nu_v \widehat{\mathbf{s}}_1 \cdot \partial_{s_2} \hat{\mathbf{n}} + \left(\mu_1 \pm \frac{\gamma_2}{2}\right) \widehat{\mathbf{s}}_1 \cdot \partial_{s_2} \widehat{\mathbf{s}}_1\right].
\end{aligned} \tag{H.8}$$

The difference of the $+$ and $-$ terms on the right-hand side of (H.8) is

$$\begin{aligned}
&(\widehat{\mathbf{s}}_1 \cdot \widehat{\mathbf{s}}_2)(-\mu_1 \partial_{s_1}\gamma_1 + \gamma_2 \partial_{s_1}\mu_2 + \tau_1 \partial_{s_1}\gamma_1 - \mu_2 \partial_{s_2}\gamma_1 - \gamma_1 \partial_{s_2}\mu_2 + \tau_2 \partial_{s_2}\gamma_1) \\
&+(\widehat{\mathbf{s}}_1 \cdot \partial_{s_1}\widehat{\mathbf{s}}_2)(-\mu_1\gamma_1 + \gamma_2\mu_2 + \tau_1\gamma_1) + (\widehat{\mathbf{s}}_1 \cdot \partial_{s_2}\widehat{\mathbf{s}}_1)(\mu_2\gamma_2 - \gamma_1\mu_1 - \tau_2\gamma_2) \\
&+(\mu_1 \partial_{s_1}\gamma_2 + \gamma_2 \partial_{s_1}\mu_1 - \tau_1 \partial_{s_1}\gamma_2 + \mu_2 \partial_{s_2}\gamma_2 - \gamma_1 \partial_{s_2}\mu_1 - \tau_2 \partial_{s_2}\gamma_2) \\
&+(\widehat{\mathbf{s}}_1 \cdot \partial_{s_2}\widehat{\mathbf{s}}_2)(-2\mu_2\gamma_1 + \tau_2\gamma_1) + (\widehat{\mathbf{s}}_1 \cdot \partial_{s_1}\hat{\mathbf{n}})\gamma_2\nu_v - (\widehat{\mathbf{s}}_1 \cdot \partial_{s_2}\hat{\mathbf{n}})\gamma_1\nu_v,
\end{aligned} \tag{H.9}$$

using $\widehat{\mathbf{s}}_i \cdot \partial_{s_i}\widehat{\mathbf{s}}_i = 0$ and $\hat{\mathbf{n}} \cdot \widehat{\mathbf{s}}_i = 0$ for $i = 1, 2$.

Combining (H.6) and (H.9), the $\widehat{\mathbf{s}}_1$ component of (H.5) is

$$\begin{aligned}
&\partial_t\gamma_2 - \partial_t\gamma_1(\widehat{\mathbf{s}}_1\cdot\widehat{\mathbf{s}}_2) - \gamma_1(\widehat{\mathbf{s}}_1\cdot\partial_t\widehat{\mathbf{s}}_2)\\
&+(\widehat{\mathbf{s}}_1\cdot\widehat{\mathbf{s}}_2)(-\mu_1\partial_{s_1}\gamma_1+\gamma_2\partial_{s_1}\mu_2+\tau_1\partial_{s_1}\gamma_1-\mu_2\partial_{s_2}\gamma_1-\gamma_1\partial_{s_2}\mu_2+\tau_2\partial_{s_2}\gamma_1)\\
&+(\widehat{\mathbf{s}}_1\cdot\partial_{s_1}\widehat{\mathbf{s}}_2)(-\mu_1\gamma_1+\gamma_2\mu_2+\tau_1\gamma_1)+(\widehat{\mathbf{s}}_1\cdot\partial_{s_2}\widehat{\mathbf{s}}_1)(\mu_2\gamma_2-\gamma_1\mu_1-\tau_2\gamma_2)\\
&+(\mu_1\partial_{s_1}\gamma_2+\gamma_2\partial_{s_1}\mu_1-\tau_1\partial_{s_1}\gamma_2+\mu_2\partial_{s_2}\gamma_2-\gamma_1\partial_{s_2}\mu_1-\tau_2\partial_{s_2}\gamma_2)\\
&+(\widehat{\mathbf{s}}_1\cdot\partial_{s_2}\widehat{\mathbf{s}}_2)(-2\mu_2\gamma_1+\tau_2\gamma_1)+(\widehat{\mathbf{s}}_1\cdot\partial_{s_1}\hat{\mathbf{n}})\gamma_2\nu_v-(\widehat{\mathbf{s}}_1\cdot\partial_{s_2}\hat{\mathbf{n}})\gamma_1\nu_v\\
&= -\partial_{s_1}[p]^+_-. \qquad \text{(H.10)}
\end{aligned}$$

We multiply (H.10) through by $\partial_{\alpha_1}s_1$ which converts $\partial_{s_1}[p]^+_-$ to $\partial_{\alpha_1}[p]^+_-$. We integrate with respect to α_1 from the trailing edge, applying $[p]^+_- = 0$ at the trailing edge, to obtain $[p]^+_-$ at all points on the membrane.

If we directly integrate $\partial_{\alpha_1}[p]^+_-$ numerically (e.g. using the trapezoidal rule), the results disagree significantly with our 2D benchmark results [113]. Using a different formulation that agrees with the 2D results in the small-amplitude regime, we have found empirically that the following method agrees well with the 2D results in both the small- and large-amplitude regimes. We first write $\partial_{\alpha_1}[p]^+_-$ as a sum of two terms:

$$\partial_{\alpha_1}[p]^+_- = (\partial_{\alpha_1}[p]^+_- + \partial_{\alpha_1}s_1\partial_t\gamma_2 + \partial_{\alpha_1}\gamma_2) + (-\partial_{\alpha_1}s_1\partial_t\gamma_2 - \partial_{\alpha_1}\gamma_2). \qquad \text{(H.11)}$$

We have added and subtracted $\partial_{\alpha_1}s_1\partial_t\gamma_2 + \partial_{\alpha_1}\gamma_2$. Its integral with respect to α_1 can be written $\partial_t\Gamma + \partial_{s_1}\Gamma$, where Γ is the integrated vortex sheet strength [149]. It is conserved at points of a free vortex sheet that move at the average of the tangential flow velocities on the two sides of the sheet, equal to 1 in this case. Hence $\partial_t\Gamma + \partial_{s_1}\Gamma = 0$ at the trailing edge, as does $[p]^+_-$ by the unsteady Kutta condition [88, 149].

Therefore we integrate the first term in (H.11) (in parentheses) with respect to α_1 using the trapezoidal rule, with the boundary condition that its integral is 0 at the

trailing edge. The integral of the remaining terms in (H.11) is $-\partial_t\Gamma - \partial_{s_1}\Gamma$ evaluated at α_1 minus its value at the trailing edge, which is zero as we have just discussed. To evaluate $-\partial_t\Gamma - \partial_{s_1}\Gamma$ on the (α_1,α_2) grid, we approximate Γ at the center point of a membrane vortex panel by the circulation of the vortex ring at that panel. Derivatives of Γ with respect to t and α_1 are obtained by the usual finite-difference formulas and extrapolation to the (α_1,α_2) grid points—i.e. the corner points of the panels.

APPENDIX I

Residual Membrane Equations in Broyden's Method

In this appendix we write down the discretized system of nonlinear membrane equations that we solve using Broyden's method. Having computed each of the quantities in the membrane equation (5.16) we keep iterating until $\mathbf{f}(\mathbf{x})$ drops below a certain tolerance that we set to 10^{-5}. Here $\mathbf{f}(\mathbf{x})$ is given by:

(I.1)

$$
\begin{aligned}
f_j(\boldsymbol{x}) = R_1 \partial_{tt} x_j^k - K_s \big\{ & (D^2_{\alpha_1}\mathbf{r}_j^k \cdot D^1_{\alpha_1}\mathbf{r}_j^k) D^1_{\alpha_1} x_j^k + \epsilon_{11} D^2_{\alpha_1} x_j^k \\
& + \nu \left((D^2_{\alpha_1\alpha_2}\mathbf{r}_j^k \cdot D^1_{\alpha_2}\mathbf{r}_j^k) D^1_{\alpha_1} x_j^k + \epsilon_{22} D^2_{\alpha_1} x_j^k \right) \\
& + (1-\nu) \left[((D^2_{\alpha_1}\mathbf{r}_j^k \cdot D^1_{\alpha_2}\mathbf{r}_j^k + D^1_{\alpha_1}\mathbf{r}_j^k \cdot D^2_{\alpha_1\alpha_2}\mathbf{r}_j^k)/2) D^1_{\alpha_2} x_j^k + \epsilon_{12} D^2_{\alpha_1\alpha_2} x_j^k \right] \\
& + (D^2_{\alpha_2}\mathbf{r}_j^k \cdot D^1_{\alpha_2}\mathbf{r}_j^k) D^1_{\alpha_2} x_j^k + \epsilon_{22} D^2_{\alpha_2} x_j^k + \nu ((D^2_{\alpha_1\alpha_2}\mathbf{r}_j^k \cdot D^1_{\alpha_1}\mathbf{r}_j^k) D^1_{\alpha_2} x_j^k + \epsilon_{11} D^2_{\alpha_2} x_j^k) \\
& + (1-\nu) \left[((D^2_{\alpha_1\alpha_2}\mathbf{r}_j^k \cdot D^1_{\alpha_2}\mathbf{r}_j^k + D^1_{\alpha_1}\mathbf{r}_j^k \cdot D^2_{\alpha_2}\mathbf{r}_j^k)/2) D^1_{\alpha_1} x_j^k + \epsilon_{12} D^2_{\alpha_1\alpha_2} x_j^k \right] \big\} \\
& + [p]_j^k \hat{\mathbf{n}}_{x,j}^k \sqrt{(D^1_{\alpha_1}\mathbf{r}_j^k \cdot D^1_{\alpha_1}\mathbf{r}_j^k)(D^1_{\alpha_2}\mathbf{r}_j^k \cdot D^1_{\alpha_2}\mathbf{r}_j^k) - (D^1_{\alpha_1}\mathbf{r}_j^k \cdot D^1_{\alpha_2}\mathbf{r}_j^k)^2},
\end{aligned}
$$

(I.2)

$$
\begin{aligned}
f_{j+(M-1)(N-1)}(\boldsymbol{x}) &= R_1\partial_{tt}y_j^k - K_s\left\{(D^2_{\alpha_1}\mathbf{r}_j^k\cdot D^1_{\alpha_1}\mathbf{r}_j^k)D^1_{\alpha_1}y_j^k + \epsilon_{11}D^2_{\alpha_1}y_j^k\right.\\
&+ \nu\left((D^2_{\alpha_1\alpha_2}\mathbf{r}_j^k\cdot D^1_{\alpha_2}\mathbf{r}_j^k)D^1_{\alpha_1}y_j^k + \epsilon_{22}D^2_{\alpha_1}y_j^k\right)\\
&+ (1-\nu)\left[((D^2_{\alpha_1}\mathbf{r}_j^k\cdot D^1_{\alpha_2}\mathbf{r}_j^k + D^1_{\alpha_1}\mathbf{r}_j^k\cdot D^2_{\alpha_1\alpha_2}\mathbf{r}_j^k)/2)D^1_{\alpha_2}y_j^k + \epsilon_{12}D^2_{\alpha_1\alpha_2}y_j^k\right]\\
&+ (D^2_{\alpha_2}\mathbf{r}_j^k\cdot D^1_{\alpha_2}\mathbf{r}_j^k)D^1_{\alpha_2}y_j^k + \epsilon_{22}D^2_{\alpha_2}y_j^k + \nu((D^2_{\alpha_1\alpha_2}\mathbf{r}_j^k\cdot D^1_{\alpha_1}\mathbf{r}_j^k)D^1_{\alpha_2}y_j^k + \epsilon_{11}D^2_{\alpha_2}y_j^k)\\
&+ (1-\nu)\left[((D^2_{\alpha_1\alpha_2}\mathbf{r}_j^k\cdot D^1_{\alpha_2}\mathbf{r}_j^k + D^1_{\alpha_1}\mathbf{r}_j^k\cdot D^2_{\alpha_2}\mathbf{r}_j^k)/2)D^1_{\alpha_1}y_j^k + \epsilon_{12}D^2_{\alpha_1\alpha_2}y_j^k\right]\Big\}\\
&+ [p]_j^k\hat{\mathbf{n}}_{y,j}^k\sqrt{(D^1_{\alpha_1}\mathbf{r}_j^k\cdot D^1_{\alpha_1}\mathbf{r}_j^k)(D^1_{\alpha_2}\mathbf{r}_j^k\cdot D^1_{\alpha_2}\mathbf{r}_j^k) - (D^1_{\alpha_1}\mathbf{r}_j^k\cdot D^1_{\alpha_2}\mathbf{r}_j^k)^2},
\end{aligned}
$$

(I.3)

$$
\begin{aligned}
f_{j+2(M-1)(N-1)}(\boldsymbol{x}) &= R_1\partial_{tt}z_j^k - K_s\left\{(D^2_{\alpha_1}\mathbf{r}_j^k\cdot D^1_{\alpha_1}\mathbf{r}_j^k)D^1_{\alpha_1}z_j^k + \epsilon_{11}D^2_{\alpha_1}z_j^k\right.\\
&+ \nu\left((D^2_{\alpha_1\alpha_2}\mathbf{r}_j^k\cdot D^1_{\alpha_2}\mathbf{r}_j^k)D^1_{\alpha_1}z_j^k + \epsilon_{22}D^2_{\alpha_1}z_j^k\right)\\
&+ (1-\nu)\left[((D^2_{\alpha_1}\mathbf{r}_j^k\cdot D^1_{\alpha_2}\mathbf{r}_j^k + D^1_{\alpha_1}\mathbf{r}_j^k\cdot D^2_{\alpha_1\alpha_2}\mathbf{r}_j^k)/2)D^1_{\alpha_2}z_j^k + \epsilon_{12}D^2_{\alpha_1\alpha_2}z_j^k\right]\\
&+ (D^2_{\alpha_2}\mathbf{r}_j^k\cdot D^1_{\alpha_2}\mathbf{r}_j^k)D^1_{\alpha_2}z_j^k + \epsilon_{22}D^2_{\alpha_2}z_j^k + \nu((D^2_{\alpha_1\alpha_2}\mathbf{r}_j^k\cdot D^1_{\alpha_1}\mathbf{r}_j^k)D^1_{\alpha_2}z_j^k + \epsilon_{11}D^2_{\alpha_2}z_j^k)\\
&+ (1-\nu)\left[((D^2_{\alpha_1\alpha_2}\mathbf{r}_j^k\cdot D^1_{\alpha_2}\mathbf{r}_j^k + D^1_{\alpha_1}\mathbf{r}_j^k\cdot D^2_{\alpha_2}\mathbf{r}_j^k)/2)D^1_{\alpha_1}z_j^k + \epsilon_{12}D^2_{\alpha_1\alpha_2}z_j^k\right]\Big\}\\
&+ [p]_j^k\hat{\mathbf{n}}_{z,j}^k\sqrt{(D^1_{\alpha_1}\mathbf{r}_j^k\cdot D^1_{\alpha_1}\mathbf{r}_j^k)(D^1_{\alpha_2}\mathbf{r}_j^k\cdot D^1_{\alpha_2}\mathbf{r}_j^k) - (D^1_{\alpha_1}\mathbf{r}_j^k\cdot D^1_{\alpha_2}\mathbf{r}_j^k)^2},
\end{aligned}
$$

where $j = 1,\ldots,(M-1)(N-1)$ and $[p]$ is the result of integrating (H.11). Here $D^1_{\alpha_i} \approx \partial_{\alpha_i}$, $D^2_{\alpha_i} \approx \partial_{\alpha_i\alpha_i}$ for $i = 1,2$ and $D^2_{\alpha_1\alpha_2} \approx \partial_{\alpha_1\alpha_2}$ are second-order accurate finite-difference matrix approximations to first and second-order derivatives (order listed in the superscript) on uniform grid nodes, one-sided at boundaries. $\partial_{tt}\{x_j^k, y_j^k, z_j^k\}$ are the second-order accurate finite difference formulas (backward differentiation formulas) at time step k based on the values of $\{x_j, y_j, z_j\}$ at times steps $k-3,\ldots,k$.

APPENDIX J

Membrane Deflections Versus Stretching Rigidity at Different Pretension Values

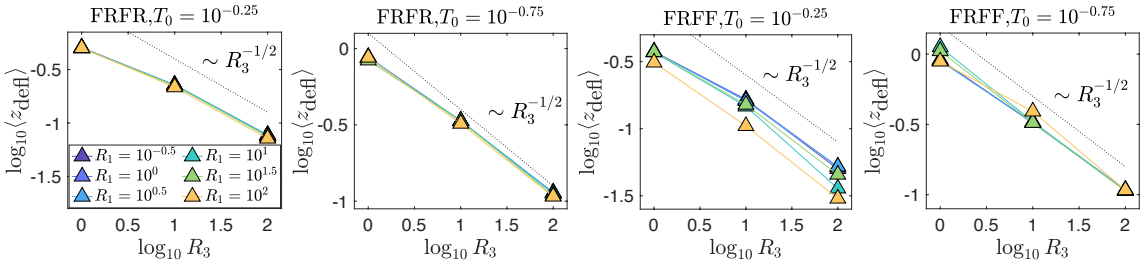

Figure J.1: Time-averaged deflections of FRFR and FRFF membranes (defined by (5.29)) versus R_3 for various R_1 and fixed T_0 ($10^{-0.25}$ and $10^{-0.75}$). The dotted black line indicates the scaling $R_3^{-1/2}$.

For two of the 12 boundary conditions (FRFF and FRFR) we plot in figure J.1 the average membrane deflection at $T_0 = 10^{-0.25}$ and $10^{-0.75}$, instead of $10^{-0.5}$ in figure 5.10, and see that the deflection values increase at smaller T_0 (similarly to [113, 183]) but the same $1/\sqrt{R_3}$ scaling holds in all cases.

BIBLIOGRAPHY

BIBLIOGRAPHY

[1] M. Abdulrahim, H. Garcia, and R. Lind. Flight characteristics of shaping the membrane wing of a micro air vehicle. *Journal of Aircraft*, 42(1):131–137, 2005.

[2] S. Alben. Optimal flexibility of a flapping appendage in an inviscid fluid. *Journal of Fluid Mechanics*, 614:355–380, 2008.

[3] S. Alben. The flapping-flag instability as a nonlinear eigenvalue problem. *Physics of Fluids*, 20:104106, 2008.

[4] S. Alben. Simulating the dynamics of flexible bodies and vortex sheets. *Journal of Computational Physics*, 228(7):2587–2603, 2009.

[5] S. Alben. Regularizing a vortex sheet near a separation point. *Journal of Computational Physics*, 229(13):5280–5298, 2010.

[6] S. Alben. The attraction between a flexible filament and a point vortex. *J. Fluid Mech.*, 697:481–503, 2012.

[7] S. Alben. Flag flutter in inviscid channel flow. *Physics of Fluids*, 27(3):033603, 2015.

[8] S. Alben. Dynamics of flags over wide ranges of mass and bending stiffness. *Physical Review Fluids*, 7(1):013903, 2022.

[9] S. Alben, A. A. Gorodetsky, D. Kim, and R. D. Deegan. Semi-implicit methods for the dynamics of elastic sheets. *Journal of Computational Physics*, 399:108952, 2019.

[10] S. Alben and M. J. Shelley. Flapping states of a flag in an inviscid fluid: bistability and the transition to chaos. *Phys. Rev. Lett.*, 100(7):074301, 2008.

[11] R. Albertani, B. Stanford, J. P. Hubner, and P. G. Ifju. Aerodynamic coefficients and deformation measurements on flexible micro air vehicle wings. *Experimental Mechanics*, 47(5):625–635, 2007.

[12] J. J. Allen and A. J. Smits. Energy harvesting eel. *Journal of fluids and structures*, 15(3-4):629–640, 2001.

[13] S. Arbós-Torrent, B. Ganapathisubramani, and R. Palacios. Leading-and trailing-edge effects on the aeromechanics of membrane aerofoils. *J. Fluids and Struct.*, 38:107–126, 2013.

[14] M. Argentina and L. Mahadevan. Fluid-flow-induced flutter of a flag. *Proceedings of the National Academy of Sciences*, 102(6):1829–1834, 2005.

[15] H. Ashley and G. Zartarian. Piston theory-a new aerodynamic tool for the aeroelastician. *Journal of the Aeronautical Sciences*, 23(12):1109–1118, 1956.

[16] F. Ayancik, F. E. Fish, and K. W. Moored. Three-dimensional scaling laws of cetacean propulsion characterize the hydrodynamic interplay of flukes' shape and kinematics. *Journal of the Royal Society Interface*, 17(163):20190655, 2020.

[17] F. Ayancik, A. Mivehchi, and K. W. Moored. Scaling laws for three-dimensional combined heaving and pitching propulsors. *AIAA Journal*, 60(5):2930–2940, 2022.

[18] S. Banerjee, B. S. H. Connell, and D. K. P. Yue. Three-dimensional effects on flag flapping dynamics. *Journal of Fluid Mechanics*, 783:103–136, 2015.

[19] G. K. Batchelor. *An introduction to fluid dynamics*. Cambridge university press, 1967.

[20] I. Borazjani, L. Ge, T. Le, and F. Sotiropoulos. A parallel overset-curvilinear-immersed boundary framework for simulating complex 3d incompressible flows. *Computers & fluids*, 77:76–96, 2013.

[21] M. Brady, A. Leonard, and D. I. Pullin. Regularized vortex sheet evolution in three dimensions. *Journal of Computational Physics*, 146(2):520–545, 1998.

[22] G. F. Carrier. On the non-linear vibration problem of the elastic string. *Quarterly of Applied Mathematics*, 3(2):157–165, 1945.

[23] G. F. Carrier. A note on the vibrating string. *Quarterly of Applied Mathematics*, 7(1):97–101, 1949.

[24] P. Chatterjee and M. Bryant. Aeroelastic-photovoltaic ribbons for integrated wind and solar energy harvesting. *Smart Materials and Structures*, 27(8):08LT01, 2018.

[25] M. Chen, L.-B. Jia, Y.-F. Wu, X.-Z. Yin, and Y.-B. Ma. Bifurcation and chaos of a flag in an inviscid flow. *J. Fluids and Struct.*, 45:124–137, 2014.

[26] Y. Chen, J. Ryu, Y. Liu, and H. J. Sung. Flapping dynamics of vertically clamped three-dimensional flexible flags in a poiseuille flow. *Physics of Fluids*, 32(7):071905, 2020.

[27] J. A. Cheney, N. Konow, A. Bearnot, and S. M. Swartz. A wrinkle in flight: the role of elastin fibres in the mechanical behaviour of bat wing membranes. *Journal of the Royal Society Interface*, 12(106):20141286, 2015.

[28] A. J. Chorin and P. S. Bernard. Discretization of a vortex sheet, with an example of roll-up. *Journal of Computational Physics*, 13(3):423–429, 1973.

[29] J. A. Cole, M. D. Maughmer, G. Bramesfeld, M. Melville, and M. Kinzel. Unsteady lift prediction with a higher-order potential flow method. *Aerospace*, 7(5):60, 2020.

[30] S. Colgate. *Fundamentals of Sailing, Cruising, and Racing*. WW Norton & Company, 1996.

[31] B. S. H. Connell and D. K. P. Yue. Flapping dynamics of a flag in a uniform stream. *J. Fluid Mech.*, 581:33–67, 2007.

[32] A. Das, K. S. Breuer, and V. Mathai. Nonlinear modeling and characterization of ultrasoft silicone elastomers. *Applied Physics Letters*, 116(20):203702, 2020.

[33] A. Das, V. Mathai, and K. Breuer. Deformation, forces, and flows associated with extremely compliant membrane disks. In *AIAA Scitech 2020 Forum*, page 1049, 2020.

[34] M. Dawoodian and A. Sau. Kinetics and prey capture by a paddling jellyfish: three-dimensional simulation and lagrangian coherent structure analysis. *Journal of Fluid Mechanics*, 912, 2021.

[35] E. de Langre, M. P. Païdoussis, O. Doaré, and Y. Modarres-Sadeghi. Flutter of long flexible cylinders in axial flow. *J. Fluid Mech.*, 571:371–389, 2007.

[36] O. Doaré and S. Michelin. Piezoelectric coupling in energy-harvesting fluttering flexible plates: linear stability analysis and conversion efficiency. *Journal of Fluids and Structures*, 27(8):1357–1375, 2011.

[37] D. Dong, W. Chen, and S. Shi. Coupling motion and energy harvesting of two side-by-side flexible plates in a 3D uniform flow. *Applied Sciences*, 6(5):141, 2016.

[38] E. H. Dowell. *Aeroelasticity of plates and shells*, volume 1. Springer Science & Business Media, 1974.

[39] E. H. Dowell and C. S. Ventres. Flutter of low aspect ratio plates. *AIAA Journal*, 8(6):1162–1164, 1970.

[40] A. Drachinsky and D. E. Raveh. Limit-cycle oscillations of a pre-tensed membrane strip. *Journal of Fluids and Structures*, 60:1–22, 2016.

[41] E. Efrati, E. Sharon, and R. Kupferman. Elastic theory of unconstrained non-Euclidean plates. *Journal of the Mechanics and Physics of Solids*, 57(4):762–775, 2009.

[42] C. Eloy, R. Lagrange, C. Souilliez, and L. Schouveiler. Aeroelastic instability of cantilevered flexible plates in uniform flow. *J. Fluid Mech.*, 611:97–106, 2008.

[43] C. Eloy, C. Souilliez, and L. Schouveiler. Flutter of a rectangular plate. *J. Fluids and Struct.*, 23(6):904–919, 2007.

[44] A. Erturk, W. G. R. Vieira, C. De Marqui Jr, and D. J. Inman. On the energy harvesting potential of piezoaeroelastic systems. *Applied Physics Letters*, 96(18):184103, 2010.

[45] S. J. Farlow. *Partial differential equations for scientists and engineers*. Courier Corporation, 1993.

[46] H. Feng. *Vortex Sheet Simulations of 3D Flows Using an Adaptive Triangular Panel/Particle Method*. PhD thesis, University of Michigan, 2007.

[47] H. Feng, L. Kaganovskiy, and R. Krasny. Azimuthal instability of a vortex ring computed by a vortex sheet panel method. *Fluid dynamics research*, 41(5):051405, 2009.

[48] F. E. Fish, C. M. Schreiber, K. W. Moored, G. Liu, H. Dong, and H. Bart-Smith. Hydrodynamic performance of aquatic flapping: efficiency of underwater flight in the manta. *Aerospace*, 3(3):20, 2016.

[49] M. Gazzola, M. Argentina, and L. Mahadevan. Scaling macroscopic aquatic locomotion. *Nature Physics*, 10(10):758–761, 2014.

[50] R. Ghias, R. Mittal, and H. Dong. A sharp interface immersed boundary method for compressible viscous flows. *Journal of Computational Physics*, 225(1):528–553, 2007.

[51] A. Giacomello and M. Porfiri. Underwater energy harvesting from a heavy flag hosting ionic polymer metal composites. *Journal of Applied Physics*, 109(8):084903, 2011.

[52] S. C. Gibbs, I. Wang, and E. Dowell. Theory and experiment for flutter of a rectangular plate with a fixed leading edge in three-dimensional axial flow. *Journal of Fluids and Structures*, 34:68–83, 2012.

[53] S. C. Gibbs IV and E. H. Dowell. Membrane paradox for solar sails. *AIAA journal*, 52(12):2904–2907, 2014.

[54] S. C. Gibbs IV, I. Wang, and E. H. Dowell. Stability of rectangular plates in subsonic flow with various boundary conditions. *Journal of Aircraft*, 52(2):439–451, 2015.

[55] M. A. Golberg. *Numerical Solution of Integral Equations*. Plenum Press, 1990.

[56] R. E. Gordnier. High fidelity computational simulation of a membrane wing airfoil. *Journal of Fluids and Structures*, 25(5):897–917, 2009.

[57] R. E. Gordnier and P. J. Attar. Impact of flexibility on the aerodynamics of an aspect ratio two membrane wing. *J. Fluids and Struct.*, 45:138–152, 2014.

[58] A. Goza, T. Colonius, and J. E. Sader. Global modes and nonlinear analysis of inverted-flag flapping. *J. Fluid Mech.*, 857:312–344, 2018.

[59] K. F. Graff. *Wave motion in elastic solids*. Oxford University Press, 1975.

[60] B. E. Griffith, R. D. Hornung, D. M. McQueen, and C. S. Peskin. An adaptive, formally second order accurate version of the immersed boundary method. *Journal of Computational Physics*, 223(1):10–49, 2007.

[61] B. E. Griffith and C. S. Peskin. On the order of accuracy of the immersed boundary method: Higher order convergence rates for sufficiently smooth problems. *J. Comp. Phys.*, 208(1):75–105, 2005.

[62] A. Grozdanov. *Transonic Static Aeroelasticity Using the 2.5D Nonlinear Vortex Lattice Method*. École Polytechnique, Montréal (Canada), 2017.

[63] C. Hamlet, A. Santhanakrishnan, and L. A. Miller. A numerical study of the effects of bell pulsation dynamics and oral arms on the exchange currents generated by the upside-down jellyfish cassiopea xamachana. *Journal of Experimental Biology*, 214(11):1911–1921, 2011.

[64] K. Haruo. Flutter of hanging roofs and curved membrane roofs. *International Journal of Solids and Structures*, 11(4):477–492, 1975.

[65] J. L. Hess and A. M. O. Smith. Calculation of potential flow about arbitrary bodies. *Progress in Aerospace Sciences*, 8:1–138, 1967.

[66] K. Hiroaki, Y. Hayashi, and M. Watanabe. Numerical simulation on a limit cycle oscillation of a rectangular sheet in three-dimensional flow: influence of vortex element model on post-critical behavior. *Nonlinear Dynamics*, 106(4):2893–2917, 2021.

[67] K. Hiroaki and M. Watanabe. Theoretical study on the instability mechanism of flutter generated on a cantilevered flexible plate in three-dimensional uniform flow. *Acta Mechanica*, 232(7):2897–2917, 2021.

[68] K. Hiroaki and M. Watanabe. Three-dimensional nonlinear analysis and wind-tunnel experiment of flutter generated on a rectangular sheet in uniform flow. *Journal of Fluids and Structures*, 101:103226, 2021.

[69] R. Hooke. De Potentia Restitutiva, or of Spring. Explaining the Power of Springing Bodies. *London*, 1678.

[70] A. P. Hoover, B. E. Griffith, and L. A. Miller. Quantifying performance in the medusan mechanospace with an actively swimming three-dimensional jellyfish model. *Journal of Fluid Mechanics*, 813:1112–1155, 2017.

[71] A. P. Hoover and E. Tytell. Decoding the relationships between body shape, tail beat frequency, and stability for swimming fish. *Fluids*, 5(4):215, 2020.

[72] A. P. Hoover, N. W. Xu, B. J. Gemmell, S. P. Colin, J. H. Costello, J. O. Dabiri, and L. A. Miller. Neuromechanical wave resonance in jellyfish swimming. *Proceedings of the National Academy of Sciences*, 118(11), 2021.

[73] G. R. Hough. Remarks on vortex-lattice methods. *Journal of Aircraft*, 10(5):314–317, 1973.

[74] H. Hu, M. Tamai, and J. T. Murphy. Flexible-membrane airfoils at low Reynolds numbers. *Journal of Aircraft*, 45(5):1767–1778, 2008.

[75] W.-X. Huang, S. J. Shin, and H. J. Sung. Simulation of flexible filaments in a uniform flow by the immersed boundary method. *J. Comput. Phys.*, 226(2):2206–2228, 2007.

[76] W. X. Huang and H. J. Sung. Three-dimensional simulation of a flapping flag in a uniform flow. *Journal of Fluid Mechanics*, 653:301–336, 2010.

[77] R. M. James. On the remarkable accuracy of the vortex lattice method. *Computer Methods in Applied Mechanics and Engineering*, 1(1):59–79, 1972.

[78] J. W. Jaworski. Thrust and aerodynamic forces from an oscillating leading edge flap. *AIAA journal*, 50(12):2928–2931, 2012.

[79] J. W. Jaworski and R. E. Gordnier. High-order simulations of low Reynolds number membrane airfoils under prescribed motion. *J. Fluids and Struct.*, 31:49–66, 2012.

[80] L.-B. Jia, F. Li, X.-Z. Yin, and X.-Y. Yin. Coupling modes between two flapping filaments. *J. Fluid Mech.*, 581:199, 2007.

[81] Y. Jin, K. Jin-Tae, S. Fu, and L. P. Chamorro. Flow-induced motions of flexible plates: fluttering, twisting and orbital modes. *J. Fluid Mech.*, 864:273–285, 2019.

[82] D. J. Johns. Supersonic membrane flutter. *AIAA Journal*, 9(5):960–961, 1971.

[83] M. A. Jones. The separated flow of an inviscid fluid around a moving flat plate. *J. Fluid Mech.*, 496:405–441, 2003.

[84] M. A Jones and M. J. Shelley. Falling cards. *J. Fluid Mech.*, 540:393–425, 2005.

[85] L. Kaganovskiy. *Adaptive panel method for particle simulation of three dimensional vortex sheet motion*. PhD thesis, University of Michigan, 2006.

[86] H. Kagemoto, M. J. Wolfgang, D. K. P. Yue, and M. S. Triantafyllou. Force and power estimation in fish-like locomotion using a vortex-lattice method. *J. Fluids Eng.*, 122(2):239–253, 2000.

[87] E. Kashy, D. A. Johnson, J. McIntyre, and S. L. Wolfe. Transverse standing waves in a string with free ends. *American Journal of Physics*, 65(4):310–313, 1997.

[88] J. Katz and A. Plotkin. *Low-speed aerodynamics*, volume 13. Cambridge university press, 2001.

[89] D. Kim, J. Cossé, C. H. Cerdeira, and M. Gharib. Flapping dynamics of an inverted flag. *Journal of Fluid Mechanics*, 736, 2013.

[90] Y. Kim and C. S. Peskin. Penalty immersed boundary method for an elastic boundary with mass. *Physics of Fluids*, 19(5):053103, 2007.

[91] J. Kimball. *Physics of sailing*. CRC Press, 2009.

[92] W. C. Knudson. Recent advances in the field of long span tension structures. *Engineering Structures*, 13(2):164–177, 1991.

[93] A. Kornecki, E. H. Dowell, and J. O'Brien. On the aeroelastic instability of two-dimensional panels in uniform incompressible flow. *Journal of Sound and Vibration*, 47(2):163–178, 1976.

[94] R. Krasny. Desingularization of periodic vortex sheet roll-up. *J. Comp. Phys.*, 65(2):292–313, 1986.

[95] R. Krasny. Computation of vortex sheet roll-up in the trefftz plane. *J. Fluid Mech.*, 184:123–155, 1987.

[96] R. Krasny. Vortex sheet computations: roll-up, wakes, separation. *Lectures Appl. Math.*, 28(1):385–401, 1991.

[97] L. D. Landau and E. M. Lifshitz. *Theory of Elasticity*. Elsevier, third edition, 1986.

[98] G. V. Lauder, E. J. Anderson, J. Tangorra, and P. G. A. Madden. Fish biorobotics: kinematics and hydrodynamics of self-propulsion. *Journal of experimental biology*, 210(16):2767–2780, 2007.

[99] O. Le Maître, S. Huberson, and E. S. De Cursi. Unsteady model of sail and flow interaction. *J. Fluids and Struct.*, 13(1):37–59, 1999.

[100] G. Li, R. K. Jaiman, and B. C. Khoo. Flow-excited membrane instability at moderate reynolds numbers. *Journal of Fluid Mechanics*, 929, 2021.

[101] T. Li, G. Li, Y. Liang, T. Cheng, J. Dai, X. Yang, B. Liu, Z. Zeng, Z. Huang, Y. Luo, et al. Fast-moving soft electronic fish. *Science advances*, 3(4):e1602045, 2017.

[102] Y. Lian and W. Shyy. Numerical simulations of membrane wing aerodynamics for micro air vehicle applications. *Journal of Aircraft*, 42(4):865–873, 2005.

[103] Y. Lian, W. Shyy, D. Viieru, and B. Zhang. Membrane wing aerodynamics for micro air vehicles. *Progress in Aerospace Sciences*, 39(6-7):425–465, 2003.

[104] J. C. Liao, D. N. Beal, G. V. Lauder, and M. S. Triantafyllou. Fish exploiting vortices decrease muscle activity. *Science*, 302(5650):1566–1569, 2003.

[105] K. Lindsay and R. Krasny. A particle method and adaptive treecode for vortex sheet motion in three-dimensional flow. *Journal of Computational Physics*, 172(2):879–907, 2001.

[106] P. Liu. *A time-domain panel method for oscillating propulsors with both chordwise and spanwise flexibility*. PhD thesis, Memorial University of Newfoundland, 1996.

[107] P. Liu and N. Bose. Propulsive performance from oscillating propulsors with spanwise flexibility. *Proceedings of the Royal Society of London. Series A: Mathematical, Physical and Engineering Sciences*, 453(1963):1763–1770, 1997.

[108] L. N. Long and T. E. Fritz. Object-oriented unsteady vortex lattice method for flapping flight. *Journal of Aircraft*, 41(6):1275–1290, 2004.

[109] A. Manela and M. S. Howe. On the stability and sound of an unforced flag. *Journal of Sound and Vibration*, 321(3-5):994–1006, 2009.

[110] A. Manela and M. Weidenfeld. The 'hanging flag' problem: on the heaving motion of a thin filament in the limit of small flexural stiffness. *Journal of Fluid Mechanics*, 829:190–213, 2017.

[111] R. Margason, S. Kjelgaard, W. Sellers, III, C. Morris, Jr., K. Walkey, and E. Shields. Subsonic panel methods-a comparison of several production codes. In *23rd Aerospace Sciences Meeting*, page 280, 1985.

[112] H. Masoud and A. Alexeev. Resonance of flexible flapping wings at low reynolds number. *Physical Review E*, 81(5):056304, 2010.

[113] C. Mavroyiakoumou and S. Alben. Large-amplitude membrane flutter in inviscid flow. *J. Fluid Mech.*, 891:A23, 2020.

[114] C. Mavroyiakoumou and S. Alben. Dynamics of tethered membranes in inviscid flow. *Journal of Fluids and Structures*, 107:103384, 2021.

[115] C. Mavroyiakoumou and S. Alben. Eigenmode analysis of membrane stability in inviscid flow. *Phys. Rev. Fluids*, 6:043901, Apr 2021.

[116] S. Michelin and S. G. Llewellyn Smith. Resonance and propulsion performance of a heaving flexible wing. *Physics of Fluids*, 21(7):071902, 2009.

[117] S. Michelin, S. G. Llewellyn Smith, and B. J. Glover. Vortex shedding model of a flapping flag. *Journal of Fluid Mechanics*, 617:1–10, 2008.

[118] J. W. Miles. On the aerodynamic instability of thin panels. *Journal of the Aeronautical Sciences*, 23(8):771–780, 1956.

[119] R. Mittal, H. Dong, M. Bozkurttas, F. M. Najjar, A. Vargas, and A. Von Loebbecke. A versatile sharp interface immersed boundary method for incompressible flows with complex boundaries. *Journal of computational physics*, 227(10):4825–4852, 2008.

[120] K. W. Moored. Unsteady three-dimensional boundary element method for self-propelled bio-inspired locomotion. *Computers & Fluids*, 167:324–340, 2018.

[121] J. Mougel, O. Doaré, and S. Michelin. Synchronized flutter of two slender flags. *J. Fluid Mech.*, 801:652–669, 2016.

[122] J. Murua, R. Palacios, and J. M. R. Graham. Applications of the unsteady vortex-lattice method in aircraft aeroelasticity and flight dynamics. *Progress in Aerospace Sciences*, 55:46–72, 2012.

[123] R. Narasimha. Non-linear vibration of an elastic string. *Journal of Sound and Vibration*, 8(1):134–146, 1968.

[124] M. Nardini, S. J. Illingworth, and R. D. Sandberg. Reduced-order modeling for fluid-structure interaction of membrane wings at low and moderate Reynolds numbers. In *2018 AIAA Aerospace Sciences Meeting*, page 1544, 2018.

[125] A. H. Nayfeh and P. F. Pai. *Linear and nonlinear structural mechanics*. John Wiley & Sons, 2008.

[126] B. G. Newman. Aerodynamic theory for membranes and sails. *Progress in Aerospace Sciences*, 24(1):1–27, 1987.

[127] B. G. Newman and H. T. Low. Two-dimensional impervious sails: experimental results compared with theory. *Journal of Fluid Mechanics*, 144:445–462, 1984.

[128] B. G. Newman and M. P. Paidoussis. The stability of two-dimensional membranes in streaming flow. *J. Fluids and Struct.*, 5(4):443–454, 1991.

[129] A. T. Nguyen, J.-K. Kim, J.-S. Han, and J.-H. Han. Extended unsteady vortex-lattice method for insect flapping wings. *Journal of Aircraft*, 53(6):1709–1718, 2016.

[130] J. N. Nielsen. Theory of flexible aerodynamic surfaces. *J. Applied Mech.*, 30(3):435–442, 1963.

[131] M. Nitsche and R. Krasny. A numerical study of vortex ring formation at the edge of a circular tube. *Journal of Fluid Mechanics*, 276:139–161, 1994.

[132] M. Nitsche, M. A. Taylor, and R. Krasny. Comparison of regularizations of vortex sheet motion. In *Computational Fluid and Solid Mechanics 2003*, pages 1062–1065. Elsevier, 2003.

[133] S. Orrego, K. Shoele, A. Ruas, K. Doran, B. Caggiano, R. Mittal, and S. H. Kang. Harvesting ambient wind energy with an inverted piezoelectric flag. *Applied energy*, 194:212–222, 2017.

[134] Y. Pan, X. Dong, Q. Zhu, and D. K. P. Yue. Boundary-element method for the prediction of performance of flapping foils with leading-edge separation. *Journal of Fluid Mechanics*, 698:446–467, 2012.

[135] W. B. Pepper and R. C. Maydew. Aerodynamic decelerators-an engineering review. *Journal of Aircraft*, 8(1):3–19, 1971.

[136] C. S. Peskin. The immersed boundary method. *Acta numer.*, 11:479–517, 2002.

[137] J. Piquee, I. López, C. Breitsamter, R. Wüchner, and K.-U. Bletzinger. Aerodynamic characteristics of an elasto-flexible membrane wing based on experimental and numerical investigations. In *2018 Applied Aerodynamics Conference*, page 3338, 2018.

[138] M. Porfiri and S. D. Peterson. Energy harvesting from fluids using ionic polymer metal composites. In *Advances in Energy Harvesting Methods*, pages 221–239. Springer, 2013.

[139] D. I. Pullin and Z. J. Wang. Unsteady forces on an accelerating plate and application to hovering insect flight. *Journal of Fluid Mechanics*, 509:1–21, 2004.

[140] A. Ralston and P. Rabinowitz. *A first course in numerical analysis*. Courier Corporation, 2001.

[141] K. Ramesh, A. Gopalarathnam, K. Granlund, M. V. Ol, and J. R. Edwards. Discrete-vortex method with novel shedding criterion for unsteady aerofoil flows with intermittent leading-edge vortex shedding. *Journal of Fluid Mechanics*, 751:500–538, 2014.

[142] R. R. Rohrschneider and R. D. Braun. Survey of ballute technology for aerocapture. *Journal of Spacecraft and Rockets*, 44(1):10–23, 2007.

[143] P. Rojratsirikul, M. S. Genc, Z. Wang, and I. Gursul. Flow-induced vibrations of low aspect ratio rectangular membrane wings. *J. Fluids and Struct.*, 27(8):1296–1309, 2011.

[144] P. Rojratsirikul, Z. Wang, and I. Gursul. Unsteady fluid–structure interactions of membrane airfoils at low Reynolds numbers. *Experiments in fluids*, 46(5):859, 2009.

[145] P. Rojratsirikul, Z. Wang, and I. Gursul. Effect of pre-strain and excess length on unsteady fluid–structure interactions of membrane airfoils. *Journal of Fluids and Structures*, 26(3):359–376, 2010.

[146] P. Rojratsirikul, Z. Wang, and I. Gursul. Unsteady fluid-structure interactions of membrane airfoils at low Reynolds numbers. In *Animal Locomotion*, pages 297–310. Springer, 2010.

[147] A. M. Roma, C. S. Peskin, and M. J. Berger. An adaptive version of the immersed boundary method. *Journal of Computational Physics*, 153(2):509–534, 1999.

[148] D. Rus and M. T. Tolley. Design, fabrication and control of soft robots. *Nature*, 521(7553):467–475, 2015.

[149] P. G. Saffman. *Vortex dynamics*. Cambridge University Press, 1992.

[150] T. Sakajo. Numerical computation of a three-dimensional vortex sheet in a swirl flow. *Fluid Dynamics Research*, 28(6):423, 2001.

[151] T. Schomberg, F. Gerland, F. Liese, O. Wünsch, and M. Ruetten. Transition manipulation by the use of an electrorheologically driven membrane. In *2018 Flow Control Conference*, page 3213, 2018.

[152] R. Scott, R. Bartels, and O. Kandil. An aeroelastic analysis of a thin flexible membrane. In *48th AIAA/ASME/ASCE/AHS/ASC Structures, Structural Dynamics, and Materials Conference*, page 2316, 2007.

[153] M. J. Shelley, N. Vandenberghe, and J. Zhang. Heavy flags undergo spontaneous oscillations in flowing water. *Physical Review Letters*, 94(9):094302, 2005.

[154] M. J. Shelley and J. Zhang. Flapping and bending bodies interacting with fluid flows. *Annual Review of Fluid Mechanics*, 43:449–465, 2011.

[155] J. X. Sheng, A. Ysasi, D. Kolomenskiy, E. Kanso, M. Nitsche, and K. Schneider. Simulating vortex wakes of flapping plates. In *Natural locomotion in fluids and on surfaces*, pages 255–262. Springer, 2012.

[156] R. K. Shukla and J. D. Eldredge. An inviscid model for vortex shedding from a deforming body. *Theoretical and Comput. Fluid Dyn.*, 21(5):343, 2007.

[157] W. Shyy, M. Berg, and D. Ljungqvist. Flapping and flexible wings for biological and micro air vehicles. *Progress in Aerospace Sciences*, 35(5):455–505, 1999.

[158] A. Song, X. Tian, E. Israeli, R. Galvao, K. Bishop, S. Swartz, and K. Breuer. Aeromechanics of membrane wings with implications for animal flight. *AIAA journal*, 46(8):2096, 2008.

[159] J. H. Spriggs, A. F. Messiter, and W. J. Anderson. Membrane flutter paradox-an explanation by singular-perturbation methods. *AIAA Journal*, 7(9):1704–1709, 1969.

[160] B. Stanford, P. Ifju, R. Albertani, and W. Shyy. Fixed membrane wings for micro air vehicles: Experimental characterization, numerical modeling, and tailoring. *Progress in Aerospace Sciences*, 44(4):258–294, 2008.

[161] K. Stein, R. Benney, V. Kalro, T. E. Tezduyar, J. Leonard, and M. Accorsi. Parachute fluid–structure interactions: 3-D computation. *Computer Methods in Applied Mechanics and Engineering*, 190(3-4):373–386, 2000.

[162] X. Sun, S.-Z. Wang, J.-Z. Zhang, and Z.-H. Ye. Bifurcations of vortex-induced vibrations of a fixed membrane wing at Re $\leq$ 1000. *Nonlinear Dynamics*, 91(4):2097–2112, 2018.

[163] M. R. Sunny, C. Sultan, and R. K. Kapania. Optimal energy harvesting from a membrane attached to a tensegrity structure. *AIAA journal*, 52(2):307–319, 2014.

[164] S. Swartz, J. Iriarte-Diaz, D. Riskin, X. Tian, A. Song, and K. Breuer. Wing structure and the aerodynamic basis of flight in bats. In *45th AIAA Aerospace Sciences Meeting and Exhibit*, page 42, 2007.

[165] S. M. Swartz, M. S. Groves, H. D. Kim, and W. R. Walsh. Mechanical properties of bat wing membrane skin. *Journal of Zoology*, 239(2):357–378, 1996.

[166] R. Sygulski. Dynamic stability of pneumatic structures in wind: theory and experiment. *Journal of fluids and structures*, 10(8):945–963, 1996.

[167] R. Sygulski. Numerical analysis of membrane stability in air flow. *Journal of sound and vibration*, 201(3):281–292, 1997.

[168] R. Sygulski. Stability of membrane in low subsonic flow. *Inter. J. of Non-Lin. Mech.*, 42(1):196–202, 2007.

[169] I. Tadjbakhsh. The variational theory of the plane motion of the extensible elastica. *International Journal of Engineering Science*, 4(4):433–450, 1966.

[170] E. B. Tadmor, R. E. Miller, and R. S. Elliott. *Continuum mechanics and thermodynamics: from fundamental concepts to governing equations*. Cambridge University Press, 2012.

[171] K. Taira and T. Colonius. The immersed boundary method: a projection approach. *Journal of Computational Physics*, 225(2):2118–2137, 2007.

[172] M. Tamai, J. Murphy, and H. Hu. An experimental study of flexible membrane airfoils at low reynolds numbers. In *46th AIAA Aerospace Sciences Meeting and Exhibit*, page 580, 2008.

[173] S. Taneda. Waving motions of flags. *J. Phys. Soc. Jpn*, 24:392–401, 1968.

[174] C. Tang, H. Huang, P. Gao, and X.-Y. Lu. Self-propulsion of a flapping flexible plate near the ground. *Physical Review E*, 94(3):033113, 2016.

[175] D. Tang and E. H. Dowell. Effects of angle of attack on nonlinear flutter of a delta wing. *AIAA journal*, 39(1):15–21, 2001.

[176] D. Tang, E. H. Dowell, and K. C. Hall. Limit cycle oscillations of a cantilevered wing in low subsonic flow. *AIAA journal*, 37(3):364–371, 1999.

[177] D. M. Tang, H. Yamamoto, and E. H. Dowell. Flutter and limit cycle oscillations of two-dimensional panels in three-dimensional axial flow. *Journal of Fluids and Structures*, 17(2):225–242, 2003.

[178] L. Tang, M. P. Païdoussis, and J. Jiang. Cantilevered flexible plates in axial flow: energy transfer and the concept of flutter-mill. *Journal of Sound and Vibration*, 326(1-2):263–276, 2009.

[179] L. Tang, M. P. Païdoussis, and J. Jiang. The dynamics of variants of two-dimensional cantilevered flexible plates in axial flow. *Journal of Sound and Vibration*, 323(1-2):214–231, 2009.

[180] F. Tian, X. Lu, and H. Luo. Onset of instability of a flag in uniform flow. *Theoretical and Applied Mechanics Letters*, 2(2):022005, 2012.

[181] F.-B. Tian, H. Luo, L. Zhu, J. C. Liao, and X.-Y. Lu. An efficient immersed boundary-lattice Boltzmann method for the hydrodynamic interaction of elastic filaments. *Journal of Computational Physics*, 230(19):7266–7283, 2011.

[182] A. Timpe, Z. Zhang, J. Hubner, and L. Ukeiley. Passive flow control by membrane wings for aerodynamic benefit. *Experiments in fluids*, 54(3):1471, 2013.

[183] S. Tiomkin and J. W. Jaworski. Unsteady aerodynamic theory for membrane wings. *arXiv preprint arXiv:2204.01204*, 2022.

[184] S. Tiomkin and D. E. Raveh. On the stability of two-dimensional membrane wings. *J. Fluids and Struct.*, 71:143–163, 2017.

[185] S. Tiomkin and D. E. Raveh. A review of membrane-wing aeroelasticity. *Progress in Aerospace Sciences*, 126:100738, 2021.

[186] L. P. Tosi and T. Colonius. Modeling and simulation of a fluttering cantilever in channel flow. *J. Fluids and Struct.*, 89:174–190, 2019.

[187] L. Tregidgo, Z. Wang, and I. Gursul. Unsteady fluid–structure interactions of a pitching membrane wing. *Aerospace Science and Technology*, 28(1):79–90, 2013.

[188] M. S. Triantafyllou and C. T. Howell. Dynamic response of cables under negative tension: an ill-posed problem. *Journal of sound and vibration*, 173(4):433–447, 1994.

[189] M. S. Triantafyllou, G. S. Triantafyllou, and D. K. P. Yue. Hydrodynamics of fishlike swimming. *Annual review of fluid mechanics*, 32(1):33–53, 2000.

[190] E. D. Tytell, C.-Y. Hsu, T. L. Williams, A. H. Cohen, and L. J. Fauci. Interactions between internal forces, body stiffness, and fluid environment in a neuromechanical model of lamprey swimming. *Proceedings of the National Academy of Sciences*, 107(46):19832–19837, 2010.

[191] G. A. Tzezana and K. S. Breuer. Thrust, drag and wake structure in flapping compliant membrane wings. *Journal of Fluid Mechanics*, 862:871–888, 2019.

[192] H. M. Voss. The effect of an external supersonic flow on the vibration characteristics of thin cylindrical shells. *Journal of the Aerospace Sciences*, 28(12):945–956, 1961.

[193] R. M. Waldman and K. S. Breuer. Shape, lift, and vibrations of highly compliant membrane wings. In *43rd AIAA Fluid Dynamics Conference*, page 3177, 2013.

[194] R. M. Waldman and K. S. Breuer. Camber and aerodynamic performance of compliant membrane wings. *Journal of Fluids and Structures*, 68:390–402, 2017.

[195] X. Wang, S. Alben, C. Li, and Y. L. Young. Stability and scalability of piezoelectric flags. *Physics of Fluids*, 28(2):023601, 2016.

[196] Y. Watanabe, S. Suzuki, M. Sugihara, and Y. Sueoka. An experimental study of paper flutter. *J. Fluids and Struct.*, 16(4):529–542, 2002.

[197] P. D. Welch. The use of fast fourier transform for the estimation of power spectra: a method based on time averaging over short, modified periodograms. *IEEE Transactions on Audio and Electroacoustics*, 15(2):70–73, 1967.

[198] C. H. K. Williamson and A. Roshko. Vortex formation in the wake of an oscillating cylinder. *Journal of Fluids and Structures*, 2(4):355–381, 1988.

[199] D. J. Willis, E. Israeli, P.-O. Persson, M. Drela, J. Peraire, S. Swartz, and K. Breuer. A computational framework for fluid structure interaction in biologically inspired flapping flight. In *25th AIAA Applied Aerodynamics Conference*, page 3803, 2007.

[200] D. J. Willis, J. Peraire, and J. K. White. A quadratic basis function, quadratic geometry, high order panel method. In *44th AIAA Aerospace Sciences Meeting and Exhibit*, page 1253, 2006.

[201] D. J. Willis, J. Peraire, and J. K. White. A combined pFFT-multipole tree code, unsteady panel method with vortex particle wakes. *International Journal for numerical methods in fluids*, 53(8):1399–1422, 2007.

[202] D. J. Willis and P.-O. Persson. Multiple-fidelity computational framework for the design of efficient flapping wings. *AIAA journal*, 52(12):2840–2854, 2014.

[203] L. Xu, M. Nitsche, and R. Krasny. Computation of the starting vortex flow past a flat plate. *Procedia IUTAM*, 20:136–143, 2017.

[204] S. Yang and C. Sultan. Modeling of tensegrity-membrane systems. *International Journal of Solids and Structures*, 82:125–143, 2016.

[205] D. T. Yeh and A. Plotkin. Vortex panel calculation of wake rollup behind a large aspect ratio wing. *AIAA journal*, 24(9):1417–1423, 1986.

[206] Z. Yu, Y. Wang, and X. Shao. Numerical simulations of the flapping of a three-dimensional flexible plate in uniform flow. *Journal of Sound and Vibration*, 331(20):4448–4463, 2012.

[207] J. Zhang, S. Childress, A. Libchaber, and M. Shelley. Flexible filaments in a flowing soap film as a model for one-dimensional flags in a two-dimensional wind. *Nature*, 408(6814):835–839, 2000.

[208] W. Zhao, M. P. Païdoussis, L. Tang, M. Liu, and J. Jiang. Theoretical and experimental investigations of the dynamics of cantilevered flexible plates subjected to axial flow. *Journal of Sound and Vibration*, 331(3):575–587, 2012.

[209] L. Zhu, G. He, S. Wang, L. Miller, X. Zhang, Q. You, and S. Fang. An immersed boundary method based on the lattice Boltzmann approach in three dimensions, with application. *Computers & Mathematics with Applications*, 61(12):3506–3518, 2011.

[210] L. Zhu and C. S. Peskin. Simulation of a flapping flexible filament in a flowing soap film by the immersed boundary method. *J. Comput. Phys.*, 179:452–468, 2002.

[211] Q. Zhu, M. J. Wolfgang, D. K. P. Yue, and M. S. Triantafyllou. Three-dimensional flow structures and vorticity control in fish-like swimming. *Journal of Fluid Mechanics*, 468:1–28, 2002.